INVESTIGATION ON THE DYNAMICS OF FLEXIBLE FILAMENTS IN VISCOUS FLUID

Thesis

Submitted in partial fulfilment of the requirements for the degree of

DOCTOR OF PHILOSOPHY

By

MITHUN VIJAY KANCHAN

DEPARTMENT OF MECHANICAL ENGINEERING

NATIONAL INSTITUTE OF TECHNOLOGY KARNATAKA,
SURATHKAL, MANGALORE – 575025

October 2020

Dedicated to my parents

DECLARATION

I hereby declare that the Research Thesis entitled **"Investigation on the Dynamics of Flexible Filaments in Viscous Fluid"** which is being submitted to the **National Institute of Technology Karnataka, Surathkal** in partial fulfillment of the requirements for the award of the Degree of **Doctor of Philosophy** in **Mechanical Engineering** is a *bonafide report of the research work carried out by me*. The material contained in this Research Thesis has not been submitted to any other Universities or Institutes for the award of any degree.

Register Number: **165011 ME16F08**

Name of the Research Scholar: **MITHUN VIJAY KANCHAN**

Signature of the Research Scholar:

Department of Mechanical Engineering

Place: NITK-Surathkal

Date: 12-10-2020

CERTIFICATE

This is to certify that the Research Thesis entitled **"Investigation on the Dynamics of Flexible Filaments in Viscous Fluid"** submitted by **Mr. Mithun Vijay Kanchan (Register Number: 165011 ME16F08)** as the record of the research work carried out by him, *is accepted as the Research Thesis submission* in partial fulfilment of the requirements for the award of the Degree of **Doctor of Philosophy.**

Dr. RANJITH M

Research Guide

Chairman-DRPC

Date: 13/10/2020

ACKNOWLEDGEMENT

ABSTRACT

Many chemical and biological systems have applications involving fluid-structure interaction (FSI) of flexible filaments in viscous fluid. The dynamics of single and multiple filament interaction is of interest to engineers and biologists working in the area of DNA fragmentation, protein synthesis, polymer segmentation etc. Some other important applications involve mixing enhancement, fluid pumping, flow rate control and drug delivery. The FSI simulations related to these applications are challenging to numerically implement. In this direction, techniques like immersed boundary method (IBM) have proved to be quite successful. In the present study, two-dimensional computational models based on finite volume immersed boundary method is developed in order to understand the dynamics and interaction of flexible filaments in different fluid flow conditions like uniform flow, shear flow and oscillatory flow. However, in order to familiarize with the implementation of immersed boundary method, a preliminary work is done to study the fluid flow behaviour in straight and wavy rigid walled channels by modelling the walls as immersed boundaries.

In the preliminary study, the continuity and Navier-Stokes equations governing the flow are solved by fractional step based finite volume method on a staggered Cartesian grid system. Fluid variables are described by Eulerian co-ordinates and solid boundary by Lagrangian co-ordinates. A four-point Dirac delta function is used to couple both the co-ordinate variables. A momentum forcing term is added to the Navier-Stokes equation in order to impose the no-slip boundary condition on the rigid wavy wall. A computer code is developed to perform numerical simulations. Parametric study is carried out to analyse passive mixing effects and fluid flow characteristics by varying amplitude and wavelength of wavy wall configurations for different Reynolds number. Configurations of wavy walls having larger amplitude (A = 0.14) and intermediate wavelength (WL = 1.0) are preferred. From this work, it is evident that incorporating rigid wavy walled passive modulators prove to be good and robust method for enhancing mixing in bio-medical devices. The preliminary computational model is extended by modelling flexible filament with additional structural forces like stretching/compression and bending. The fractional step

method is also replaced by SIMPLE algorithm to solve the fluid velocity and pressure terms of the governing equations. With the help of this extended model, simulations are carried out in various phases depending on the interaction of flexible filament with incoming fluid under different channel flow conditions.

In the first phase, the flexible filament is modelled as diatom chain interacting in oceanic shear flow. The computational model is first verified with the deformation study of a tethered flexible filament in uniform fluid flow. Next, the shape deformations for flexible filament placed freely in shear flow are compared with the studies of previous researchers. Finally, the present results are validated with Jeffery's equation for particles immersed in shear flow along with classification plot for filament orbit regimes. All of these comparisons provide a reasonable validity for the present model. The effect of bending rigidity and shear rate on the deformation and migration characteristics is ascertained with the help of parametric studies. A non-dimensional parameter called viscous flow forcing value (VFF) is calculated to quantify the parametric results. An optimum VFF value is determined which indicates the transition of filaments exhibiting either a recuperative (regaining original shape past deformation) or non-recuperative (permanently deformed) behaviour. The present model is thus successful in capturing fluid motion, buckling, shape recurrences and recuperation dynamics of diatom chains subjected to shear flow.

In the second phase, two cases of oscillatory flow conditions are used with the flexible filament tethered at the centre of bottom channel wall. The first case is sinusoidal oscillatory flow with phase shift (SOFPS) and second case is sinusoidal oscillatory flow without phase shift (SOF). The simulation results are validated with filament dynamics studies of previous researchers. Further, parametric analysis is carried to study the effect of filament length, filament bending rigidity and Reynolds number on the complex deformation and behaviour of flexible filament interacting with nearby oscillating fluid motion. It is found that selection of right filament length and bending rigidity is crucial for fluid mixing scenarios. The phase shift in fluid motion is also found to critically effect filament displacement dynamics especially for rigid filaments. Symmetric deformation is

observed for filaments subjected to SOFPS condition irrespective of bending rigidity whereas medium and low rigidity filaments placed in SOF condition show severe asymmetric behaviour. Two key findings of this study are - 1) Symmetric filament conformity without appreciable bending produces sweeping motion in fluid flow which is highly suited for mixing application and 2) Asymmetric behaviour shown by the filament depicts antiplectic metachronism commonly found in beating cilia. As a result, it is possible to pin point the type of fluid motion governing fluid mixing and fluid pumping.

In the third phase, two-dimensional numerical simulation of flexible membrane fixed at two end points and subjected to uniform fluid flow is carried out at low Reynolds number in a rectangular channel. The model is validated using previous research work and numerical simulations are carried out for different parametric test cases. Different membrane conformations or mode shapes are observed due to the complex interplay between the hydrodynamics and structural elastic forces. Since the membrane undergoes deformation with respect to inlet fluid conditions, a variation in flow rate past the flexible structure is confirmed. It is found that, by changing the membrane length, bending rigidity and its initial position in the channel, flow rate can be controlled. Also, for membranes that are placed at the channel mid-plane undergoing self-excited oscillations there exists a critical dimensionless membrane length condition $L > =1.0$ that governs this behaviour. Also, an artificial neural network (ANN) model is developed that successfully predicts flow rate in the channel for different membrane parameters.

Finally, the dynamics and mutual interaction of two flexible filaments placed side-by-side in shear flow is studied. Viscous flow forcing value (VFF) and fractional contraction terms are incorporated so as to effectively categorize filament motion into various deformation regimes. A detailed analysis is carried out to study the effects of tumbling motion on the filament migration and recuperative aspects. Also, an artificial neural network (ANN) model is developed from the immersed boundary simulation results to predict tumbling counts for different filament parameters.

x

TABLE OF CONTENTS

LIST OF FIGURES

LIST OF TABLES

NOMENCLATURE

A	Amplitude of wavy wall
D	Distance between two filament mid-points
d_{ee}	Filament end-to-end distance
F(s,t)	Dimensionless Lagrangian forcing term
f	frequency of oscillation
f(x,t)	Dimensionless momentum forcing term
H	Dimensionless channel height
H_y	Dimensionless position of membrane with respect to channel height
H/L_c	Channel geometry ratio
h	Eulerian grid size
K	Dimensionless shear rate
K_s	Membrane stretching co-efficient
K_b	Membrane bending rigidity
L_{ref}	Characteristic length scale
L_c	Dimensionless channel length
L	Dimensionless filament length
L/H	Filament aspect ratio
L_x	Dimensionless position of membrane leading edge
n	initial time level
p	Dimensionless fluid pressure
Re	Reynolds number
r	Distance between immersed boundary point and neighbouring fluid grid point
St	Strouhal number
s	Lagrangian material point
t	Dimensionless time
t_{sb}	Dimensionless symmetry breakage time

t_p	Dimensionless turning point time
t_d	Dimensionless deformation time
t_r	Dimensionless recurrence time
U(s,t)	Dimensionless Lagrangian velocity
u_{ref}	Characteristic velocity scale
u(x,t)	Dimensionless fluid velocity
WL	Wavelength of wavy wall
X	Dimensionless position vector of IB points (Lagrangian)
x	Dimensionless position vector of fluid grid (Eulerian)
Δt	Time step
Δs	Distance between two successive immersed boundary points

Greek symbols

α	Angle made by the filament with respect to vertical plane
β	Exterior angle defined between end points of the filament
δ (**x-X**)	Discrete dirac delta function
ε	Filament length error
θ	Angle made by the filament with respect to horizontal plane
μ	Fluid viscosity (kg/m.s)
ρ	Fluid density (kg/m^3)
φ	Probability distribution of time spent by filament at various angles
ϕ	Pseudo pressure term

Superscripts

*	Dimensional value

CHAPTER 1

1 INTRODUCTION

Microfluidics is a multidisciplinary field mainly concerned with fluids that are geometrically constrained to a small, typically sub-millimetre scale. Many practical applications use microfluidics that involve processing a small volume of fluid to achieve functions such as high-throughput screening, automation, multiplexing etc. Microfluidics is interlinked to various fields such as engineering, biotechnology, microbiology, nanotechnology and other applied areas. The emergence of microfluidics can be traced back to 1980s and since then it has been used in the development of various technologies like lab-on-chip, organ-on-chip, DNA strips, inkjet head and micro-devices for propulsion and heat transfer. There is a great challenge involved in manipulating and precisely controlling the flow characteristic of fluids at such miniature scales that require mixing, moving, sorting and other related processing to be done. The fluid motion can be induced either passively or actively. A well-known example of fluid control done in a passive manner is the application of capillary forces or introduction of geometric constraints in flow direction. On the other hand active manipulation or directed movement of working media involves use of micro-components such as micro-pumps or micro-valves for transporting fluid on passive chips. Many tests that are conducted in labs can be converted into miniaturized versions on a single microfluidic chip in order to enhance mobility and efficiency. This also helps in reducing reagent and sample volumes. The area of biomedical microfluidics is thus been an active research component for the last few years. In order to design and fabricate microfluidic devices, it is very important to have a   better understanding of its fluid flow behaviour. This can be achieved either experimentally, analytically or numerically. With recent advances in technologies such as particle image velocimetry (PIV), it is possible to study microfluidic devices and their respective flow physics. However, such methods are limited in revealing the detailed hydrodynamics and are also proved to be expensive and time consuming. Analytical studies rely on approximations and physical assumptions which hinder revelation of significant

information. The above limitations facilitated the development of numerical models and techniques to solve microfluidics based problems. Computational fluid dynamics (CFD) has evolved into an ever growing field that has served engineers and researchers all around the globe in performing numerical simulations based on microfluidic systems. The numerical models developed with the help of CFD has helped in providing detailed information that even experimental studies could not reveal. Also, it provides a convenient way for analysing the effect of different physical parameters that govern the flow physics. This has resulted in optimum design and development of various microfluidic based technologies for the above mentioned applications.

1.1   Fluid-structure interaction

Microfluidics can be combined with CFD techniques to tackle various problems related to fluid-structure interaction (FSI) for biomedical applications. In FSI, the complex interplay between solid structures and surrounding internal or external fluids is carefully studied. A broad range of effects can be observed when fluid interacts with micro-organisms. In Figure 1.1, various FSI examples are given as follows. (1) Periodic rotation (Jeffery orbits) of non-motile phytoplankton cells such as diatoms, (2) Trajectory of motile bacteria for different shear magnitudes, (3) Jeffery orbits of non-motile bacterium, (4) Gyrotaxis of phytoplankton, (5) Gyrotactic trapping of phytoplankton, (6) Upstream swimming of bacteria, (7) Upstream twitching of bacteria and (8) Surface colonization by a stalked, curved bacterium under flow. The first example in Figure 1.1 is quite interesting as it deals with FSI of a group of diatoms, non-motile unicellular phytoplankton that form the primary foundation of aquatic food webs. While it is unicellular, diatoms have developed the ability to form colonies as chains linked together. The phytoplankton lives in these chains whose size vary from 5 micrometres to a few millimetres (Guasto et al. 2012). The mechanical properties of these chains change according to morphology and linking structure material. The diatoms are also photosynthetic micro-organisms which require dissolved nutrients in the form of nitrates, phosphates, etc., delivered to the surface of its cells by fluid motion. The ability of the diatoms to uptake nutrients depends on its

interaction with surrounding fluid thus highlighting that ambient fluid motion is crucial for survival. Other examples illustrated in Figure 1.1 focus on the swimming behaviour of bacterium under different flow conditions.
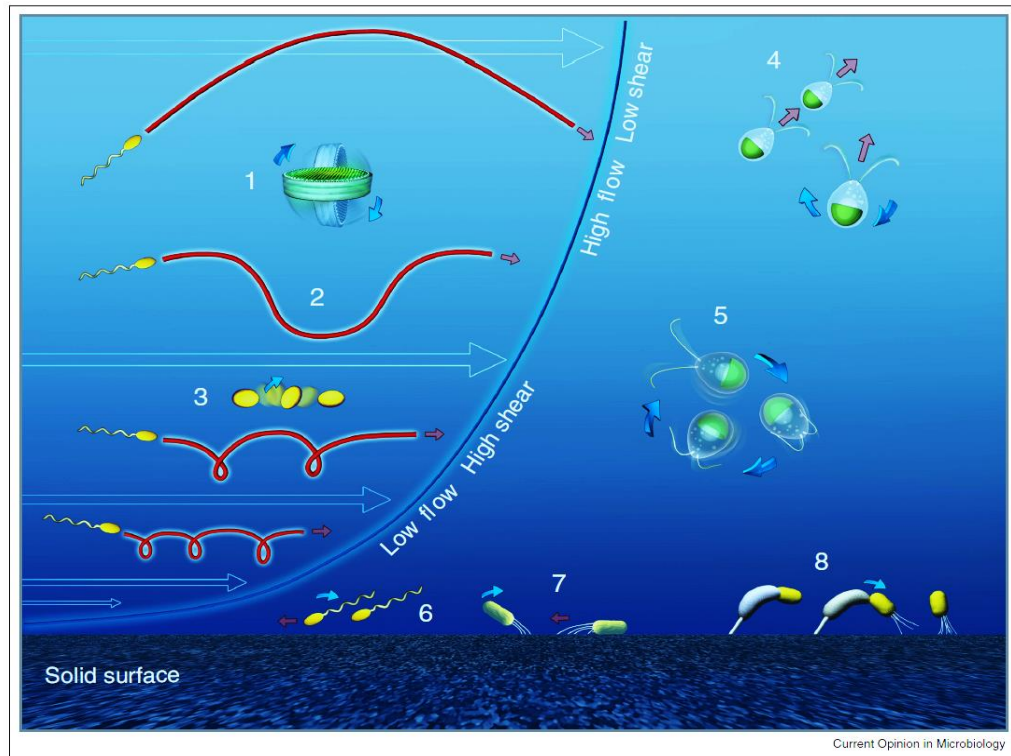
Figure 1.1 Fluid interaction effects on micro-organisms, both in the bulk fluid and vicinity of surfaces. The arrows and line define velocity profile of the flow. The flow velocity is zero at the solid surface (no-slip boundary condition). Image taken from (Rusconi and Stocker 2015).

Flagellum and cilium are basically thin, membrane extensions of cells that produce a regular beating pattern. This natural mechanism causes many bacterial organisms and sperms to swim, as well as aids in mucus transport in oviducts and human lungs. The propulsion and beating pattern of these flexible structures are shown in Figure 1.2. *Escherichia coli* is another example of multi-flagellated bacterium that uses rotating helical filaments to propel in fluids. The counter clockwise rotation of the flagella causes it to bundle and a behaviour of bacteria called 'run' is observed. When the flagellar motors

reverse their direction, a behaviour called 'tumble' is seen that leads to erratic movement of bacterial cell.
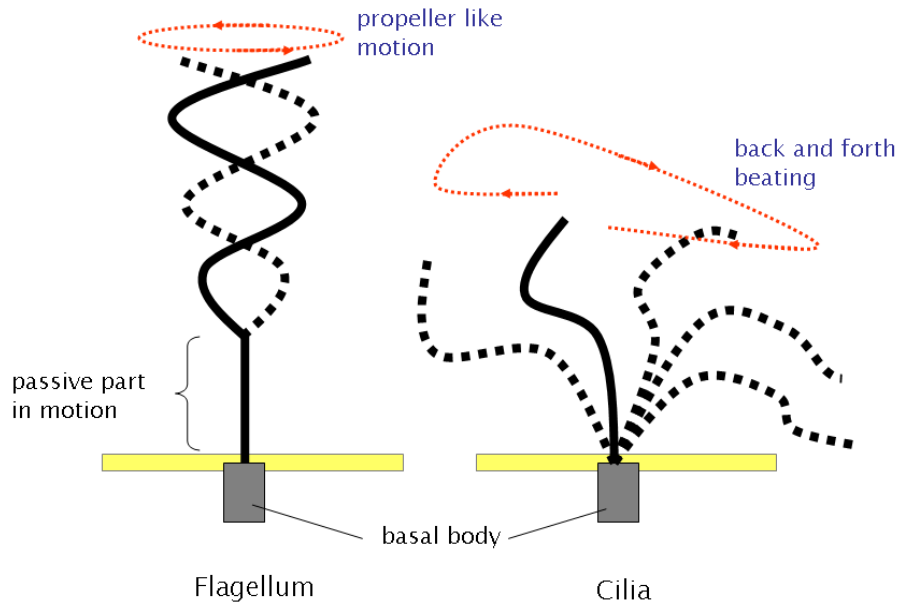
Figure 1.2 Flagellum propulsion and cilia beating. Image credits to Kohidai, L 2008.

The above mentioned behaviour of bacterial flagellum/microfibers can be employed to develop bio-inspired artificial robots. An ancient biological phenomenon on the evolutionary point of view is the beating mechanism of cilia. This beating pattern contains two phases: one is effective stroke where the cilium moves closely resembling a straight rod, and other is recovery stroke where the cilium deforms into a tangential motion by rolling close to its surface. The role of these two phases from a design perspective is that the effective stroke uses the strong viscous effect of fluid and develops thrust while the recovery stroke brings the cilium back to its original position by preventing any viscous resistance. Many such cilium beating in co-ordination is referred to as metachronism. It is thus believed to be result of an autonomous hydrodynamic interaction in the system. This metachronism function of cilia can be used to generate fluid flow in the required direction. They can also be used to propel cells, particles or mucus layers through a given fluid medium. A common aspect that is noticed in non-motile diatom linked chains, flagellar propulsion and beating cilia is that these biological microfilaments can be modelled as

4

flexible fibres either moving or fixed at a location in the flow field. Thus, the deformability, dynamics of filaments and their interaction with stationary and flowing fluids can be investigated by accurate modelling of flexible fibres.

In order to better understand the transport and suspension properties of biological micro-molecules, it is necessary to investigate the behaviour of elastic filaments in parallel wall micro-channels subjected to pressure driven flow. Deformation and migration of flexible filaments is mainly due to the dynamic change of shape along the length of the channel and due to confinement effects of impenetrable wall. However, the fundamental question that remains a mystery despite decades of theoretical studies is regarding the mobility and deformation of these biological macro-molecules due to hydrodynamic interaction from surrounding fluid motion. The factors which affect dynamics of filament in micro-channels are filament contour length, Reynolds number, viscosity ratio of filament and surrounding fluid, conformation of filament, location of filament, stiffness of filament and critical distance of migration. Flexible molecules undergo deformation and migrate away from the confined walls which involve phenomenon such as folding and unfolding sequence, bending, stretching etc., whereas stiff fibres tend to accumulate near the walls with slight bending (Slowicka et al. 2015). A higher level of complexity arises when more than one filaments are used in the study. The ability to sort, manipulate and analyse single or multiple biomolecules in micro-channel based devices is key to several applications involving microfluidics, DNA segmentation and fragmenting, biotechnology, cell movement, drug delivery etc. (Slowicka et al. 2012). It is thus possible to study and analyse a large group of problems involving deformation, migration, suspension, entanglement and flocculation of individual and multiple flexible filaments interacting in viscous fluid medium.

Even though FSI plays a crucial role in many engineering and scientific areas, the multidisciplinary nature of this field poses several challenges for comprehensive study. Over the years researchers have developed various analytical and theoretical models to study interaction of filaments in viscous fluid. Slender body theory, resistive force theory,

multi-pole expansion method, multi-particle collision dynamics, dumbbell kinetic theory and bead model to name a few of them. As mentioned earlier these methods rely on assumptions and approximations thus avoiding useful information. Also, the problems pertaining to flexible filaments deforming in viscous fluids are often too difficult to solve analytically and so experiments or numerical simulation is necessary for accurate analysis. Since experiments have to be carried out at micro-channels of sizes below 1 mm, with the deforming molecules in the range of nanometre, various complications and inaccuracies are observed. This is mainly due to the optical techniques used at these levels which lead to compromise between spatial and temporary resolution. Developing a cost effective and efficient numerical model is essential in this situation. With the advent of computer technology, scientific computing has become complicated and sophisticated. The numerical procedure that has been employed over the years to solve FSI problems can be classified into two approaches: the monolithic approach and partitioned approach. In monolithic approach, the mathematical framework related to structure and fluid dynamics is treated as a single set of governing equations. An unified algorithm can be used to solve the resulting equations simultaneously for the entire problem. The interface with regards to solution procedure is usually implicit in nature. The monolithic approach provides better accuracy for a large set of multidisciplinary problems, but requires expertise and resources to develop and maintain specialized code. In partitioned approach, the structural and fluid governing equations are solved separately and a coupling algorithm is used to combine the solution schemes of both these interfaces. The FSI problems can be further grouped based upon how the meshes are treated, i.e. conforming meshes or non-conforming meshes. In conforming meshes, the interface conditions are treated as physical boundary conditions and interface locations are taken as part of the solution. Thus, the meshes have to conform to the interface. Any form of deformation or movement of the solid boundary results in mesh update or re-meshing as the solution advances. The non-conforming meshes on the other hand, treat the interface conditions and boundary locations as constraints imposed on the governing equations. This results in a convenient solution of solid equations and fluid

6

equations on their respective grids independent of each other without any form of re-meshing.

When a grid-based simulation technique is used to study FSI, it is always convenient to describe the fluid region as a Eulerian frame of reference and the solid region as a Lagrangian formulation. Meshing techniques in FSI can be grouped into body-fitted/conformal methods and non-conformal methods. Body-fitted methods consist of widely known Arbitrary Lagrangian-Eulerian formulation (ALE) which use the finite element method (FEM) (Hu et al. 2001). For complex geometries, however, the quality of the grid may deteriorate since the mesh has to adapt to the moving boundaries and an iterative grid refinement algorithm may be required to prevent convergence failure. There are other numerical methods such as fictitious-domain method (DLM), smooth particle hydrodynamics (SPH) (Li et al. 2018) and lattice Boltzmann method (LBM) that avoid grid conformation and provide better fluid-structure coupling capabilities. An approach of simulating flexible structure and fluid interaction problems using computational grid based numerical methods using immersed boundary method has gained popularity in recent years. Combined strategies involving IB-LBM have also been extensively studied for fluid and thermal problems (Adeeb et al. 2018; Bamiro and Liou 2013). DLM and LBM were initially developed for fluid-structure interaction problems involving rigid bodies (Ladd 1994; Krafczyk et al. 2001; Lallemand and Luo 2003; Diaz-Goano et al. 2003; Ardekani et al. 2008) while IBM could handle thin elastic structures like membranes and filaments. A more elaborate discussion on IBM is provided here.

1.2 Immersed boundary method

Immersed boundary method (IBM) is a class of FSI methods that is based upon the framework of monolithic, non-conforming mesh methods. In IBM, a momentum forcing term is included in governing fluid equations to incorporate the effect of structure or imposition of no-slip condition due to presence of structure on the fluid domain. This helps to prevent updating mesh in the numerical procedure. The immersed boundary can be either two-dimensional or three-dimensional elastic or rigid structures. The original IBM was

developed by Peskin in 1977 in order to study blood flow in heart and since then has been extensively applied to a wide variety of FSI problems. Some examples include cell and capsule deformation (Rejniak and Dillon 2007; Huang et al. 2012; Shin and Sung 2012; Kim et al. 2015), locomotion of jellyfish (Huang and Sung 2009; Park et al. 2014; Park et al. 2015), flagellum of bacteria (Qin et al. 2012; Maniyeri et al. 2012; Maniyeri and Kang 2014a, 2014b), two- and three-dimensional parachute aerodynamics (Kim and Peskin 2006; Kim and Peskin 2009), droplet dynamics in shear flow (Hua et al. 2014), valveless pumping (Shin and Sung 2010; Shin et al. 2012), flexible propulsor and fins (Kim et al. 2016; Kim et al. 2017), multiphase flow (Francois et al. 2004), immersed heat transfer (Shu et al. 2013; De Marinis et al. 2016; Santarelli et al. 2016) etc. The fluid domain, on one hand, is discretized using Eulerian grids while on the other the immersed boundary is discretized by moving Lagrangian grid points, also called IB points. An immersed boundary illustration is provided in Figure 1.3.
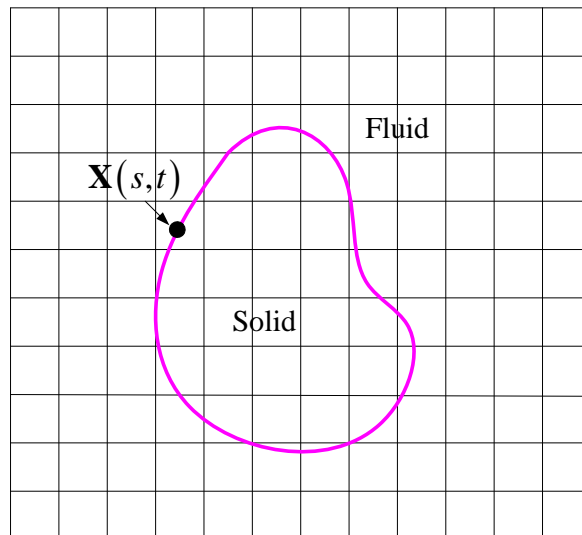
Figure 1.3 Illustration of the immersed boundary method. The boundaries are represented by Lagrangian points and the fluid by Eulerian grid points.

The traction jump across the immersed boundary is modified into body force, which gets distributed onto the fluid volumetric mesh in vicinity of boundary. Thus, to account for the presence of structure and to impose no-slip boundary condition, a momentum

forcing term is added to the Navier–Stokes equations. If the momentum forcing term is unified into the governing equation before discretization, then such a method is called Continuous forcing approach (Mittal and Iaccarino 2005). Here the formulation occurs irrespective of the original spatial discretization. The interaction between the Eulerian variables and Lagrangian variables can be modelled by a well-chosen Dirac delta function which smoothens the sharp interface caused by the presence of solid structure. No form of discontinuity arises in solution across the immersed surface. Continuous forcing approach as originally introduced by Peskin, is naturally well suited for elastic bodies. Irrespective of the shape and geometric features of the structure, IBM has been quite powerful with regards to computational efficiency. Thus the present work uses continuous forcing based immersed boundary method to numerically solve fluid-structure interaction problems related to flexible filaments in viscous fluid flow.

In order to understand the effect of various structural and fluid flow parameters on the dynamics and mutual interaction of flexible filaments in viscous fluid flow, it is possible to carry out IBM based simulations for few parametric test cases. The results obtained from IBM simulations can be used to develop empirical models that can accurately perform predictions for different input parametric conditions. In this direction, development of prediction model based on artificial neural networks are quite popular.

1.3 Artificial neural networks

The results obtained from numerical simulations can be used to develop mathematical models that can accurately perform predictions for different input parametric conditions. One such technique commonly used for non-linear systems is artificial neural networks (ANN). ANN is inspired by the human brain system. They have the ability to learn, memorize and develop relationship between seemingly random data. This gives it an ability to solve new problems based on the information obtained from past experience. ANN is made up of three basic building blocks i.e., network architecture, training method and transfer functions. The network architecture usually consists of one input layer, single or multiple hidden layers and one output layer. The hidden layers are made up of parallel

processing elements or neurons with each neuron being connected to neuron of the proceeding layer by interconnected weights (w). Training is referred to as the process by which interconnected weights between network layers are adjusted to obtain the desired output (Sivanandam and Deepa 2006). The back-propagation algorithm is commonly used for training. The central idea of the back-propagation algorithm is to minimize the error between hidden and output layers and train network. Initially random weights are assigned and continuously adjusted until the minimization criteria is fulfilled. This is achieved by using Levenberg-Marquardt algorithm. Finally, a transfer function is used that transforms the output of the neural network to the required form. The transfer function used for the hidden layer is either logistic sigmoid or tangent sigmoid and linear transfer function is considered for output layer. The advantages of using sigmoid function in order to achieve faster convergence of the back-propagation algorithm was discussed by (Vogl et al. 1988) and (Harrington 1993). Thus, for the present study prediction models are developed by using feed-forward, back-propagation based Artificial Neural Networks.

1.4   Outline of the thesis

The rest of the thesis is organized as below,

In **Chapter 2**, a detailed literature review pertaining to the present investigation is given. The literature review contains experimental, analytical and numerical methods used to study fluid-filament interactions. Also, a review on immersed boundary methods relevant to bio-fluid dynamics problems is presented.

In **Chapter 3**, a numerical model is developed based on immersed boundary formulation. The developed IBM model is verified by simulating straight virtual walls and wavy-walls in a channel flow. The results are validated with experimental and numerical data.

In **Chapter 4**, numerical simulation of buckling and recuperation dynamics of flexible filaments in planar shear flow is studied. The developed model is extensively validated with previous studies. The effect of bending rigidity and shear rate on the deformation and migration characteristics is ascertained with the help of parametric studies.

In **Chapter 5**, a computational study of flexible filaments undergoing asymmetric shape deformation in channel when subjected to inlet oscillating fluid flow is done at low Reynolds number. The simulation results are validated with filament dynamics studies of previous researchers. Further, parametric analysis is carried to study the effect of filament length (aspect ratio), filament bending rigidity and Reynolds number on the complex deformation and behaviour of flexible filament interacting with nearby oscillating fluid motion.

In **Chapter 6**, fluid-structure interaction study and flow rate prediction model development past a flexible membrane subjected to Poiseuille flow is carried out. The developed IBM model is validated using previous research work and numerical simulations are carried out for different parametric test cases. Based on the simulation data, an ANN prediction model is developed.

In **Chapter 7**, numerical simulation to study the hydrodynamics and mutual interaction of multiple flexible filaments in shear flow is provided. Also, an ANN prediction model is developed for each filament and their corresponding parametric test cases. Further, a detailed analysis is carried out to study filament migration and recuperative aspects.

Finally in **Chapter 8**, the key findings and conclusions of the various simulation studies carried out throughout the thesis is summarized and presented.

CHAPTER 2

2   LITERATURE REVIEW

A broad review regarding experimental and theoretical analysis of fluid-structure interaction of flexible filaments in viscous flow along with immersed boundary implementation to various similar problems is given below.

2.1   Experimental studies

An early study by (Jeffery 1922) provided a mathematical understanding for the motion of a single rigid elliptical particle in shear flow. The analysis of these idealized ellipsoids was successfully approximated to describe the behaviour of rigid cylindrical filaments. However, the same was not applicable to flexible filaments. Flexible fibres exhibit a rich range of motions when subjected to background shear flow. This was experimentally observed by (Forgacs and Mason 1959). The experimental setup was made up of a Couette geometry with two counter rotating cylinders and elastomer fibres of millimetric size dispersed in corn syrup. A critical fibre length was identified above which the elastic fibres undergo buckling. This was in qualitative agreement with theoretical analysis of (Jefferey 1922). A wide range of complex shape deformations such as "snake turns" were observed. Complex dynamics such as formation of helix patterns, coiling and rotation were also reported with the onset of buckling. They also demonstrated that hydrodynamic drag forces and fibre bending forces play a critical part in filament shape transitions. The dynamics of flexible filaments in flowing soap solution was studied by (Zhang et al. 2000). An interface technique was used to visualize flow. When a single flexible filament was fixed at its upstream end and downstream end is unconstrained, stable deformation states were seen. The first is a stretched straight filament state in which the fibre is aligned parallel to flow. The second is flapping filament state in which the fibre displaces itself reminiscent to the flag flapping in wind.

The effect of self-similar bending of flexible filament on drag reduction was studied experimentally by (Alben et al. 2002). The flexible body when subjected to fluid forces undergo reconfiguration. This leads to substantial drag reduction which is very beneficial for organisms. In the experimental setup, a vertical channel contains flexible filament fixed at its centre and subjected to viscous fluid flow in the form of flowing soap film entering the channel from top. The flexible filament undergoes various bending transitions and a drag model is developed that scales with length of self-similarity rather than fibre profile width in contrast to classical theory. The predictions of the model are supported by experimental data. Fluorescence microscopy technique was used to study the dynamics of DNA by (Shaqfeh 2005). The effect of confinement on the dynamics of DNA strand was examined. The DNA mimicking flexible fibre moves towards the channel centreline when subjected to Poiseuille flow. Also, a sequence of tumbling behaviour was seen when one section of the chain close to wall creates disturbance in flow field thus causing other chain section to move away from the wall. Pertaining to low Reynolds number flows, (Sadlej et al. 2010) performed experimental and numerical investigation to study the dynamics of nano-fibres. The Stokes equation was solved using multi-pole expansion method and results compared with experimental data. The shape conformation of the fibre is governed by its bending rigidity. Also, the location of fibre from the wall and filament length play important roles while studying migration behaviour.

(Lopez et al. 2015) studied the deformation of flexible fibres past an obstacle. The study was carried out to understand the effect of local flow velocity and its relation to global velocity and orientation of fibres. This work was in contrast with many previous studies that dealt with confining the fibre between two parallel walls that kept the motion of fibre bi-directional and enhanced the viscous forces due to partial flow blockage. In order to understand the physical phenomena responsible for the transport properties and shape deformations of long bio-object like DNA, proteins or flexible fibres, an experimental analysis of hydrogel nano-filaments in flow was studied by (Pawlowska 2016). A pulsatile velocity flow was used to study deformation of nano-fibres. The bending dynamics is strongly associated to the cross-flow migration phenomenon. The rate of

migration is also influenced by bending, rotation and knot formation of filaments. The viscosity ratio between the materials of filament and fluid also effects migration rate.

An experimental framework to study the mechanics of flexible filaments in air cross flow was carried out by (Silva et al. 2017). In order to get a good picture of the system dynamics and to avoid noise and disturbances arising in experimental data, a standard time series analysis is considered. Inclusion of several time series analysis tools was found to be useful when studying dynamics systems experimentally. They also found that dynamics of longer filaments was richer when compared to short filaments. Long slender filaments tend to show higher amplitude of motion at certain critical speeds. The investigation on the conformation of actin filament in micro-channel using fluorescence microscopy was done by (Liu et al. 2018). A dimensionless elasto-viscous number i.e. ratio of viscous drag force to bending force was used to quantify filament dynamics. A quasi-periodic tumbling phenomenon was observed for short and rigid filaments. Also, above a critical flow strength, buckling instability arises. A motion referred to as "snaking" is induced along the filament structure due to larger values of elasto-viscous number. This transition results in a strongly deformed shape characterized by localized high-curvature bends.

2.2 Theoretical and numerical studies

An overview of various theoretical and numerical models used to study filament dynamics in viscous fluid is given below.

2.2.1 Resistive force theory (RFT)

Resistive force theory (RFT) is quite popular and widely used to model flexible filaments in viscous fluids at low Reynolds numbers. Local geometry-dependent drag coefficients are used to simplify the viscous loading effects. RFT was first used to carry out theoretical analysis of bacterial flagellum propulsion (Gray and Hancock 1955). Further, motility of bacterial flagellum was studied by (Holwill and Burger 1963). The mechanism of this problem was simplified by approximating filament as network of springs. (Powers 2010) studied the effect of coupling long-range hydrodynamics with

spring elasticity to develop small deflections in filaments. More recently (Vogel and Stark 2012), modelled bacterial flagellum as elastic rods made up of chain of spheres connected together and governed by Kirchhoff's theory. This model is coupled to RFT and the resulting simulations reproduced buckling instability that arise during flagellum propulsion. The non-local hydrodynamic effects were studied by (Rodenborn et al. 2013) that assumed the filament to be rigid while elastic forces were ignored.

2.2.2 Slender body theory (SBT)

When considering numerical studies involving single bio-polymers like actin filament and microtubules, continuum formulation techniques such as slender-body theory (SBT) have been quite popular (Batchelor 1970). They are easy to implement but fail to capture far-field fluid motion accurately. Slender body theory (SBT) was also used by (Lighthill 1976) to study hydrodynamics of bacterial flagellum. The study analysed motion of bacteria by modelling flagellar filament bundles. Also, the propagation of bends along the surface of flagella was also considered. (Keller and Rubinov 1976) developed a non-local SBT that captures the global effect on the fluid velocity arising from the presence of the filament, making use of the theory of fundamental solutions for Stokes flow. (Goetz 2008) established connection with Legendre polynomials by deriving non-local SBT and performing simulation for straight filaments. Motivated by the phenomenon of phase change in smectic-A crystals, (Shelley and Ueda 2000) designed non-local SBT to study deformation of flexible filaments. The focus was to analyse buckling and growing behaviour of flexible filaments. (Tornberg and Shelley 2004) employed non-local SBT to study dynamics of slender filaments in Stokesian fluids. The relationship between forces exerted on the body by fluid and filament velocity was established with the help of integral equations. The simulations show shear induced buckling of suspended elastic fibres which are characteristic traits of visco-elastic fluids. However, the above method becomes invalid when considering multiple elastic members in close vicinity.

2.2.3 Bead and rod models

Flexible filaments in bead and rod model are represented as one-dimensional chain made up of rigid spheres or spheroids interlinked between rod structures. The chain experiences local drag forces due to interaction with surrounding fluids while neglecting hydrodynamic interactions in long-range. The simulation of flexible filament modelled as series of rigid beads linked by flexible springs was carried out by (Yamamoto et al. 1993). The Newton's law of linear and angular momentum is used to govern the network of beads. The method was successful in handling particles of varying flexibility and arbitrary shapes. From the simulations it was observed that bending deformation growth of the filament caused rapid decrease in filament rotation as seen in analytical results. The model was further extended by (Ross and Klingenberg 1997) who studied the suspension and flow dynamics of rigid and flexible filaments by performing a particle-level simulation with the filament made up of linked rigid prolate spheroids. The simulation reasonably demonstrated Jeffery orbits for rigid fibres and experimental works of (Forgacs and Mason 1959) for flexible filaments. (Lindstrom and Uesaka 2007; Lindstrom and Uesaka 2009) modified bead-rod model to simulate rigid and flexible fibres by using the Navier-Stokes equation as the fluid governing equation. The basic bead model configuration was elaborated by imposing constraints with the help of new Lagrange multiplier method. Several flow problems such as buckling of fibre in shear, swimming of actuated filaments and Jeffery orbits were studied by approximate accounting of Stokesian flows.

2.2.4 Regularized Stokeslet method

Regularized Stokeslet method of (Cortez 2001) is another popular method used to approximately solve the Stokes equation. The dynamics of moving flagellate was studied by (Flores et al. 2005). The simulation uses superposition of regularized Stokeslets and Rotlets and the flagellum is made up of a network of flexible springs with its shape being helical and torque is applied at its base. (Bouzarth et al. 2011) simulated non-local dynamic effects of flexible fibres by modelling a one-dimensional curve of two-dimensional

Stokeslets. The dynamics of slender rod having an internal mechanisms of intrinsic twists and curvatures was studied by (Olson et al. 2013).

2.2.5 Immersed boundary method

The term immersed boundary method was first associated with works of Charles Peskin in 1981, who used this technique to simulate the mechanism of heart and related blood flow. The modelled heart valve leaflet was a neutrally buoyant boundary (i.e. both fluid and structure have same density). A novel approach adopted in this method was that the entire simulation was performed on a Cartesian grid and the grid did not conform according to the geometry of heart. In order to impose the effect of structure or immersed boundary on the flow, a new procedure was formulated. With reference to dynamics of flexible filament, the filament is made up of Lagrangian points and the response of filament's elasticity is calculated by its relative displacement with respect to fluid flow. The calculated filament elastic forces are distributed onto the background fluid grid as momentum forces acting on the fluid thereby altering the fluid flow (Peskin 2002). In order to distribute the filament Lagrangian forces onto the surrounding fluid, a distribution function named dirac delta function is used. The main advantage of this method is that by definition, the enforcement of no-slip condition is achieved on the boundary (the velocity of Lagrangian points is equal to the local fluid velocity).

The simulation of wood pulp fibre modelled as flexible filament undergoing deformation and buckling in viscous shear flow at low Reynolds number was carried out by (Stockie and Green 1998) using an immersed boundary method. The flow was two-dimensional and the filament was discretized using 40 to 80 Lagrangian points. The study was able to distinguish filament deformation into various orbit classes as seen in experimental studies of (Forgacs and Mason 1959). (Stockie, 2002) further simulated single three-dimensional wood pulp fibre in shear flow, to understand the behaviour of long, flexible filament in suspension. The pulp fibre model was made up of several layers of cellulose fibrils, interwoven to form a complex network, making up the wood cell. The linking elements were made up of springs which resist stretching and bending forces. This

gave a more realistic and detailed representation of the fibre model. (Lai and Peskin 2000) simulated flow past a cylinder by developing a formally second-order immersed boundary method. The new method produced results that were much closer to experimental studies and thus superior to first-order schemes. The new scheme also had lower numerical viscosity that provided significant benefits for performing immersed boundary simulations at higher Reynolds numbers.

The simulation of flexible filament in flowing film of soap was carried out by (Zhu and Peskin 2002) using IBM. The stretching/ compression energy function was derived from Hooke's law and bending energy function was obtained from the principle of least action. The flapping filament states were studied by including mass and changing filament length. A sustained filament flapping occurs with the inclusion of mass and the amplitude of flapping increases as mass increases. Depending on the initial conditions, sustained flapping also occurs when the length of the filament is above a critical value. The results obtained from the simulation was the same as that of experimental studies by (Zhang et al. 2000). To study the effect of drag on flexible fibres, (Zhu and Peskin 2007) performed two-dimensional numerical simulations using IBM. The model problem and essential materials were taken from experimental studies of (Alben et al. 2002) in which the flexible fibre was fixed in a vertical channel and subjected to flowing film of soap. The elastic and bending forces acting on the filament were also taken from the numerical study of (Zhu and Peskin 2002). It is found that flexible filament experiences reduced drag as compared to stiff one and role of bending rigidity on drag is significant. Even though there is a large difference in Reynolds number between experimental and numerical works, the drag values for both the studies have roughly same order of magnitude. Thus by observing the above two set of studies, i.e. 1) experimental studies of (Zhang et al. 2000) and its numerical counterpart (Zhu and Peskin 2002) and 2) experimental works of (Alben et al. 2002) and its replicated numerical study (Zhu and Peskin 2007), it is seen that the Peskin's immersed boundary methodology adopted in both the above numerical studies are quite powerful in reproducing and simulating the full fluid-structure interaction of neutrally buoyant flexible filament in viscous incompressible fluid.

(Musielak et al. 2009) used IBM to numerically model rigid and flexible diatoms in nutrient rich uniform shear flow and study its respective nutrient transport and acquisition. Also, the effect of fluid motion on advective and diffusive fluxes is studied. The length and flexibility of diatom chains are varied along with the background nutrient concentration. It is found that rigid fibres absorb more nutrients thus resulting in higher nutrient uptake per cell as compared to flexible fibres. (Nguyen and Fauci 2014) developed a three-dimensional immersed boundary framework to study the elasto-hydrodynamics of diatom chains modelled as semi flexible fibres in a moving fluid. Based on the quantified bending rigidity of several diatom species, the effect of flexibility on nutrient uptake and aggregate formation was carefully analysed. The developed IBM was also successful in capturing the buckling and recuperation dynamics exhibited by these diatom chains. The flexible filament suspended in viscous shear flow undergoing two-dimensional orbit classes or deformation regimes was successfully recreated using IBM by (Weins and Stockie 2015). The filament was modelled as Kirchhoff rod and fluid solver was pseudo-compressible. The solution algorithm was parallelized and scaled so as to analyse flocculation of several suspended semi-dilute filaments. These examples clearly illustrate how IBM can be used to study and simulate fluid-structure interaction problems related to flexible filaments.

2.2.6 Other methods

(Qi 2007), conducted direct simulation of flexible filaments suspended in non-zero Reynolds number flow using lattice boltzman method (LBM) formulation. The simulation could reproduce various orbits such as 'springy', 'snake', 'S' and 'complex orbits', consistent with experimental and numerical results. (Usta et al. 2007), demonstrated the transverse migration of polymer confined in a narrow channel using dumbbell kinetic theory. A comparison of external forces and pressure force, driving fluid flow is done and its effect on filament migration is studied. There is a dominant effect of local shear rate than applied force on polymer rotation and wall interaction. (Chelakkot et al. 2011), studied the flow behaviour of semi-flexible polymer in micro-channels using multi-particle

collision dynamics simulation technique. Steric repulsion effect from wall and hydrodynamic lift forces are studied. Analysing bending rigidity and flow velocity effects on deforming fibres is a complex feature. A kinetic theory dumbbell model was developed by (Jandrejack et al. 2004), to simulate flexible polymers keeping DNA as a reference molecule. It was found that flow strength was fundamental in stretching and deforming highly confined DNA chains from its equilibrium position. Also, the DNA chains migrate back to channel centreline in agreement with experimental studies. In the work of (Sadlej et al. 2010), multipole expansion method was used to simulate flexible filaments in channel flow. (Slowicka et al. 2013), solved dynamics of non-brownian flexible fibres using accurate hydro multi-pole simulation. Different modes of dynamics are studied based on shear to bending parameter. The motion of stiff fibres mainly depends on presence or absence of wall. Flexible fibres move towards the centre of the wall and get deformed in C-shaped and S-shaped configurations for varying filament flexibility.

All the above method focused on simulating flexible filaments in viscous fluid. In most studies involving parametric test cases, performing simulation for each and every test case is time consuming and also increases the computational cost substantially. These parametric studies can be further simplified by developing prediction models by performing linear or non-linear regression analysis. One such technique popular in recent years is artificial neural networks, details of its applications are provided below.

2.3 Artificial neural networks applications

The credit for developing the first "Perceptron" learning algorithm goes to (Rosenblatt 1958). The popular back-propagation learning algorithm was subsequently developed by (Werbos 1974). The ANN model divides the random data sample into training set and testing set. It uses inductive learning technique to learn from training set and validates the same with testing set. Today, ANN is used for classification, regression, pattern recognition, forecasting etc. in fields like engineering, science and biology. Some common examples include viscoelastic annular extrusion (Huang and Miao 2007), critical submergence in intake pipe (Kocabas 2008), enhancement of low fidelity CFD results

(Pena et al. 2012), micro-bubble drag reduction in turbulent flow (Ouyang et al. 2013), solid particle erosion (Pandya et al. 2017), fatigue damage effect (Moises and Mariel 2019), computing development length in magneto-hydrodynamics (MHD) channel flow (Taheri et al. 2019), etc.

2.4 Research gap and critical review

From the above review it is realized that experimental studies are not only difficult to implement but also prone to large inaccuracies. Some of the techniques like fluorescence microscopy and particle image velocimetry used by researchers in flow visualization of filaments are exorbitant. Due to very small time and length scales, there are limited possibilities to describe interaction of flexible filaments with viscous fluids on a molecular level. Understanding the complex fluid dynamics and its potential effects on it interaction with flexible filament is very difficult at such small scales. Also, verifying the numerical models from available experimental studies that are not sufficiently precise is an additional challenge. The complex shape deformation is greatly influenced by hydrodynamics or flow field in the immediate vicinity of the filament structure. Visualizing these flow fields is difficult in experimental studies. Thus many researchers have diverted their attention to study deformation and dynamics of flexible filaments interacting in viscous fluid using theoretical and numerical methods.

Numerical and analytical methods like resistive force theory, slender body theory, kinetic theory and particle dynamics have been used to simulate deformation of flexible filaments. From the works of (Lighthill 1976) who used slender body theory, it is seen that slenderness ratio is the key parameter in modelling flexible fibres. The solution scheme is approximated and the problem is simplified by exploiting the fact that fibres have large aspect ratio. This technique also relies on the assumption that Stokes equation is linear and singular solutions are super positioned for flows around deforming or moving filaments. Also, for complex shapes determining the expression of forces is very complicated. Resistive force theory is a simplified version of slender body theory, that works well for asymptotically thin filament. Resistive force theory describes only local fluid filament

interaction since the fluid medium is considered passive and complex interplay of fluid dynamics and structural response occurring in the vicinity of moving or deforming filament is neglected. Thus resistive force theory does not consider the full hydrodynamic interactions. Since time derivative does not appear in the Stokes equation, the hydrodynamics forces acting on the filament are dependent only on geometry, shape at that instance and filament velocity. In majority of these studies, the hydrodynamic interactions were neglected thus providing limited information of the underlying FSI. The coupling between the structure and fluid is one-way, i.e., fluid was considered as a passive medium, and the fibre did not exert any force back onto the fluid. The computational complexity may reduce significantly, but they cannot effectively elucidate deformation and mobility of bio-molecules subjected to hydrodynamic stresses due to surrounding fluid motion, as compared to grid-based methods. The immersed boundary method can thus be used to investigate the dynamics of flexible filaments in viscous fluid flow. There is no restriction on the aspect ratio of filaments and hence parametric study can be carried out for a wide range of filament dimensions. The linear diffusion terms as well as non-linear inertia terms can be incorporated in the flow governing equation.

Through literature review it is revealed that the dynamics of flexible filament in viscous fluid flow is of vast research potential both from the underlying physics and application point of view. Hence, a detailed and careful study in this direction is essential. The migratory and shape deformation obtained when filament interacts with fluid is dependent on various parameters like filament length, bending rigidity, filament initial position, viscous drag, Reynolds number etc. There is a need to develop and identify other structural and flow parameters that govern the complex fluid-filament interplay. Developing a unified computational model that can address filament conformation for various flow conditions like uniform, shear and oscillatory flow along with boundary constraints imposed on the filament like both ends tethered, one end tethered and both ends held freely has never been carried out. The study will thus help in understanding the behaviour of non-motile micro-organisms as well as developing microfluidic based devices for various applications like fluid mixing, flow rate control etc. Also, the effect of multiple

22

flexible filaments on hydrodynamics and mutual interaction in shear flow is rarely carried out by previous researchers. Development of prediction model based on artificial neural networks supporting immersed boundary simulations of filament-fluid dynamics is a novel approach. The benefits of using such models is to predict output parameters from the known input data without carrying out numerical simulations. Motivated by previous studies and research gaps, the following objectives are presented.

2.5 Objectives

The prime objective of the present work is to investigate the dynamics of flexible filament in viscous fluid flow. Accordingly, two-dimensional computational models will be developed using immersed boundary finite volume method,

- To study the fluid flow behaviour in straight and wavy-walled channel configurations.
- To explore the buckling and recuperation behaviour of non-motile diatom chains modelled as flexible filament in viscous shear flow.
- To investigate the deformation and asymmetric dynamics of flexible filaments in oscillating flow.
- To capture the self-excitation behaviour of thin membrane modelled as flexible filament in uniform flow.
- To understand the hydrodynamics and mutual interaction of multiple flexible filaments in shear flow.

In addition, suitable prediction models using artificial neural networks coupled with immersed boundary simulation results will be developed for the fluid-structure interactions of single and multiple flexible filaments.

CHAPTER 3

3 SIMULATION OF FLUID FLOW IN STRAIGHT AND WAVY RIGID WALL CHANNELS

In the present thesis finite volume based immersed boundary method is used to study the fluid-structure interaction of flexible filaments in fluid flow. In order to familiarize with the implementation of immersed boundary method, a preliminary work is done to study the fluid flow behaviour in straight and wavy rigid walled channels by modelling the walls as immersed boundaries. A detailed discussion is provided in subsequent sections.

3.1 Background

Accurate control and handling of fluids in microfluidic based bio-medical devices is very important in diverse range of applications such as lab-on-chip (LOC), drug delivery and bio-technology. Mass transport enhancement by mixing is an important aspect in modern day biomedical devices. Flow through medical devices such as kidney dialyzer and membrane oxygenator can be considered as laminar due to low Reynolds number and narrow channel geometry, thus requiring efficient utilization of passive modulation systems to improve fluid mixing in these devices. Hydrodynamic instabilities can be produced by introducing eddy promoters or passive modulation systems to improve mixing (Sui et al. 2012). Inducing chaotic mixing effects in such devices is difficult. Since mixing is achieved primarily through diffusion, long micro-channels are required in order to achieve satisfactory mixing results. This also leads to slower blending of fluids (Cho 2008). Maintaining a diminutive scale of these devices and improving its mixing efficiency is a major challenge researchers are facing today. Active perturbations in fluid flow created by employing mechanical components or passive chaotic mixing induced by modifying the geometry of the mixer devices are some of the techniques used to overcome this problem. Recently wavy channels have been introduced in low Reynolds number and creeping flow conditions which are pertaining to microfluidics and application of fluid mixing such as lab-on-chip and micro-evaporators (Gong et al. 2011a). For moderate Reynolds number

(20-300), (Tatsuo et al. 1990) conducted experimental investigation on flow and mass transfer in symmetric wavy wall channels. They demonstrated that flow separation phenomenon was observed in wavy and arc shaped channels thus exhibiting early transition to turbulence at low Reynolds number. (Wang and Vanka 1995) numerically studied converging-diverging channels based on experimental work of (Tatsuo et al. 1990) for steady and unsteady flow condition. Compared to straight channels, wavy channels produce self-sustaining oscillations which destabilize laminar boundary layers thus improving heat transfer and mixing capabilities. (Bahaidarah et al. 2005) also performed numerical simulation of wavy walled channels for Reynolds number ranging from 25-400. The work focuses on improving computational effort by demonstrating the adequacy of using a single wavy module as computational domain. Periodic boundary conditions which uses stream-wise constant pressure drop were used in these works. The effects of phase shift of wavy walled channels on the hydraulic performance was investigated by (Ahmed et al. 2014). The sinusoidal wavy channel with 0° phase shift provided the best thermo-hydraulic performance for low Reynolds number. Finite volume simulations were performed by (Aslan et al. 2016) to study comparison of experimental and numerical results of wavy walled channels. It is found that the performance of channels with rounded wavy peaks is better in comparison with sharp peaks. The work is concluded with the observation that finite volume based numerical predictions are close to experimental results. Based on the examination of all experimental and numerical works, it can be inferred that introducing wavy walled channels improve mixing performance at moderate Reynolds number. However simulating flow behaviour of complex geometries such as wavy channels is a computationally intensive procedure. This chapter emphasis on applying immersed boundary method to perform numerical simulations at relatively less computational effort and time.

In this chapter, numerical simulation is performed to study Poiseuille flow in a micro-channel with crest-crest (CC Model) wave configuration and crest-trough (CT-Model) wave configuration using continuous forcing based immersed boundary method. The continuity and Navier-Stokes equations governing the flow are solved on a staggered

grid system using fractional-step based finite volume method. A FORTRAN code is developed to capture the flow behaviour of various geometries in micro-channel for different Reynolds numbers.

3.2 Mathematical modelling and numerical procedure

The schematic representation of CC-Model i.e. crest and crest of the two wavy walls lying on the same unit length section and CT-Model i.e. crest and trough facing each other for both the wavy walls is shown in Figure 3.1. The amplitude of wavy wall is given as A and wavelength WL. L is the channel length and H is channel height.
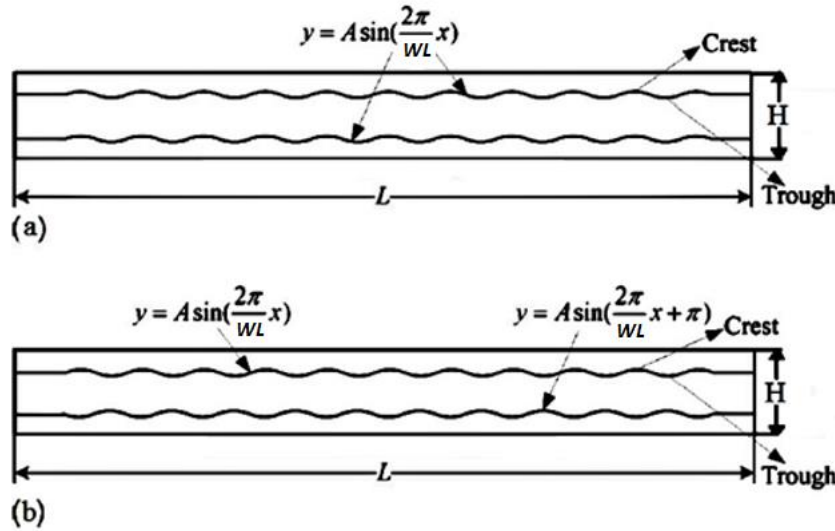
Figure 3.1 Schematic illustration of (a) CC-Model and (b) CT-Model. Image adopted from (Gong et al. 2011a)

Immersed boundary method is a combined Eulerian–Lagrangian technique to study the fluid flow interaction with structures. The Cartesian co-ordinates $\mathbf{x}^* = (x^*, y^*)$ are the Eulerian variables used to define the fluid flow on a fixed $M \times N$ grid. A Lagrangian frame of reference is used to define the rigid wall displacement, given by a curvilinear material co-ordinate s^* and time t^*. The flow variables are velocity $\mathbf{u}^* (\mathbf{x}^*, t^*)$, pressure $p^* (\mathbf{x}^*, t^*)$ and Eulerian force density $\mathbf{f}^*(\mathbf{x}^*, t^*)$. The rigid wall position $\mathbf{X}^* (s^*, t^*)$, rigid wall velocity $\mathbf{U}^*$

(s^*, t^*) and Lagrangian force density $\mathbf{F}^*$ (s^*, t^*) are the structural variables. The Eulerian grid points are fixed but the Lagrangian boundary points or immersed boundary points move with respect to fluid flow and they usually do not coincide with each other. The governing continuity and Navier-Stokes equations along with Eulerian forcing term are given by equation (3.1) and equation (3.2) respectively.

$$\nabla^* . \mathbf{u}^* = 0 \tag{3.1}$$

$$\rho \frac{\partial \mathbf{u}^*}{\partial t^*} + \mathbf{u}^* \cdot \nabla^* \mathbf{u}^* = -\nabla^* p^* + \mu \nabla^{*2} \mathbf{u}^* + \mathbf{f}^*(\mathbf{x}^*, t^*) \tag{3.2}$$

where, the constant μ is the fluid viscosity and ρ the fluid density. The flow governing equations are non-dimensionalized based on the following characteristic scales: the height of the channel as the reference length L_{ref}, constant inlet fluid velocity as u_{ref}, time scale t_{ref} as L_{ref} / u_{ref}, pressure p_{ref} as ρu^2_{ref} and for momentum forcing f_{ref} as $\rho u^2_{ref} / L_{ref}$. Thus, we have

$$x = \frac{x^*}{L_{ref}}, y = \frac{y^*}{L_{ref}}, t = \frac{t^*}{t_{ref}}, u = \frac{u*}{u_{ref}}, p = \frac{p^*}{p_{ref}}, f = \frac{f^*}{f_{ref}}$$

The resulting non-dimensionalized equations are given as,

$$\nabla . \mathbf{u} = \mathbf{0} \tag{3.3}$$

$$\frac{\partial \mathbf{u}}{\partial t} + \mathbf{u} . \nabla \mathbf{u} = -\nabla p + \frac{1}{Re} (\nabla^2 \mathbf{u}) + \mathbf{f}(\mathbf{x}) \tag{3.4}$$

where, $Re = \frac{\rho u_{ref} L_{ref}}{\mu}$ is the Reynolds number

At the beginning of time step, $\mathbf{u}^n(\mathbf{x})$ and $\mathbf{X}^n(\mathbf{s})$ are given and hence the solution has to march to $\mathbf{u}^{n+1}(\mathbf{x})$ and $\mathbf{X}^{n+1}(\mathbf{s})$. Since the straight and wavy-walls have to be maintained as rigid structures, an appropriate choice of $\mathbf{F}^n(\mathbf{s})$ has to be made. The boundary force $\mathbf{F}^n(\mathbf{s})$ is computed from the boundary configuration $\mathbf{X}^n(\mathbf{s})$ given by equation (3.5). The interpretation of equation (3.5) is that, the immersed boundary points $\mathbf{X}^n(\mathbf{s})$ are fixed to equilibrium points $\mathbf{X}_e(\mathbf{s})$ with stiff springs having spring constant S. Thus, with passage of

time the immersed boundary points remain close to the desired configuration. The calculated Lagrangian force is applied to the fluid in equation (3.6).

$$\mathbf{F^n(s)} = \mathbf{S}(\mathbf{X_e(s)} - \mathbf{X^n(s)}) \tag{3.5}$$

$$\mathbf{f^n(x)} = \sum_s \mathbf{F^n}(\mathbf{s})\boldsymbol{\delta}(\mathbf{x} - \mathbf{X^n(s)})\Delta\mathbf{s} \tag{3.6}$$

where, discrete delta function is given by equation (3.7) and equation (3.8). The Dirac delta function (equation (3.8)) chosen in the present work is based upon the works of (Maniyeri and Kang 2012).

$$\boldsymbol{\delta(x)} = \mathbf{d_h(x)d_h(y)} \tag{3.7}$$

And,

$$\mathbf{d_h(r)} = \begin{cases} \frac{1}{8h}\left(3 - \frac{2|r|}{h} + \sqrt{1 + \frac{4|r|}{h} - 4\left(\frac{|r|}{h}\right)^2}\right), & |r| \le h \\ \frac{1}{8h}\left(5 - \frac{2|r|}{h} - \sqrt{-7 + \frac{12|r|}{h} - 4\left(\frac{|r|}{h}\right)^2}\right), & h \le |r| \le 2h \\ 0, & \text{otherwise} \end{cases} \tag{3.8}$$

where, h is Eulerian grid size, Δs is the distance between two successive immersed boundary points and r is the distance between immersed boundary point and neighbouring fluid grid point. No slip boundary conditions are used at the bottom and top walls. Periodic boundary condition is applied in the positive x-direction with a constant pressure gradient of 12/Re. Now the Navier-Stokes equation is solved with the force term $\mathbf{f^n(x)}$ to update the velocity field to $\mathbf{u^{n+1}(x)}$. A fractional step based finite volume method is used to discretize the governing equation. Second order Adams-Bashforth scheme is used to discretize non-linear convection terms and Crank-Nicolson scheme is used for linear diffusion terms. The discretized Navier-Stokes equation is given by equation (3.9).

$$\frac{\mathbf{u^t - u^n}}{\Delta t} = -\boldsymbol{\nabla}\mathbf{p^n} - \frac{1}{2}[3\mathbf{A(u^n)} - \mathbf{A(u^{n-1})}] + \frac{1}{2Re}\boldsymbol{\nabla}^2(\mathbf{u^t + u^n}) + \mathbf{f^n(x)} \tag{3.9}$$

where, $\mathbf{u^t(x)}$ is the intermediate velocity. In order to satisfy the continuity equation given in equation (3.3), a pseudo–pressure term is used to correct the velocity field at each

computational step. The pressure Poisson equation given by equation (3.10) is solved to obtain the pseudo-pressure term ϕ^{n+1}. The solved pseudo-pressure term is used to calculate the velocity $\mathbf{u^{n+1}(x)}$ given by equation (3.11) at next time level and the pressure value is corrected by equation (3.12).

$$\frac{\partial^2 \phi^{n+1}}{\partial x^2} + \frac{\partial^2 \phi^{n+1}}{\partial y^2} = \frac{1}{\Delta t} \left(\frac{\partial u^t}{\partial x} + \frac{\partial u^t}{\partial y} \right) \tag{3.10}$$

$$\mathbf{u^{n+1}} = \mathbf{u^t} - \Delta t \, \frac{\partial \phi^{n+1}}{\partial x} \tag{3.11}$$

$$\mathbf{p^{n+1}} = \mathbf{p^n} + \boldsymbol{\phi^{n+1}} - \frac{\Delta t}{Re} \left(\frac{\partial^2 \phi^{n+1}}{\partial x^2} + \frac{\partial^2 \phi^{n+1}}{\partial y^2} \right) \tag{3.12}$$

The new velocity from the Eulerian grid $\mathbf{u^{n+1}(x)}$ is interpolated into the immersed boundary point given by equation (3.13) and boundary point is moved to new position $\mathbf{X^{n+1}(s)}$ given by equation (3.14).

$$\mathbf{U^{n+1}(s)} = \sum_x \mathbf{u^{n+1}(x)} \delta(\mathbf{x} - \mathbf{X^n(s)}) \Delta h^2 \tag{3.13}$$

$$\mathbf{X^{n+1}(s)} = \mathbf{X^n(s)} + \Delta t \, \mathbf{U^{n+1}(s)} \tag{3.14}$$

where, Δt is the time step. Thus the formulation of finite volume based immersed boundary method is complete. Next, the validation of the developed computational model and resulting flow fields obtained from the simulation for straight and wavy walled channels are presented below.

3.3 Results and discussions

Fluid flow behaviour is analysed by performing parametric study for wide range of variables shown in Table 3.1. The parameters are suitably non-dimensionalized. The governing equations are solved on a two-dimensional rectangular dimensionless domain of 4×1. The Eulerian grid size is 251×101. Total of 501 immersed boundary points are taken for straight walls and wavy walls. The grid sizes are selected based on an extensive grid refinement study. Numerical results related to flow over straight, CC-Model and CT-Model

wavy wall configurations are obtained by developing a FORTRAN code. Simulations are carried for five different Reynolds number i.e. Re = 1, 5, 10, 15 and 20. The value of stiffness constant S is chosen as 10000 and time step, $\Delta t = 1 \times 10^{-3}$. The validation of the present code is done in two parts. Firstly, two virtual rigid walls are placed in the channel at a distance of 0.75 and 0.25. Immersed boundary method enforces the no-slip boundary condition on the walls. Simulations are carried out until steady state solution is reached for Reynolds number, Re = 20. Figure 3.2 shows the velocity vector plot for this case.
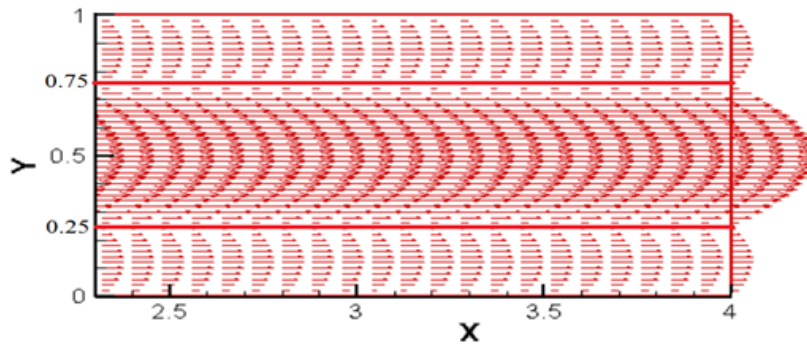
Figure 3.2 Velocity vector plot for straight wall in channel at Re = 20.

From the figure, three different flow fields are observed adjacent to the walls, thus clearly highlighting the imposition of no-slip boundary condition due to the presence of immersed structure. The results are qualitatively validated with (Arruda et al. 2002). This serves as first part of validation for the developed code. Second part of the validation consists of comparing the results obtained from the IBM code for rigid wavy walls with the experimental work of (Gong et al. 2011b). Two rigid wavy walls are generated given by expressions in Figure 3.1. Results are compared for a test condition of amplitude, A = 0.2, wavelength, WL = 2.0 and Reynolds number, Re = 20 at x-location of 1.25 for CC-Model type configuration. Figure 3.3 shows the comparison of velocity profile between experimental and numerical values. A good agreement is established between experimental and numerical results.

Table 3.1 Non-dimensional parametric study variables

Fixed Amplitude, A=0.1 and varying wavelength	Fixed Wavelength, WL = 1.0 and varying amplitude
WL = 0.5	A = 0.06
WL = 1.0	A = 0.1
WL = 2.0	A = 0.14
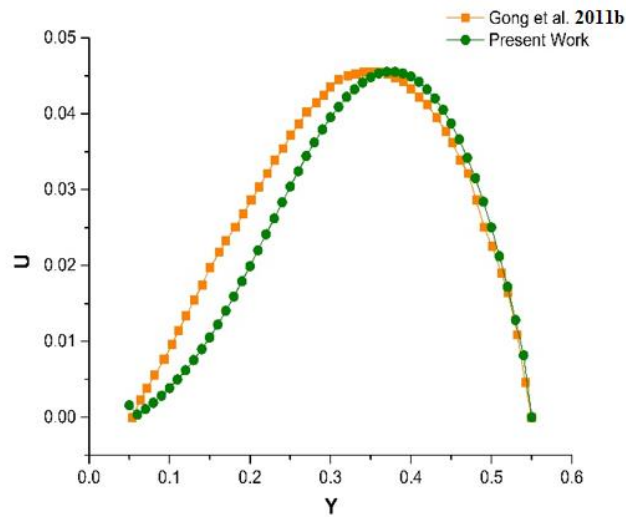
Figure 3.3 Velocity profile comparison between experimental works of (Gong et al. 2011b) and present numerical work for A=0.2 and WL=2.0 at x-location of 1.25.

The fluid velocity contour plots of CC-Model and CT-Model configurations for different amplitude and wavelengths are shown in Figures 3.4 - 3.5 and Figures 3.6 - 3.7 respectively. From the figures it is observed that the flow is streamlined and contoured along the walls of the wavy channel and no significant vortical structure formation or regeneration pattern is seen. This is because the flow is dominated by viscous forces and a fully developed Poiseuille flow type behaviour is exhibited. Velocity contour plots identical to the present study are observed in the works of (Gong et al. 2011a; Ahmed et. al 2015; Zontul et. al 2017).
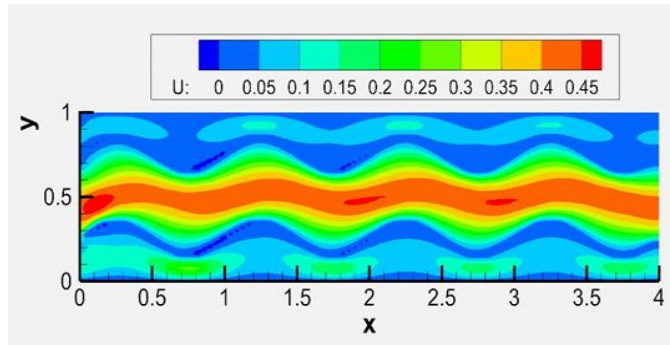
Figure 3.4 CC-Model velocity contour plots for A=0.1, WL=1.0.
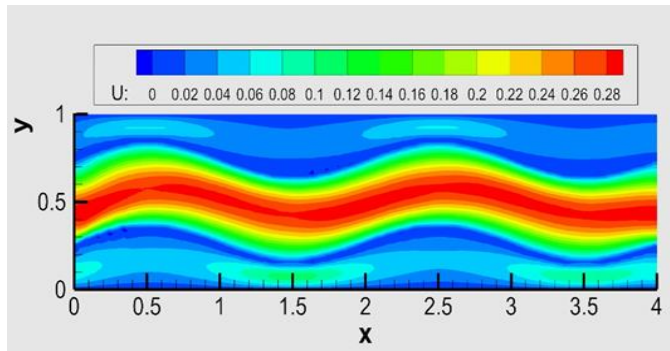
Figure 3.5 CC-Model velocity contour plots for A=0.1, WL=2.0.
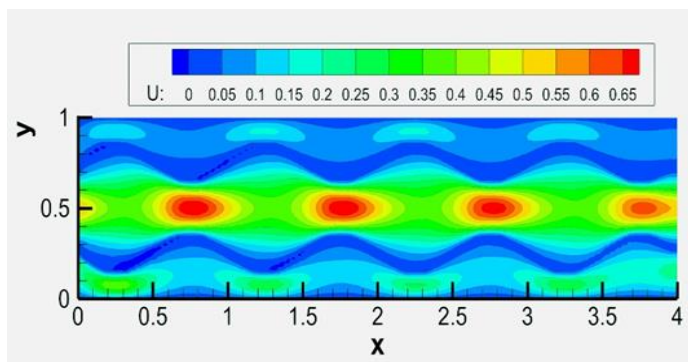
Figure 3.6 CT-Model velocity contour plots for A=0.1, WL=1.0.
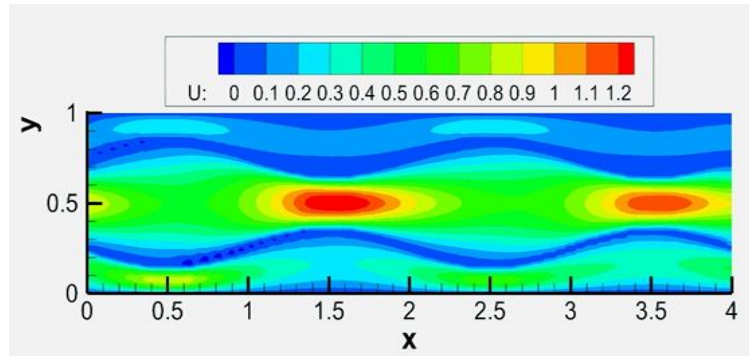
Figure 3.7 CT-Model velocity contour plots for A=0.1, WL=2.0.

Variation of amplitude and wavelength with velocity across crest and trough for CC-Model and CT-Model is shown in Figures 3.8 - 3.9 respectively. As we can see from Figure 3.8, a biased shift in the centreline velocity occurs. This is seen in cases where hydrodynamic boundary layer separation is present (Gong et al. 2011b). Even though heat transfer analysis is not conducted in the present work, from literature we know that such biased shifting of centreline leads to enhanced mixing and thermal performance. Also, the centreline velocity increases with increase in amplitude but decreases for case of A=0.14. This occurs due to lower pressure drop resulting in better mixing phenomenon. From Figure 3.9, we see that the centreline velocity decreases with increase in wavelength. Velocity shifting is not observed across crest and trough. Narrow contracting sections as seen from Figure 3.7 produces larger pressure drop along the centreline eventually increasing the velocity almost three times that of CC-Model. Since the fluid ejects at such large velocities mixing efficiency is hampered substantially (Ramgadia and Saha 2013).
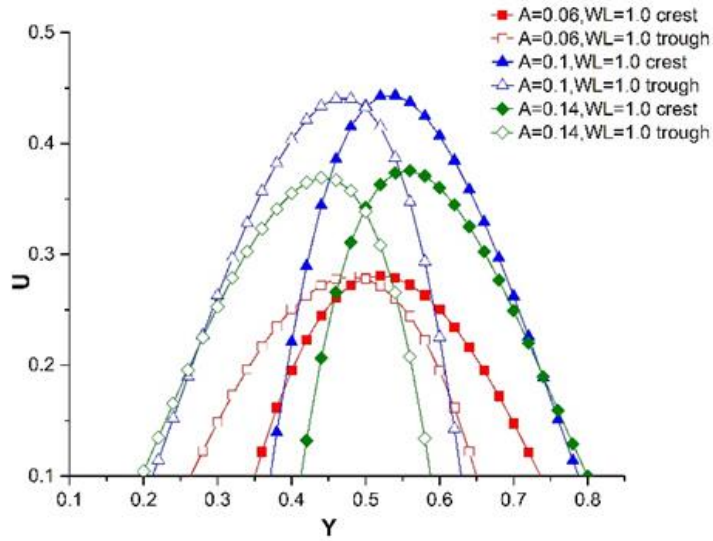
Figure 3.8 Velocity distribution along y-axis for CC-Model with varying amplitude and fixed wavelength.
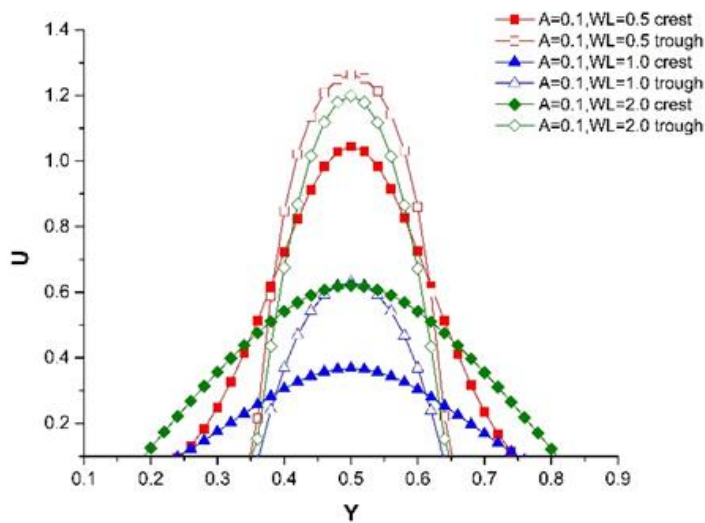
Figure 3.9 Velocity distribution along y-axis for CT-Model with varying wavelength and fixed amplitude.

Finally, the effect of maximum velocity with increase in Reynolds number for both CC-Model and CT-Model is shown in Figure 3.10 and Figure 3.11 respectively. A straight wall in channel is compared with all possible wavy wall geometries. Configurations showing higher amplitude have higher maximum velocity when Reynolds number is increased. Increasing the wavelength reduces the maximum velocity thus suggesting lower pressure drop. The model with straight wall in channel shows constant maximum velocity variation for both CC-Model and CT-Model.

Thus the developed computational model to simulate fluid flow behaviour in straight and wavy rigid walled channel can be easily extended for the case of flexible filament interacting with incoming fluid under different channel flow conditions.
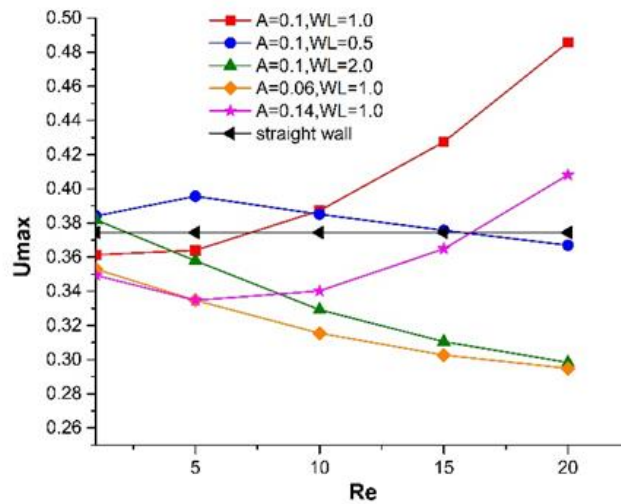
Figure 3.10 Variation of maximum velocity with Reynolds number for CC-Model.
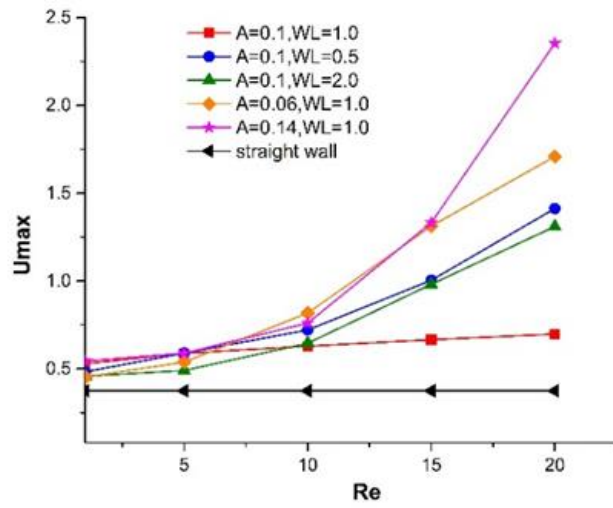
Figure 3.11 Variation of maximum velocity with Reynolds number for CT-Model.

CHAPTER 4

4 SIMULATION OF FLEXIBLE FILAMENT IN VISCOUS SHEAR FLOW

The developed computational model based on finite volume based immersed boundary method to simulate fluid flow behaviour in straight and wavy rigid walled channel is now extended for the case of flexible filament interacting in viscous shear flow. More details can be found below.

4.1 Background

Fluid-structure interaction (FSI) comprises a large number of problems in the field of bio-fluid dynamics and biophysics. Some examples include microtubules and F-actin biopolymer cells, red blood cell conformation, DNA, diatom chains, opening and closing of heart valve leaflet, cilia and flagella of micro-organism, cellulose fibre bundling etc. To understand the hydrodynamics and factors causing the fibres to behave recuperatively or nonrecuperatively in an incompressible viscous fluid is very important for a wide range of medical and engineering applications. The impact of oceanic fluid motion on solute transport to micro-organisms is fundamental to marine ecology. Of particular interest is the FSI of a group of diatoms, non-motile unicellular phytoplankton which forms the primary foundation of aquatic food webs. A detailed description of diatom chains is provided in section 1.1. The dynamics of diatom chain modelled as flexible filament in oceanic shear flow thus falls under the purview of filament-fluid interaction. In many of the two-way fluid-structure interaction problems, forces generated from both solid and fluid have a tremendous influence on the resulting motion of each other and hence cannot be neglected. When a passive flexible filament interacts with fluid, the structure forcefully adheres to the dynamics of the surrounding fluid flow and undergoes deformation accordingly. In return, the fluid produces hydrodynamic stresses on the filament. This combined interactive effect can produce stretching/compression and bending of the body. To describe the physics adequately and develop numerical models for such interactions is a significant challenge. However, in the last few years, researchers have successfully captured the interaction of

flexible filaments in a viscous fluid with the help of numerous methods and techniques supported by experimental studies. The same has been explained in section 2.1 and section 2.2.

(Stockie 2002) simulated a single three-dimensional wood pulp fibre in shear flow, to understand the behaviour of long, flexible filament which is in suspension. This work was an extension of the previously developed two-dimensional model (Stockie and Green 1998). The pulp fibre model is made up of several layers of cellulose fibrils, interwoven to form a complex network, making up the wood cell. The linking elements were made up of springs which resist stretching and bending forces. This gives a more realistic and detailed representation of the fibre model. (Slowicka et al. 2015) studied the fibre dynamics in shear flow for different values of bending rigidity. A bead-spring model based multi-pole method was used to simulate fibre dynamics for a wide range of applications involving DNA, polymers, proteins, and biological macromolecules. The work emphasized the importance of using a non-dimensional number which is the ratio of fibre bending force to viscous drag force and thus categorized fibre deformation to bending rigidity. Depending on the selected bending rigidity and resulting hydrodynamic interactions, fibres were grouped into either behaving rigid or flexible. They also observed that fibres with high stiffness placed in shear flow, later stay in a plane perpendicular to shear gradient and at an angle to vorticity direction for a large portion of simulation time. They found rigid fibres tending to straighten out and flexible fibres coil thus indicating distinct evolution patterns for rigid and flexible fibres. (Weins and Stockie 2015) had successfully recreated two-dimensional orbit classes for flexible filaments suspended in a viscous fluid using the immersed boundary method. A pseudo-compressible fluid solver was used, and filaments were modeled as Kirchhoff rod. (Nguyen and Fauci 2014)studied the hydrodynamics of diatom chains and flexible fibres in three-dimensions using an adaptive grid-based immersed boundary method. They were successful in capturing recuperation and buckling dynamics for a wide range of diatom species. In order to capture the full fluid motion around the fibre, the fluid grid has to be refined. Since the simulation was three-dimensional and contained an unstructured grid scheme, the computational model was complex and

expensive in nature. A two-dimensional model which on one hand effectively predicts dynamics for flexible filament and on the other hand reduces the computational expense is of practical importance. In this direction, (Musielak et al. 2009) had studied the role of fluid motion on nutrient uptake in diatoms using a two-dimensional immersed boundary method. The study focused on understanding nutrient uptake and diatom behaviour for different filament lengths and bending rigidity. Diatoms were made up of linked chains, and that behaving rigid tend to experience high nutrition gradients as compared to flexible ones. However, at that time no laboratory measurements of bending rigidity were reported for diatom chains. As a result, a direct relationship between the modeled diatoms and its experimental counterpart could not be accurately assessed. (Young et al. 2012) experimentally quantified the bending rigidity for various types of diatom chains. The diatoms were suspended in a medium of seawater and exposed to hydrodynamic forces across a hollow capillary tube. They analysed the response of the diatoms to the applied force, and thus a measure of its bending ability was determined. By studying the deformation of the filament and measuring the chain dimensions, the flexural rigidity of different diatom chains was experimentally obtained by them. Numerical studies of (Slowicka et al. 2015) and (Musielak et al. 2009) have thus shown that fibre dynamics largely depends on flow strength, bending rigidity and fibre length respectively. Hence it can be seen that a two-dimensional numerical study can accurately predict the behavior of diatom chains subjected to shear flow at lower computational costs. Studies by (Lazier et al. 1989) had indicated that since diatom chains are typically smaller than the Kolmogorov length scales in the ocean, they experience turbulence as linear shear. (Jumars et al. 2009) also suggested the importance of background flows leading to the formation of dissipative vortices around diatom structures. Thus, we can ascertain from the above literature reviews that, very few studies have reported and quantified transition of filaments from recuperative to non-recuperative behaviour especially for the case of diatom chains and thus parametric study is essential in this direction. Quantitative information like bending rigidity obtained from the experimental values of (Young et al. 2012) was not used in two-dimensional diatom simulations by previous researchers. Three-dimensional simulations and adaptive

mesh refinement techniques have high computational costs and thus have hindered design and dynamic coupling of more mechanically realistic diatom model with an incompressible fluid (Vanella et al. 2014). A point to be noted in this regard is that the two-dimensional model can never possibly capture the full fluid dynamics as compared to three-dimensional one. However, capturing the essential and prominent fluid motion and filament deformation characteristics using a simplified model of diatom chains with minimum mesh generation overhead outweighs the drawback of costly computations. Also, very few studies have captured fluid motion in the vicinity of the filament which is essential for understanding the hydrodynamic interactions over successive time periods. Through the present work, an attempt is made to capture and visualize dissipative vortices formed in the vicinity of diatom chains to understand how such vortices are formed and what advantages the organism can achieve to nutrient uptake. This will help to realize the underlying mechanism responsible for shape formations and transitions observed during deformation of rigid and flexible filaments. Finally, there is a need to capture the migratory behaviour of filaments in order to understand its behavior to external factors better. These shortcomings from previous works are the real motivation for the present problem.

In this chapter, a two-dimensional numerical model based on an immersed boundary method is developed to capture the hydrodynamic interaction of rigid and flexible filaments in shear flow. A parametric analysis is carried out by varying filament length, bending rigidity and shear rate. The numerical method incorporated in this study is provided in section 4.2. The simulation results and details regarding filament deformation and migration are provided in section 4.3.

4.2 Mathematical framework and numerical procedure

The physics of the problem involves a flexible filament which is massless and neutrally buoyant, suspended in a viscous incompressible fluid medium. The immersed boundary framework is made up of two distinct grid systems. One is a Cartesian co-ordinate system $\mathbf{x}^* = (x^*, y^*)$ that encompasses the fluid domain and other is Lagrangian system for flexible filament structure (immersed boundary). The immersed boundary

equations are written in Lagrangian form made up of one-dimensional unknown variable $\mathbf{X}^*(s^*, t^*)$. The parameter s^* is used to assign a material point and $\mathbf{X}^*(s^*, t^*)$ describes motion of immersed boundary along with its spatial configuration at any given time t^*. The flow variables are velocity $\mathbf{u}^*(\mathbf{x}^*, t^*)$, pressure $p^*(\mathbf{x}^*, t^*)$ and Eulerian force density $\mathbf{f}^*(\mathbf{x}^*, t^*)$ while Lagrangian force density $\mathbf{F}^*(s^*, t^*)$ is the filament variable. The shear flow is developed by moving the top and bottom walls horizontally. The top and bottom wall move in positive and negative x-direction respectively with a constant speed $\mathbf{U}^*_{\text{wall}}$. In the absence of filament, a linear shear flow is developed with velocity profile given by equation (4.1).

$$\mathbf{u}^* = G^* \left(y^* - \frac{H^*}{2}\right) \tag{4.1}$$

where, $G^* = \frac{2U^*_{\text{wall}}}{H^*}$ is the shear rate and H^* is the height of the channel. The equation of motion for fluid flow and filament are given below.

$$\nabla^* \cdot \mathbf{u}^* = 0 \tag{4.2}$$

$$\rho \frac{\partial \mathbf{u}^*}{\partial t^*} + \mathbf{u}^* \cdot \nabla^* \mathbf{u}^* = -\nabla^* p^* + \mu \nabla^{*2} \mathbf{u}^* + \mathbf{f}^*(\mathbf{x}^*, t^*) \tag{4.3}$$

where, the constant μ is the fluid viscosity and ρ the fluid density. Equation (4.2) and equation (4.3) are the continuity equation and incompressible Navier-Stokes equation with a momentum forcing term. They can be non-dimensionalized based on the following characteristic scales: the length of the filament as the reference length L_{ref}, constant velocity of moving walls as U_{ref}, time scale t_{ref} as $L_{\text{ref}} / U_{\text{ref}}$, shear rate G_{ref} as $U_{\text{ref}} / L_{\text{ref}}$, pressure p_{ref} as ρU^2_{ref} and for momentum forcing f_{ref} as $\rho U^2_{\text{ref}} / L_{\text{ref}}$ and bending rigidity as $\rho U^2_{\text{ref}} L^3_{\text{ref}}$. Thus, we have

$$x = \frac{x^*}{L_{\text{ref}}}, y = \frac{y^*}{L_{\text{ref}}}, t = \frac{t^*}{t_{\text{ref}}}, K = \frac{G^*}{G_{\text{ref}}}, u = \frac{U^*_{\text{wall}}}{u_{\text{ref}}}, p = \frac{p^*}{p_{\text{ref}}}, f = \frac{f^*}{f_{\text{ref}}}$$

The resulting non-dimensionalized equations are given as,

$$\nabla \cdot \mathbf{u} = 0 \tag{4.4}$$

$$\frac{\partial \mathbf{u}}{\partial t} + \mathbf{u} \cdot \nabla \mathbf{u} = -\nabla p + \frac{1}{Re} \nabla^2 \mathbf{u} + \mathbf{f}(\mathbf{x}, t) \tag{4.5}$$

41

where, $Re = \frac{\rho u_{ref} L_{ref}}{\mu}$ is the Reynolds number

The extra force term $\mathbf{f}(\mathbf{x}, t)$ in equation (4.5), also called the momentum forcing term is the force applied to incorporate the presence of structure in fluid domain. This forcing term is given by equation (4.6).

$$\mathbf{f}(\mathbf{x}, t) = \int \mathbf{F}(s, t) \delta(\mathbf{x} - \mathbf{X}(s, t)) ds \tag{4.6}$$

The flexible filament is made up of a number of Lagrangian points connected together by means of resistance links having resting length Δs. The function $\mathbf{F}(s, t)$ in equation (4.6) is the force density term which defines the elastic or mechanical contribution of the immersed boundary on the fluid. This is given by equation (4.7).

$$\mathbf{F}(s, t) = -\frac{\partial E[\mathbf{X}(s,t)]}{\partial \mathbf{X}} \tag{4.7}$$

where the term $-\partial E / \partial \mathbf{X}$ is the variational derivative containing the elastic energy functional $E[\mathbf{X}(s, t)]$. The energy functional for the present study given in equation (4.8) consists of two properties. One that resists elongation / compression and another that resists bending (Zhu and Peskin 2002). An illustration of the resultant stretching and bending forces acting on the linkages are provided in Figure 4.1(a) and Figure 4.1(b) respectively. In the figure, X_s is the Lagrangian point surrounded by nearby points X_{s+1} and X_{s-1}.

$$E[\mathbf{X}(s, t)] = \frac{1}{2} K_s \int \left(\left| \frac{\partial \mathbf{X}}{\partial s} \right| - 1 \right)^2 ds + \frac{1}{2} K_b \int \left| \frac{\partial^2 \mathbf{X}}{\partial s^2} \right|^2 ds \tag{4.8}$$

where, T_{elas} and S_{ben} are the stretching co-efficient and bending co-efficient of the elastic boundary respectively.
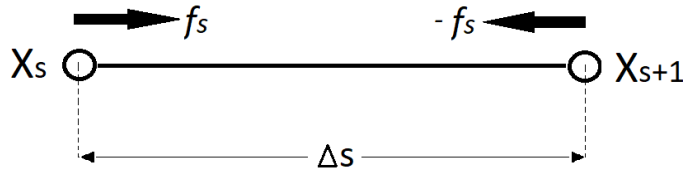
a) Stretching / compression link
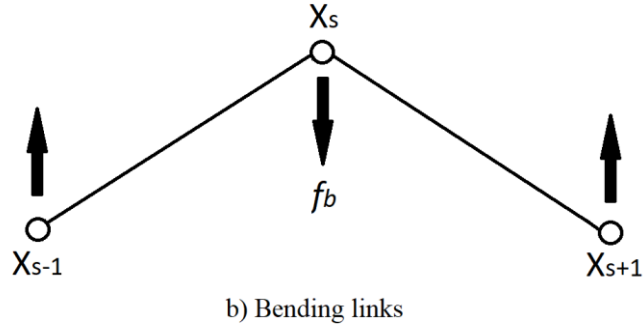
b) Bending links

Figure 4.1 The two types of filament linkages used in the present study. a) Stretching/compression resistance linkage and b) Bending resistance linkage between Lagrangian points.

By solving the energy functional $E[\mathbf{X}(s,t)]$, the Lagrangian force density $\mathbf{F}(s,t)$ can be calculated. Finally, the momentum forcing term in equation (4.6) is substituted in the governing Navier-Stokes equation (equation (4.5)) to produce new fluid flow variables at next time step. Based on the newly calculated flow variables, corresponding deformation and new position of the elastic immersed boundary is obtained by substituting it in equation of motion given by equation (4.9).

$$\frac{\partial \mathbf{X}}{\partial t}(s,t) = \int \mathbf{u}(\mathbf{x},t)\delta(\mathbf{x} - \mathbf{X}(s,t))\mathbf{dx} \tag{4.9}$$

The numerical scheme used in the present study is temporally second-order in nature. The advantage of using formally second-order scheme is that it produces results with improved accuracy (Lai and Peskin 2000; Kim and Peskin 2007). The total time step is divided into two stages. One is the preliminary stage and other is final stage. In the preliminary stage, the governing equations are solved for time level $(n + \frac{1}{2})$ from data available at time level n using a first-order accurate scheme. The results of the preliminary stage are used to proceed in the final stage n to reach time level (n+1) in a formally second-order manner. If Δt is the time step, the fluid velocity for present time n is depicted as $\mathbf{u}^n$ while boundary configuration is $\mathbf{X}^n$. The objective of the numerical procedure is to compute updated $\mathbf{u}^{n+1}$ and $\mathbf{X}^{n+1}$ using the data given at time level n. As discussed above a typical time step in the

43

formulation will proceed in two stages. In the preliminary stage from time level n to level $(n + \frac{1}{2})$, the force density term $\mathbf{F}^n$ is calculated at IB points using equation (4.10). Further momentum forcing term $\mathbf{f}^n$ is determined at Cartesian grid points using equation (4.11), so as to be applied in the governing Navier-Stokes equations. This will update the fluid velocity to new time level $(n + \frac{1}{2})$. The discretized form of $\mathbf{F}^n$ and $\mathbf{f}^n$ are given below as,

$$\mathbf{F}^n = -\frac{\partial E[\mathbf{X}^n(s,t)]}{\partial \mathbf{X}} \tag{4.10}$$

$$\mathbf{f}^n = \sum_s \mathbf{F}^n(s)\delta_h\big(x - \mathbf{X}^n(s,t)\big)\Delta s \tag{4.11}$$

where, h is the Cartesian mesh width and δ_h is the two-dimensional Dirac delta function. In this methodology δ_h is chosen such that,

$$\delta_h(\mathbf{x}) = \frac{1}{h^2} d\left(\frac{x}{h}\right) d\left(\frac{y}{h}\right) \tag{4.12}$$

where,

$$d(r) = \begin{cases} \frac{1}{4}\left(1 + \cos\left(\frac{\pi r}{2}\right)\right), & \text{if } |r| \le 2, \\ 0, & \text{otherwise} \end{cases} \tag{4.13}$$

where, r is the distance between immersed boundary point and neighbouring fluid grid point. The Dirac delta function (equation (4.13)) chosen in the present work is based upon the numerical study of (Maniyeri et al. 2012). The continuity and Navier-Stokes equations are solved next by using equation (4.14) and equation (4.15) given below.

$$[\nabla \cdot \mathbf{u}]^{(n+1)/2} = 0 \tag{4.14}$$

$$\frac{\mathbf{u}^{(n+1)/2} - \mathbf{u}^n}{\left(\frac{\Delta t}{2}\right)} = -\nabla p^n - [\mathbf{u} \cdot \nabla \mathbf{u}]^n + \frac{1}{Re}\nabla^2 \mathbf{u}^n + \mathbf{f}^n \tag{4.15}$$

Finally, the boundary configuration is updated to new position $\mathbf{X}^{(n+1)/2}$ by discretizing equation (4.16) as,

$$\frac{\mathbf{X}^{(n+1)/2} - \mathbf{X}^n}{\left(\frac{\Delta t}{2}\right)} = \sum_x \mathbf{u}^{(n+1)/2}(x)\delta_h\big(x - \mathbf{X}^n(s,t)\big)h^2 \tag{4.16}$$

This concludes the preliminary stage. The final stage starts again at time level n to reach level n+1 using intermediate variables $\mathbf{u}^{(n+1)/2}$ and $\mathbf{X}^{(n+1)/2}$ obtained from the preliminary stage. First, the Lagrangian force density $\mathbf{F}^{(n+1)/2}$ which consists of elastic forces acting on immersed boundary points is discretized and calculated as,

$$\mathbf{F}^{(n+1)/2} = -\frac{\partial E[\mathbf{X}^{(n+1)/2}]}{\partial \mathbf{X}} \tag{4.17}$$

Next, the Eulerian force density is calculated which is obtained by discretizing equation (4.6) as

$$\mathbf{f}^{(n+1)/2} = \sum_{\mathbf{s}} \mathbf{F}^{(n+1)/2}(s)\delta_h\left(x - \mathbf{X}^{(n+1)/2}(s,t)\right)\Delta s \tag{4.18}$$

Finally, the fluid velocity $\mathbf{u}^{(n+1)/2}$ is updated to new time (n+1) and shown below.

$$[\nabla \cdot \mathbf{u}]^{n+1} = 0 \tag{4.19}$$

$$\frac{\mathbf{u}^{n+1} - \mathbf{u}^n}{\Delta t} = -\nabla p^{(n+1)/2} - [\mathbf{u} \cdot \nabla \mathbf{u}]^{(n+1)/2} + \frac{1}{Re}\nabla^2\mathbf{u}^{(n+1)/2} + \mathbf{f}^{(n+1)/2} \tag{4.20}$$

Using this new fluid velocity value, the boundary configuration $\mathbf{X}^{n+1}$ is updated as,

$$\frac{\mathbf{X}^{n+1} - \mathbf{X}^n}{\Delta t} = \sum_{\mathbf{x}} \mathbf{u}^{n+1}(x)\delta_h\left(x - \mathbf{X}^{(n+1)/2}(s,t)\right)h^2 \tag{4.21}$$

This marks the end of the final stage. Since the present immersed boundary method is temporally second order in nature, we use two steps in the numerical procedure. For better understanding, a step by step immersed boundary implementation is provided below:

Step 1: By using the variables $\mathbf{u}^n$ and $\mathbf{X}^n$ available at present time level n, the force density $\mathbf{f}^n$ is calculated at IB points using equation (4.10) and equation (4.11) with the dirac delta function given by equation (4.12) and equation (4.13).

Step 2: The force density term $\mathbf{f}^n$ calculated in step 1 is added to the Navier-Stokes equation and fluid velocity $\mathbf{u}^{(n+1)/2}$ is determined by solving equation (4.14) and equation (4.15).

Step 3: The new boundary configuration $\mathbf{X}^{(n+1)/2}$ is calculated next using equation (4.16). This marks the end of preliminary stage.

Step 4: The variables $\mathbf{u}^{(n+1)/2}$ and $\mathbf{X}^{(n+1)/2}$ available at preliminary stage (time level (n+1)/2) are used to determine force density term $\mathbf{f}^{n+1}$, fluid velocity $\mathbf{u}^{n+1}$ and filament displacement $\mathbf{X}^{n+1}$ using equation (4.17) to equation (4.21). This marks the end of final stage (time level (n+1)).

Step 5: The steps 1 – 4 are repeated and the filament positions are evolved with time. Thus, the present numerical immersed boundary scheme completes a typical time step Δt.

The fluid Cartesian grid is arranged in a staggered manner, and the flow variables are solved using an implicit time advancement scheme based on finite volume method (FVM). The method of deferred correction is used to treat the convective and diffusive fluxes obtained from the finite-volume discretization of the Navier-Stokes equation. (Hayase et al. 1992) had described this scheme to discretize systems having oscillatory solutions and for maintaining the diagonal dominance. The source term is modified to contain the difference between the first-order upwind scheme and central differencing. The spatial derivatives are discretized using a second-order difference scheme. The continuity and momentum equations are solved using a SIMPLE algorithm. The technique involves an iterative procedure with pressure correction. A pressure value is guessed, and an intermediate velocity is first calculated which is used as input to the pressure Poisson equation. The ICCG (Incomplete Cholesky Conjugate Gradient) method is used to solve the pressure equation. The newly calculated pressure is used to determine the fluid velocity at the new time step thus keeping the solution divergent free. The new fluid velocity is used and the deformation of filament for different time steps is captured. A periodic boundary condition is applied in the positive x-direction with flow driven by a constant pressure gradient. A dimensionless parameter called Viscous Flow Forcing value (VFF) is used to quantify viscous drag effects of the fluid with respect to filament elastic forces which is given in equation (4.22) as,

$$\text{VFF} = \frac{\mu G^*(L^*)^3}{K_b^*} \tag{4.22}$$

where, $K_b^* = EI$ is the bending rigidity such that, E is Young's modulus of filament material, and I is the moment of area in the bending plane. The Viscous Flow Forcing value is related to the viscosity of the fluid, length of the filament, shear rate and bending rigidity of the filament.

4.3 Results and Discussion

4.3.1 Model validation

The numerical model described in the previous section is compared with filament deformation problem done by (Vahidkhah and Abdollahi 2012) who performed two-dimensional numerical simulation using an immersed boundary-lattice Boltzmann method. The deformation problem involves a massless flexible filament placed in a rectangular channel and subjected to uniform Poiseuille flow. The fluid is viscous and incompressible while the filament is placed horizontally with an inclination of $\alpha = 45°$. The dimensionless length of channel (L_c) and height of the channel (H) are taken as 4.0 and 1.0 respectively. The length of the filament (L) is 0.43, and the leading edge is fixed at the location $L_1 = 1.0$ and $H/2 = 0.5$, while the trailing edge is free to move along the fluid flow direction. No-slip boundary condition is applied to the top and bottom channel walls. A Periodic boundary condition is applied in the positive x-direction with the flow being driven by a constant pressure gradient. A schematic representation of the problem and the boundary condition applied is provided in Figure 4.2. The Reynolds number chosen for this study is 1.0 and the total simulation time is 1.0.

Before considering the solution to the problem, the inextensible property of the filament is tested for varying time step Δt and stretching co-efficient K_s for fixed bending co-efficient K_b. This serves as a stability analysis for the numerical model. Next, the spatial convergence of the model is analysed by considering different Eulerian grids in x and y-directions. The objective of these two tests is to obtain a divergence free and accurate solution to the filament deformation study. In order to perform the inextensible test, %

inextensible error (ε) is used which calculates the deviation from the original filament length. This is given in equation (4.23).

$$\varepsilon (t) = \max \left| \frac{\partial \mathbf{X}}{\partial s} \cdot \frac{\partial \mathbf{X}}{\partial s} - 1 \right| \times 100 \tag{4.23}$$
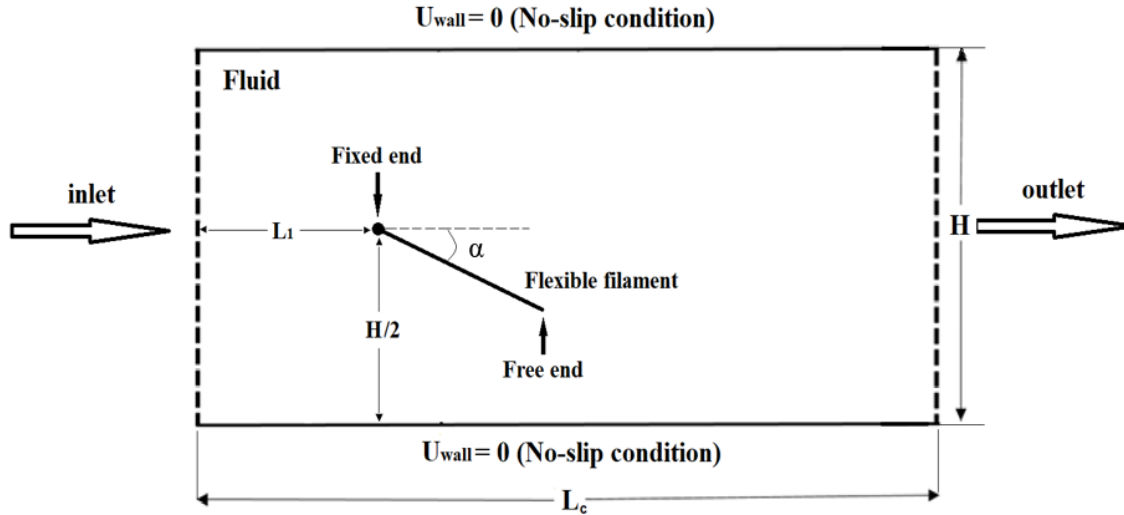
Figure 4.2 Schematic illustration of flexible filament placed at a channel location in the direction of viscous fluid flow.

The inextensible error equation is taken from simulation study of flexible filament in uniform flow by (Huang et. al 2007). Their methodology strictly enforces the filament inextensibility condition with no restrictions on time step. Table 4.1 shows different cases that are analysed by varying time step and stretching co-efficient for fixed bending co-efficient of $K_b=1.0$. The filament cannot resist the fluid forces at low stretching co-efficient ($K_s=1000$), thus producing a large % inextensible error of 7.35. There is a need to increase the stretching co-efficient in order to keep the filament in-extensible. However, the time step needs to be reduced to 1×10^{-5} in order to minimize the effect of oscillations in the solution caused by incorporating higher stretching co-efficient as observed in Table 4.1. Increasing stretching co-efficient reduces % inextensible error and the best value of stretching co-efficient ($K_s=5000$) produces the least % error of 1.86. Filaments with stretching co-efficient greater than 5000 tend to develop an initial compression state

between time $t = 0.0$ to $t = 0.15$. This factor significantly increases the % error for cases of higher stretching co-efficient.

Table 4.1 Comparison of % inextensible error (ε) for varying time step (Δt) and varying stretching co-efficient (K_s) for fixed value of bending co-efficient ($K_b=1.0$)

Stretching co-efficient (K_s)	Time step (Δt)	% Inextensible error (ε)
1000	1.0×10^{-4}	7.35
5000	1.0×10^{-5}	1.86
7500	1.0×10^{-5}	2.64
10000	1.0×10^{-5}	2.95

Regarding filament inextensibility, the spatial convergence test for different Eulerian grids is carried out. A uniform grid is considered for all cases and compared with % inextensible error as seen in Table 4.2. It is clear from Table 4.2 that the best possible grid configuration is 512×128.

Table 4.2 Comparison of % inextensible error (ε) with different uniform Eulerian grids in x and y-direction

Grids	Time step (Δt)	% Inextensible error (ε)
256×64	1.0×10^{-5}	5.26
512×128	1.0×10^{-5}	1.86
1024×256	1.0×10^{-5}	1.82

Based on inextensibility and grid convergence tests, two-dimensional numerical simulation of inclined flexible filament placed in a uniform flow is carried out. The filament deformation for different time instances is provided in Figure 4.3(a) – Figure 4.3(d). The filament which is initially inclined shown in Figure 4.3(a) aligns itself with the flow direction. Finally, at t = 0.6, the filament attains mechanical equilibrium straight state, and no further motion or deformation is seen. A qualitative similarity is achieved in filament deformations and flow fields when compared with the results of (Vahidkhah and Abdollahi 2012). This proves the validity of the developed model.

4.3.2 Filament in shear flow

The verified numerical model is modified to incorporate the physical problem of flexible filament subjected to shear flow. (Forgacs and Mason 1959) had performed experimental studies, and (Stokie and Green 1998; Weins and Stockie 2015) had carried out numerical simulation on dynamics of the flexible filament by varying filament length, shear rate and bending rigidity. They were successful in categorizing filament deformation into various orbit classes. The present two-dimensional model is employed to obtain these filament orbit classes. A schematic representation is provided in Figure 4.4 which depicts a flexible filament placed freely in channel mid-plane subjected to viscous shear flow. In the figure, α is the angle made by the filament with respect to the vertical. The dimensional physical parameters are provided in Table 4.3. In order to bring an asymmetry in filament motion, the filament is initially placed at an inclination angle of 5°. A large value of stretching co-efficient is assumed in-order to maintain filament inextensibility constraint. The physical parameters are non-dimensionalized with respect to characteristic length and velocity. The dimensionless filament length, shear rate, and bending rigidity are given as L, K, and K_b respectively.
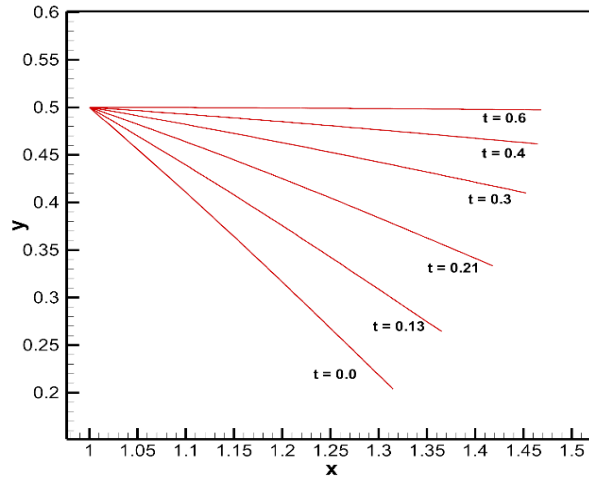
Figure 4.3 Filament deformations for different time intervals from t = 0.0 to t = 0.6.
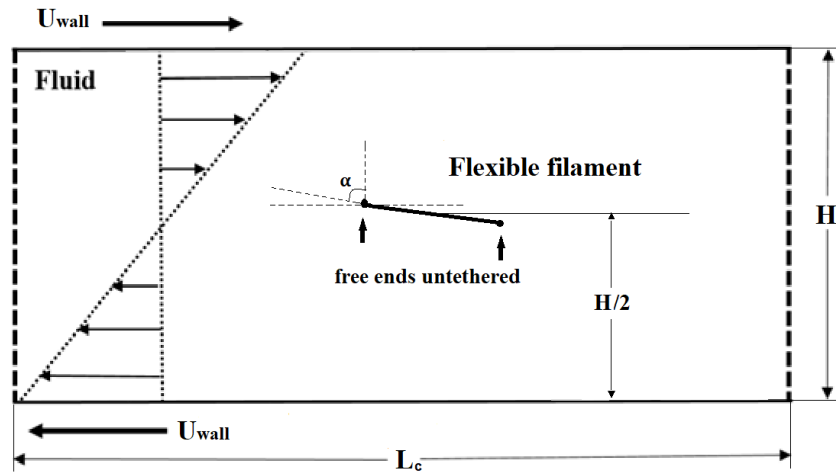
Figure 4.4 Schematic illustration of flexible filament placed untethered in viscous shear flow. The boundary conditions are specified in equation (4.1).

Table 4.3 Physical parameters used for the filament in the shear flow simulation study

Physical parameters	Dimensional values
Channel height (H*)	0.5 cm
Channel width (L$_c$*)	2.0 cm
Fluid Density (ρ)	1.0 g/cm^3

Fluid Viscosity (μ)	8 – 10 g/cm.s
Shear rate (G*)	8 – 64 /s
Filament length (L*)	0.1 – 0.3 cm
Bending rigidity (K_b*)	$1.0 – 5.0 \times 10^{-4}$ g.cm^3/s^2
Reynolds number (Re)	0.1- 0.5
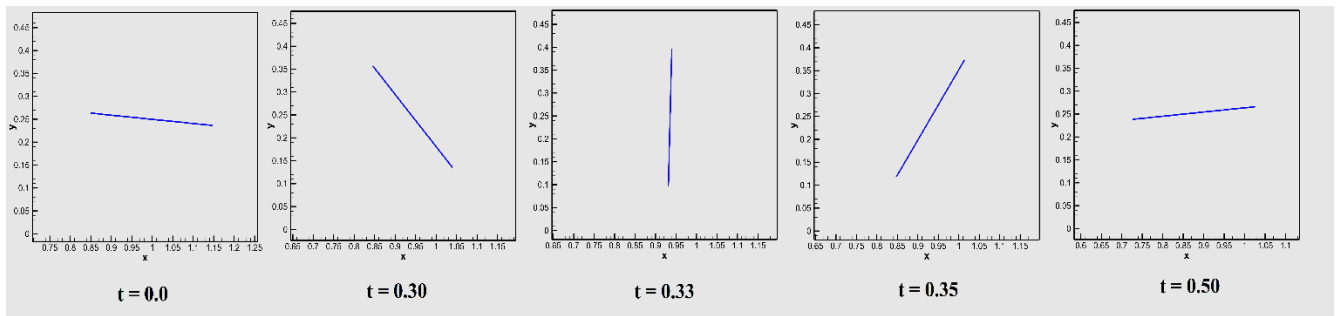
a) Rigid deformation (L = 0.3, K = 32, K_b =1.0)
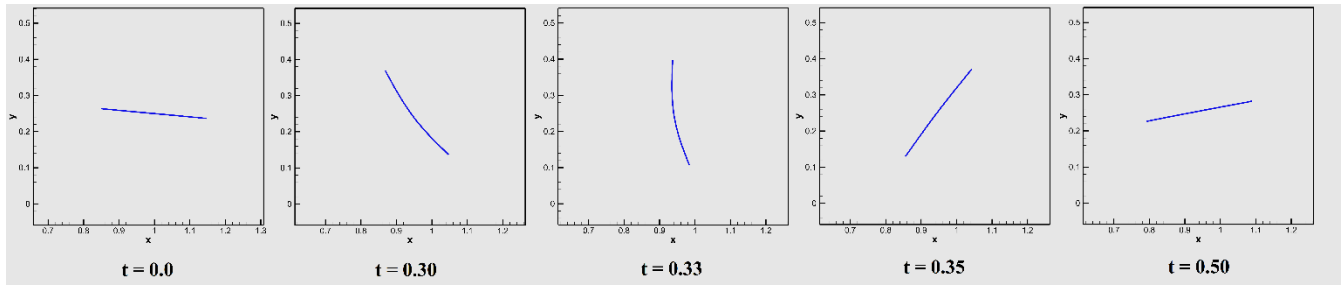
b) Springy deformation (L = 0.3, K = 32, K_b =0.7)
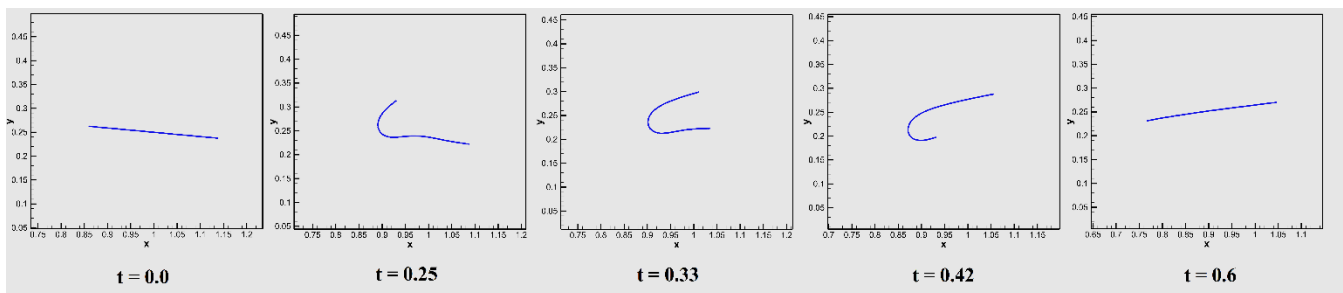
c) Snake turn (C – Shape) deformation (L = 0.3, K = 32, K_b =2.5×10^{-2})
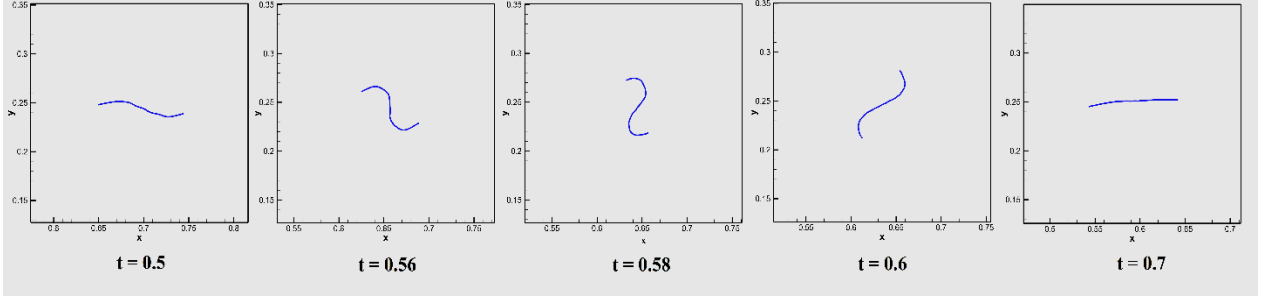
d) S – shape deformation ($L = 0.1$, $K = 64$, $K_b = 6 \times 10^{-3}$)
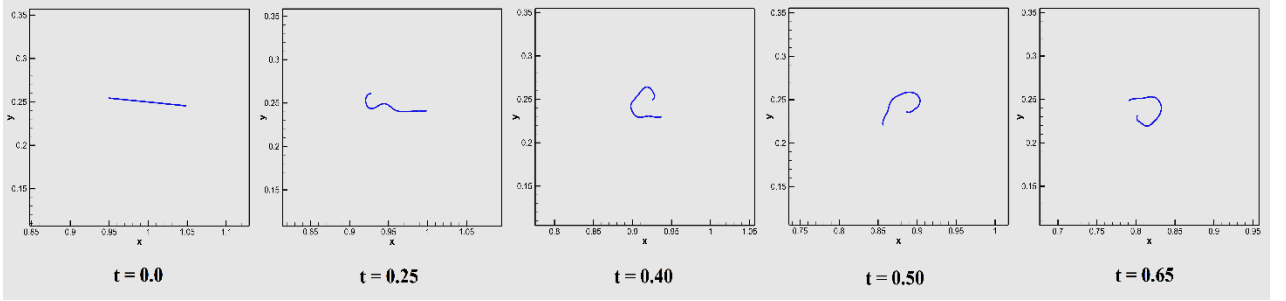
e) Complex deformation ($L = 0.1$, $K = 64$, $K_b = 5 \times 10^{-4}$)

Figure 4.5 Deformation of filament at different time instances for Rigid, Springy, C-shape, S-shape and Complex orbit classes for parameters defined in Table 4.3.

The snapshots of fibre deformation for different values of filament length, shear rate, and bending rigidity is provided in Figure 4.5. Rigid filament rotation is observed for high bending rigidity $K_b = 1.0$. The filament initially in an inclined position undergoes rotation and remains in the straight undeformed state throughout the rotation. When bending rigidity is reduced to 0.7, the filament undergoes slight bending at the centre to form springy deformation. Further reduction in bending rigidity to 2.5×10^{-2} causes the filament to buckle about its centre thereby deforming into C-shape and at $K_b = 6 \times 10^{-3}$, S-shape filament deformation is captured. With the reduction in bending rigidity, the filament can no longer resist the hydrodynamic stresses acting on its surface. Finally, complex deformations are seen for $K_b = 5 \times 10^{-4,}$ and the filament cannot retain its original straight shape. In order to further demonstrate the ability of the present model to capture filament deformation and shape formation in shear flow, angle (α) made by the filament with respect

53

to the vertical is analysed for two cases of filament deformation. One for the rigid case and other for S -shape deformation case. Since the filament is initially inclined at 5°, the angle (α) made by it with respect to vertical is 85°. Figure 4.6 compares angle (α) for two cases with respect to time. The time taken for the deformation of the flexible filament (S -shape) is faster when compared to rigid filaments as seen in Figure 4.6. Also, with the completion of the first filament deformation cycle, the filament either rigid or flexible has a tendency to remain in horizontal equilibrium position for an extended period of time. This is seen in Figure 4.7 which compares the angle (α) made by a filament for rigid, springy and C-shape deformation cases with respect to time. Similar observations were reported by (Stokie and Green 1998). Thus, the present model successfully demonstrates its qualitative ability to yield filament dynamics as observed in previous experimental and numerical studies with the planar shear flow.

Further, it is widely known that Jeffery's equation is used to describe the motion of rigid fibres in shear flow. The Jeffery's equation is given in equation (4.24).

$$\alpha\,(t) = \tan^{-1}\left(r_e \tan\left(\frac{K\,r_e t}{r_e^2+1}\right)\right) \tag{4.24}$$

where, $\alpha\,(t)$ is the angle made by the rigid filament with respect to vertical, K is the shear rate and r_e is the filament aspect ratio. A numerical simulation is carried out for fixed filament length L = 0.3, fixed bending rigidity K_b = 1.0 and three different values of shear rate (K = 8, 16, 32) specifically for the case of a rigid filament. The angle (α) made by the filament with respect to the vertical for the above three test cases is recorded. The total simulation time is maintained at t = 3.0. The angle $\alpha\,(t)$ based on Jeffery's equation is also determined for the above same set of shear rates by fixing the aspect ratio r_e = 60. Cylindrical fibres of length 0.1 to 0.3 typically have aspect ratio r_e ranging between $60 \le r_e \le 400$. Similar to (Stokie and Green 1998), a probability distribution φ indicating the time spent by the filament at various angles (α) is plotted in Figure 4.8 for both the present simulation results and Jeffery's equation results. As seen from the plot, the results are found to be in good agreement with Jeffery's equation.
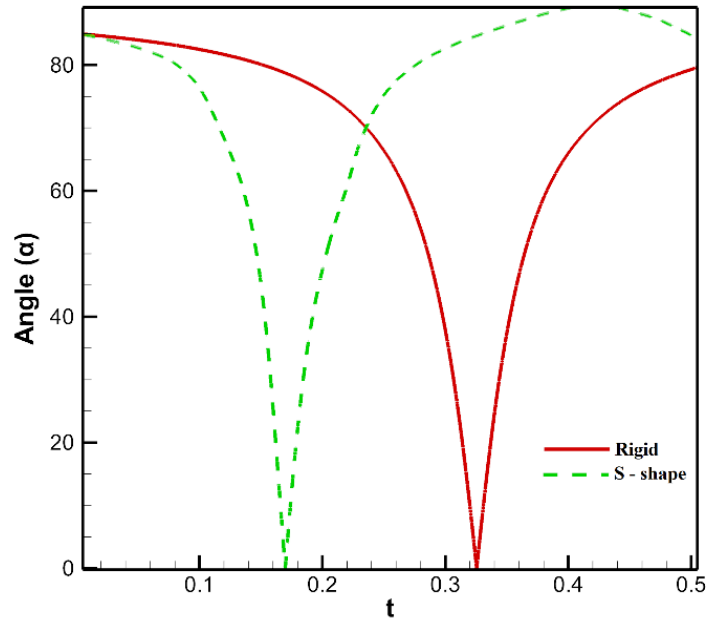
Figure 4.6 Comparison of angle (α) between Rigid deformation (L = 0.3, K = 32, K_b =1.0) and S – shape deformation (L = 0.1, K = 64, $K_b = 6 \times 10^{-3}$).
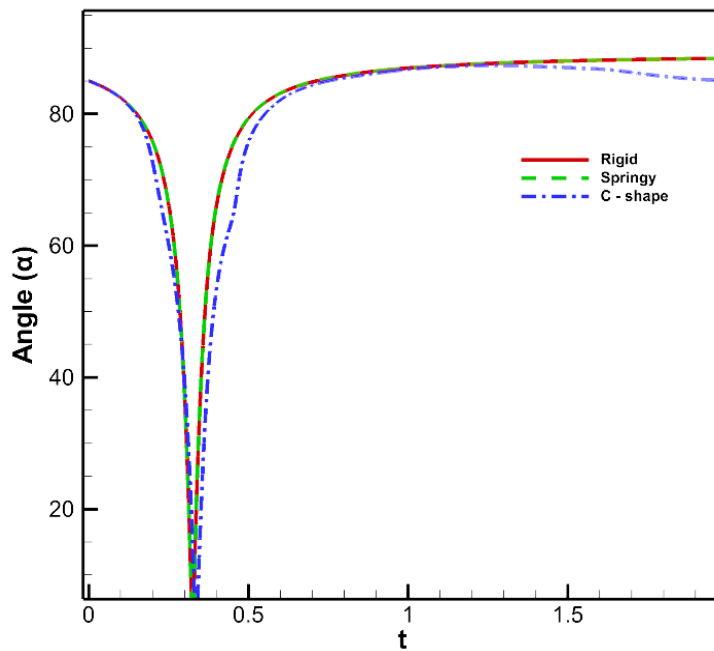
Figure 4.7 Angle (α) for Rigid (L = 0.3, K = 32, K_b =1.0), S – shape (L = 0.1, K = 64, $K_b = 6 \times 10^{-3}$) and C – Shape (L = 0.3, K = 32, K_b =2.5 $\times 10^{-2}$) deformations.

Finally, a detailed parametric analysis is performed for fixed filament length L = 0.1, three different values of shear rates (K = 10, 16, 32) and 14 different values of bending rigidity (K_b). The Viscous Flow Forcing value (VFF) is also calculated. For each of the 42 parametric test conditions, an additional parameter called exterior angle β defined as shown in Figure 4.9 is determined. In the figure, A and B are the ends of the filament and connected to a fixed-point O (Refer to Figure 11 in (Stockie and Green 1998)). (Stockie and Green 1998) had developed a criterion based on the exterior angle (β) to classify filament orbit classes. The filament can be considered to be rigid if 175° < β < 180°, the filament is springy if 90° < β < 175° and for β < 90° < 30°, the filament ends move independently of each other forming C-shapes. Further, from the filament deformations, it is observed that complex shape orbit class can be specified for β < 30°. The resulting flexible filament regimes are classified and plotted in Figure 4.10 with respect to Viscous Flow Forcing value (VFF) and bending rigidity (K_b). Along with the present simulation results, the experimental results of (Forgacs and Mason 1959) and numerical results of (Stokie and Green 1998) are also included in the classification plot.
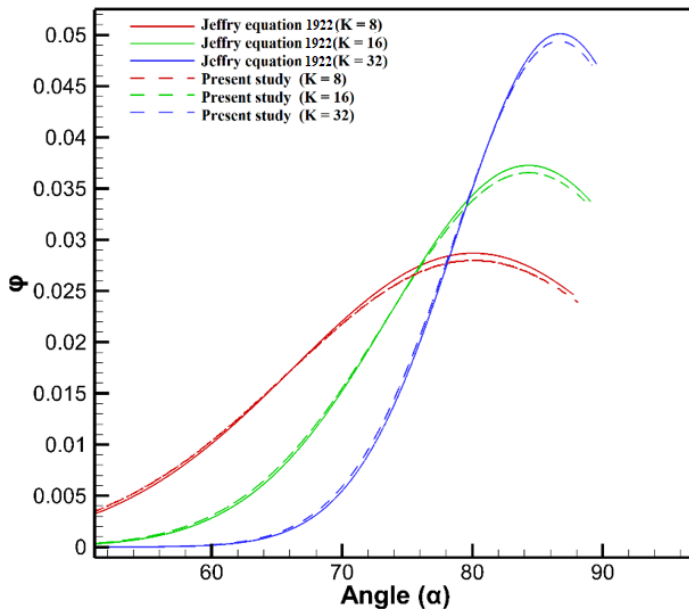
Figure 4.8 A probability distribution plot indicating the time spent by the rigid filament at various angles (α).
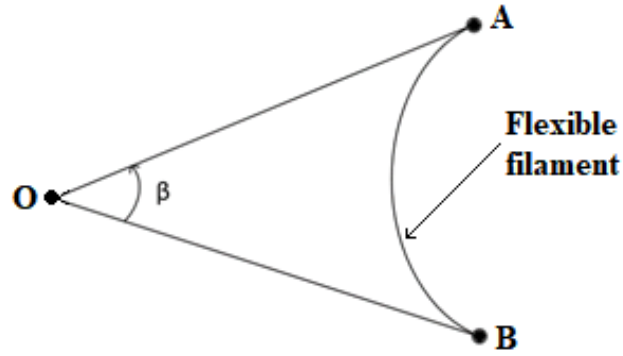
Figure 4.9. Exterior angle β, defined between the ends A and B of the filament.
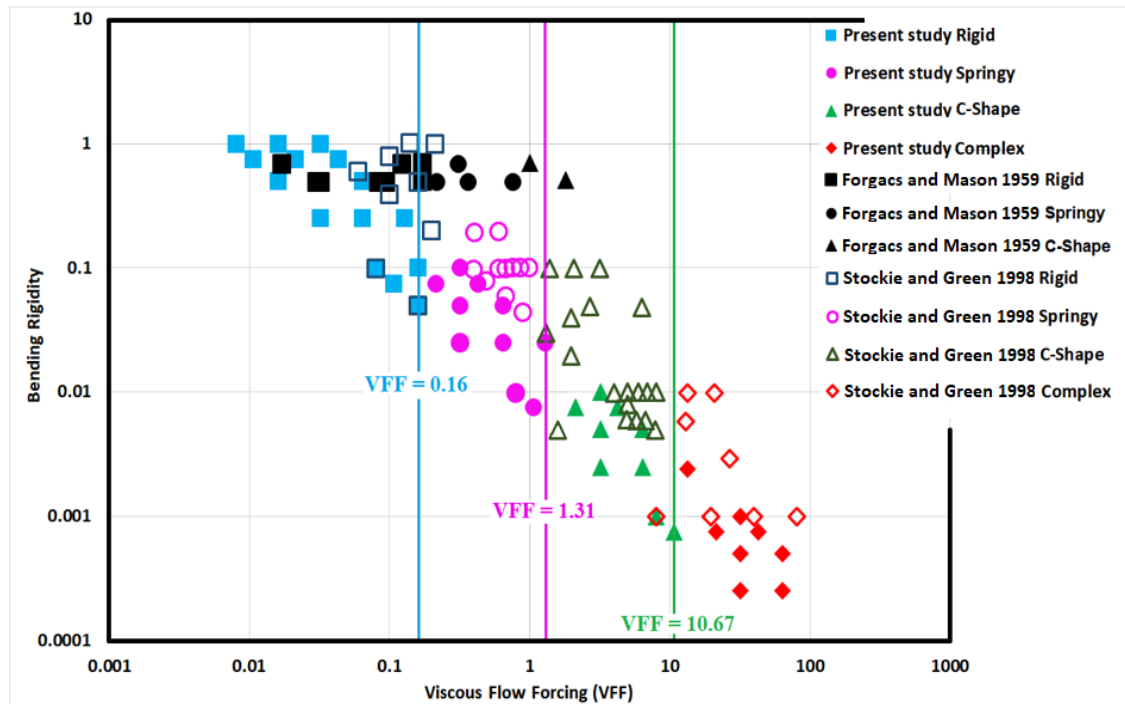
Figure 4.10 Classification of flexible filament deformation into various orbit classes like Rigid, Springy, C – Shape and Complex shapes.

57

In Figure 4.10, the vertical solid lines demarcate filament orbit regimes. In the plot, the black solid points indicate experimental results of (Forgacs and Mason 1959), the colour open points indicate numerical results of (Stokie and Green 1998) and colour solid points indicate present simulation results. As observed from Figure 4.10, most of the present study results coincide with experimental results of (Forgacs and Mason 1959) and numerical results of (Stokie and Green 1998), especially for rigid, springy and C-shape regimes. The division in orbit regimes from rigid to springy to C-shape are obtained at VFF = 0.16, 1.31 and 10.67, consistent with the criterion stipulated by (Stokie and Green 1998). Thus, the results of the present study are found to be in excellent agreement with previous experimental and computational results. The two aspects discussed in Figure 4.8 and Figure 4.10 serve as the quantitative validation for the present model. All of the above results and observations actively demonstrate the ability of the developed model to simulate the dynamics of a flexible filament in shear flow.

Next, the two-dimensional simulation of diatom chains in viscous shear flow is considered. The case analysed here is that of unicellular phytoplankton which is a non-motile diatom made up of linkages. The diatom chains are thus modelled in the present study as flexible filaments. The phytoplankton (diatom chains) in the ocean typically experience shear rate in the range of 0.01 to 1 s^{-1}. Also, the length of the diatom chains is estimated to be between 0.25mm to 4mm. The limits for both shear rate and characteristic length observed for diatom chains is ascertained by (Karp-Boss et al. 1996). The Reynolds number which depends on shear rate and diatom chain length for this case lies between $6.25 \times 10^{-4} \leq \mathrm{Re} \leq 16$ as confirmed by simulation studies of (Nguyen and Fauci 2014). Considering the properties of seawater and bending rigidity of diatom chains, the Reynolds number for the present study is fixed at 1.75. Here, the Reynolds number is computed based on the length of the filament as characteristic length and oceanic shear rate as the reference for characteristic velocity. The chosen physical parameters and their corresponding non-dimensionalized values are tabulated in Table 4.4.

Table 4.4 Physical parameters and dimensionless values considered for the two-dimensional simulation of diatom chain.

Physical Parameters	Dimensional value	Non-dimensional value
Filament length (L^*)	0.47mm	0.25
	0.58mm	0.3125
Shear rate (G^*)	0.5/s	1.0
	1.0/s	2.0
Bending rigidity ($K_b{}^*$)	5.72×10^{-16} Nm^2	1×10^{-4}
	5.72×10^{-17} Nm^2	1×10^{-5}

In order to perform the parametric study, eight different cases are analyzed based on non-dimensionalized filament length (L), shear rate (K) and bending rigidity (K_b). To simplify explanations for various cases, the filament having length $L \leq 0.25$ are considered short and that with length $L > 0.25$ are considered as long. Also, filaments with bending rigidity $K_b = 1 \times 10^{-4}$ are identified as type-A, and those with rigidity $K_b = 1 \times 10^{-5}$ are called type-B. The chosen bending rigidity of diatoms lies between that of L. annulata and G. delicatula species. The shear rate and Reynolds number in the study are very similar to that experienced by diatom chains in the ocean.

The continuity and momentum equations are solved on a two-dimensional rectangular channel of dimensionless length 8.0 and height 1.0. The fluid domain is made up of 1024 $\times$ 128 grid points and a time step of 1×10^{-5} is used to satisfy the stability of the numerical scheme. The physical problem defined for this study consists of a flexible filament held horizontally at the centre position of the simulation domain. The filament is modelled with 100 IB points. In literature, it is observed that the flexible filament is initially curved and placed horizontally at the channel mid-plane. This will help the filament to come out of the mechanical equilibrium position and subsequently undergo deformations. However, in the

present study, the filament is kept inclined at a particular angle to the horizontal in order to allow it to deviate from its equilibrium position. When diatom chain simulation is performed, the filament would initially take considerable amount of time to undergo any significant deformation. Thus, it is necessary to maintain a higher initial angle of inclination of 10° so as to obtain different filament orbits in a reasonable amount of time. The filament is placed at the centre of the computational domain at location (4, 0.5). The value of stretching co-efficient K_s is fixed as 5000 for all cases. A computer code based on FORTRAN is developed to perform two-dimensional simulations. The simulations are carried out for t = 60.0, and the evolution of diatom links for each case is systematically investigated. The deformation of the filaments is recorded at respective time intervals for all cases.

4.3.3 Case study

The evolution of filament collectively depicts the various deformation states the filament undergoes at different time steps. The study is carried out by performing simulations for short and long filaments based on their lengths. Also, shear rates and bending rigidity are varied.

Case 1: L = 0.25, K = 1.0, $K_b = 1 \times 10^{-4}$.

The filament belonging to this group is short, type-A and subjected to a lower shear rate. Figures 4.11 and 4.12 show filament evolution and streamlines obtained near the filament surface respectively. In Figure 4.11, the filament does not deform for the initial time sequence and remains in the horizontal position for a larger portion of simulation. At t = 54.0 (Figure 4.12), the filament breaks symmetry and at t = 60.0 folds onto itself to form a C-shape buckling. Similar shapes were reported in the experimental works of (Forgacs and Mason 1959), numerical studies of (Stockie and Green 1998; Stockie 2002; Ross and Klingenberg 1997). These deformations are referred to as snake turns. No form of shape replication is observed. A sequence of single and multiple recirculation zones are observed throughout. Streamlines as observed at t = 50.0 (Figure 4.12), show the formation of a large elliptical recirculation zone at the bottom right portion of the filament. This zone travels

left along the filament surface. At t = 54.0, the zone grows sufficiently large to push the filament upwards thus making the filament to bend at the centre. The formation of such large primary circulation zones indicates symmetry breakage for filaments.

| t =2.5 | t =5.0 | t =7.5 | t =10.0 | t =12.5 | t =15.0 | t =17.5 | t =20.0 | t =22.5 | t =25.0 | t =27.5 | t =30.0 |

| t =32.5 | t =35.0 | t =37.5 | t =40.0 | t =42.5 | t =45.0 | t =47.5 | t =50.0 | t =52.5 | t =55.0 | t =57.5 | t =60.0 |

Figure 4.11 Evolution of filament in shear flow for L=0.25, K=1.0, K_b=1 × 10^{-4}.

| t = 20.0 | t = 25.0 | t = 30.0 | t = 35.0 |

| t = 40.0 | t = 45.0 | t = 50.0 | t = 52.0 |

| t = 54.0 | t = 56.0 | t = 58.0 | t = 60.0 |

Figure 4.12 Streamlines obtained at the vicinity of filaments at different time sequences for L=0.25, K=1.0, K_b=1 × 10^{-4}.

Case 2: L = 0.25, K = 2.0, $K_b = 1 \times 10^{-4}$.

The filament in this group is short, type-A and subjected to higher shear rate. Figures 4.13 and 4.14 show filament evolution and streamlines obtained near the filament surface respectively. Symmetry breaks at t = 22.0 as seen in Figure 4.14. The filament undergoes a snake-like turn and returns back to a horizontal, inclined position at t = 30.0. The deformation time t_d is observed to be 4.0 (between t = 22.0 and t = 26.0). When filament deformation is observed at t = 25.0 and at t = 47.5, a snake turn shape replication is seen (Figure 4.13). The images at t =14.0,16.0, 18.0 and 20.0 (Figure 4.14) show multiple recirculation zones along the length of filament owing to instability caused by the combination of fluid impingement and compression states of the filament. Similar to case 1, a large elliptical zone is produced at left filament corner which pushes it upwards. At t = 30.0 (Figure 4.14), the elliptical zone spans across the entire length of the filament with the recirculation centre close to filament midpoint.
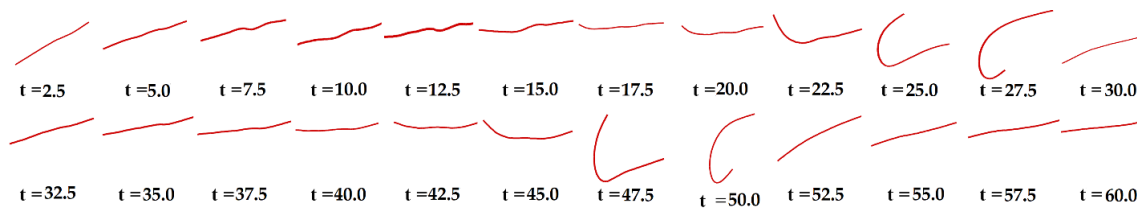
Figure 4.13 Evolution of filament in shear flow for L=0.25, K=2.0, K_b=1 × 10^{-4}.

Case 3: L = 0.25, K = 1.0, $K_b = 1 \times 10^{-5}$.

The filament is type-B, short and subjected to a lower shear rate in this case. Figures 4.15 and 4.16 show filament evolution and streamlines obtained near the filament surface respectively. The symmetry break occurs early at t = 24.0 (Figure 4.16), thus highlighting that symmetry break occurs faster for type-B filaments when compared to type-A as in case 1. When the filament is observed at t = 32.5 (Figure 4.15), an incomplete "S" shape is seen. Such S-turns are a characteristic feature of flexible filaments, and similar shapes are observed in the numerical works of (Weins and Stockie 2015), (Ross and Klingenberg 1997) and experimental works of (Forgacs and Mason 1959). Deformation time t_d is found

to be 10.0 (between t = 24.0 and t = 34.0). Also, shape replication is seen when deformation is observed at t = 27.5 and t = 52.5.

t = 10.0   t = 14.0   t = 16.0   t = 18.0

t = 20.0   t = 22.0   t = 24.0   t = 26.0

t = 28.0   t = 30.0   t = 32.0   t = 34.0

Figure 4.14 Streamlines obtained at the vicinity of filaments at different time sequences for L=0.25, K=2.0, K_b=1 × 10^{-4}.

t =2.5   t =5.0   t =7.5   t =10.0   t =12.5   t =15.0   t =17.5   t =20.0   t =22.5   t =25.0   t =27.5   t =30.0

t =32.5   t =35.0   t =37.5   t =40.0   t =42.5   t =45.0   t =47.5   t =50.0   t =52.5   t =55.0   t =57.5   t =60.0

Figure 4.15 Evolution of filament in shear flow for L=0.25, K=1.0, K_b=1 × 10^{-5}.
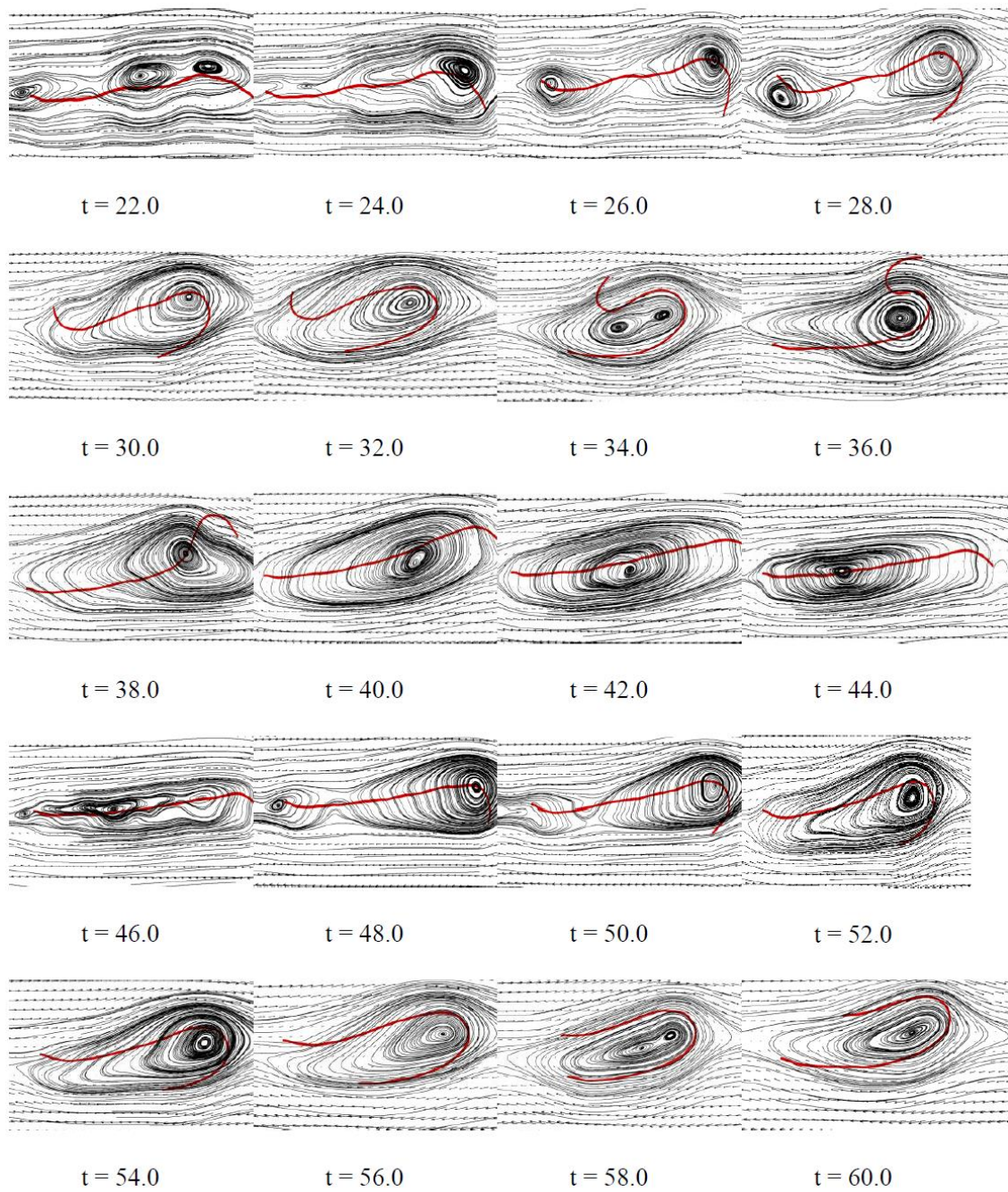
Figure 4.16 Streamlines obtained at the vicinity of filaments at different time sequences for L=0.25, K=1.0, $K_b=1 \times 10^{-5}$.

In Figure 4.16 at t = 26.0, two recirculation zones appear with the primary zone at right side and secondary zone at the left end of the filament. The primary zone pushes the right side of the filament downwards whereas the secondary zone pushes the left tip upwards. This can be observed at t = 28.0 in Figure 4.16. As time advances, the secondary zone is absorbed by the primary one to form a single eye shaped recirculation zone at t = 32.0. The centre of the primary zone splits up and then merges back to form a circularly shaped zone at t = 36.0. Finally, the filament reaches the horizontal position with an elliptical zone spanning the entire filament length at t = 42.0. The replication of S-shape begins at t = 44.0. Primary and secondary zones are observed at t = 48.0. However, the secondary zone is unable to grow to a bigger size as seen at t = 28.0 which prevents the left filament tip to move upwards, and thus the left portion aligns with the primary zone. This leads to the formation of C-shape buckling, and hence a combination of S and C-shapes are observed throughout in Figure 4.16. Throughout the simulation, the ends of the filament never return back to its original position and remain in a deformed state, thus indicating non-recuperation.

Case 4: $L = 0.25$, $K = 2.0$, $K_b = 1 \times 10^{-5}$.

In this case, the filament is type-B, short and subjected to higher shear rate. Figures 4.17 and 4.18 show the evolution pattern and corresponding streamlines obtained near the filament surface. Symmetry breaks early at t = 7.5 (Figure 4.17). The lowest end-to-end distance d_{ee} is seen at t = 15.0. Deformation time t_d is found to be 7.5 (between t = 7.5 and t = 15.0). Folding of the filaments occur at t = 15.0, t = 25.0 and close to t = 32.5. Beyond this point, a transition of filament shape from straight to S-shape occurs between t = 40.0 to t = 48.0. The mechanism with which S-shape is formed is similar to case 3. However, an important aspect of this case is the formation of two equally sized recirculation zones post S-shape formation. This is observed at t = 50.0 .

t =2.5   t =5.0   t =7.5   t =10.0   t =12.5   t =15.0   t =17.5   t =20.0   t =22.5   t =25.0   t =27.5   t =30.0

t =32.5   t =35.0   t =37.5   t =40.0   t =42.5   t =45.0   t =47.5   t =50.0   t =52.5   t =55.0   t =57.5   t =60.0
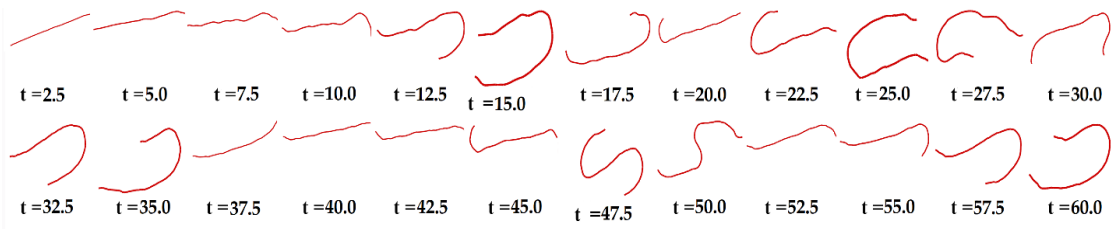
Figure 4.17 Evolution of filament in shear flow for L=0.25, K=2.0, K_b=1 × 10^{-5}.

t = 36.0   t = 38.0   t = 40.0   t = 42.0

t = 44.0   t = 46.0   t = 48.0   t = 50.0
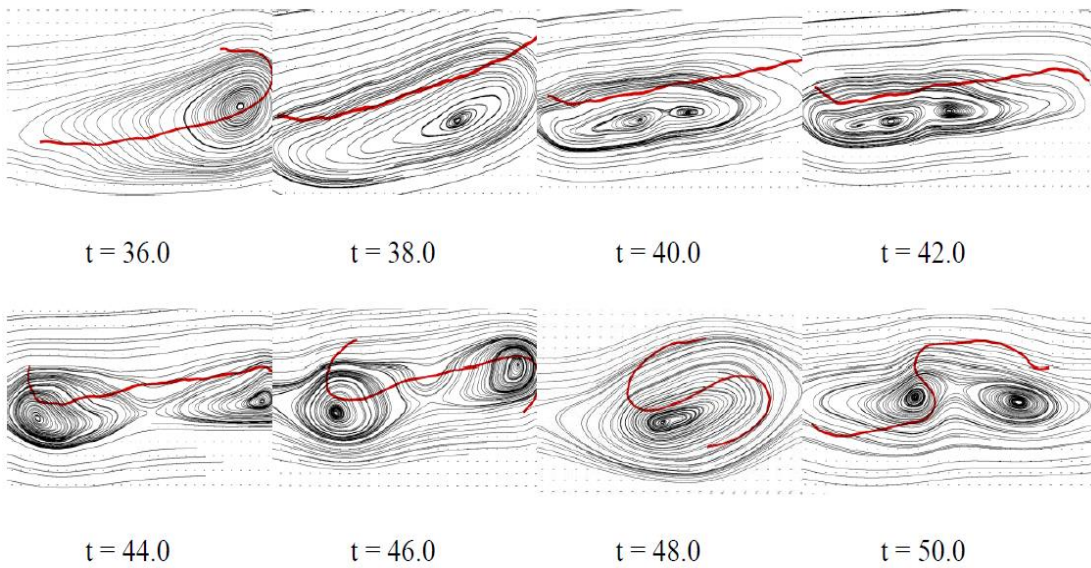
Figure 4.18 Streamlines obtained at the vicinity of filaments at different time sequences for L=0.25, K=2.0, K_b=1 × 10^{-5}.

Case 5: L = 0.3125, K = 1.0, K_b = 1 × 10^{-4}.

Figure 4.19 depicts a type-A, long filament subjected to lower shear rate. Figure 4.20 shows the streamlines obtained near the filament surface. Symmetry break occurs at t = 58.0 (Figure 4.20), which is closer to the simulation end time. No substantial deformation is observed making it similar to case 1. This also indicates that longer filaments tend to take more time compared to short filaments to undergo noticeable deformation when subjected to the same shear flow conditions. The formation mechanism of C-shape buckling is similar

66

to case 1. Throughout the simulation, multiple recirculation zones ranging from two to four are observed near the filament surface.

| t =2.5 | t =5.0 | t =7.5 | t =10.0 | t =12.5 | t =15.0 | t =17.5 | t =20.0 | t =22.5 | t =25.0 | t =27.5 | t =30.0 |

| t =32.5 | t =35.0 | t =37.5 | t =40.0 | t =42.5 | t =45.0 | t =47.5 | t =50.0 | t =52.5 | t =55.0 | t =57.5 | t =60.0 |
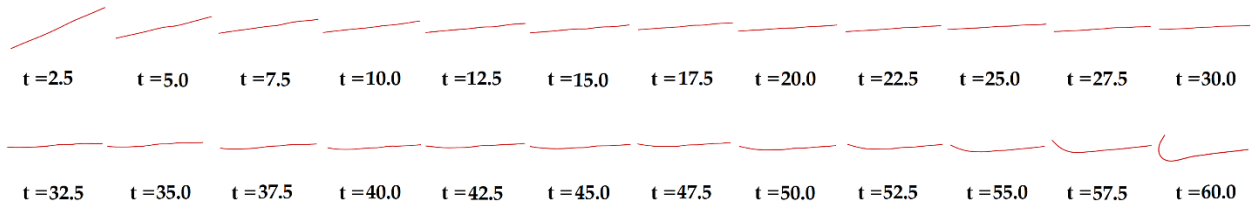
Figure 4.19 Evolution of filament in shear flow for L=0.3125, K=1.0, K_b=1 × 10^{-4}.

| t = 20.0 | t = 25.0 | t = 30.0 | t = 35.0 |

| t = 40.0 | t = 45.0 | t = 50.0 | t = 52.0 |

| t = 54.0 | t = 56.0 | t = 58.0 | t = 60.0 |
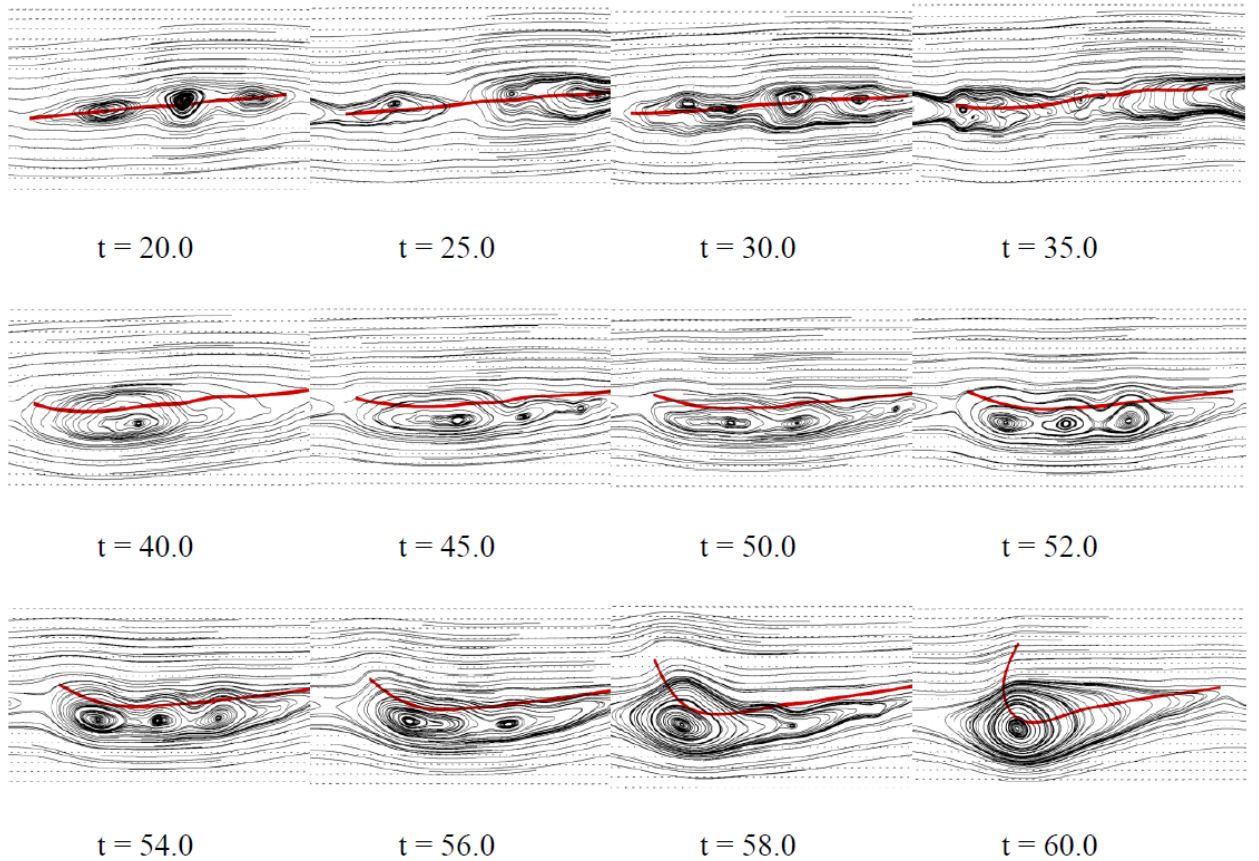
Figure 4.20 Streamlines obtained at the vicinity of filaments at different time sequences for L=0.3125, K=1.0, K_b=1 × 10^{-4}.

Case 6: L = 0.3125, K = 2.0, K_b = 1 × 10^{-4}.

In this group a type-A, long filament subjected to higher shear rate is considered. Figures 4.21 and 4.22 depict filament evolution and resulting streamlines near the surface respectively. The filament remains horizontal for the first half of the total simulation time and undergoes symmetry break at t = 30.0. Snake-like turns are also observed here which is similar to case 2. The deformation time t_d is observed to be 4.0 (between t = 30.0 and t = 34.0). Replication of the snake turn shape occurs when observed for deformation at t = 34.0 (Figure 4.22) and t = 57.5(Figure 4.21). The ends of the filament return back to its original position, thus showing rigidity. The mechanism of snake turn is similar to case 2.
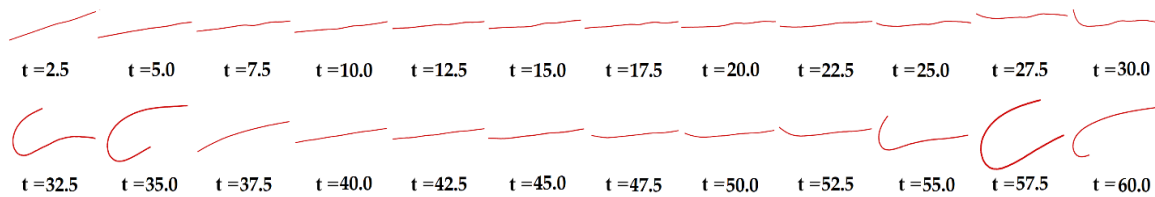
Figure 4.21 Evolution of filament in shear flow for L=0.3125, K=2.0, K_b=1 × 10^{-4}.

Case 7: L = 0.3125, K = 1.0, K_b = 1 × 10^{-5}.

Figure 4.23 illustrates the deformation of type-B, long filaments in the fluid flow of high shear rate. Figure 4.24 show streamlines occurring near the surface of the filament. The deformations observed are very similar to case 3. The symmetry breaks at t = 27.5. An incomplete S-shape is formed at t = 37.5. The mechanism of S shape formation is very similar to case 3 given in Figure 4.16. Shape replication is observed for t = 35.0 and t = 57.5. It can be seen in Figure 4.16 corresponding to case 3 that the filament gains S-shape. However, when observing the same filament from t = 50.0 to t = 60.0, there is a transition to C-shape. Such transitions are not observed here, and S-shapes appear to occur in a cyclic manner. This may be due to the extended length of the filament in the present case. The streamlines from t = 50.0 to t = 60.0 are shown in Figure 4.24.

t = 10.0   t = 15.0   t = 20.0   t = 22.0

t = 24.0   t = 26.0   t = 28.0   t = 30.0

t = 32.0   t = 34.0   t = 36.0   t = 38.0
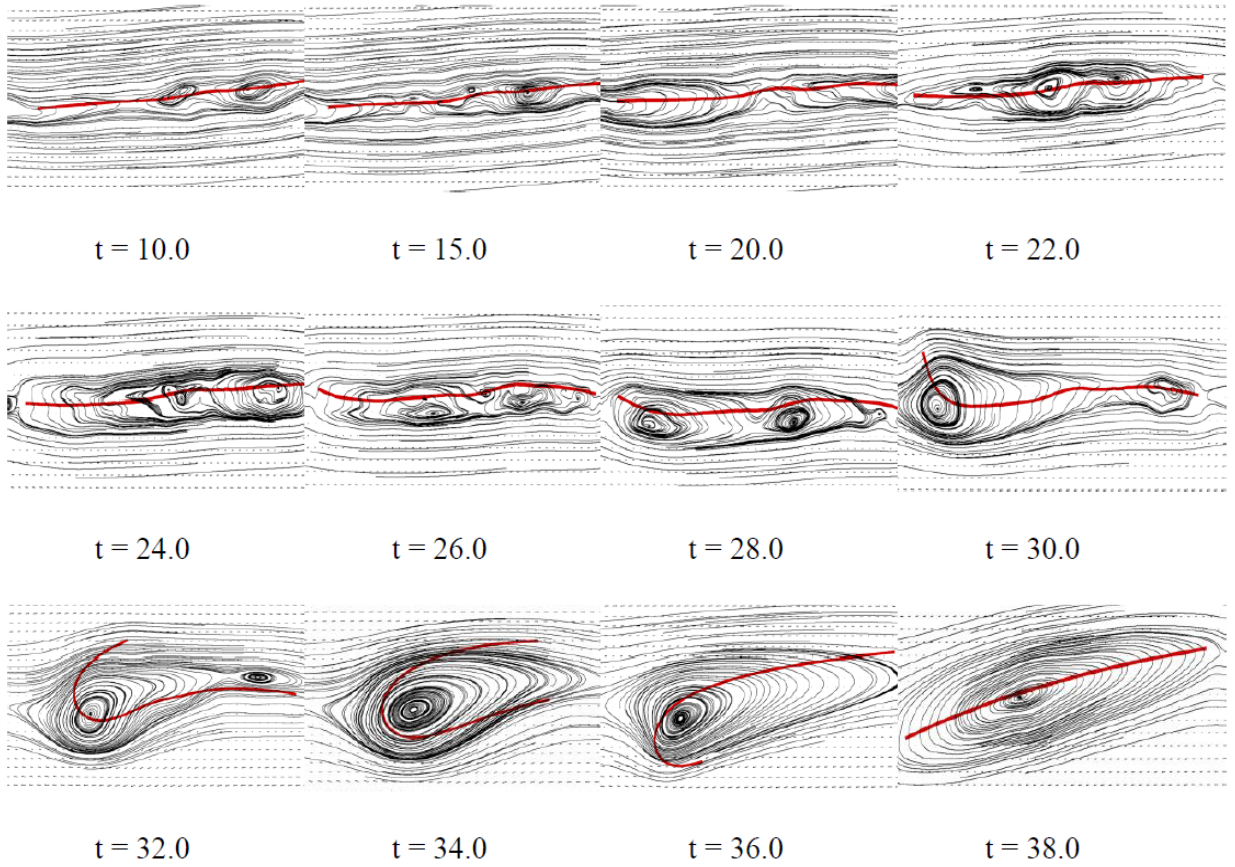
Figure 4.22 Streamlines obtained at the vicinity of filaments at different time sequences for L=0.3125, K=2.0, K_b=1 $\times$ 10^{-4}.

t =2.5   t =5.0   t =7.5   t =10.0   t =12.5   t =15.0   t =17.5   t =20.0   t =22.5   t =25.0   t =27.5   t =30.0

t =32.5 t =35.0 t =37.5 t =40.0   t =42.5   t =45.0   t =47.5   t =50.0   t =52.5   t =55.0   t =57.5   t =60.0
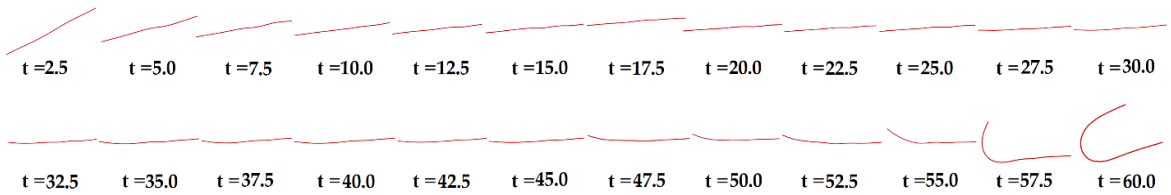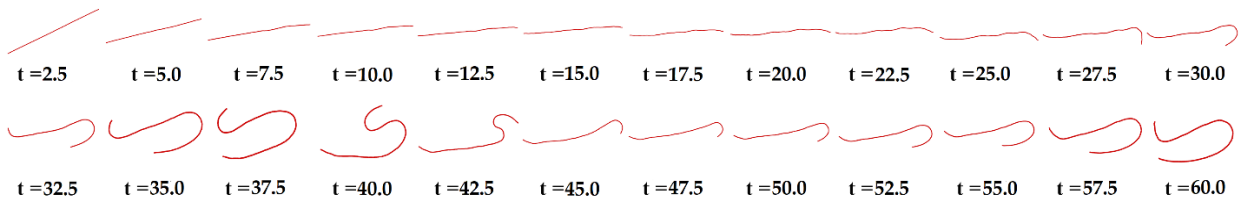
Figure 4.23 Evolution of filament in shear flow for L=0.3125, K=1.0, K_b=1 $\times$ 10^{-5}.
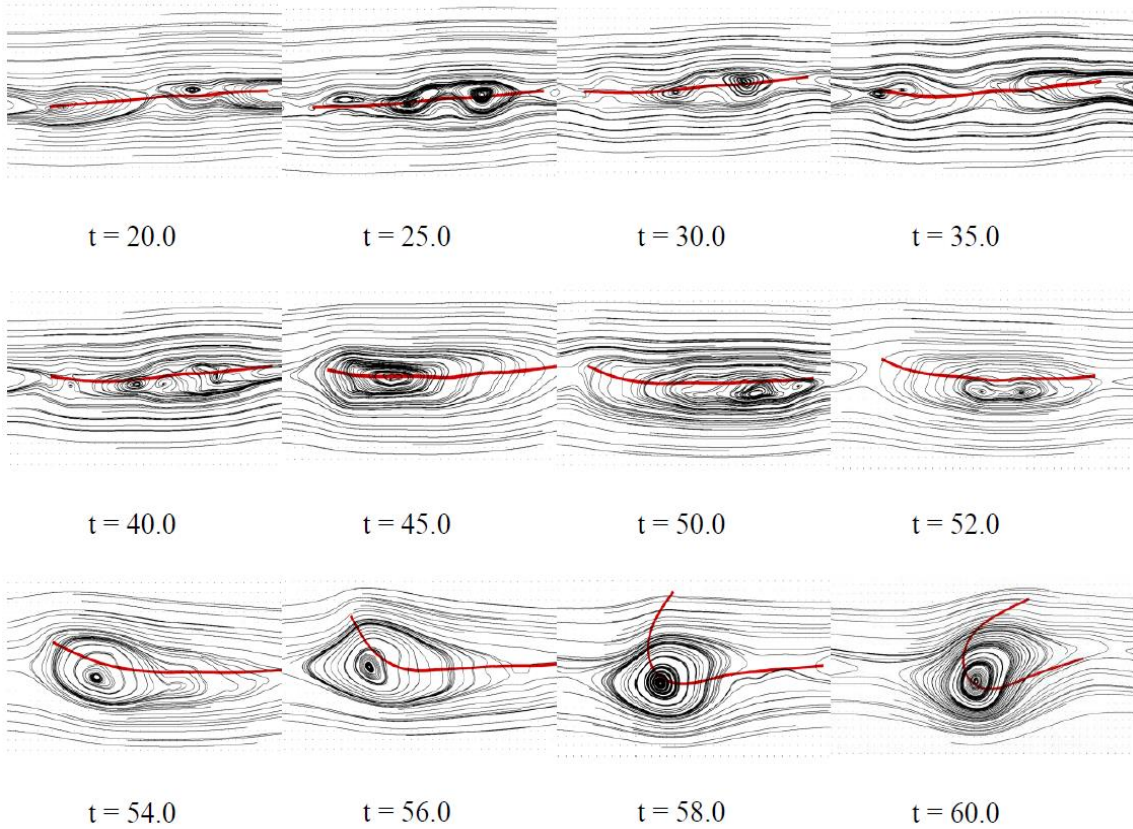
69
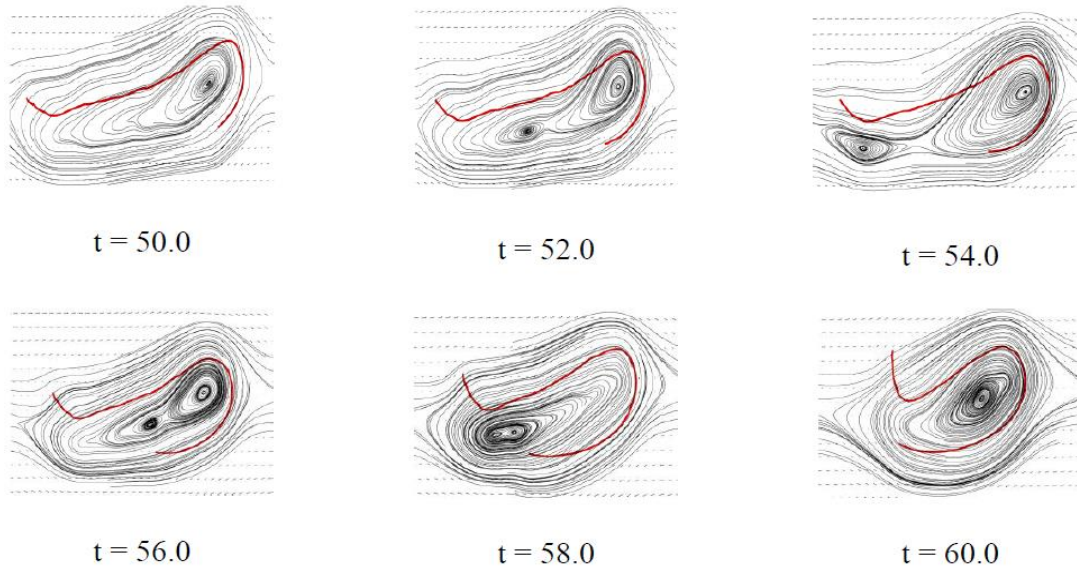
Figure 4.24 Streamlines obtained at the vicinity of filaments at different time sequences for L=0.3125, K=1.0, K_b=1 × 10^{-5}.

Case 8: L = 0.3125, K = 2.0, K_b = 1 × 10^{-5}.

In the last case, the filament considered is type-B, long and subjected to a high shear rate. The symmetry break is obtained at t = 10.0 as seen in Figure 4.25. Figure 4.26 shows the streamlines obtained near the filament surface for complex shapes. A wide range of complete and incomplete S-shapes are observed during the simulation. The filament undergoes incomplete S turns at t = 17.5 and t = 35.0, while complete S-turns are found at t = 42.5 (Figure 4.25) and t = 50.0 (Figure 4.26). Shape replications are obtained for t = 30.0 and t = 60.0. The deformation time t_d is observed to be 7.5 (between t = 10.0 and t = 17.5).The filament is highly flexible in nature and produces the highest number of turning point replications. It shows the least resistance to fluid flow. Along with S-turns, some complex shapes have also been found at t = 27.5, 37.5 and 52.5 (Figure 4.25). Apart from t = 38.0 and t = 42.0, all images show one large circular recirculation zone around which the filament rotates.

t =2.5 t =5.0 t =7.5 t =10.0 t =12.5 t =15.0 t =17.5 t =20.0 t =22.5 t =25.0 t =27.5 t =30.0

t =32.5 t =35.0 t =37.5 t =40.0 t =42.5 t =45.0 t =47.5 t =50.0 t =52.5 t =55.0 t =57.5 t =60.0
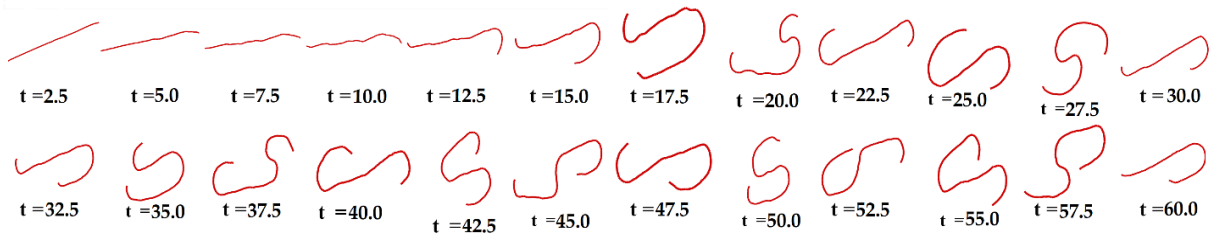
Figure 4.25 Evolution of filament in shear flow for L=0.3125, K=2.0, $K_b=1 \times 10^{-5}$.

t = 36.0

t = 38.0

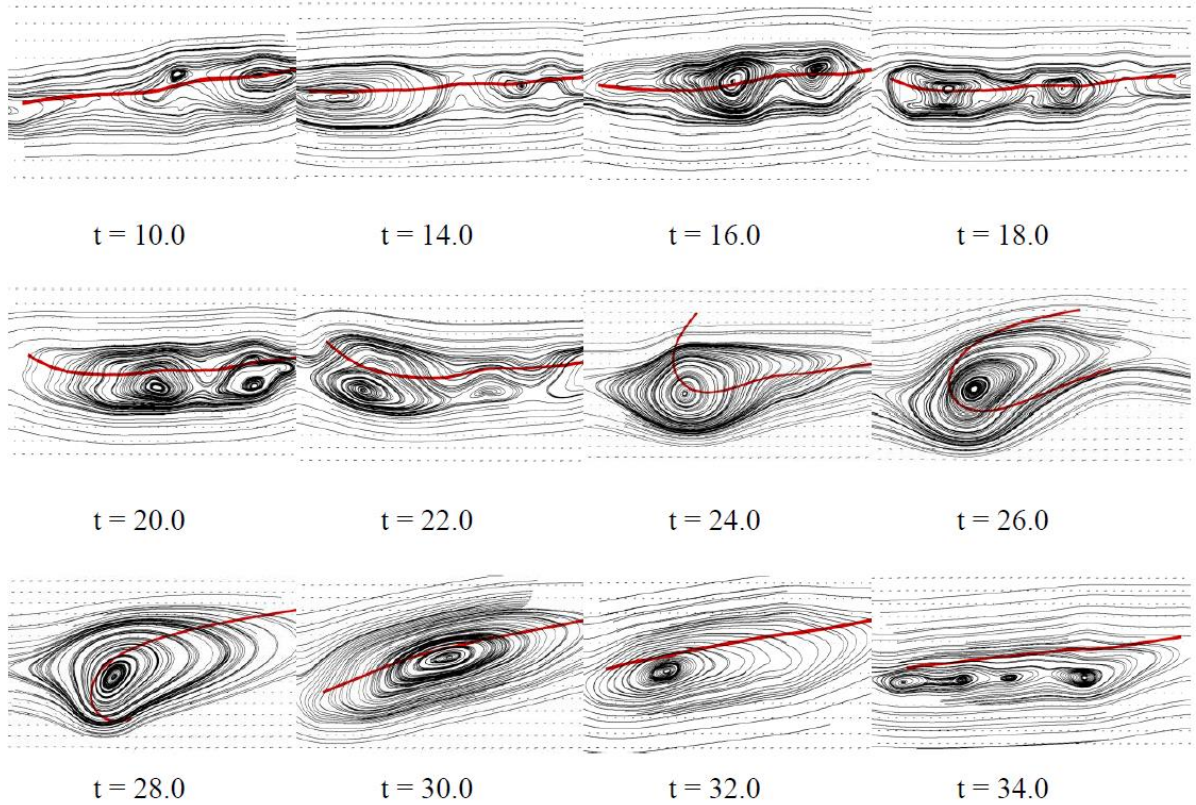t = 40.0

t = 42.0

t = 44.0

t = 46.0

t = 48.0

t = 50.0

t = 52.0
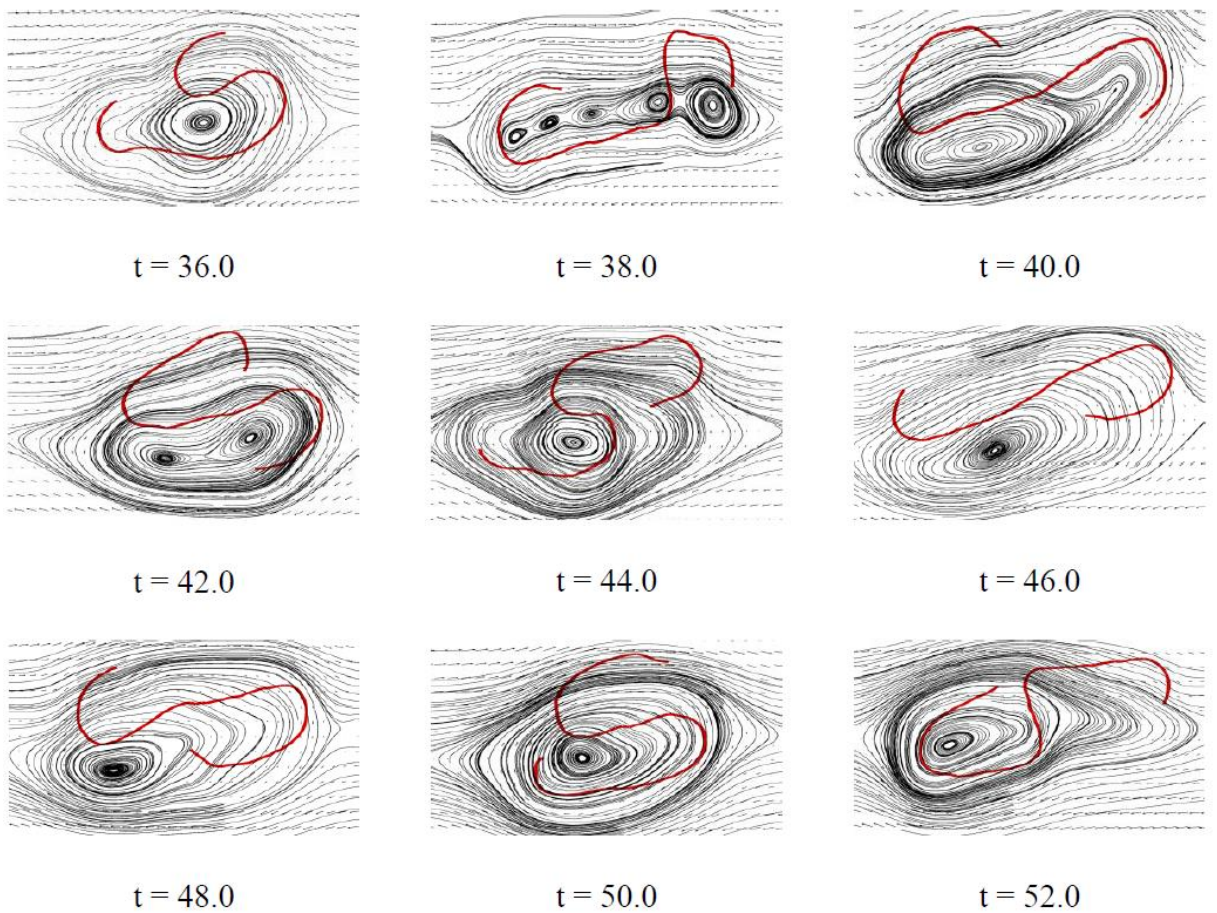
Figure 4.26 Streamlines obtained at the vicinity of filaments at different time sequences for L=0.3125, K=2.0, $K_b=1 \times 10^{-5}$.
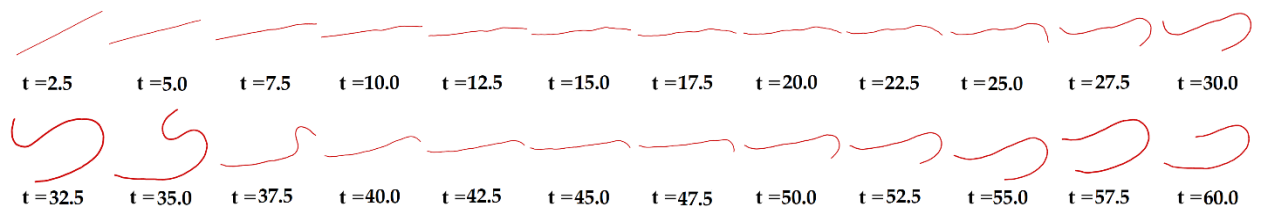
71

The dimensional physical parameters available in Table 4.4 are required for the calculation of Viscous Flow Forcing value (VFF) for all the cases considered. The same is calculated and provided in Table 4.5.

Table 4.5 Viscous Flow Forcing term (VFF) calculated for different cases of varying filament length, shear rate and bending rigidity for Reynolds number 1.75.

Case No. and condition (length, shear, rigidity type)	Diatom chain length, L_{diatom} (m) $\times 10^{-3}$	Shear rate, G (s^{-1})	Bending rigidity, K_b (Nm^2)	Viscous Flow Forcing (VFF) $\times 10^3$
1 (short, low shear, type-A)	0.47	0.5	5.72×10^{-16}	0.0894
2 (short, high shear, type-A)	0.47	1.0	5.72×10^{-16}	0.1788
3 (short, low shear, type-B)	0.47	0.5	5.72×10^{-17}	0.8942
4 (short, high shear, type-B)	0.47	1.0	5.72×10^{-17}	1.788
5 (long, low shear, type-A)	0.58	0.5	5.72×10^{-16}	0.1744
6 (long, high shear, type-A)	0.58	1.0	5.72×10^{-16}	0.3489
7 (long, low shear, type-B)	0.58	0.5	5.72×10^{-17}	1.744
8 (long, high shear, type-B)	0.58	1.0	5.72×10^{-17}	3.489

The Viscous Flow Forcing value for the present diatom chain problem involving all the test cases ranges from $5.0 \times 10^{-4} \leq VFF \leq 1.1 \times 10^5$ as provided in the simulation studies of (Nguyen and Fauci 2014). By observing the Viscous Flow Forcing term calculated for all cases in Table 4.5 and by analysing filament deformation from the case study, it is ascertained that cases 1,2,5 and 6 all produce VFF value less than 350. These are also the cases for which the filaments undergo initial deformation and with the progression of simulation time retain their original shape. Filaments belonging to these groups are thus classified as recuperative. Recently, (Liu et al. 2018) analysed the morphological

transitions of elastic filaments in shear flow. The transition between different orbit classes or regimes of elastic filaments is studied using experimental and local slender-body theory. Tumbling, C-buckling and U-turn regimes are observed and their corresponding Viscous Flow Forcing values are calculated. In their theoretical study, the filament contour lengths are in the range 4 - 40µm and shear rate is in the range $1 - 10$ s^{-1}. In the experimental setup, the Reynolds number is of the order 10^{-4}. For the case of non-Brownian filament motion, the first transition from tumbling to C-buckling occurs at a Viscous Flow Forcing value of 306.4 which is also verified by them through experiments. A phase chart diagram (Refer to Figure 4 in (Liu et al. 2018)) is also provided by them to highlight the various filament transition regimes. The filament is highly recuperative in nature and beyond the Viscous Flow Forcing value of 306.4, the filament transitions from C-buckling to U-turn shape indicating non-recuperative behaviour. Accordingly, the results are in reasonable agreement with that of (Liu et al. 2018).

Filaments belonging to cases 3,4,5 and 7 have VFF value higher than 350. These filaments never retain their original shape once initially deformed. Thus they can be grouped as non-recuperative. The fluid motion or pattern of recirculation zones leading to the formation of snake turns (C-shape) and S-shapes are similar in all cases. Fluid flow around recuperative filaments as observed in case 1 and case 5 show the formation of single and multiple recirculation zones along the length of the filament. This is an indication of filament resistance to fluid motion. The flow is drag induced making it an ideal condition for nutrient absorption in diatoms (Karp-Boss et al. 1996). Also, recuperative filaments produce flat elliptical zones around the filament body as compared to non-recuperative ones which produce circularly shaped zones. Elliptical zones prevent nutrients from spreading locally, thus providing diatom with a rich nutrient surrounding. Long recuperative filaments deform at a slow pace when compared to short filaments. An increase in length also contributes to more number of zones. Short filaments as in cases 3 and 4 have an ability to transit from S-shape to C-shape irrespective of their bending rigidity. However long filaments have cyclic nature of shape formation without transitions. The non-reuperative filaments tend to deform faster along the orbit of the circulation zone and also show less

73

resistance to fluid motion. This prevents the filament from sweeping nutrients as compared to recuperative filaments (case 2 and case 6).

In the above case study, the analysis was carried out for a fixed Reynolds number Re = 1.75. Now let us examine the effect of varying Reynolds number on diatom chain deformations. Two Reynolds numbers (Re = 0.875, by varying shear rate) and (Re = 8.0, by varying diatom chain length) are computed. The critical Viscous Flow Forcing value also varies for different Reynolds numbers. The simulations for the Reynolds numbers mentioned above are carried out. The dynamics and evolution of diatom chains for these two cases of Reynolds number Re = 0.875 and Re = 8.0 is analysed and provided in figures below.

| t = 2.5 | t = 5.0 | t = 7.5 | t = 10.0 | t = 12.5 | t = 15.0 | t = 17.5 | t = 20.0 | t = 22.5 | t = 25.0 | t = 27.5 | t = 30.0 |

| t = 32.5 | t = 35.0 | t = 37.5 | t = 40.0 | t = 42.5 | t = 45.0 | t = 47.5 | t = 50.0 | t = 52.5 | t = 55.0 | t = 57.5 | t = 60.0 |
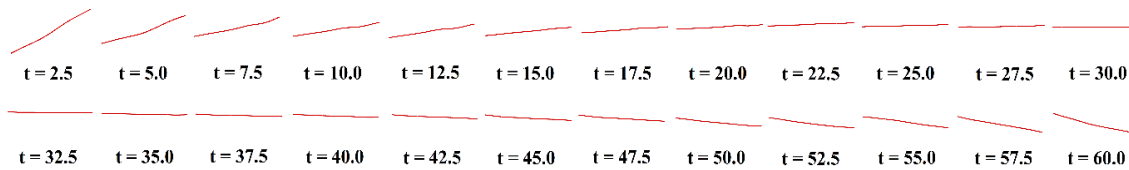
Figure 4.27 Evolution of filament in shear flow for L=0.25, K=1.0, K_b=1 × 10^{-4}, (Re = 0.875, VFF = 44.0).

The analysis from diatom simulation studies has revealed that up to a critical VFF value of 350, the diatom behaves recuperatively and beyond the critical value, they tend to be non-recuperative. Reducing the Reynolds number to 0.875, also causes VFF to decrease and in this case, it is 44.0. When comparing Figure 4.11 pertaining to case 1 of the present study for which Re = 1.75 and VFF = 89.4 and Figure 4.27, we see that not much difference can be seen in filament dynamics throughout the entire simulation period, except towards the end (t = 60.0) where the diatom in Figure 4.27 just begins to undergo buckling. Also, in Figure 4.27 it can be observed that the diatom still behaves recuperatively. Thus, reducing the Reynolds number causes the diatom to deform slowly.

t = 2.5　t = 5.0　t = 7.5　t = 10.0　t = 12.5　t = 15.0　t = 17.5　t = 20.0　t = 22.5　t = 25.0　t = 27.5　t = 30.0

t = 32.5　t = 35.0　t = 37.5　t = 40.0　t = 42.5　t = 45.0　t = 47.5　t = 50.0　t = 52.5　t = 55.0　t = 57.5　t = 60.0
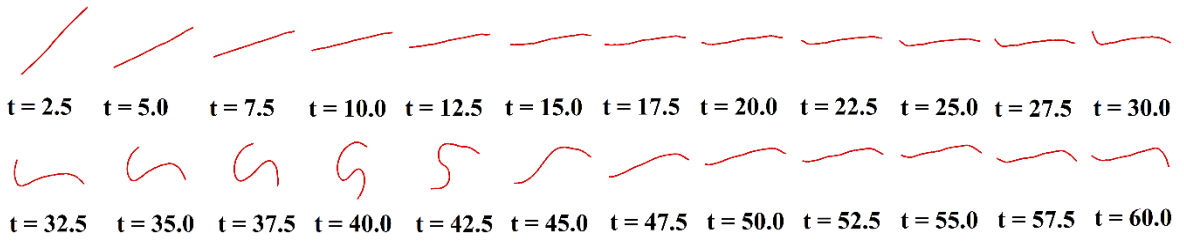
Figure 4.28. Evolution of filament in shear flow for L=0.25, K=1.0, $K_b = 1 \times 10^{-4}$
(Re = 8.0, VFF = 872.0).

If the VFF value is greater than 350, the diatoms do not retain their original shape and their dynamics is concentrated more towards the formation of S-shape deformations. When observing filament evolution for higher Reynolds number, Re = 8.0 and VFF = 872.0 as shown in Figure 4.28 and comparing it with Figure 4.15 which belongs to case 3 of the present study for which the Re = 1.75 and VFF = 894.2 , we see a slight deviation in filament dynamics. We also see that in Figure 4.15, S – shape diatom deformation initiates and completes between time t = 30.0 and t = 40.0. A similar observation is obtained in Figure 4.28 where this time gap is between t = 30.0 to t = 45.0. The slight difference may be due to variation in VFF values for both these scenarios. Higher Reynolds number produced larger Viscous Flow Forcing value. The above analysis also confirms that lower VFF value produces slower filament deformations. Even though Reynolds number is important, VFF values play a critical role in better understanding the dynamics when filaments are subjected to shear flow. The above analysis is comprehensive in that it covers VFF values for a wide range between $0 \leq VFF \leq 3500$, which includes most of the critical parameters like diatom chain length, shear rates and Reynolds numbers.

Next, we shall define some analysis factors that describe motion, shape replication and deformation of filament for the simulation cycle.

Symmetry breakage time (t_{sb}) defined as the time for which the filament breaks symmetry for the first time.

End-to-end distance (d_{ee}) defined as the distance between the two ends of the filament.

Turning point time (t_p) defined as the time at which the filament attains the lowest end-to-end distance.

Deformation time (t_d) defined as the time difference between first symmetry breakage and lowest end-to-end distance.

Recurrence time (t_r) defined as the average time difference between two successive turning point occurrences in the simulation cycle.

We now compare their effects and understand the variation for different cases. It is essential to understand the significance of symmetry breakage time t_{sb}, turning point time t_p, deformation time t_d and recurrence time t_r in the present study. Higher symmetry breakage time signifies that the filament remains in the undeformed state for a large portion of time. This gives ample time for the filament to interact with the surrounding environment. In the case of diatom chains, it provides more time for it to absorb necessary nutrients. Ideally, the diatom has to remain in the undeformed state with an assumption that the surrounding is risk-free. Remaining in the undeformed state allows orientation of filament to high drag inducing fluid motion (Guasto et al. 2012). Once deformation is initiated by fluid motion, the diatoms ability to catch nutrients is lowered. Turning point time indicates the time for which the filament achieves a shape having the lowest end-to-end distance. It also helps to identify the highly deformed state of the filament. With reference to turning points, deformation time can be calculated. The deformation time indicates the ability of the initially deformed filament to reach its highly deformed state. Low deformation time indicates a faster recovery for the filament to reach undeformed position. Thus, the diatom can regain the undeformed state in a shorter period of time. Finally, recurrence time determines the frequency at which subsequent filament turning points occur. Smaller the recurrence time, higher is the turning point frequency. The filaments with high recurrence time tend to remain in the undeformed state longer. Therefore, the best possible condition is that filament must have high symmetry breakage time, low deformation time and high recurrence time (low recurrence frequency). However, these findings have never considered the role of nutrient uptake in diatom corresponding to diffusion, advection and

76

chemical composition of diatom environment. The focus here is understanding the passive alignment of diatom chains based on an accurate representation of external turbulences or recirculation zones in its vicinity.

Table 4.6 Analysis factors such as symmetry breakage time, turning point time, deformation time and recurrence time calculated for all filament case conditions.

Case No. and condition (length, shear, recovery type)	Symmetry breakage time, t_{sb}	Turning point time, t_p	Deformation time, t_d	Recurrence time, t_r
1 (short, low shear, recuperative)	54.0	-	-	-
2 (short, high shear, recuperative)	22.0	26.0	4.0	22.5
3 (short, low shear, non-recuperative)	24.0	34.0	10.0	25.0
4 (short, high shear, non-recuperative)	7.5	15.0	7.5	11.0
5 (long, low shear, recuperative)	58.0	-	-	-
6 (long, high shear, recuperative)	30.0	34.0	4.0	22.0
7 (long, low shear, non-recuperative)	27.5	37.5	10.0	23.0
8 (long, high shear, non-recuperative)	10.0	17.5	7.5	7.4

The above-mentioned analysis factors for all cases are tabulated in Table 4.6 according to filament case conditions. The deformation time t_d is dependent on symmetry breakage time t_{sb}. When observing symmetry breakage time for all cases, it can be seen that $t_{sb} = 7.5$ for case 4 which indicates that symmetry break occurs early for non-recuperative filaments subjected to higher shear rate. Short filaments break symmetry faster as compared to longer ones. Another observation when comparing filaments of the same length and same shear rate is that non-recuperative filaments break symmetry faster than recuperative filaments. Since non-recuperative filaments tend to bend the most, their end to end distance is also smaller. When observing filaments of the same length and same shear as in case 2 and 4, the turning point time is small for non-recuperative filaments. Filaments subjected to lower shear rate also have higher turning points when compared with high shear filaments. The deformation time largely varies with respect to the shear rate as seen in case pairs corresponding to 2,4 and 6,8. The recurrence time t_r for all cases can be calculated by analysing Figures 4.29 – 4.32. Lower recurrence time indicates faster reproduction of turning points by the filament. Non-recuperative filaments which are placed in higher shear rates show higher recurrence rates at $t_r = 11.0$ for case 4 (Table 4.6) and $t_r = 7.4$ for case 8 (Table 4.6). Thus, non-recuperative filaments have a high frequency of recurrence. When comparing filaments based on length for fixed shear and rigidity, long filaments have higher symmetry breakage time, higher turning point time and lower recurrence time. This indicates that long filaments take less time to achieve repeated turning behaviour once the deformation is initiated. From the above discussion, the following ideal cases can be identified. Long recuperative filament subjected to low shear rate (high symmetry breakage time), Short and long recuperative filament placed in high shear rate (low deformation time) and Short non-recuperative filament in low shear flow (high recurrence time).

SB and TP with numeric case number notations are symmetry breaking points and turning points respectively which are indicated in all Figures 4.29 – 4.32. The effect of varying shear rate on d_{ee} of short recuperative filaments is given in Figure 4.29. The dotted line indicates filament subjected to lower shear rate and solid line for higher shear rates. A

higher shear rate in case 2 shows the lowest end to end distance, higher recurrence of turning points and faster symmetry breakage. In Figure 4.30, the effect of shear rate on d_{ee} for short non-recuperative filaments is plotted for the simulation cycle. The recurrence of turning points is highest for non-recuperative filaments subjected to higher shear rate with lower d_{ee}. The behaviour of long filaments to different shear rate is plotted in Figures 4.31 and 4.32 respectively. Figure 4.31 also confirms that filaments at higher shear rate tend to deform faster which is shown by its early symmetry breakage and frequent recurrences within the simulation cycle. High recurrence frequency occurs for long non-recuperative filaments as seen in Figure 4.32 (Case 8).

4.3.4 Filament migration

The fact that the filaments undergo deformation and turning for recuperative and non-recuperative cases prone to varying shear rates is well established in the last section. We now focus on the migration and displacement produced by these filaments for various cases. The movement of the filament in the x-direction indicate its motion towards the entrance or exit of the channel and movement of the filament in the y-direction depicts motion towards upper or lower moving walls. The migration of short filaments subjected to lower shear rate with different bending rigidity in x-direction and y-direction is shown in Figures 4.33 and 4.34 respectively. The filaments in Figure 4.33 move towards the inlet irrespective of rigidity. However non-recuperative filament (case 3) moves towards the top wall indicating that progression in shape causes a significant portion of the filament to move above the centreline (Figure 4.34). Since recuperative filament (case 1) has not achieved considerable deformation, it still remains below the centreline (y = 0.5). The maximum displacement in the x-direction with respect to channel midpoint (4.0, 0.5) is 0.1, and in the y-direction is 0.25. The same set of filaments are now subjected to higher shear rate as shown in Figures 4.35 and 4.36 respectively. The deformation in the y-direction is similar to the previous case where recuperative filament (case 2) tend to deform mostly below the centreline (y = 0.5) as seen in Figure 4.36. The migration of both filaments (case 2 and case 4) is now shifted towards the exit of the channel with maximum

displacement in x-direction being 0.42 and in y-direction 0.3 with respect to channel midpoint (4.0, 0.5). These displacements are higher when compared to low shear rate cases of Figure 4.33 and Figure 4.34, thus confirming that filaments at higher shear tend to be displaced the farthest. Figures 4.37 and 4.38 show migration of long filaments of different bending rigidity subjected to lower shear rate. Both the filaments in Figure 4.37 moves initially towards the inlet and returns back to the original position. In Figure 4.38 non-recuperative filament (case 7) move towards the top wall while the recuperative filament (case 5) remains in the centreline position. The effective displacement in the x-direction is negligible whereas in the y-direction displacement is 0.3 with respect to channel midpoint (4.0, 0.5). When the same case is tested for higher shear rate, there is a drastic difference in x-direction displacement for recuperative and non-recuperative filaments as seen in Figure 4.39. Recuperative filament (case 6) is displaced the farthest when compared to non-recuperative (case 8) towards the channel exit. The frequent occurrences of filament deformation cause the non-recuperative filament to migrate a short distance. The maximum displacement in the x-direction for this case is found to be 0.38. This displacement, when compared to that of short filament subjected to the same shear condition (Figure 4.35, x-displacement = 0.42) is small, showing that short recuperative filament moves the farthest for all cases. The same behaviour of short non-recuperative filament migrating above the centreline and recuperative filament moving below centreline is also observed for long filaments in Figure 4.40. Shear rate and flexibility have a significant contribution in deciding the direction of filament migration. Filaments subjected to higher shear rate tend to move towards the exit portion of the channel, and non-recuperative filaments move towards the top moving wall irrespective of the filament lengths considered in this study.

The developed computational model is used to study deformation, buckling and recuperation behaviour of diatom chain modelled as flexible filament in viscous shear flow. It is necessary to further study filament behaviour for other fluid flow conditions, details of which are provided in subsequent chapters.
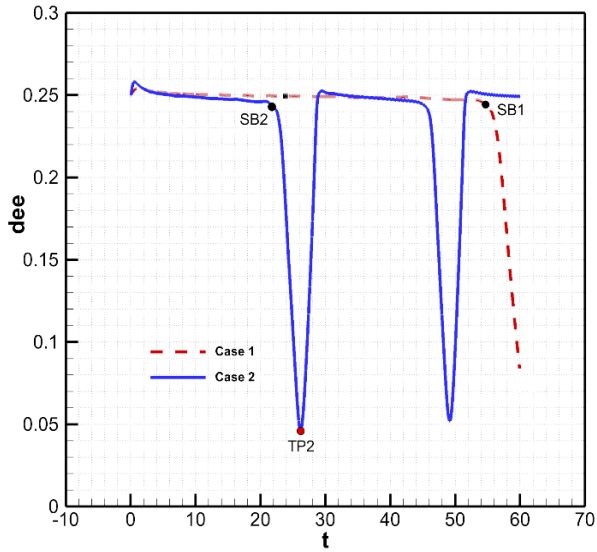
Figure 4.29 Effect of d_{ee} with respect to time for varying shear rate (short recuperative filament)
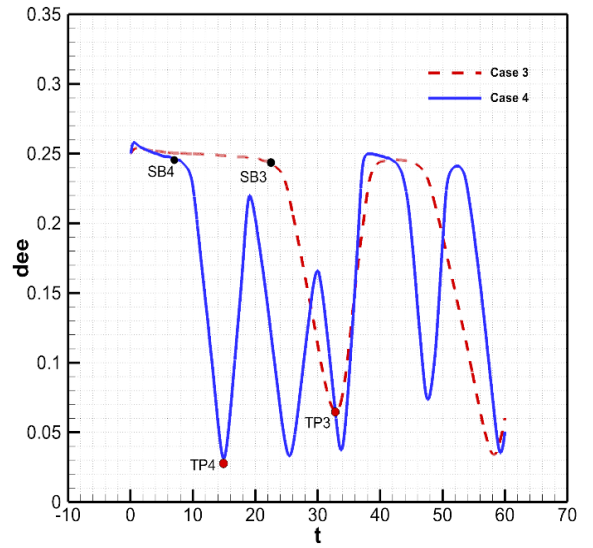
Figure 4.30 Effect of d_{ee} with respect to time for varying shear rate (short non-recuperative filament)
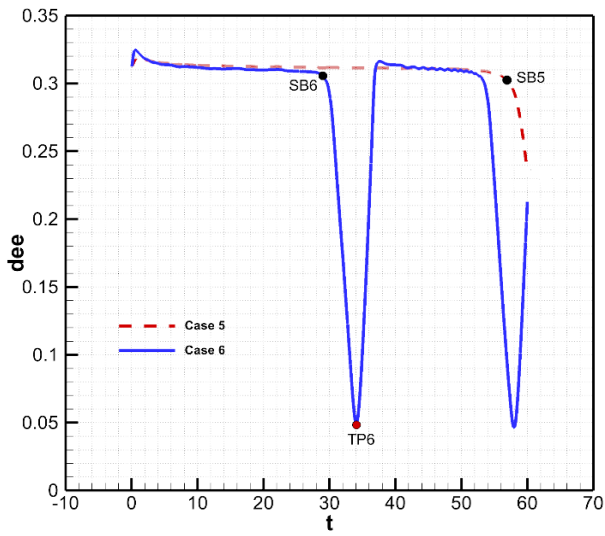
Figure 4.31 Effect of d_{ee} with respect to time for varying shear rate (long recuperative filament)
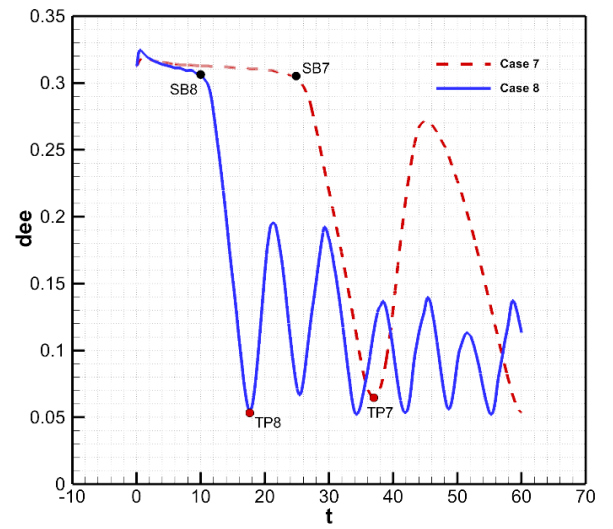
Figure 4.32 Effect of d_{ee} with respect to time for varying shear rate (long non-recuperative filament)

81
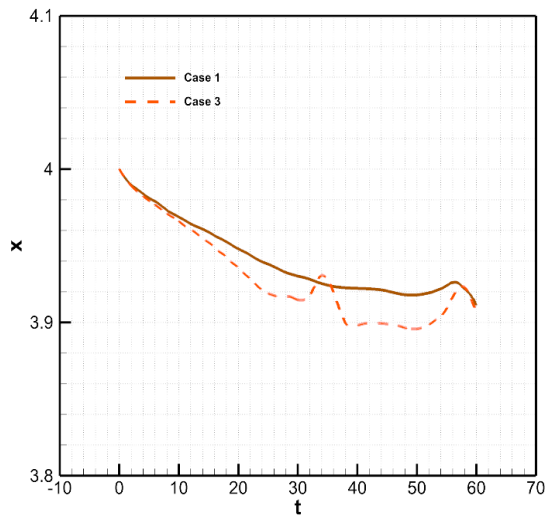
Figure 4.33 Filament migration in the x-direction for varying bending rigidity (short filament in low shear flow)
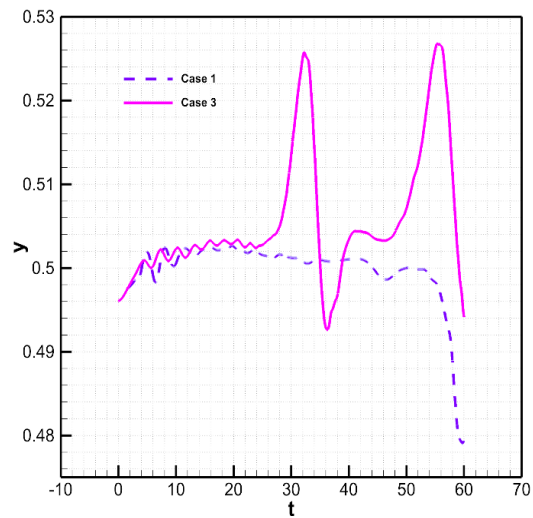
Figure 4.34 Filament migration in the y-direction for varying bending rigidity (short filament in low shear flow)
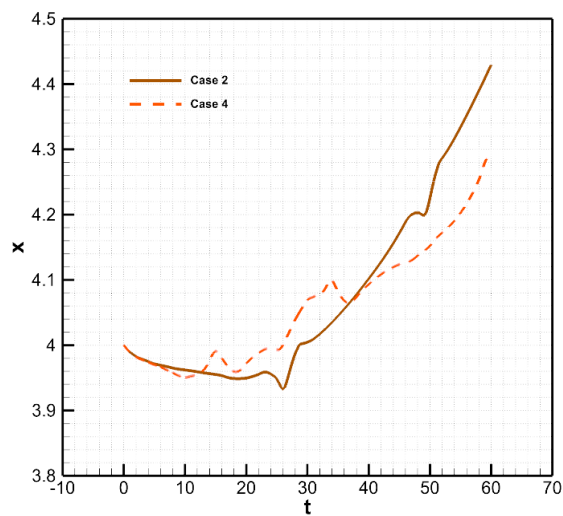
Figure 4.35 Filament migration in the x-direction for varying bending rigidity (short filament in high shear flow)
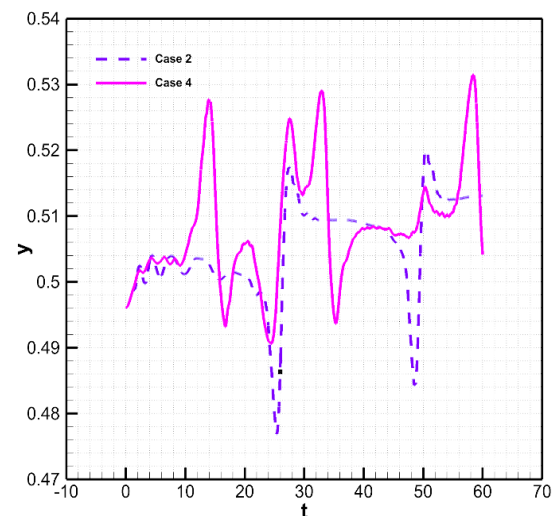
Figure 4.36 Filament migration in the y-direction for varying bending rigidity (short filament in high shear flow)
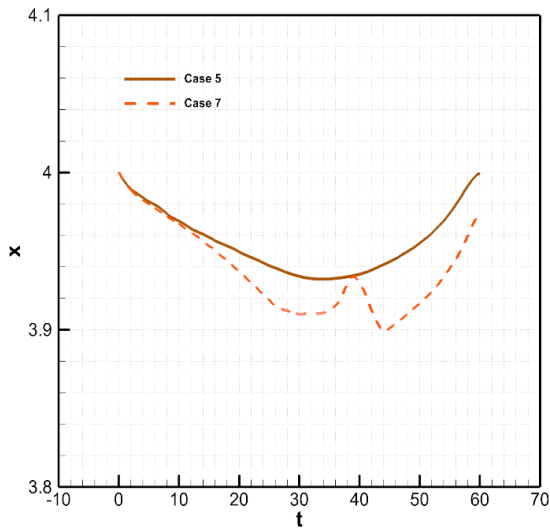
Figure 4.37 Filament migration in the x-direction for varying bending rigidity (long filament in low shear flow)
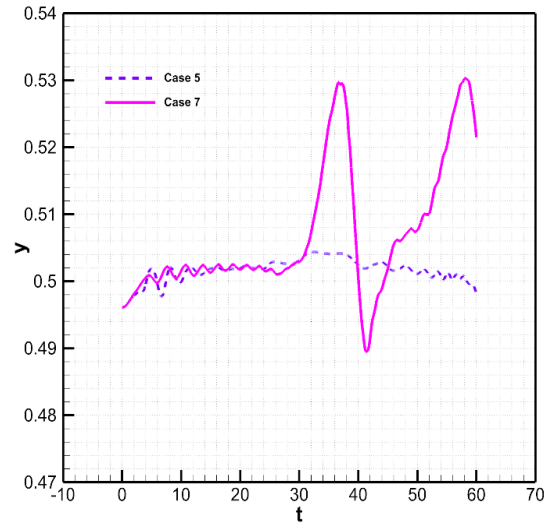
Figure 4.38 Filament migration in the y-direction for varying bending rigidity (long filament in low shear flow)
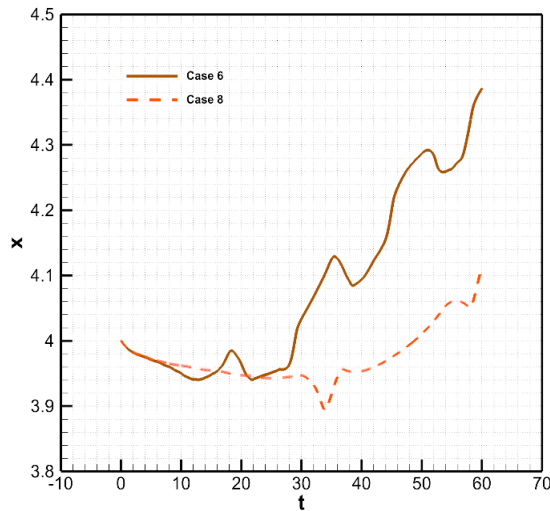
Figure 4.39 Filament migration in the x-direction for varying bending rigidity (long filament in high shear flow)
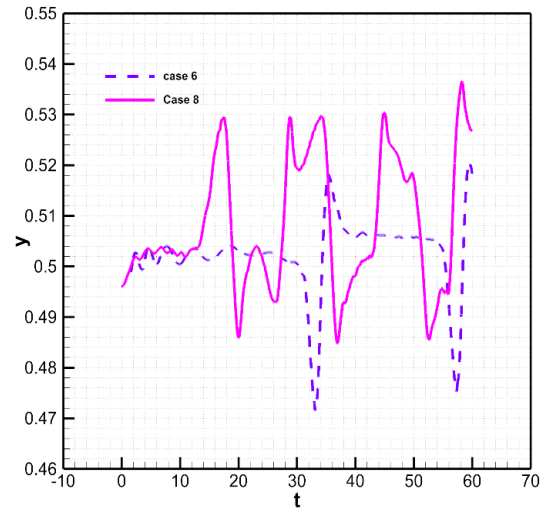
Figure 4.40 Filament migration in the y-direction for varying bending rigidity (long filament in high shear flow)

83

CHAPTER 5

5 SIMULATION OF FLEXIBLE FILAMENT IN VISCOUS OSCILLATING FLOW

5.1 Background

The interaction between flexible filament and fluid are encountered in wide range of natural and industrial scenarios. Many studies have been carried out in the field of dynamics of flexible filament motion which includes flapping filament and flag problem (Connel and Yue 2007; Huang et al. 2007; Xia and Lin 2008; Huang and Sung 2010; Ryu et al. 2018), filament motion in soap film (Zhu and Peskin 2002; Farnell et al. 2004), valve motion in channel (Baaijens 2001; Yu 2005) and actuated cilia motion (Alexeev et al. 2008; Dauptain et al. 2008). Specific applications related to flapping filament dynamics in biomimetics involve fluid pumping and fluid mixing. In this direction, (Khatavkar et al. 2007) had analysed active micro-mixers based on cilia propulsion. By generating a proper scheme of actuation, two filament actuators placed on the same side of channel wall can produce chaotic mixing in an effective manner. The aspect ratio i.e. the ratio of filament length to channel height in their study was taken between 0.2 to 0.4 and channel geometry ratio i.e. the ratio of channel height to channel length was taken as 0.1667. In another work, (Lambert and Rangel 2010) studied the effect of filament flap deformation on fluid mixing. They demonstrated that an aspect ratio of 0.667 can produce optimum mixing. Further, they observed that a single filament can also produce rapid mixing in an enhanced manner as compared to multiple flaps. However, the channel geometry ratio in their work was 0.48.

An interesting study reported by (Ulrike 2003) clearly demonstrated that an analogy exists between passive flapping flag and active swimming fish. The similarity in the dynamics of both cases may not be superficial but both share a common physical mechanism governing their motion. To minimize the energy cost due to locomotion, the flag and fish modify their swimming pattern to generate motion in their natural oscillation frequency. These oscillations generate vortices in fluid around the object. The entire study clearly proves the effectiveness of studying the dynamics of passive objects in order to get

a concise picture of their active behaviour. By inducing fluid motion and analysing the behaviour of passive structures, a similar co-relation can be achieved for understanding motion and flow behaviour of stationary fluid placed in an active structural deformation. Also, in studying the dynamics of flexible filaments in oscillating flow, an analogy can be developed to understand similar behaviour in engineering applications such as fluid micro-mixing and micro-pumping. (Zhang and Gay 2007) had studied the effect of deformation in heart-valve leaflets modelled as flexible filament at low Reynolds number for oscillating fluid flow with phase shift condition. Also, from the studies of (Khatavkar et al. 2007) it is known that phase lag in filament deformation has a tremendous influence on the surrounding fluid domain. Phase lag in a passive filament can be achieved by inducing phase shift in the oscillatory fluid motion and its comparison with fluid motion without phase shift is another interesting study which has not been reported earlier. Finally, by comparing studies of (Khatavkar et al. 2007) and (Lambert and Rangel 2010), it is observed that channel geometry ratio and aspect ratio critically effect fluid mixing. The behavior and deformation of flexible filament and its consequence on fluid mixing for an intermediate channel geometry ratio ranging between 0.1667 and 0.48 is worth investigating. These aspects from literature serve as the prime motivation for the present study.

In this chapter, a two-dimensional numerical model based on a formally second order immersed boundary framework is used to capture fluid-structure interaction of flexible filament subjected to oscillating flow. A detailed parametric study is carried out by varying filament bending rigidity, length, Reynolds number and oscillating fluid flow conditions. The numerical model used, validation and simulation results of filament deformation study are provided in the sections below.

5.2 Mathematical formulation and numerical scheme

The immersed boundary formulation along with step-by-step numerical procedure for flexible filament interacting in viscous fluid has been explained in detail in section 4.2 of Chapter 4. The IBM formulation provided in section 4.2 applies for the present study as well.

5.3 Results and discussions

5.3.1 Validation

The numerical method discussed in section 4.2 has already been verified and validated in in section 4.3.1 and section 4.3.2 involving flexible filament placed in uniform and shear flow conditions. The model is further validated with numerical works of (Zhang and Gay 2007), who studied the behaviour of flexible leaflet subjected to sinusoidally oscillatory fluid flow with phase shift using immersed finite element method. Accordingly, in the present study the leaflet is modelled as a one-dimensional filament which is made up of connected spring systems, each having fixed stretching and bending rigidity. The two-dimensional rectangular fluid domain has height of 1.0 and length 4.0. The leaflet is placed vertically and leading edge is fixed to the centre of the channel at a location $X_0 =$ (2,0) while trailing edge is free to move in fluid flow direction. The length of the leaflet is fixed as 0.8. The initial position of the filament is maintained at $\theta = 90°$. A schematic representation of flexible filament tethered at the centre of channel in oscillating flow condition along with boundary conditions are provided in Figure 5.1. The length of the channel is taken as L_c and height as H.
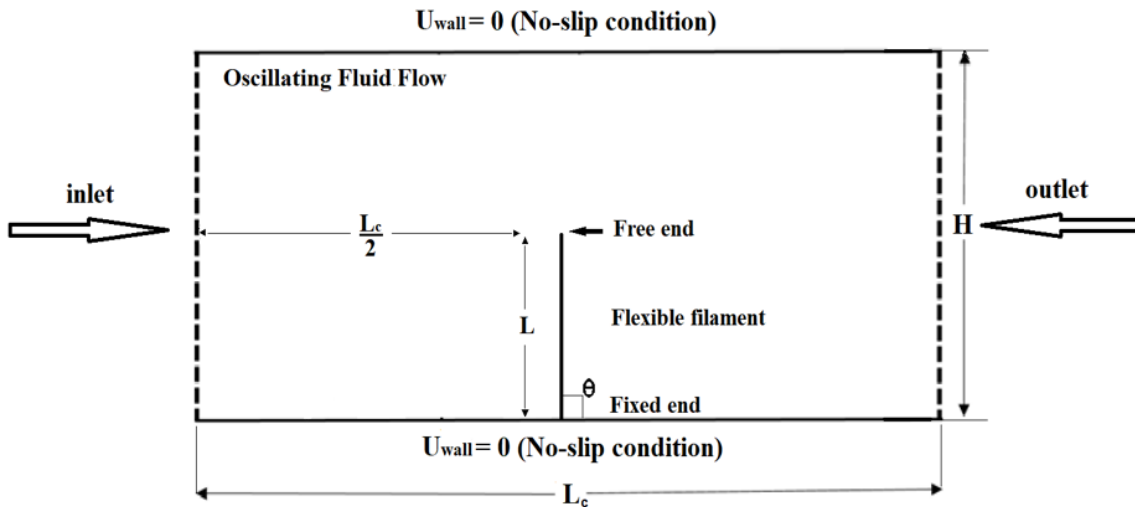
Figure 5.1 Schematic diagram of flexible tethered filament placed in viscous oscillating fluid flow. The boundary condition for fixed end of filament is $X_0 =$ (2,0).

Before considering the solution to the validation problem, the inextensibility of the leaflet modelled as a flexible filament has to be ascertained. The inextensibility condition governs the extension of the filament thus preventing it from undergoing spurious stretching or deformations. Failure to maintain the condition causes oscillating instability in the solution scheme. Since the tension and bending forces are calculated explicitly in the formulation, a large value of K_s is considered while K_b remains constant at 1.0. Numerical stability of the method can be maintained for large values of K_s provided there is small time step. Hence the time step Δt for the present study is fixed as 1×10^{-5}. A length error $\varepsilon(t)$, is calculated which determines the deviation of filament length from original value. It is given by equation (5.1).

$$\varepsilon(t) = \max \left| \frac{\partial \mathbf{X}}{\partial s} \cdot \frac{\partial \mathbf{X}}{\partial s} - 1 \right| \tag{5.1}$$

Comparison of average length error (ε) indicating elongation and compression behaviour of flexible filament for different stretching co-efficient (K_s) values over total simulation time, t = 3.0 is provided in Table 5.1. There is deviation of 3.67% between $K_s = 1000$ and $K_s = 10000$ length error values. Thus, an optimum value of $K_s = 10000$ is fixed which maintains the inextensibility condition. The inextensible error equation is taken from simulation study of flexible filament in uniform flow by (Huang et al. 2007). Their methodology strictly enforces the filament inextensibility condition implicitly with no restrictions on time step. Next, the refinement of the computational grid is carried out by performing grid convergence test. Based on inextensibility test data, three cases of uniform Eulerian grids in x and y direction are considered and their average length error over a simulation time t = 3.0 is recorded in Table 5.2. The percentage change in length error between the first and second grid size is found to be 19% while that between the second and third is 2.1%. Since the later difference in average error is marginal as compared to the first and second grid difference and in order to minimize computational time, the best possible configuration of fluid grid for the present study is chosen to be 512×128.

Table 5.1 Comparison of average length error (ε) for varying time step (Δt) and varying stretching co-efficient (K_s) for fixed value of bending co-efficient (K_b = 1.0).

Stretching co-efficient (K_s)	Time step (Δt)	Average length error (ε)
1000	1.0×10^{-4}	9.33×10^{-4}
2500	1.0×10^{-5}	9.30×10^{-4}
5000	1.0×10^{-5}	9.20×10^{-4}
7500	1.0×10^{-5}	9.08×10^{-4}
10000	1.0×10^{-5}	9.0×10^{-4}

Table 5.2 Comparison of average length error (ε) with different uniform Eulerian grids in x and y direction.

Grids	Time step (Δt)	Average length error (ε)
256×64	1.0×10^{-5}	1.07×10^{-3}
512×128	1.0×10^{-5}	9.0×10^{-4}
1024×256	1.0×10^{-5}	8.81×10^{-4}

With reference to grid convergence study and inextensibility tests, two-dimensional numerical simulation of flexible leaflet subjected to pressure driven oscillating flow is carried out, similar to leaflet deformation of (Zhang and Gay 2007). The filament is massless and its physical thickness is not considered in the study. The Reynolds number is fixed at 10.0 and the total simulation time is 3.0. The motion of filament is examined for two different Strouhal numbers (St) of 0.5 and 1.0 respectively, where St is given by equation (5.2).

$$St = \frac{f\,H}{U_{ref}} \tag{5.2}$$

where, f = frequency of oscillation. The fluid is driven by sinusoidal pressure gradient in positive x-direction defined by equation (5.3).

$$\frac{\Delta p}{L} = \frac{12}{Re} \times \sin(\pi ft + \pi/2) \tag{5.3}$$

The tip velocity of the filament at St = 0.5 and St = 1.0 are shown in Figure 5.2(a) and Figure 5.2(b) respectively and compared with the works of (Zhang and Gay 2007). The results are also found to be in close agreement which depicts the validity of the developed model.
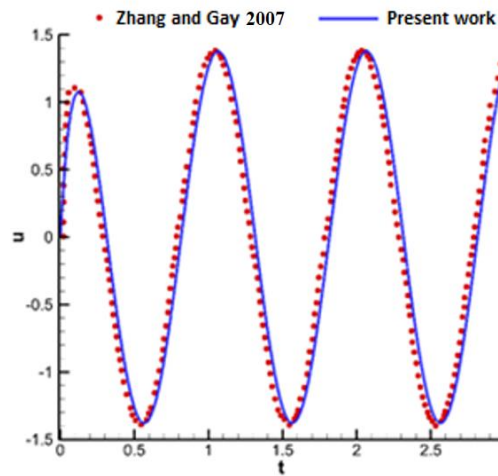
Figure 5.2(a) Filament tip velocity comparison of present study with work of (Zhang and Gay, 2007) at Re = 10.0 and St = 1.0.
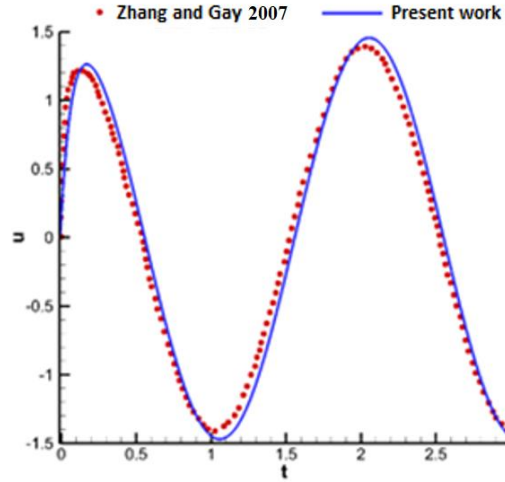
Figure 5.2(b) Filament tip velocity comparison of present study with work of (Zhang and Gay, 2007) at Re = 10.0 and St = 0.5.

5.3.2 Filament deformation parametric study

The behaviour of the vertically fixed flexible filament shown in Figure 5.1 subjected to pressure driven oscillating fluid flow is studied. A parametric analysis is carried out for three filament lengths, L = 0.4, 0.6 and 0.8, two bending rigidities, $K_b = 1 \times 10^{-3}$ and 1×10^{-4} and three different Reynolds numbers, Re = 50, 75 and 100. Two types of oscillating fluid flow conditions are considered for fixed filament length, L = 0.8 and St = 0.5. The first type is sinusoidally oscillatory flow with phase shift (SOFPS) as discussed in validation study given by equation (5.3). The second is sinusoidally oscillatory flow without phase shift (SOF) which is given by equation (5.4).

$$\frac{\Delta p}{L} = \frac{12}{Re} \times \sin(\pi ft) \tag{5.4}$$

A series of velocity vector plots depicting the motion of fluid for a total time period t = 1.0 is provided in Figure 5.3(a) and Figure 5.3(b) for SOFPS and SOF flow conditions respectively. For SOFPS fluid flow conditions, zero fluid velocities are observed at t = 0.0, 0.3 and 0.8 whereas zero fluid velocities are observed at t = 0.0, 0.5 and 1.0 for SOF condition. The fluid reaches maximum velocity value of 1.38, two times in the positive

cycle for SOFPS flow condition while minimum fluid velocity of -1.38 is achieved only once in the negative cycle spanning the entire time period.
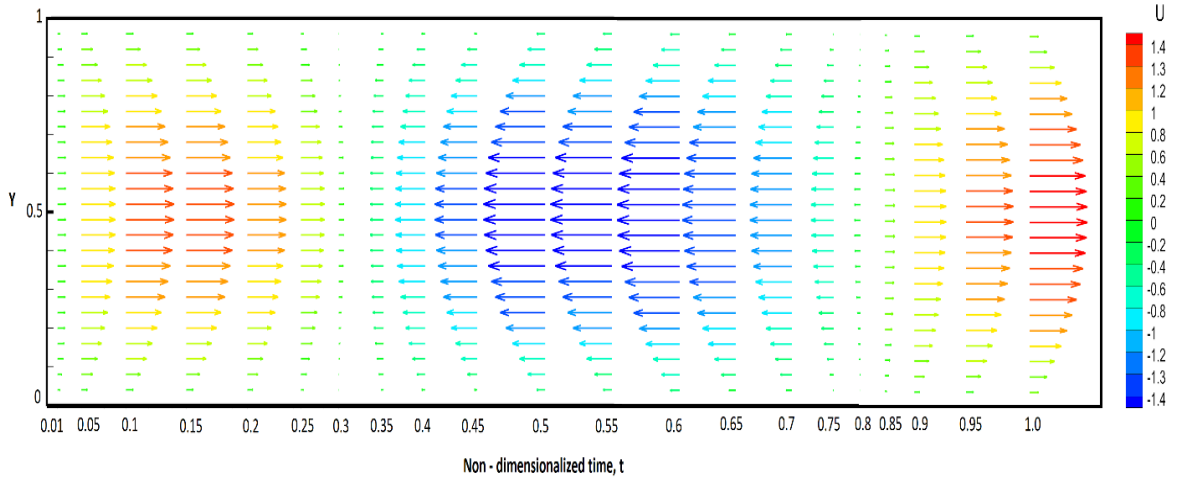
Figure 5.3(a) Series of velocity vector plots obtained at channel location x = 2.0 for different non-dimensionalized time sequences taking SOFPS flow condition.
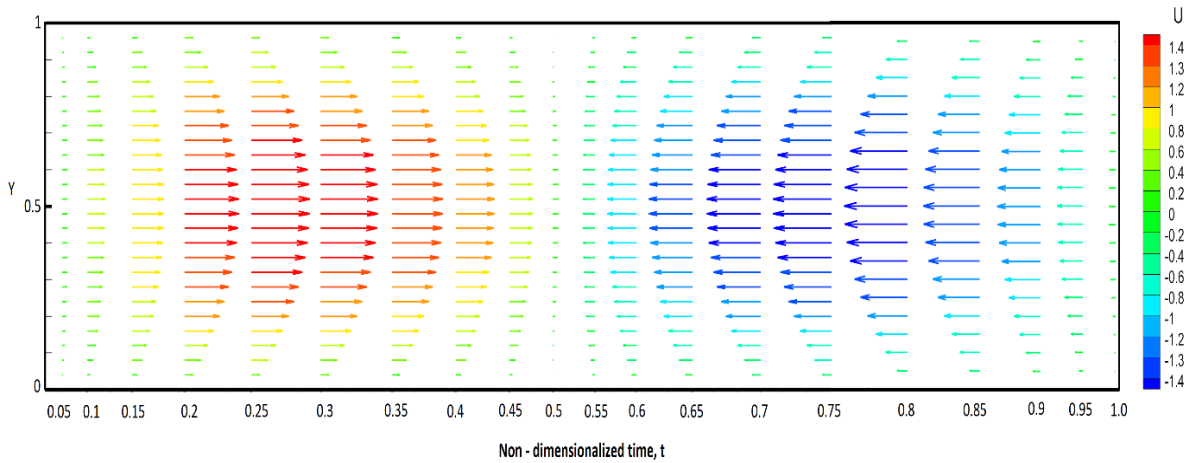
Figure 5.3(b) Series of velocity vector plots obtained at channel location x = 2.0 for different non-dimensionalized time sequences taking SOF flow condition.

However, an observation of velocity vectors corresponding to SOF condition shows that, fluid attains positive and negative cycle only once during the time period. The magnitude of maximum and minimum velocities remains the same for both flow conditions. Hence both these flow condition will have varying effects on filament displacement and dynamics. The flexible filament is placed vertically and tethered at the centre of the rectangular channel of height, H = 2.0 and length, L_c = 8.0 which produces a channel geometry ratio (H/L_c) = 0.25. The effect of varying filament length, bending rigidity, Reynolds number and flow conditions are ascertained with the help of the parametric study. A detailed discussion is provided below.

The presence of flexible filament in the fluid region is analysed by plotting the X-component and Y-component of velocity. Figures 5.4(a) – 5.4(c) shows the X-component of velocity for different filament lengths at time t = 3.48, 3.72 and 3.96 respectively. The results are plotted with respect to channel length along the y-centreline of channel for Re = 100. As shown in Figures 5.4(a) – 5.4(c), sharp deviation in velocity is observed at channel mid-length position, due to presence of filament. The magnitude of the deviation increases for increase in filament length.

Similar deviation in velocity is also observed in Y-component of velocity as shown in Figures 5.5(a) – 5.5(c) caused by the presence of flexible filament. However, there is no significant difference in deviations between filament lengths as compared to X-component velocities. This also indicates that the effect of increasing filament length has more impact in the longitudinal direction as compared to transverse direction.

Next the effect on fluid velocity by varying bending rigidity of the filament is determined by plotting X and Y-components of velocity as shown in Figure 5.6(a) and Figure 5.6(b) respectively. In both the figures there is an appreciable difference in deviation between filaments with different rigidities. Rigid filaments tend to have much higher influence in longitudinal and transverse direction as compared to flexible filaments. The filament dynamics is thus strongly governed by filament length and bending rigidity.
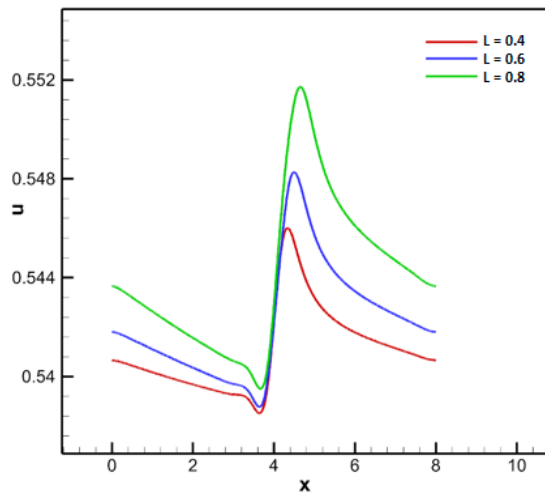
(a) t = 3.48
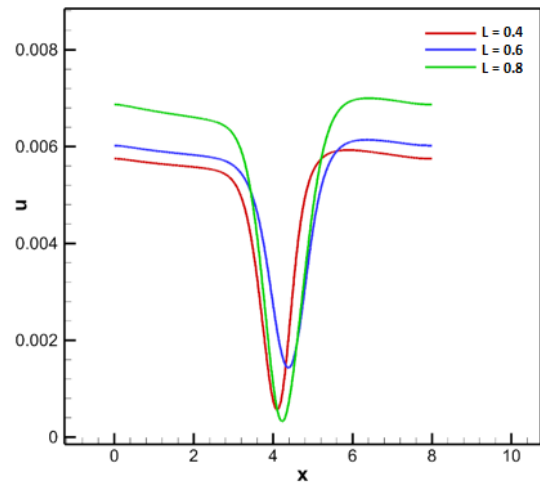
(b) t = 3.72
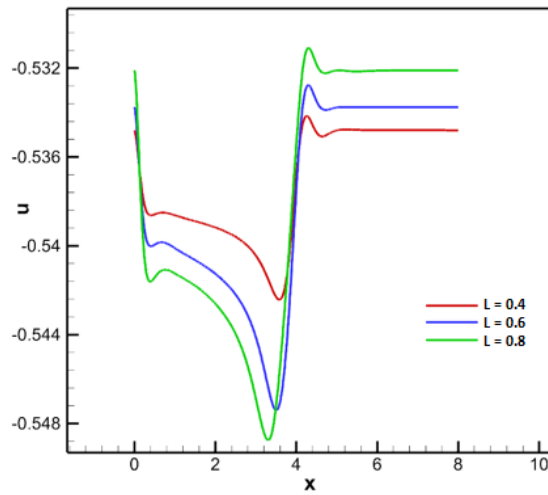
(c) t = 3.96

Figure 5.4 X-component of velocity plotted with respect to channel length along the channel y-centreline for different filament length, L = 0.4, 0.6, 0.8 at Reynolds number, Re = 100 and fixed bending rigidity, $K_b = 1 \times 10^{-4}$.
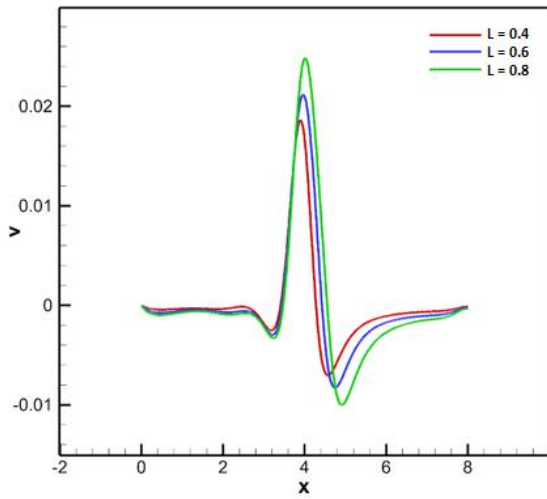
(a) t = 3.48
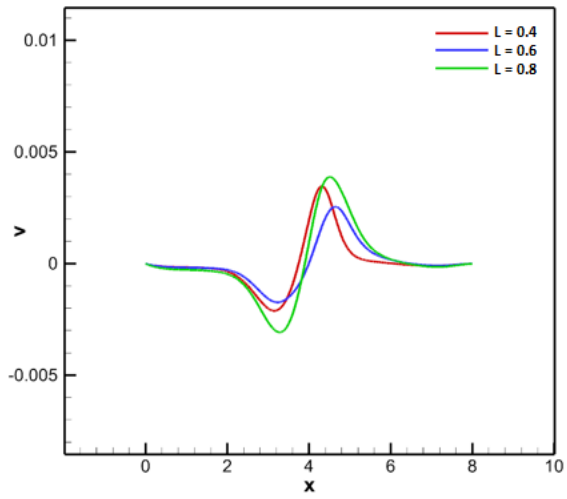
(b) t = 3.72
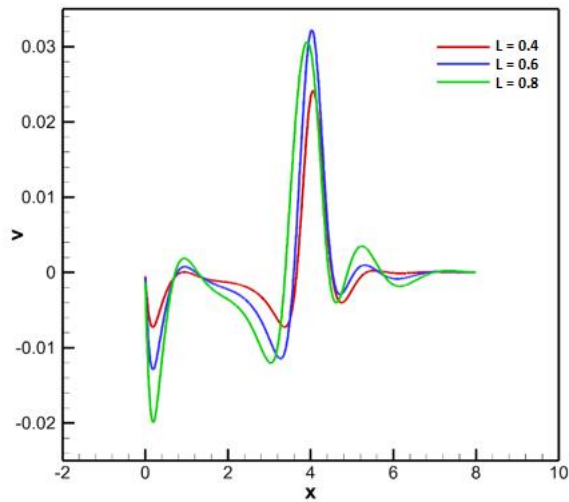
(c) t = 3.96

Figure 5.5 Y-component of velocity plotted with respect to channel length along the channel y-centreline for different filament length, L = 0.4, 0.6, 0.8 at Reynolds number, Re = 100 and fixed bending rigidity, $K_b = 1 \times 10^{-4}$.
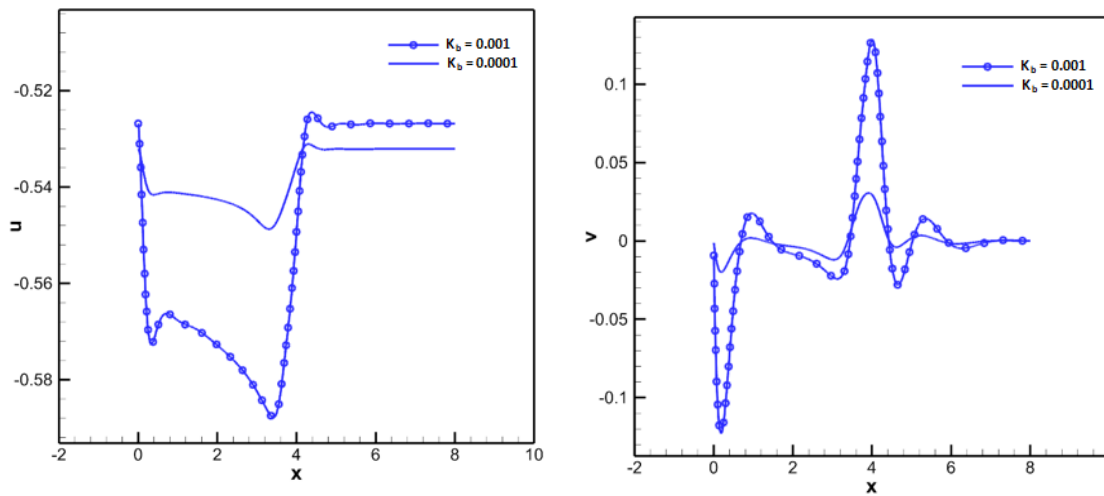
(a) X-component of velocity   (b) Y-component of velocity

Figure 5.6 X and Y component of velocity at time, t = 3.96 plotted with respect to channel length along the channel y-centreline for different bending rigidities, $K_b = 1 \times 10^{-3}$, 1×10^{-4} at Reynolds number, Re = 100 and fixed filament length, L = 0.8.

Another way of understanding the filament dynamics and its corresponding effect on the fluid domain is by observing the instantaneous filament deformations and streamlines for different filament lengths and bending rigidity. The hydrodynamic forces have a great influence on filament bending or deformation. Figure 5.7(a) and Figure 5.7(b) shows the filament deformation for filament length, L = 0.4 in the positive x-direction for different rigidities at Re = 100. Flexible filament produces a full symmetrical sweeping pattern with good extensions in x-direction whereas the rigid filament has a retarded extension and has a smaller sweep span. This retardation is due to the dominance of elastic forces over hydrodynamic forces. The filament exhibits higher resistance to fluid motion. The implications of these two types of filament deformation on the fluid region is observed by looking at the streamline plots in Figure 5.7(c) and Figure 5.7(d). Observing Figure 5.7(c), a recirculation zone is created behind the filament in its immediate vicinity and the filament obstructs zone formations in the opposite direction. On the other hand, in Figure 5.7(d) the recirculation zone extends out along the length of channel, behind and as well as

in front of the filament due to the symmetrical sweeping pattern. The size of the recirculation zone however is restricted to the lower half portion of the channel and no considerable mixing is observed above the filament.
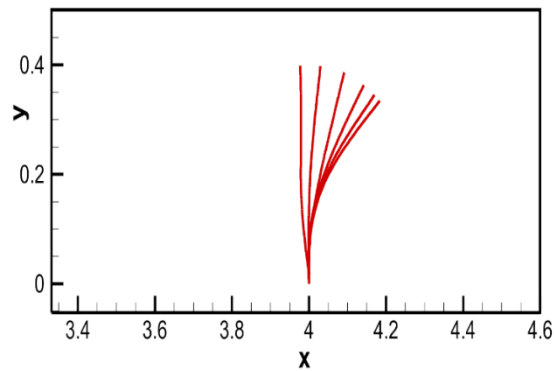
Figure 5.7(a) Instantaneous filament deformations for fixed filament length, L = 0.4 and fixed bending rigidity, $K_b = 1 \times 10^{-3}$ at Reynolds number, Re = 100.
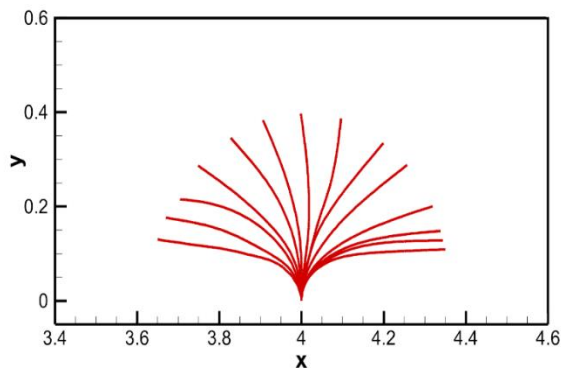
Figure 5.7(b) Instantaneous filament deformations for fixed filament length, L = 0.4 and fixed bending rigidity, $K_b = 1 \times 10^{-4}$ at Reynolds number, Re = 100.
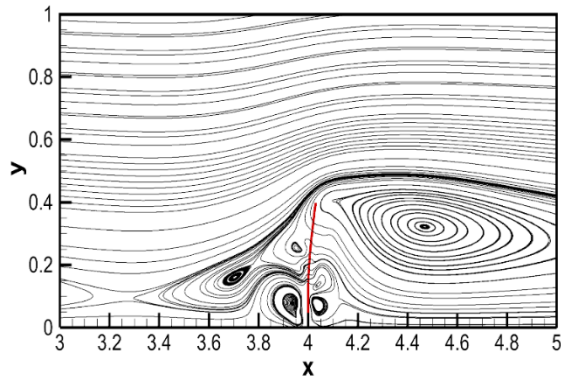
Figure 5.7(c) Streamlines obtained at the vicinity of filament for fixed filament length, L = 0.4 and fixed bending rigidity, $K_b = 1 \times 10^{-3}$ at Reynolds number, Re = 100.
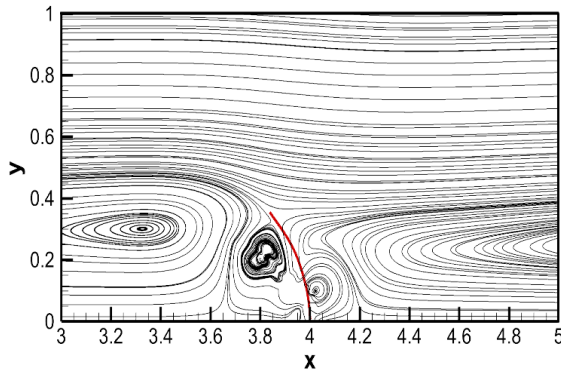
Figure 5.7(d) Streamlines obtained at the vicinity of filament for fixed filament length, L = 0.4 and fixed bending rigidity, $K_b = 1 \times 10^{-4}$ at Reynolds number, Re = 100.

Figure 5.8(a) and Figure 5.8(b) shows the filament deformation for filament length, L = 0.6 in the positive x-direction for different rigidities at Re = 100. Retarded motion for rigid filament and sweeping motion for flexible filament is seen here as well. The symmetrical sweeping pattern in flexible filament is accompanied by bending deformation. A similar phenomenon in streamlines as observed in Figure 5.7(c) is also found in Figure 5.8(c). Looking at the streamlines obtained in Figure 5.8(d), the recirculation zones extends out in the longitudinal direction. Also, the size of the zone is larger, covering a major portion of channel. Even though the top area of the channel does not see any recirculation

zone formations, the mixing is much better for this case as compared to the smaller filament.
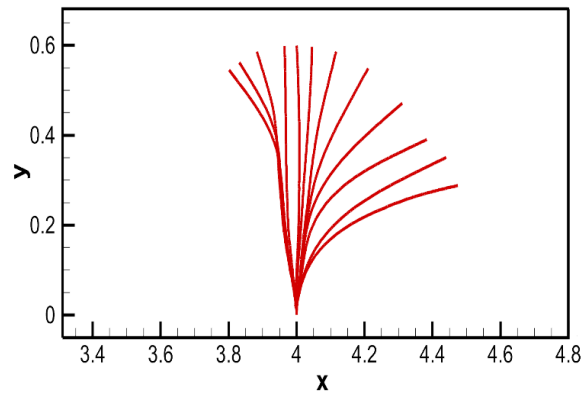
Figure 5.8(a) Instantaneous filament deformations for fixed filament length, L = 0.6 and fixed bending rigidity, $K_b = 1 \times 10^{-3}$ at Reynolds number, Re = 100.
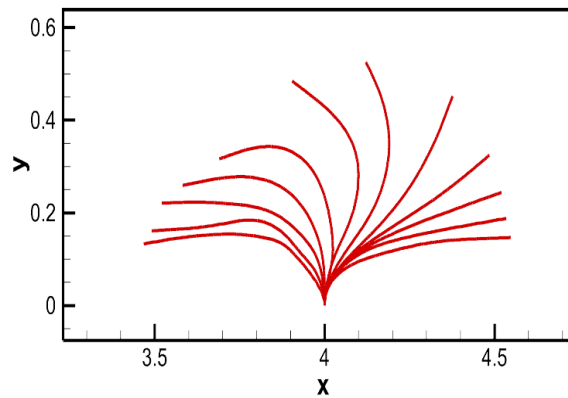
Figure 5.8(b) Instantaneous filament deformations for fixed filament length, L = 0.6 and fixed bending rigidity, $K_b = 1 \times 10^{-4}$ at Reynolds number, Re = 100.
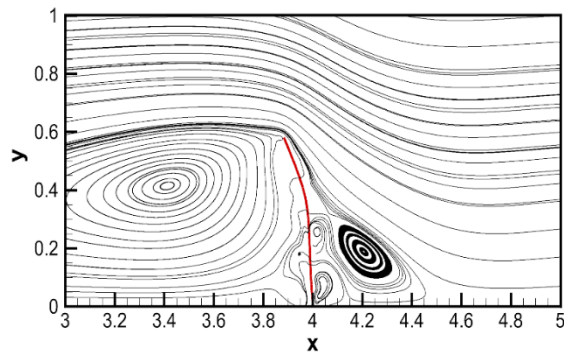
Figure 5.8(c) Streamlines obtained at the vicinity of filament for fixed filament length, L = 0.6 and fixed bending rigidity, $K_b = 1 \times 10^{-3}$ at Reynolds number, Re = 100.
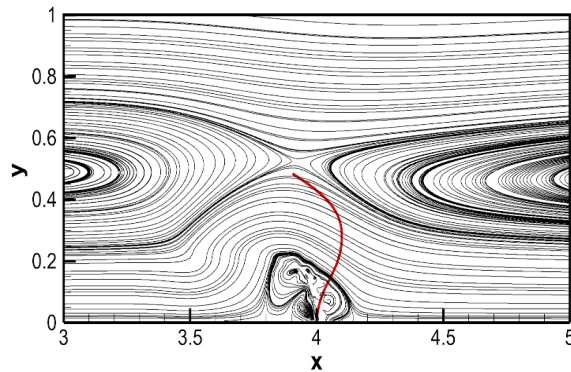
Figure 5.8(d) Streamlines obtained at the vicinity of filament for fixed filament length, L = 0.6 and fixed bending rigidity, $K_b = 1 \times 10^{-4}$ at Reynolds number, Re = 100.

Finally, the instantaneous deformations and streamline for filament length, L = 0.8 is shown in Figures 5.9(a) – 5.9(d). As it can be seen in Figure 5.9(a) and Figure 5.9(b), there is no form of retardation in filament motion. Symmetrical sweeping motion is seen for both rigid and flexible filament. There exists a balance between elastic and hydrodynamics forces which produces the symmetrical sweep motion in rigid filament. Due to higher filament length, flexible filament tends to produce appreciable bending deformation. This also indicates that due to lower rigidity, the effect of hydrodynamic forces on the filament are stronger and the filament shows least resistance to deformation.

99

In Figure 5.9(c), due to the sweeping filament motion the recirculation zones are formed along the channel length. Additionally, a large recirculation zone is formed in front of the filament covering the transverse extent of the channel. These recirculation zones are generally formed when there is opposition to fluid motion. This opposition to fluid motion is in turn caused by flap bending motion formed by fluid resistance. There is better distribution of recirculation zones for a larger portion of channel geometry. However, the same is not true for flexible filament case (Figure 5.9(d)). There are hardly any recirculation zones at the top and bottom channel portion indicating poor mixing capability.
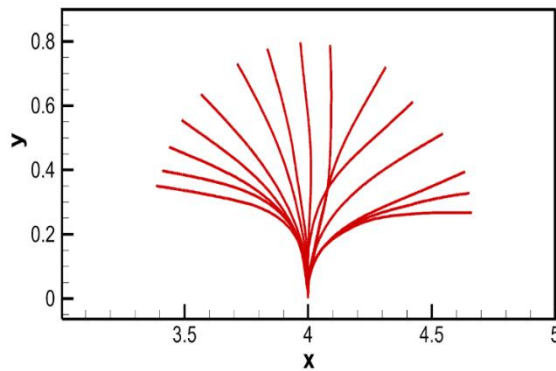
Figure 5.9(a) Instantaneous filament deformations for fixed filament length, L = 0.8 and fixed bending rigidity, $K_b = 1 \times 10^{-3}$ at Reynolds number, Re = 100.
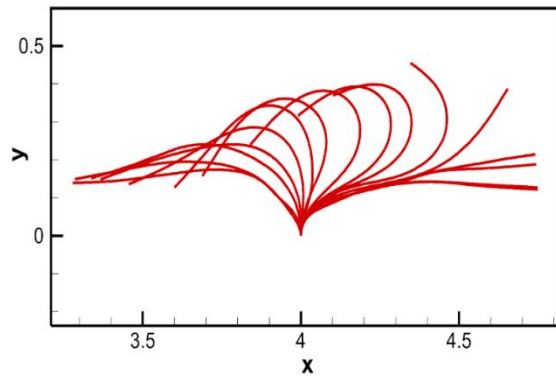
Figure 5.9(b) Instantaneous filament deformations for fixed filament length, L = 0.8 and fixed bending rigidity, $K_b = 1 \times 10^{-4}$ at Reynolds number, Re = 100.
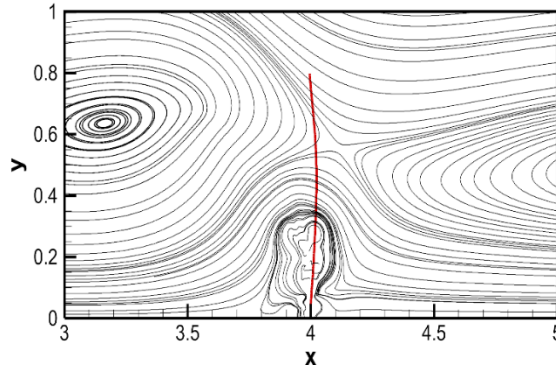
Figure 5.9(c) Streamlines obtained at the vicinity of filament for fixed filament length, L = 0.8 and fixed bending rigidity, $K_b = 1 \times 10^{-3}$ at Reynolds number, Re = 100.
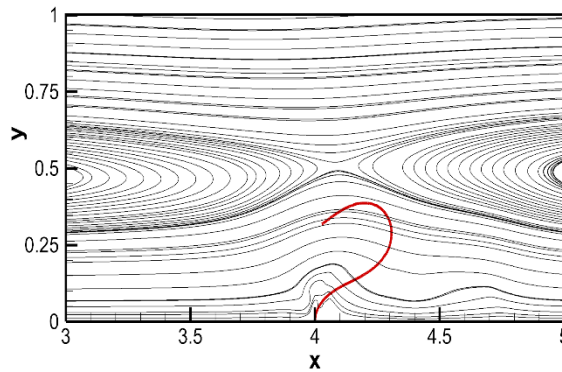
Figure 5.9(d) Streamlines obtained at the vicinity of filament for fixed filament length, L = 0.8 and fixed bending rigidity, $K_b = 1 \times 10^{-4}$ at Reynolds number, Re = 100.

It is realized that filament sweep or flap dynamics has a tremendous impact on the surrounding fluid motion. The flap dynamics can be further quantified by measuring the angle θ made by the filament with respect to the horizontal during its sweep motion. Every parametric variation either filament length, bending rigidity or Reynolds number significantly effects sweeping time. To get better understanding of this scenario, a probability distribution φ indicating the time spent by the flexible filament at various angles θ is calculated for all parametric test cases. It also provides a measure of the sweep span related to filament deformation for all cases.
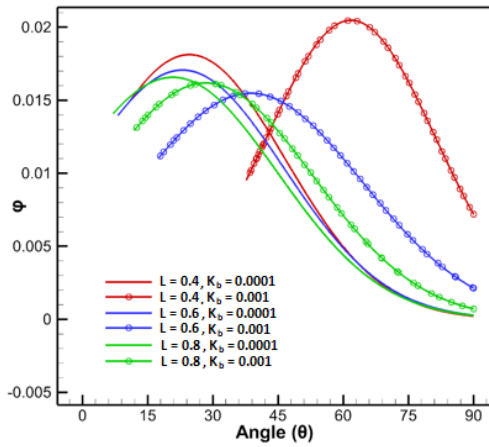
Figure 5.10(a) Probability distribution of time spent by flexible filament at various angles for filament lengths, L = 0.4, 0.6, 0.8 and bending rigidities, $K_b = 1 \times 10^{-3}$, 1×10^{-4} at Reynolds number, Re = 50.
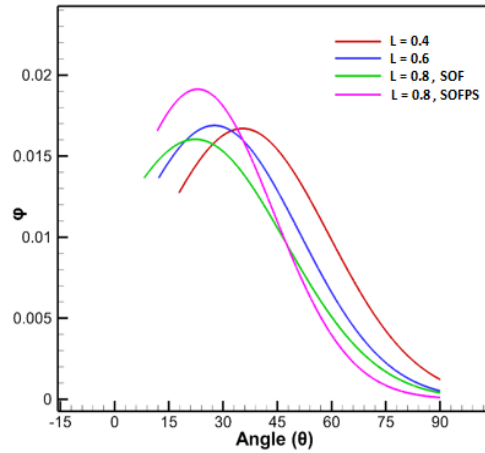
Figure 5.10(b) Probability distribution of time spent by flexible filament at various angles for filament lengths, L = 0.4, 0.6, 0.8 and fixed bending rigidity, $K_b = 1 \times 10^{-4}$ at Reynolds number, Re = 100.

Figure 5.10(a) depicts the probability distribution with respect to angle θ for three different filament lengths and two bending rigidities at Re = 50. The probability peaks also show the least angle attained by the filament during its alignment parallel to the horizontal. Such alignments are usually seen during the end of positive or negative cycles. As shown in Figure 5.10(a), rigid filaments show a greater probability of retaining large angle θ. This is seen by comparing the distribution peaks for all the cases. It also proves the retarded filament deformation observed for rigid filaments of length, L = 0.4 and 0.6. Flexible filaments on the other hand produce better sweeping motion thus showing a finer distribution. The distribution peaks for flexible filaments are more towards lower angles θ, thus capturing the flapping span. Flexible filaments of all lengths have similar span whereas the flapping span for rigid filaments keep increasing as length increases. The effect of varying fluid flow conditions on flexible filaments of different length subjected to higher Reynolds number, Re = 100 is shown in Figure 5.10(b). It is seen that for higher Reynolds number, the span of the filament sweep keeps increasing as filament length increases.
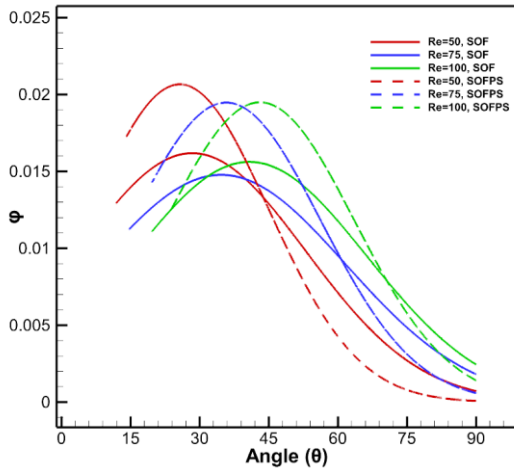
Figure 5.10(c) Comparison of SOF and SOFPS flow conditions at different Reynolds numbers, Re = 50, 75, 100 using probability distribution plot of time spent by the flexible filament at various angles for fixed filament length, L = 0.8 and fixed bending rigidity, $K_b = 1 \times 10^{-3}$.
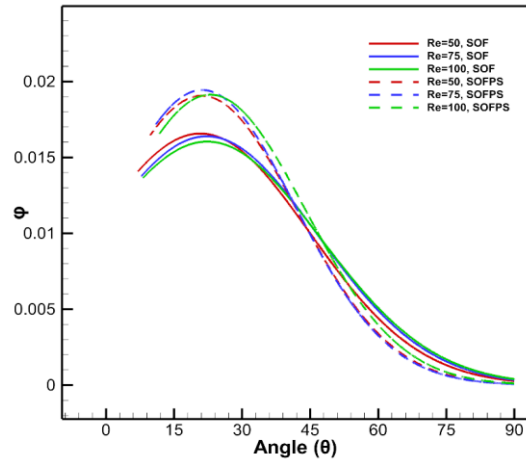
Figure 5.10(d) Comparison of SOF and SOFPS flow conditions at different Reynolds numbers, Re = 50, 75, 100 using probability distribution plot of time spent by the flexible filament at various angles for fixed filament length, L = 0.8 and fixed bending rigidity, $K_b = 1 \times 10^{-4}$.

Also, when comparing filaments of same length, L = 0.8 subjected to SOF and SOFPS flow conditions, the filament span for both cases are similar with the exception that filament subjected to SOFPS condition remains in the lowest angle position for larger portion of time. Similar observations are also seen in Figure 5.10(c) and Figure 5.10(d) where the rigid and flexible filaments are compared for different Reynolds numbers at different fluid flow conditions. Also, in Figure 5.10(c) the sweep span of rigid filament keeps decreasing as Reynolds number increases whereas in flexible filament (Figure 5.10(d)), the sweep span remains constant irrespective of changing Reynolds number.

The effect of Reynolds number on the sweep pattern can be further analysed by comparing the minimum angle and mean angle produced by the filament for various filament lengths, bending rigidity and flow conditions as shown in Figures 5.11(a) – 5.11(f). Figures 5.11(a) – 5.11(c) compares different bending rigidities for individual filament lengths. Figure 5.11(d) looks at a particular case where SOFS flow condition is concerned. In Figure 5.11(e) and Figure 5.11(f), the comparison of mean and minimum angle is carried out for fixed length, L = 0.8 subjected to different oscillating flow conditions. By looking at all the figures, it is found that the mean and minimum angles keep increasing as Reynolds number increases irrespective of filament length. Rigid filaments have higher mean and minimum angles as compared to flexible filaments for all cases. It is possible to categorize filament deformation patterns by calculating the slope of mean angle curve. The slope of mean angle curve generated by the flapping of flexible filaments is calculated for all filament lengths from Figures 5.11(a) – 5.11(f). The values are tabulated in Table 5.3 along with their corresponding lengths, bending rigidity and flapping patterns.
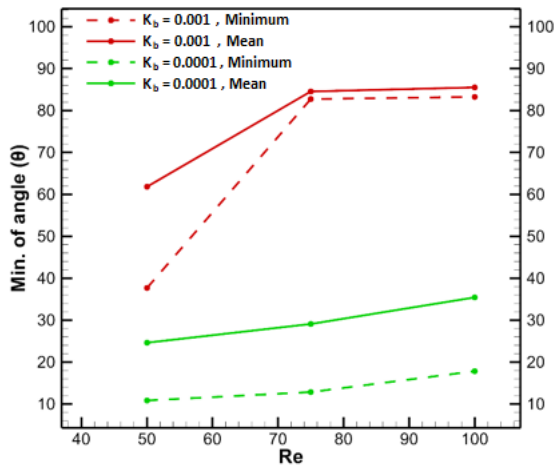
(a) L = 0.4
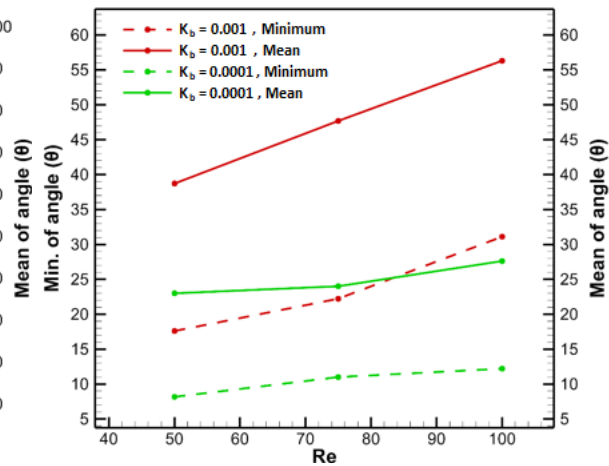
(b) L = 0.6
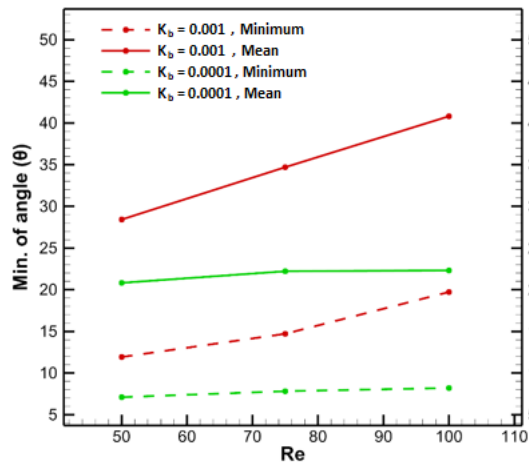
(c) L = 0.8 with SOF condition
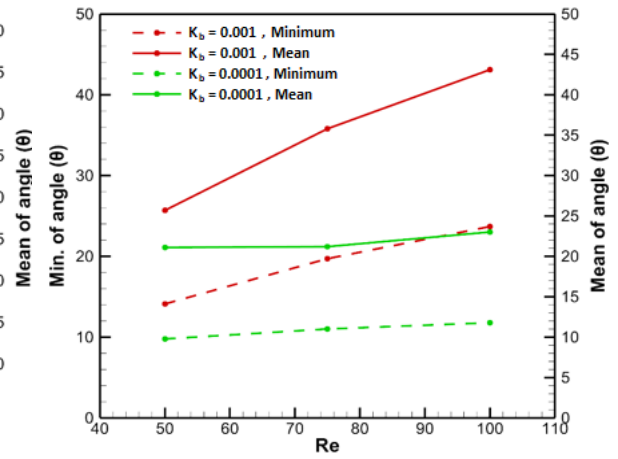
(d) L = 0.8 with SOFPS condition
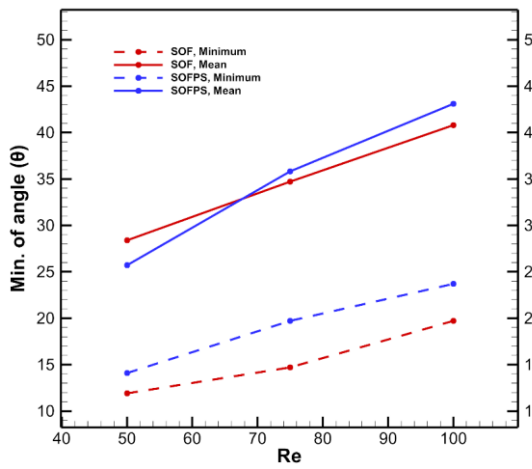
(e) $K_b = 1 \times 10^{-3}$
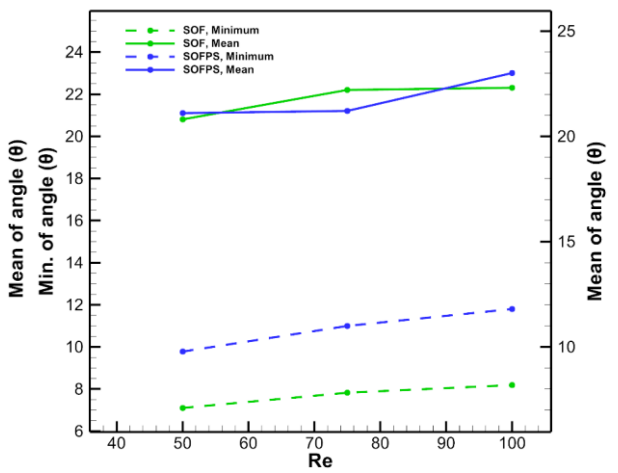
(f) $K_b = 1 \times 10^{-4}$

Figure 5.11 The mean and minimum angle attained by the filament with respect to Reynolds number.

Table 5.3 Tabulation of slope of mean angle θ curve for different filament lengths and bending rigidities along with their corresponding filament deformation patterns.

Filament Length, L	Bending Rigidity, K_b	Filament deformation pattern	Slope of mean angle θ curves, obtained from Figures 5.11(a) – 5.11(f).
0.4	1×10^{-3} (Rigid)	Retarded	0.474
	1×10^{-4} (Flexible)	Symmetrical sweep	0.216
0.6	1×10^{-3} (Rigid)	Retarded	0.352
	1×10^{-4} (Flexible)	Symmetrical sweep	0.092
0.8	1×10^{-3} (Rigid)	Symmetrical sweep	0.248
	1×10^{-4} (Flexible)	Symmetrical sweep with appreciable bending	0.03
0.8 (SOFPS)	1×10^{-3} (Rigid)	Symmetrical sweep	0.348
	1×10^{-4} (Flexible)	Symmetrical sweep with appreciable bending	0.038

From the details observed in Table 5.3, the filaments producing symmetrical sweep pattern have slope of mean angle θ curve value ranging between 0.09 and 0.35. The slope values existing outside this range produces either a retarded deformation or filament sweep with appreciable bend. The above slope values are obtained for fixed channel geometry ratio of 0.25, Reynolds number ranging from 50 to 100 and aspect ratios ranging from 0.2 to 0.4. Further investigation is required to determine the range of slope values for different filament lengths, bending rigidity and Reynolds number since there is a possibility of changes in slope value range according to parametric variations. From the present study it is demonstrate that by calculating slope of mean angle θ curves, filament deformation patterns can be easily categorized.

The extent of filament flap can be characterized by looking at the trajectory of filament tip as shown in Figure 5.12(a) and Figure 5.12(b). The figure in 5.12(a) provides the trajectory for rigid filaments of different filament lengths at Re = 100. It is evident from the figure that filaments with length, L = 0.4 and 0.6 show retarded motion whereas L = 0.8 shows full sweeping pattern. When observing flexible filaments in Figure 5.12(b), the trajectories for length, L = 0.6 and 0.8 results in octave-shaped pattern. Such patterns were also observed in beating cilia studies of (Dauptain et al., 2008). The size of the pattern increases with filament length. It also provides an indication of appreciable filament bend observed for both these length cases.

Figures 5.13(a) and 5.13(b) shows the filament tip displacement with fixed filament length, L = 0.8 for varying Reynolds number considering rigid and flexible filaments respectively. A flattened behaviour in tip displacement is observed for all cases which indicated that filament remains aligned in the fluid flow direction. The path followed by tip displacement is similar irrespective of changing Reynolds number for both rigid and flexible filaments.
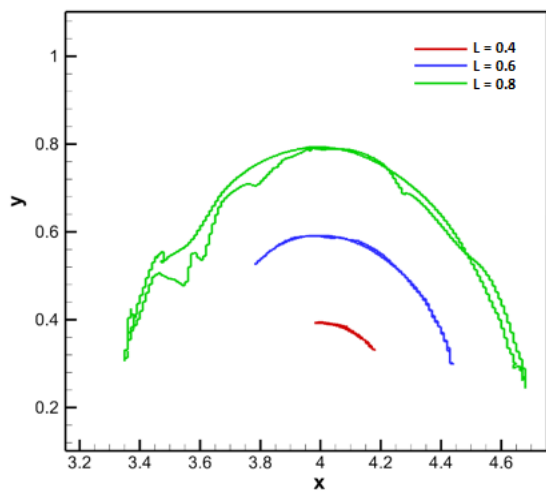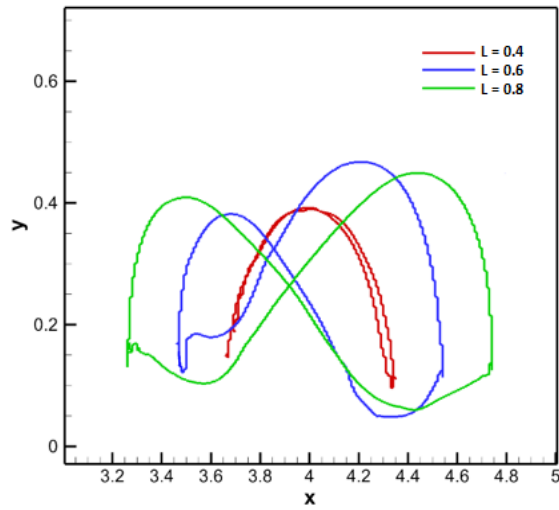
(a) $K_b = 1 \times 10^{-3}$ (b) $K_b = 1 \times 10^{-4}$

Figure 5.12 Trajectory of filament tip with respect to x and y displacement for different filament length, L = 0.4, 0.6, 0.8 at fixed Reynolds number, Re = 100.
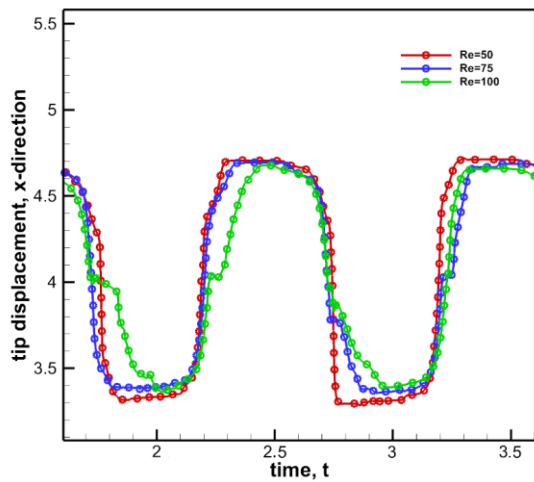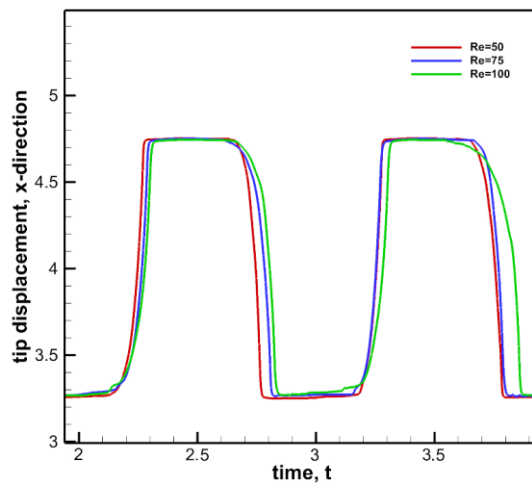
(a) $K_b = 1 \times 10^{-3}$ (b) $K_b = 1 \times 10^{-4}$

Figure 5.13 Filament tip displacement in x-direction with respect to time for different Reynolds numbers, Re = 50, 75, 100 considering fixed filament length, L = 0.8.

Figures 5.14(a) and 5.14(b) shows the effect of filament length on tip displacement for rigid and flexible filaments respectively at Re = 50. The trajectory path is different for individual filaments since they belong to different length categories. As expected, the longest filament shows the highest displacement irrespective of rigidity. When comparing filament of length, L = 0.4 for both rigid and flexible case, the trajectory path for rigid filament gets staggered near channel mid-length as compared to flexible filament were the profile is smooth. This may be due to the retarded deformation experienced by rigid filaments of lower filament length.

(a) $K_b = 1 \times 10^{-3}$ (b) $K_b = 1 \times 10^{-4}$
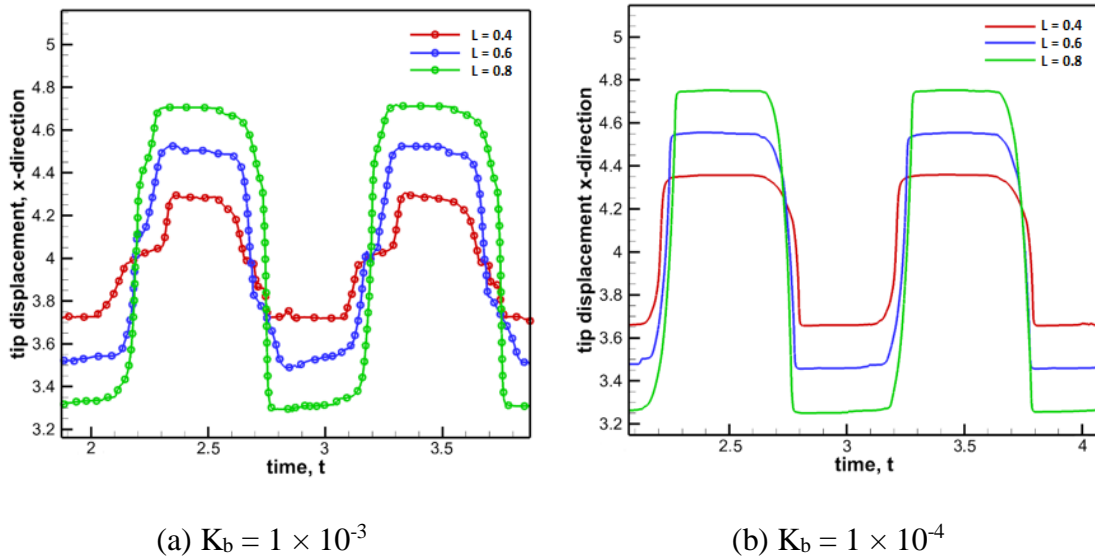
Figure 5.14 Filament tip displacement in x-direction with respect to time for different filament length, L = 0.4, 0.6, 0.8 at Reynolds number, Re = 50

Increasing the Reynolds number to 100 has different effect on tip trajectory as shown in Figures 5.15(a) and 5.15(b). There is clear difference in sweep dynamics for rigid filaments with different length (Figure 5.15(a)). Filaments belonging to length, L = 0.4 and 0.6 show no displacement below channel mid-plane thus showing retarded pattern. Higher length filament (L = 0.8) shows displacement both above and below mid-plane thus indicating sweep pattern. When comparing rigid filaments in Figure 5.14(a) and Figure 5.15(a), it is seen that as Reynolds number increases, there is greater retardation of filament

displacement for lower filament lengths. The filaments show higher resistance to hydrodynamic forces. Finally, rigid and flexible filaments subjected to SOF and SOFPS flow conditions are compared in Figure 5.16. Irrespective of the flow conditions, rigid filament has lower displacement as compared to flexible filament. Due to the phase shift in fluid flow, there is shift in x-direction tip displacement for rigid and flexible filaments. The displacement path for flexible filaments are quite similar for both the fluid conditions. However, rigid filaments subjected to SOFPS flow condition has lower sweep span as compared to filaments in SOF condition.

(a) $K_b = 1 \times 10^{-3}$ (b) $K_b = 1 \times 10^{-4}$
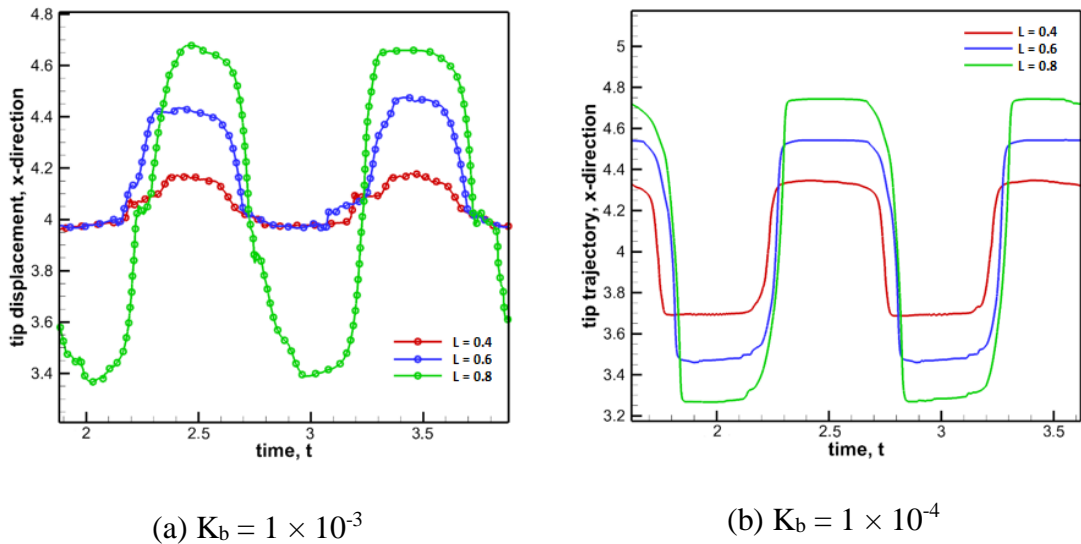
Figure 5.15 Filament tip displacement in x-direction with respect to time for different filament length, L = 0.4, 0.6, 0.8 at Reynolds number, Re = 100

Filaments of length, L = 0.8 producing symmetrical sweep patterns help in better distribution of recirculation zones for a larger portion of channel geometry. The presence of such recirculation zones is beneficial for chaotic fluid mixing applications (Anand et al. 2017). From, the above discussions on parametric studies it is clear that a minimum aspect ratio (L/H) of 0.4 is needed to produces the best results for mixing application with respect to channel geometry ratio (H/L_c) of 0.25. It also shows that the optimum value of filament

length for mixing in micro-devices is critically influenced by channel geometry as well as bending rigidity.
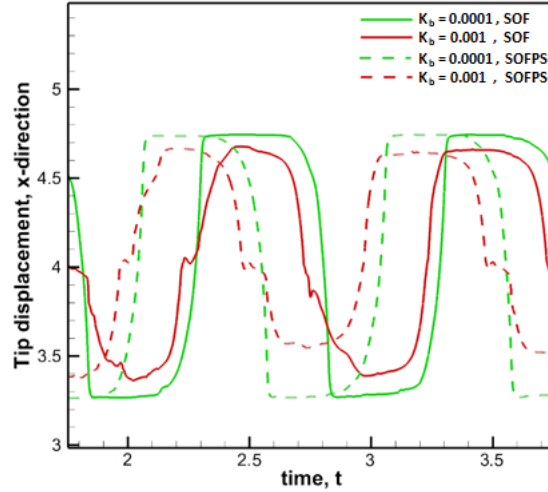
Figure 5.16 SOF and SOFPS flow condition comparison of filament tip displacement in x-direction with respect to time at Reynolds number, Re = 100 for fixed filament length, L = 0.8 and bending rigidities, $K_b = 1 \times 10^{-3}, 1 \times 10^{-4}$.

5.3.3 Effect of inlet fluid conditions and bending rigidity on filament deformation

Phase shift in fluid motion has a great impact on filament displacement dynamics especially for rigid filaments. In order to obtain a better understanding of filament deformation and bending characteristics for different bending rigidities and fluid flow conditions, further analysis is carried out in which the filament length, L is fixed to 0.8 spanning three different bending rigidity $K_b = 0.01, 0.1$ and 1.0. Studies by (Lambert and Rangel 2010) had emphasized the importance of analysing flap dynamics for low Reynolds number ranging from 0.3 – 80. Thus, fixed Reynolds number of 10.0 is considered for this study. The corresponding filament deformation is analysed for the two flow conditions keeping a constant value of stretching co-efficient $K_s = 10000$. The numerical simulation is carried out for fixed frequency of oscillation given by St = 0.5. The total simulation time is kept as 3.0. The filament movement and resulting fluid motion is observed for time period of 2.0 – 3.0. The filament positions are captured at fixed time intervals of 0.125. An

account of hydrodynamics surrounding the flexible filament is also obtained. The filament deformation and its direction of motion is synonymous with fluid flow direction. In Figure 5.17, the various positions of the filament are marked by numbers which indicate the sequence of motion on a sample sinusoidally oscillating fluid flow profile. The nine filament positions can be grouped into two parts i.e. positive fluid cycle and negative cycle. Each cycle can be further divided into forward filament motion and backward filament motion. This is clearly shown in Table 5.4. The fluid cycle and its corresponding filament motion is applicable to all subsequent cases. The change in fluid and filament directions are observed at position 3 and position 7.
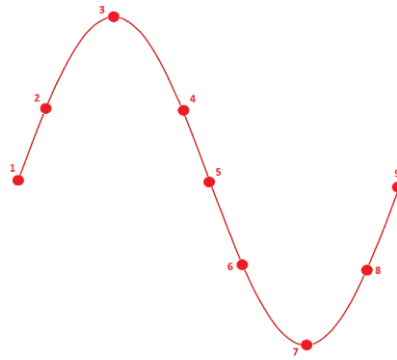
Figure 5.17 Various filament positions depicted on a sample profile of oscillating fluid flow.

Table 5.4 Fluid flow direction and its corresponding filament positions.

Filament positions	Type of fluid cycle	Type of filament motion	Filament position with respect to initial fluid motion	Filament position with respect to final fluid motion
1 – 3	Positive	Forward	Position 1	**Position 3**
3 – 5	Positive	Backward	Position 3	Position 5
5 – 7	Negative	Backward	Position 5	**Position 7**
7 – 9	Negative	Forward	Position 7	Position 9

5.3.3.1 Sinusoidally oscillatory flow with phase shift (SOFPS)

The type of pressure driven fluid flow equation used for the present case is given by equation (5.3). Three cases of bending rigidity are analysed. 1) High rigidity ($K_b = 1.0$), 2) Medium rigidity ($K_b = 0.1$) and 3) Low rigidity ($K_b = 0.01$).

Case 1: High rigidity ($K_b = 1.0$)

The motion of the filament in positive x – direction is marked in red and motion in negative direction is marked in blue. The same convention is applied for all figures. Figure 5.18 describes the deformation and position of flexible filament for the case of $K_b = 1.0$. Starting from position 1 in positive cycle, the filament undergoes a forward motion and steadily elongates with appreciable bending. It reaches maximum extension at position 3 where the fluid direction changes. Next, the filament returns back to the centre of channel at position 5 thus completing the positive cycle. A similar extension and bending occur in negative cycle with filament changing direction at position 7 and the negative cycle thus concludes at position 9. Another important observation is that, the filament motion in both positive and negative cycle is symmetric. This is an indication of sweeping filament conformity which is also observed in previous filament deformation studies of (Anand et al. 2017), thus making it a good case for fluid mixing applications.

It is clear from the above discussion that, the fluid direction changes at position 3. While the fluid changes direction, a series of streamline images describing the hydrodynamics around the filament is captured. This is shown in Figure 5.19. The corresponding time are provided with the images. At t = 2.24, the filament is in elongated position with respect to positive fluid cycle. A recirculation zone is formed near the base of filament. As observed from time t = 2.26 – 2.30, a secondary recirculation zone emerges close to the filament structure and moves from the filament centre to tip, gradually increasing in size. The size of the primary zone also increases and at t = 2.30, the secondary zone combines with primary to form a large V shaped zone around the filament. The V shaped recirculation zone encompasses large portion of channel mid-section and reaches maximum size at t = 2.32. At t = 2.33 the fluid velocity reaches minimum. With the change

in fluid direction at t = 2.34, the V shaped zone shrinks and an oval shaped zone is formed near the filament base. The size of the ovals shaped zone gradually decreases with time as seen from t = 2.34 to 2.37. The formation of V shaped zones and subsequent oval shaped one indicates that fluid molecules near the filament tend to adhere to its surface. First, the filament is high in rigidity and thus moves slowly with respect to fluid motion. This prevents the filament to deform considerably and the fluid itself offers high resistance to filament motion. Secondly this phenomenon increases mixing efficiency since the fluid is mostly circulating within the large V-shaped zone for case of lower channel geometry ratio. Thus, it is believed that this case can be considered as ideal for fluid mixing.

Figure 5.18 Instantaneous filament deformation due to SOFPS condition for the case of bending rigidity $K_b = 1.0$ at fixed time interval of 0.125 between time periods 2.0 – 3.0.
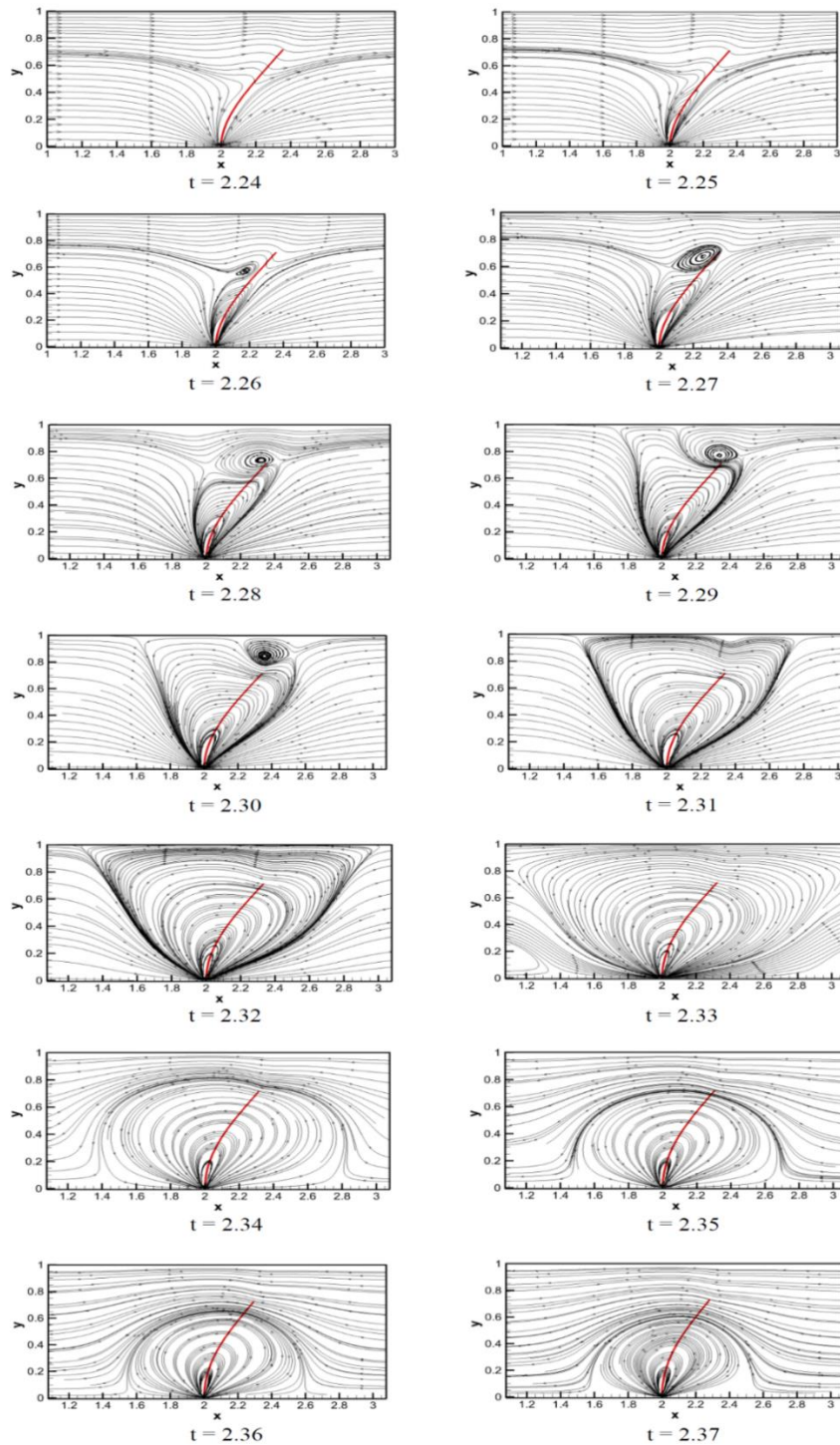
Figure 5.19 Streamlines visualization at the vicinity of filament (position 3) at different non-dimensionalized time sequences for $K_b = 1.0$ during positive fluid cycle.

Case 2: Medium rigidity ($K_b = 0.1$)

The bending rigidity of filament in the present case is $K_b = 0.1$ and considered to be medium in nature. Figure 5.20 shows the various filament positions and deformations for SOFPS condition. From position 1, filament deforms into an arc shape depicted in position 2. The filament appears to be bent at the centre due to lower bending rigidity. Similar arc shape is also observed in negative cycle at position 6. The deformation of filament at position 4 and 5 is also very similar to that seen in position 8 and position 1 respectively but in opposite filament direction. The movement of filament in both positive and negative fluid cycle is thus found to be symmetric in nature. Figure 5.21 depicts the series of flow field images captured in the form of streamlines around the flexible filament while the fluid changes direction (position 3). Similar to previous case two recirculation zones, one at the base called primary and other at filament centre called secondary are formed as seen at time $t = 2.25$. With increase in time, the size of both the zones gradually increases. However, the secondary zone grows at a much faster rate compared to primary. This can be observed for images from $t = 2.28$ to $t = 2.31$. The upper half section of the flexible filament has a quick motion when compared to lower half. Also, the movement of secondary zone from the centre to filament tip is slower than the previous case where filament had bending rigidity $K_b = 1.0$. The size of the secondary zone reaches maximum at $t = 2.32$. Apart from the primary and secondary zones, few other recirculation zones can be observed close to channel edges. Once the fluid reverses direction at $t = 2.34$, the shape of primary zone turns to oval and size of secondary zone gradually diminishes. The secondary zone starts moving towards the tip of filament and finally disappears at $t = 2.35$. Due to the formation of several recirculation zones near channel edges and domination of secondary zone near filament surface, good amount of fluid mixing is seen. Fluid entrapment in circulation zones is observed which also enhances mixing efficiency. Similar types of fluid motion are reported in fluid mixing studies (Lambert and Rangel 2010).

116

Figure 5.20 Instantaneous filament deformation due to SOFPS condition for the case of bending rigidity $K_b = 0.1$ at fixed time interval of 0.125 between time periods 2.0 – 3.0.

Case 3: Low rigidity ($K_b = 0.01$)

Similar to previous cases the deformation and positions of filament is recorded for equal time intervals as shown in Figure 5.22. The filament as observed for position 1 shows a buckling behaviour at the lower half section while the upper half remains straight. This buckling behaviour continues with progression of time and is further seen in upper half section at position 2. The forward motion of the filament in the positive fluid cycle ends with formation of an arc shaped filament as seen at position 3. Thus, three different filament shape deformations can be seen for positive fluid cycle. Similar shape deformation is also observed for negative fluid cycle. To summarize, single buckling phenomenon is observed for positions 1 and 5, multiple filament buckling is seen for positions 2 and 6. Rest of the filament deformations are of arc shaped with bending at the centre location.

117

Figure 5.21 Streamlines visualization at the vicinity of filament (position 3) at different non-dimensionalized time sequences for $K_b = 0.1$ during positive fluid cycle.

118
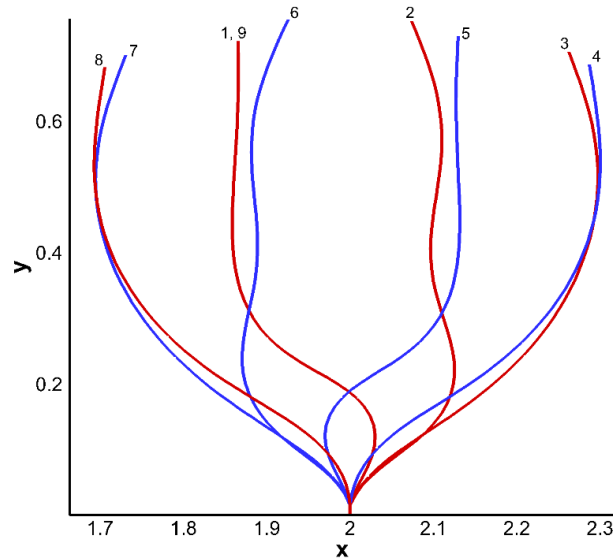
Figure 5.22 Instantaneous filament deformation due to SOFPS condition for the case of bending rigidity $K_b = 0.01$ at fixed time interval of 0.125 between time periods 2.0 – 3.0.

The fluid flow around flexible filament is shown for filament position 3 in Figure 5.23. As compared to the previous two cases, the filament bending rigidity is the least. When observing fluid motion for time $t = 2.25 – 2.30$, the size of primary and secondary recirculation zones as compared that of previous cases are found to be quite small. This indicates that the filament is moving in tandem with fluid flow and is thereby offering least resistance. At $t = 2.31$, the size of secondary zone exceeds that of primary. Apart from primary and secondary zone, two other zones are formed near the top left and right channel edges at $t = 2.32$ during which time the fluid velocity is minimum. The fluid changes direction at $t = 2.33$ which causes the secondary zone to move slightly away from filament surface. Finally, the secondary zone disappears at $t = 2.34$. An observation from the above study indicates that the fluid flow around the filament is laminar in nature with small disturbances near the filament structure. The presence of the filament has practically no effect on fluid mixing in the present case.
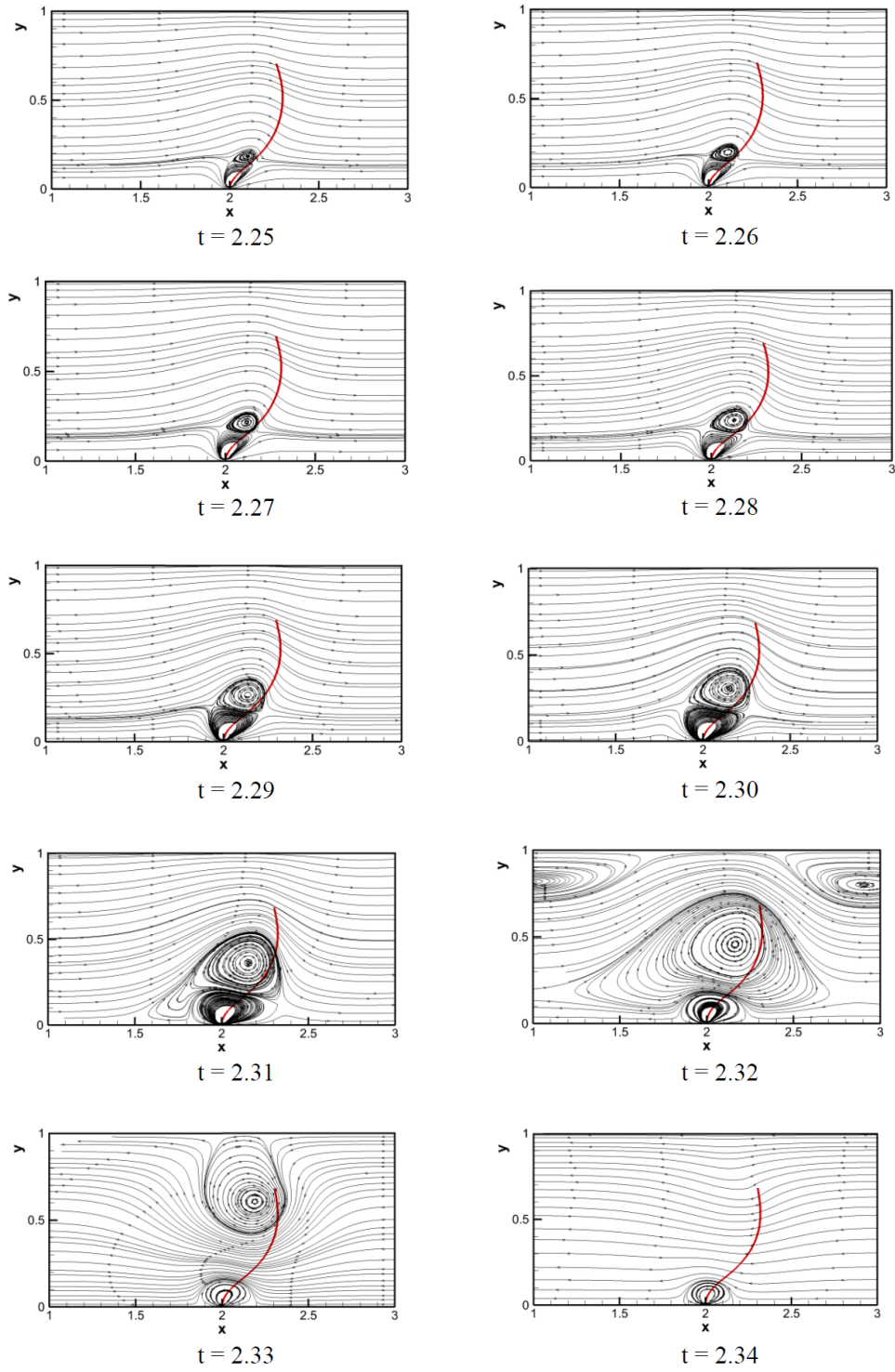
Figure 5.23 Streamlines visualization at the vicinity of filament (position 3) at different non-dimensionalized time sequences for $K_b = 0.01$ during positive fluid cycle.

5.3.3.2 Sinusoidally oscillatory flow without phase shift (SOF)

The fluid equation governing the flow for the present section is sinusoidal in nature without phase shift (SOF). The corresponding sinusoidal pressure gradient driving the flow is given by equation (5.4). Similar to SOFPS condition, three cases of bending rigidity are analysed here. 1) High rigidity ($K_b = 1.0$), 2) Medium rigidity ($K_b = 0.1$) and 3) Low rigidity ($K_b = 0.01$).

Case 1: High rigidity ($K_b = 1.0$)

Figure 5.24 describes the deformation and position of flexible filament for the case of SOF condition with high rigidity $K_b = 1.0$. From the figure, a steady elongation coupled with bending is observed for filament position 1- 3 in the positive fluid cycle. The fluid changes direction at position 3 and the filament achieve maximum extension in this position. Next, the filament returns back to the centre of channel at position 5 thus completing the positive cycle. A similar extension and bending occur in negative cycle with filament changing direction at position 7 and the negative cycle thus concludes at position 9. An important observation is that, the filament motion in both positive and negative cycle is symmetric. The shape deformation seen in the present case is very similar to that observed for SOFPS condition.

Case 2: Medium rigidity ($K_b = 0.1$)

The filament at position 1 in Figure 5.25 is almost straight and undergoes bending at the centre with passage of time. The positive fluid cycle also produces elongation in filament. When deformations are seen for positions 4 – 7 in the backward motion, the filament achieve considerable bending mixed with compression at centre. Finally, the filament returns to its original position 1 at the end of fluid negative cycle. Contrary to SOFPS condition, the filament changes direction in negative cycle at position 8. A simple observation of filament movement with respect to positions reveal that none of the deformations are similar to each other. Shape replication of filament positions for both positive and negative fluid cycle is not observed. During the forward motion of filament,

the fluid is fairly straight, remains elongated and achieves slight bending with time. When looking at the same filament behaviour in backward motion, more pronounced compression and bending is noticed. The filament behaves differently during forward and backward motion. This behaviour of filament is very similar to beating cilia and its propulsion mechanism (Barlow et al. 1993; Dauptain et al. 2007). In the present study, the filament has no self-propelling feature and is completely passive. It responds to only hydrodynamics stresses acting on its surface. On the other hand, beating cilia produces antiplectic metachronism (Barlow et al. 1993; Dauptain et al. 2007) which creates an oscillating fluid motion responsible for effective stoke. This effective stroke pushes the fluid in the opposite direction thereby causing the cilia bearing micro-organism to propel further. For the case of SOF condition, the filament behaves in an asymmetric fashion similar to beating cilia. Thus, the present case clearly depicts the form of fluid motion produced during ciliary propulsion.
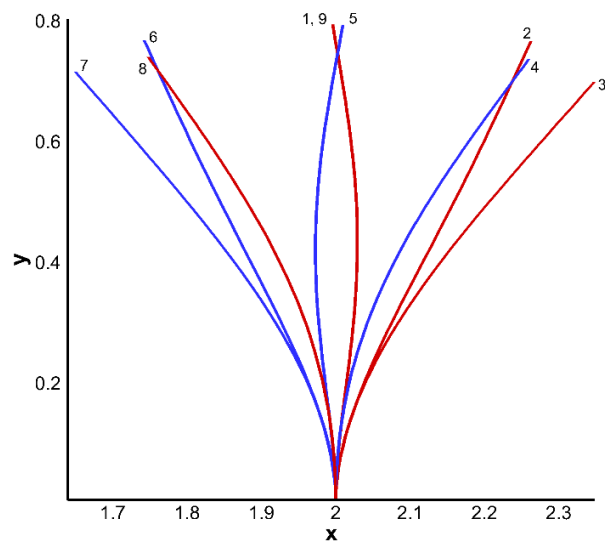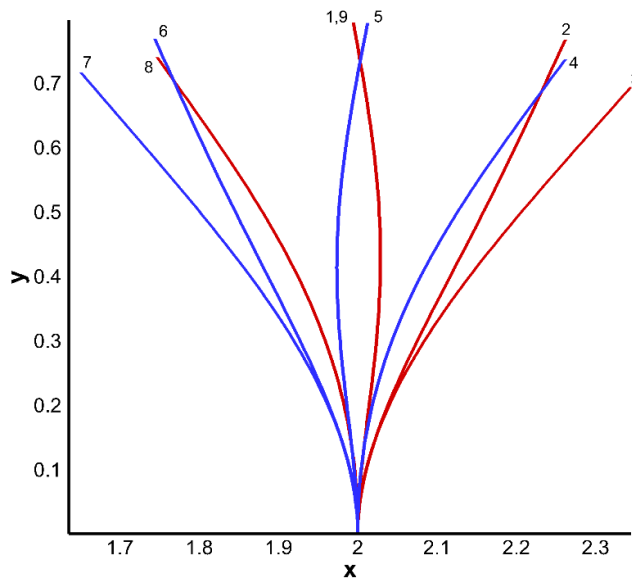

Figure 5.24 Instantaneous filament deformation due to SOF condition for the case of bending rigidity $K_b = 1.0$ at fixed time interval of 0.125 between time periods 2.0 – 3.0.
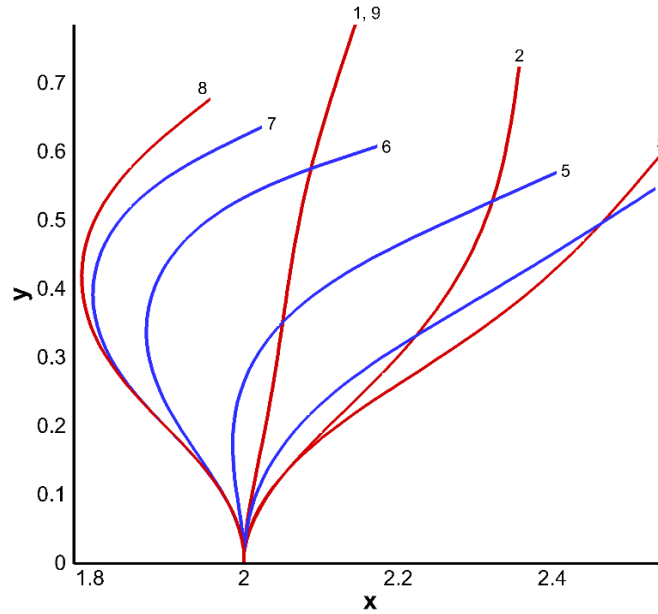
Figure 5.25 Instantaneous filament deformation due to SOF condition for the case of bending rigidity $K_b = 0.1$ at fixed time interval of 0.125 between time periods 2.0 – 3.0.

To further demonstrate that the present case depicts cilia beating, streamlines plots are generated near filament surface for position 8 as shown in Figure 5.26. The fluid is moving from right to left in the negative fluid cycle. A primary recirculation zone is formed at the base of filament at $t = 2.04$. With time, a secondary zone emerges from the upper channel edge while a tertiary zone is created behind the filament. The size of the secondary zone increases in size has more fluid gets entrapped within it. As fluid velocity becomes minimum at $t = 2.07$, tertiary and secondary zone combine to form large high velocity zone behind the filament. With change in fluid direction from left to right, the secondary zone is released towards the right in same direction of fluid flow as seen from images $t = 2.08$ to $t = 2.10$. This phenomenon is called cross-stream fluid flow which can be potentially employed for micro-pumping applications (Anand et al. 2017). All recirculation zones disappear at $t = 2.11$. Another important observation is that, bending rigidity also plays a critical role in producing the asymmetric beat pattern in filament.
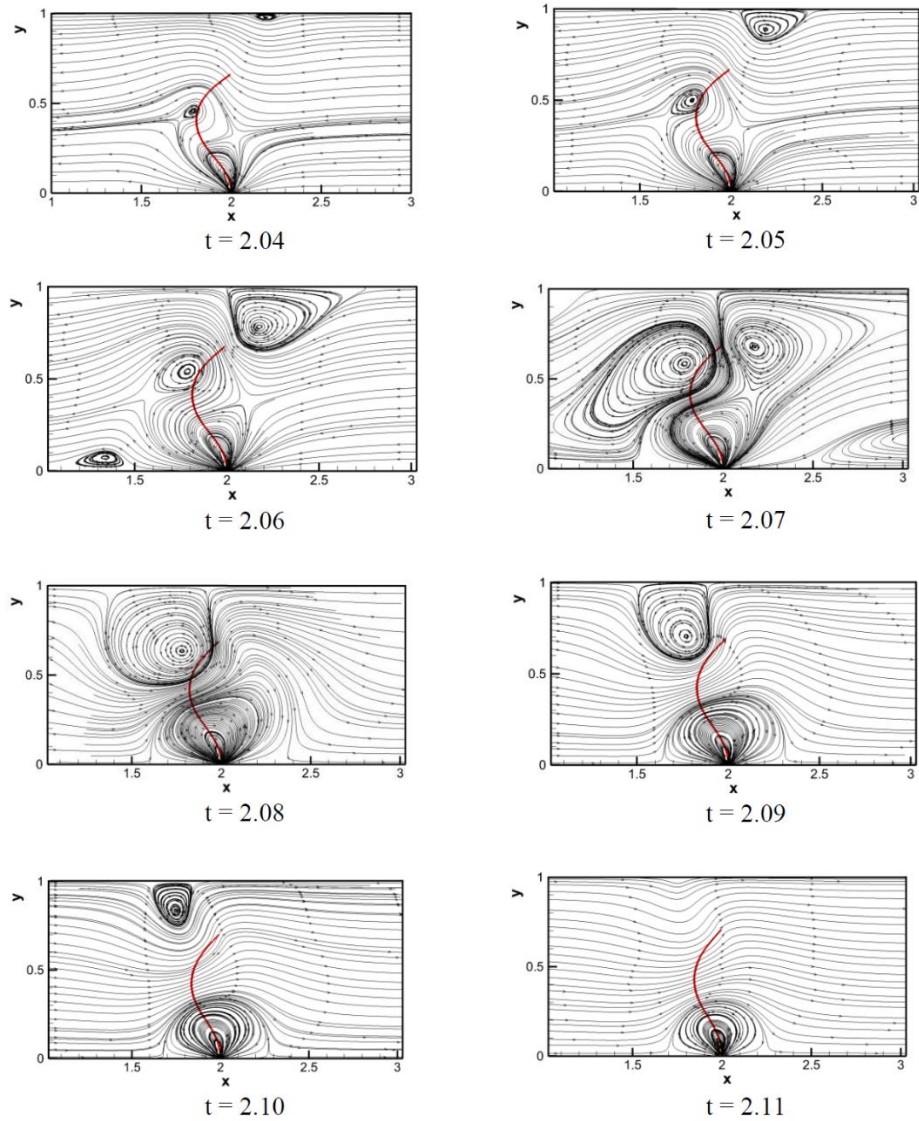
Figure 5.26 Streamlines visualization at the vicinity of filament (position 8) at different non-dimensionalized time sequences for $K_b = 0.1$ during negative fluid cycle.

Case 3: Low rigidity ($K_b = 0.01$)

The deformation and filament positions for the case of $K_b = 0.01$ subjected to SOF condition is given in Figure 5.27. The filament shows slight buckling at position 1 and continues to elongate with minimum bending during forward motion. A significant

buckling is seen at the lower half of filament at position 5 and position 6 during backward motion. By keeping x co-ordinate 2 as reference, the movement of the filament in positive and negative x-direction is analysed. The movement of the filament is restricted to x co-ordinate 1.8 during negative cycle (position 7) while filament elongates and moves beyond x co-ordinate 2.6 during positive cycle (position 3). Thus, a clear asymmetry exists in filament deformation during both fluid cycles. Even though asymmetry exists, the filament positions at fixed intervals of time do not match that of beating cilia. This can also be observed by comparing the filament positions formed during forward and backward motion between the present case and that of medium rigidity $K_b = 0.1$ case.
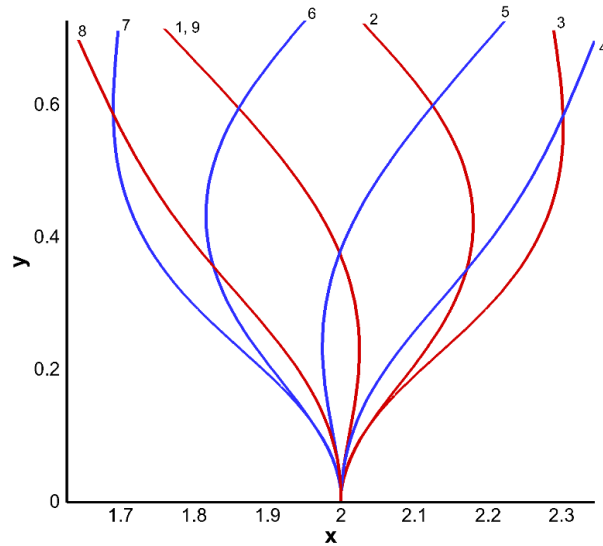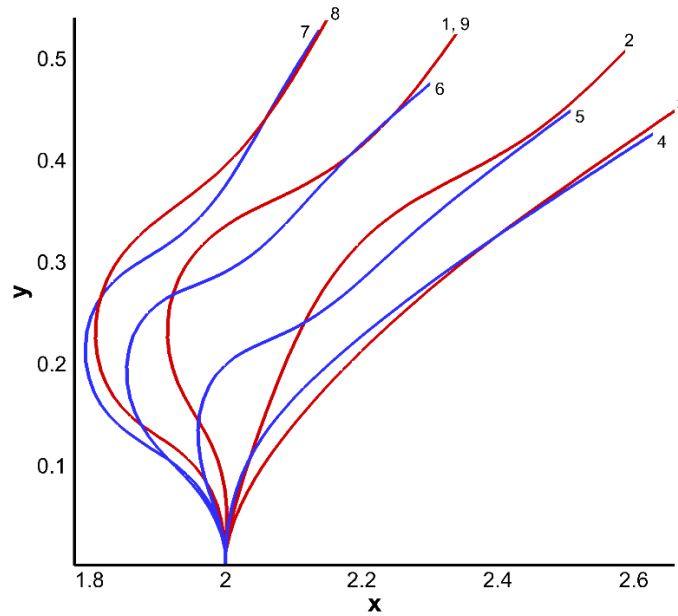

Figure 5.27 Instantaneous filament deformation due to SOF condition for the case of bending rigidity $K_b = 0.01$ at fixed time interval of 0.125 between time periods 2.0 – 3.0.

Fluid flow surrounding flexible filament at position 8 is provided in Figure 5.28 in the form of streamlines. The present case has the lowest bending rigidity. Due to this feature, the filament offers very low resistance to fluid motion. In the location of filament bending, a small recirculation zone is formed as seen at time t = 2.06. Two large zones are observed at t = 2.07. This is the time at which the fluid velocity becomes minimum. With

change in fluid direction (t = 2.08), small zones are created near filament surface which do not show any significant impact on the surrounding fluid dynamics. The fluid is laminar in nature with small oval shaped primary zones created near the base as seen at time t = 2.09 and t = 2.10.
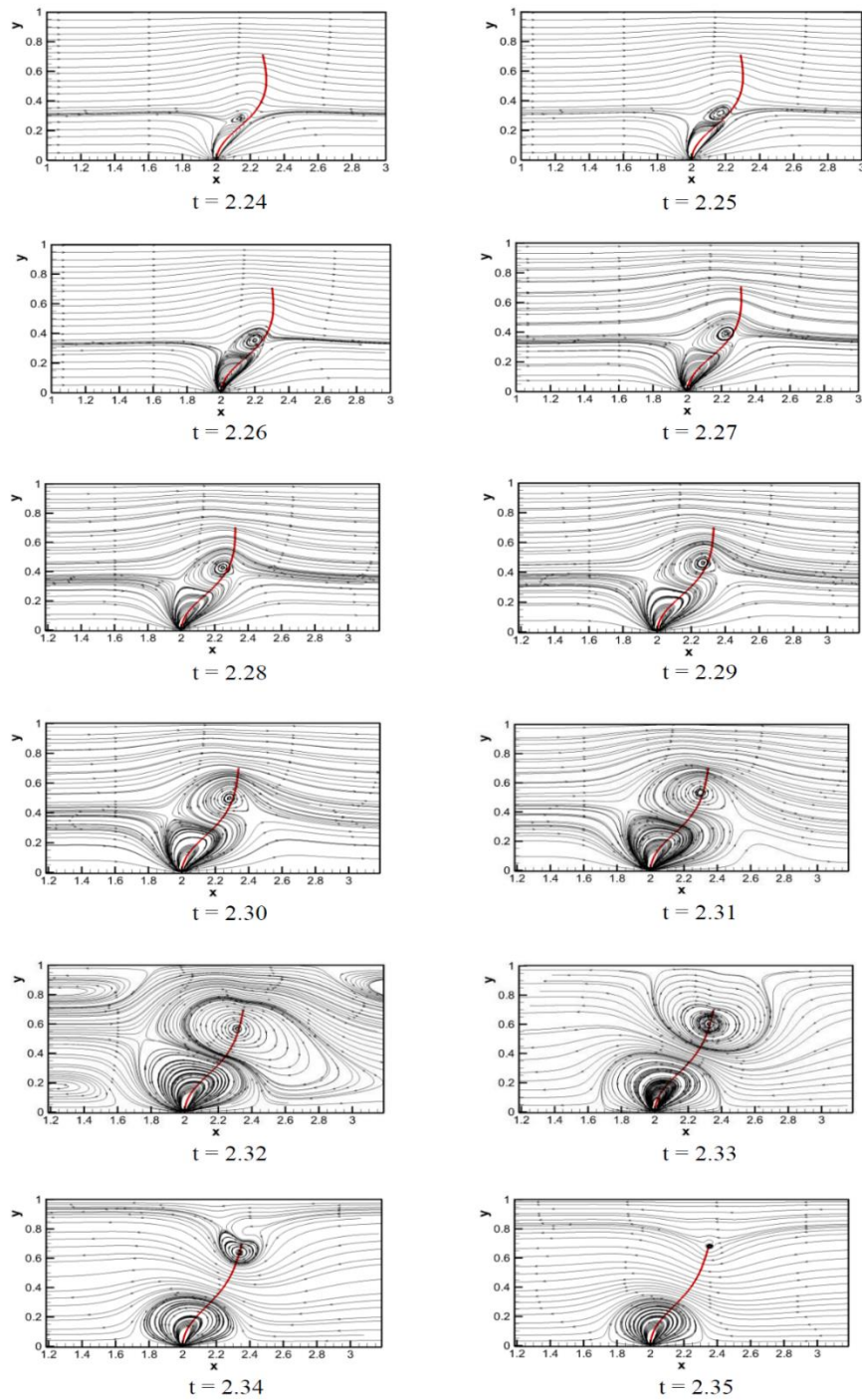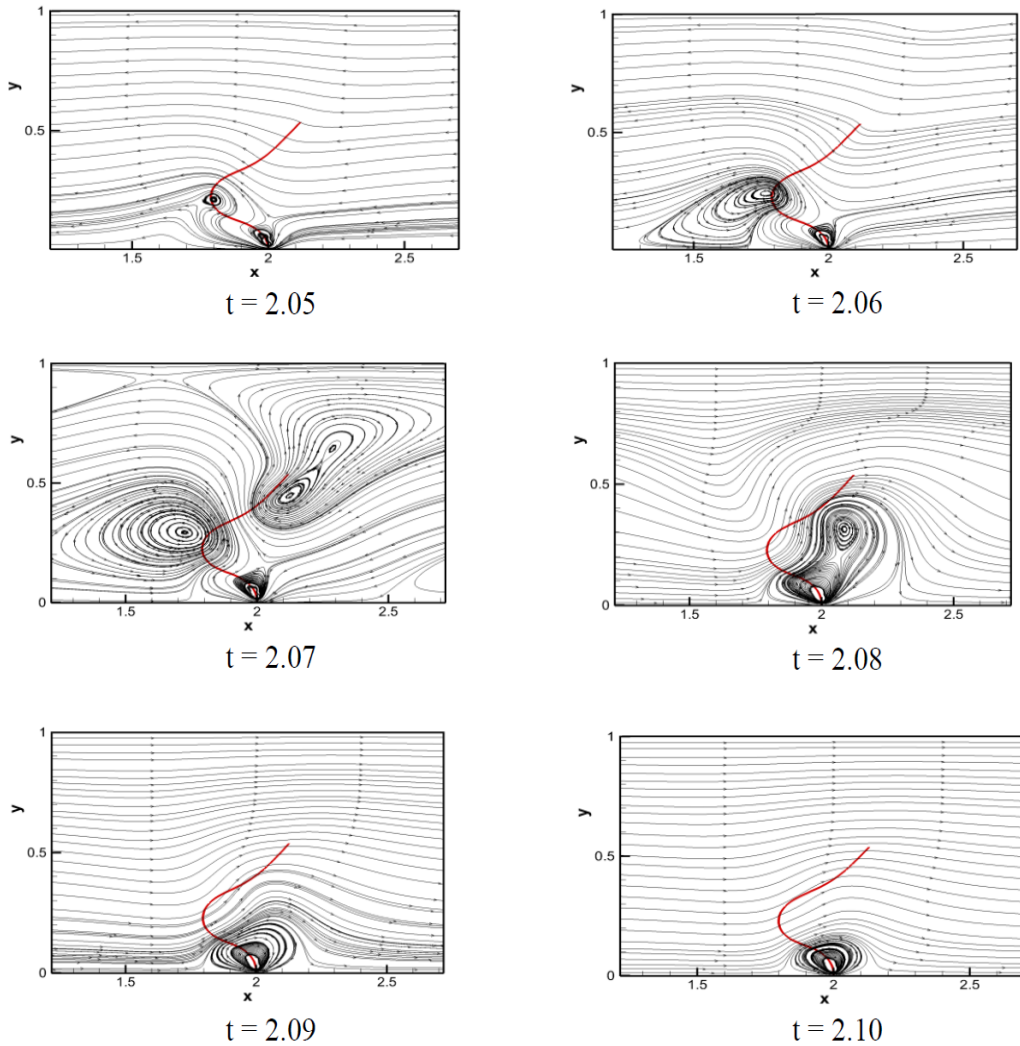

Figure 5.28 Streamlines visualization at the vicinity of filament (position 8) at different non-dimensionalized time sequences for K_b = 0.01 during negative fluid cycle.

5.3.4 Comparison between SOFPS and SOF conditions

In the previous sections the filament deformation and fluid flow surrounding the filament are analysed by comparing positions and streamlines for both SOFPS and SOF conditions. In the present section, the end-to-end distance (d_{ee}) and tip trajectory for the two flow conditions are studied.

5.3.4.1 End-to-end distance

The factor end-to-end distance (d_{ee}) signifies the amount of stretching/compression, bending or buckling produced by the filament. It is defined as the shortest distance between the fixed and free filament ends. The length of the filament is the actual end-to-end distance before the start of simulation. The filament end-to-end distance (d_{ee}) for case of high rigidity $K_b = 1.0$ is shown in Figure 5.29(a).

Table 5.5 Percentage deviation of filament end-to-end distance for different bending rigidity and flow condition with corresponding filament behaviour and deformation observations.

Bending rigidity of flexible filament (K_b)	Fluid Flow conditions with filament behaviour		Filament deformation
	SOFPS	SOF	
High, 1.0	2.5% (symmetry)	3.12% (symmetry)	Stretching /Compression
Medium, 0.1	10.6% (symmetry)	30% (asymmetry)	Bending
Low, 0.01	8.75% (symmetry)	33.75% (asymmetry)	Buckling

A percentage (%) deviation of end-to-end distance with respect to original filament length is tabulated in Table 5.5. Filaments in this group show considerable amount of stretching and compression. The filament subjected to SOFPS show lower levels of deviation within the first time period compared to SOF condition. From time period 1 onwards, the level of deviation remains the same for both conditions. A phase shift is observed between filament end-to-end distances due to the two flow conditions. Filament in SOFPS condition has lowest deviation of 2.5% while SOF condition produce 3.12%. Filaments having high rigidity ($K_b = 1.0$) and subjected to varying flow conditions produce symmetric behaviour in filament deformation. Similar observations are noted when analysing filament positions in previous sections and the same can be confirmed from Figure 5.29(a). The end-to-end distance (d_{ee}) of filament having medium rigidity ($K_b = 0.1$) is shown in Figure 5.29(b). Filament subjected to both conditions exhibit an initial bending state and remain in the same state throughout the simulation time. Filament placed in SOFPS condition shows lowest deviation of 10.6% whereas filament in SOF condition shows about 30% deviation. The amount of deviation for SOF condition reduces with passage of time while that for SOFPS condition remains almost constant as seen in Figure 5.29(b). Finally, Figure 5.29(c) shows d_{ee} for filament with lowest rigidity $K_b = 0.01$. Both flow conditions produce buckling states in filament. The pattern of end-to-end distance plot for SOFPS condition is not sinusoidal nor uniform in nature when compared to high and medium rigidity cases. This also indicates filament buckling during successive time periods. The lowest deviation obtained for SOFPS condition is 8.75% and that for SOF condition is 33.75%. With increase in time, the level of deviation keeps on increasing for SOF condition whereas it remains almost constant for SOFPS condition. The filaments that are subjected to both the flow conditions have three things in common. 1) Filament having high rigidity ($K_b = 1.0$), undergo cyclic stretching and compression, 2) Filament having medium rigidity ($K_b = 0.1$), show successive bending and 3) Filament having low rigidity ($K_b = 0.01$), undergoes buckling. These observations are obtained from visual inspection and qualitative comparison of filament deformation study carried out in previous section with end-to-end distance plots in the present section. Thus, it can be inferred from the above

discussion that, high rigidity filaments show greater levels of stretching while medium and low rigidity filaments exhibit better bending and buckling respectively. Also, filament buckling is seen only in low rigidity filament placed in SOFPS and SOF condition. When comparing end-to-end distances for medium and low rigidity filaments placed in both flow conditions, filaments in SOF condition show significant deviation as seen in Table 5.5. This also indicates asymmetric behaviour of medium and low rigidity filaments in SOF condition.

5.3.4.2 Filament tip trajectory

The trajectory of filament tip provides useful information regarding the overall extent of movement of filament structure either in the positive or negative x – direction. Since the filament is initially held vertical, the trajectory will begin at x – location 2.0. The symmetric and asymmetry behaviour of filament can be analysed by observing the trajectory in the positive and negative direction. Figure 5.30(a) shows the tip trajectory of high rigidity (K_b = 1.0) filaments placed in SOFPS and SOF conditions. Except for first time period, the movement of trajectory in both positive and negative direction is approximately equal for both flow conditions. The solution attains stability with time and hence initial variations in solution are observed for all case studies. Figure 5.30(b) provides details of tip trajectory with respect to simulation time for medium rigidity filament. When observing SOFPS condition plot, the trajectory is found to be moving in both positive and negative direction. The same pattern is seen in Figure 5.30(c) for SOFPS condition which relates filaments of lower rigidity. By analysing tip trajectory of SOF condition for both medium and lower rigidity filaments, it can be seen that the highest and lowest tip expansions are present only in positive x – direction. The filament tip never enters the negative x - direction region. This is another proof of asymmetry in low and medium rigidity filaments. Thus, it can be inferred that, the filament behaves in a symmetric fashion irrespective of bending rigidity when subjected to SOFPS conditions. Also, asymmetric deformation of filament is observed for the ones placed in SOF conditions provided the bending rigidity is medium or lower in nature. It also indicates that filaments that have

equi-spaced sweeping trajectories are well suited for mixing applications while those exhibiting asymmetry behaviours are applicable for fluid pumping.

Thus the deformation, buckling and asymmetric behaviour of flexible filament when subjected to SOFPS and SOF flow conditions are systematically analysed. The impact of constraining both ends of the filament and positioning the filament in different channel locations is discussed in the next chapter.
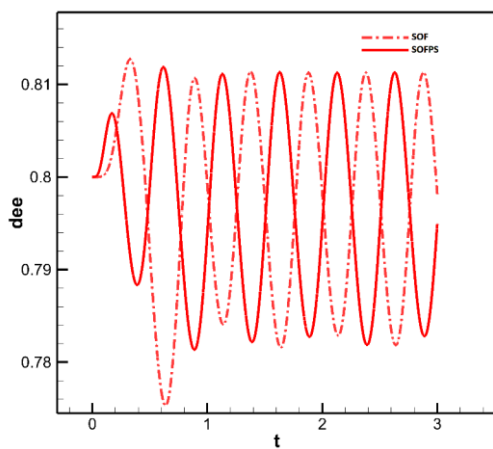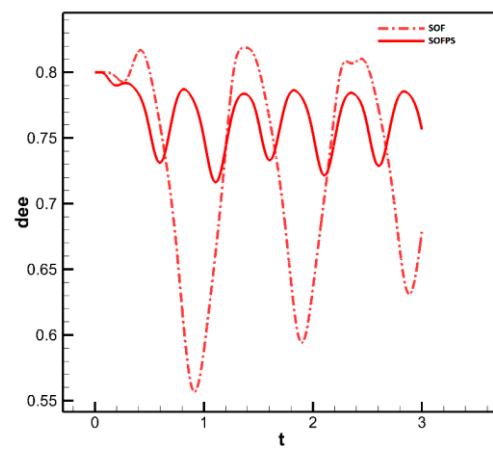
(a) $K_b = 1.0$ (b) $K_b = 0.1$
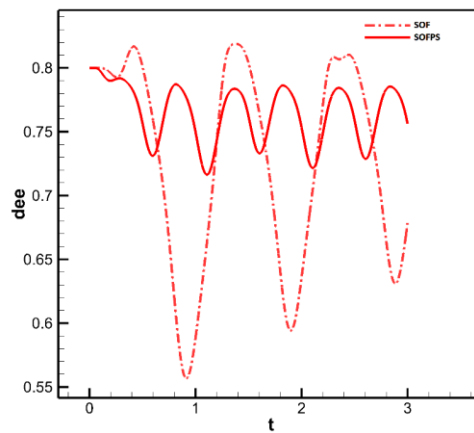
(c) $K_b = 0.01$

Figure 5.29 End-to-end distance (d_{ee}) obtained by filament for total simulation time when subjected to SOFPS and SOF conditions.
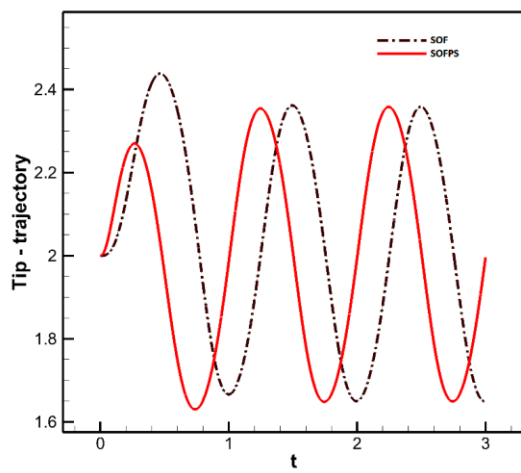
(a) $K_b = 1.0$
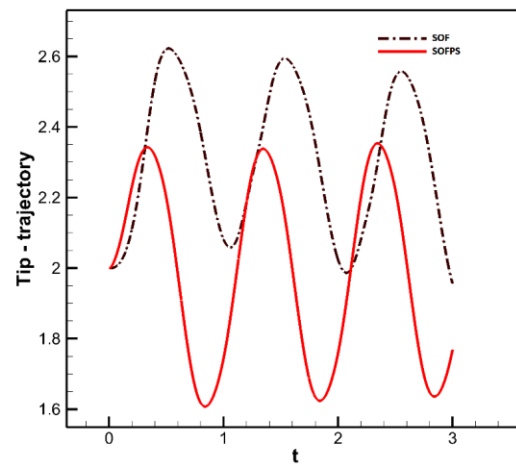
(b) $K_b = 0.1$
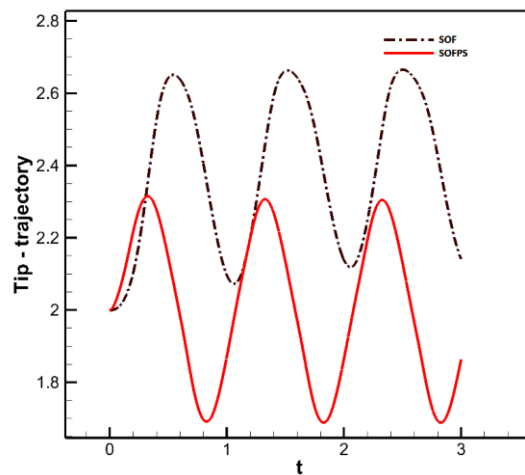
(c) $K_b = 0.01$

Figure 5.30 Trajectory of filament tip when subjected to SOFPS and SOF conditions over total simulation time 3.0.

CHAPTER 6

6 SIMULATION OF TETHERED FLEXIBLE MEMBRANE AND FLOW RATE PREDICTION USING IBM AND ANN TECHNIQUES

6.1 Background

Fluid-structure interaction (FSI) involving moving flexible boundaries and the surrounding hydrodynamic instabilities are a prime area of concern in many biomedical, physiological, chemical and engineering applications. For instance, air flow through flexible respiratory channels in human lungs, fluid-conveying elastic vessels in human body, flexible filaments in fluid flow, flow induced collapsible tubes, lab-on-chip and organ-on-chip diagnostic devices, thin-film coating etc. utilize FSI. The above mentioned FSI problems can be broadly grouped into two classes. The first deals with fluttering structures or flap type analysis driven by inertial domination. The flapping of flexible sheets, flags and filaments are a subset of this class (Shelley et al. 2011). Some interesting applications include energy harvesting (Allen et al. 2001), paper processing industry (Watanabe et al. 2002) and turbulence reduction (Shen et al. 2003). In biology, understanding the response and behavior of organisms like fish to environmental flow conditions is important. The structural deformation leads to formation of bending, twisting and folding sequences (Vogel 1994; Liao et al. 2003; Muller 2003). Experimental and numerical studies have also been carried out in this direction (Taneda 1968; Zhang et al. 2000; Zhu and Peskin 2002; Farnell et al. 2004; Shelley et al. 2005; Kim and Peskin 2006; Huang et al. 2007; Eloy et al. 2008). The second class of FSI problems deal with collapsible tubes and membranes that produce self-excited oscillations with large amplitudes. In human body, fluid transporting vessels subjected to positive transmural pressure maintain an approximately circular cross-section which reduce flow resistance. The vessels have higher stiffness relative to fluid loading and undergo small negligible deformations. However, when subjected to negative transmural pressure, the vessel undergoes buckling or collapse. These collapsed vessels easily develop self-excited oscillations due to induced

flow. Experimental aspects of membrane deformation have been explored in previous studies (Sygulski 2007). The deformation of collapsible tubes and the corresponding flow-induced oscillations were studied using a Starling resistor (Bertram 2003). The system is a two-dimensional channel model in which a particular wall segment is modified to contain a thin membrane thus representing a collapsible tube. The deforming mechanism for low Reynolds number flow is significantly different from that of rigid tubes (Krindel and Silberberg 1979). The effect of membrane flexibility at low Reynolds number on flow dynamics had been investigated for gel-walled tubes. The oscillation of the gel-walled surface generated a destabilized flow pattern. (Chakraborty et al. 2012) in their recent experimental study which consisted of an elastic membrane positioned in PDMS microchannel observed that there was substantial deformation of the flexible membrane due to externally applied pressure. The formation of unstable flow patterns in the vicinity of deformable membrane at low Reynolds number were also reported by (Thaokar and Kumaran 2002) for a wide range of membrane and fluid flow parameters.

Initial theoretical studies on Starling resistor were done using lumped parameter or spatially one-dimensional models (Heil and Jensen 2003). The simplicity of these models provided mathematical analysis that would identify the underlying mechanism of system behavior. Since the framework is one-dimensional and flow model is cross-sectionally averaged, the main drawback of this model is that it fails to capture viscous dissipation effects unless some closure assumptions are given. The use of such closure assumptions can be prevented by modelling the system based on Navier-Stokes equations and elastic theory. Two-dimensional simulations based on Navier-Stokes equations were carried out to study flow in Starling resistor (Luo and Pedley 1996; Liang et al. 1997; Huang 2001; Luo et al. 2008; Liu et al. 2009). They observed for steady solution, a balance should exist between axial tension induced by fluid flow and elastic restoring force due to wall stiffness. For small wall stiffness, the viscous pressure drop along the channel produces wall deformations of large amplitude thus making the system unstable. On the other hand, for large wall stiffness the fluid perturbations generate only small wall deflections and oscillations. The oscillatory wall motion is thus governed by certain critical membrane

stiffness value that maintains the dynamic balance between hydrodynamic forces and wall elastic forces. However, the above-mentioned approaches due to the unsteady behavior of membrane dynamics often become ill-conditioned and are also computationally expensive. In this direction, immersed boundary method can handle such complex fluid-membrane interaction problems in an effective way.

The results obtained from numerical simulations can be used to develop empirical models that can accurately perform predictions for different input parametric conditions. One such technique commonly used for non-linear systems is Artificial neural networks (ANN). Recently, (Anand et al. 2016) performed dissipative particle dynamics simulation study of deformable membranes in micro-channel at low Reynolds number. The membrane was pinned at both ends and placed parallel to flow. They observed different steady state membrane conformations (mode shapes) for varying bending rigidities. These mode shapes had differential effect on flow rate past the membrane in the channel. This aspect of the study can be further exploited to understand how membrane deformations can be used to control flow rate in micro-devices thus providing tremendous application perspectives. It is important to develop a model that can effectively predict flow rates for different combinations of membrane length, membrane position in the channel and membrane bending rigidity. Even though different mode shapes were achieved in the works of (Anand et al. 2016), the study primarily focuses on bending rigidities in the range of 10 – 300. The effect on mode shapes at lower rigidities i.e., (0.1-10) were not investigated. Also, from literature it is known that self-excited oscillation of flexible membrane can be achieved at a critical bending rigidity. The importance of membrane length and membrane position in channel and its effect on self-excited oscillations is not widely studied. Also, from literature it is observed that determination of flow rate in channel through immersed boundary simulations of deformable membrane has not been carried out previously. The desired functionality of the membrane can be achieved by considering the full fluid-structure interaction effects through IBM. Further, development of suitable ANN model to predict flow rate past fixed conforming membranes has never been carried out for such low

Reynolds number fluid-membrane interaction problems. Keeping these aspects as the prime motivation the present study is carried out.

In this chapter the two-dimensional numerical model based on finite-volume immersed boundary method developed in Chapter 4, section 4.2 is used to simulate flexible membrane fixed at two end points subjected to Poiseuille flow in a channel. The membrane conformations for different parametric cases are obtained and corresponding channel flow rate for each case is measured. From the IBM simulation results an ANN prediction model is developed. The numerical method and ANN model developed for this study is provided in section 6.2. The numerical model is validated and simulation results of membrane deformation study along with ANN predictions are provided in section 6.3.

6.2 Mathematical formulation and numerical procedure

6.2.1 Immersed boundary method

The schematic representation of flexible membrane tethered horizontally at both ends and placed in a viscous fluid flow domain at low Reynolds number is shown in Figure 6.1. The immersed boundary formulation along with step-by-step numerical procedure for flexible filament interaction in viscous fluid flow has been explained in detail in section 4.2 of Chapter 4. Based on this formulation, the present study is carried out.

6.2.2 Artificial neural network

Artificial neural networks (ANN) is made up of three basic building blocks i.e., network architecture, training method and transfer functions. A multilayer feed-forward network is proposed which consists of input, hidden and output layers for the present study. The layers are made up of parallel processing elements with each layer being connected to proceeding layer by interconnected weights (w). The multi-layer network model used in the present study is provided in Figure 6.2.

Training is referred to as the process by which interconnected weights between network layers are adjusted to obtain the desired output (Sivanandam and Deepa 2006).

The back-propagation algorithm is used for training. The central idea of the back-propagation algorithm is to minimize the error between hidden and output layers and train network. Initially random weights are assigned and continuously adjusted until the minimization criteria is fulfilled. This is achieved by using Levenberg-Marquardt algorithm. The above-mentioned feed-forward network with back propagation algorithm is one of the commonly used networks (Haykin 1994). The mathematical form of the training process is given by equation (6.1).

$$Y_j = f(\sum_{i=1}^{M} w_{ji}X_i + b_j) \tag{6.1}$$

where, M is the number of input vectors to the jth neuron, X_i is the input variable, Y_j is the output from the jth neuron, w_{ji} is the weight that characterizes the strength of the neuron links, b is the jth neuron bias and f is called the transfer function. In the present study, the input variables are membrane length, membrane position in channel and bending rigidity of membrane while the output variable is flow rate. The transfer function used for the hidden layer is logistic sigmoid given by equation (6.2) and linear transfer function is considered for output layer. The advantages of using sigmoid function in order to achieve faster convergence of the back-propagation algorithm was discussed by (Vogl et al. 1988) and (Harrington 1993).

$$f_t(x) = \frac{1}{1+e^{-x}} \tag{6.2}$$

The accuracy of prediction for the best ANN configuration is evaluated using MSE (Mean Squared Error) and R^2 (absolute fraction of variance) given by equation (6.3) and equation (6.4) respectively.

$$MSE = \frac{1}{N}\sum_{i=1}^{N}(tr_i - y_i)^2 \tag{6.3}$$

$$R^2 = 1 - \frac{\sum_{i=1}^{N}(tr_i - y_i)^2}{\sum_{i=1}^{N}(tr_i)^2} \tag{6.4}$$

where, N is the number of data points, tr is the numerically obtained target value and y is the predicted value. The neural network is implemented in MATLAB and corresponding

details regarding implementation and further applications can be found in MATLAB R2018b documentation.
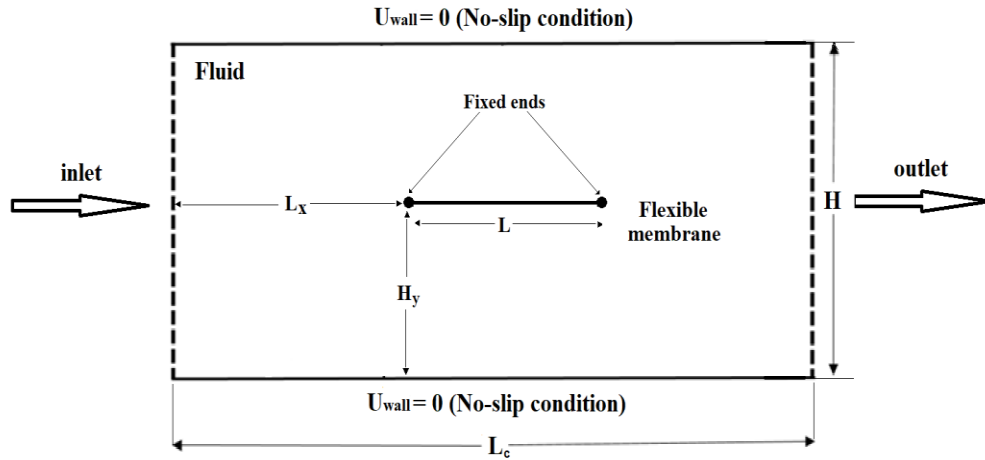
Figure 6.1 Schematic representation of deformable membrane fixed at both ends in channel. The boundary conditions for leading edge of filament is $X_0 = (L_x, H_y)$ and trailing edge is $X_L = (L_x+L, H_y)$.
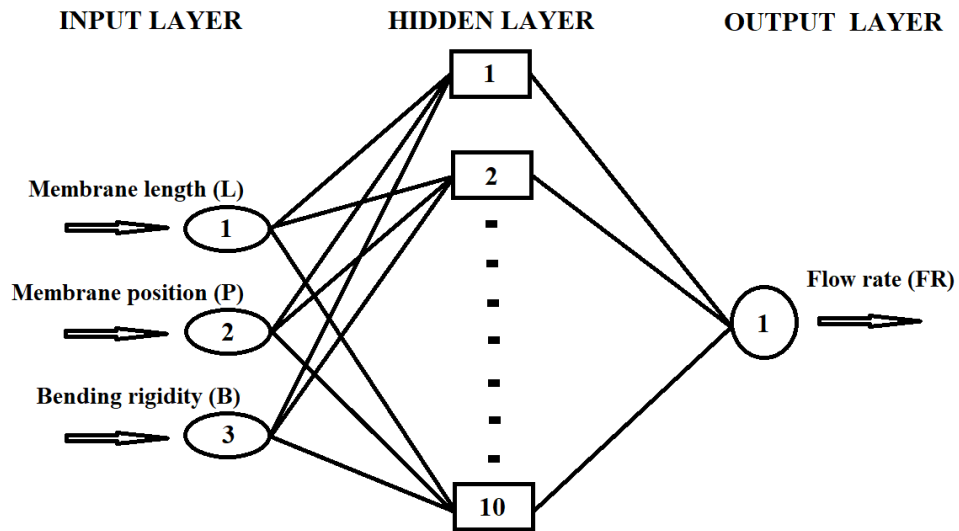
Figure 6.2 The ANN architecture used for the prediction of flow rate (FR).

6.3 Results and Discussion

6.3.1 Validation

In the present chapter, IBM simulation results for rigid membrane is compared with that of finite dissipative particle dynamics (FDPD) simulation and Ansys Fluent simulations of (Anand et al. 2016). The geometry of channel and membrane length are identical to that studied by (Anand et al. 2016). Accordingly, the problem description is given in Figure 6.1 where, channel length, $L_c = 3.0$, channel height, $H = 0.2$, membrane length, $L = 1.0$ and distance of membrane from inlet, $L_x = 1.0$. For the purpose of validation, two locations, $H_y = 0.5$ and 0.75 are used to position the membrane in the channel. The best possible configuration of fluid grid for the present study is chosen to be 512 X 128, whereas 100 IB points are considered. A low Reynolds number, Re = 1.0 is fixed. In calculating Re, the reference length taken is 1 cm and reference velocity is 10^{-2} cm/s. Since the membrane is assumed to be rigid, an elongation stiffness, $K_s = 10000$ and bending rigidity, $K_b = 10.0$ is used. In order to avoid any oscillatory instability in the solution scheme a time step of $\Delta t = 1 \times 10^{-4}$ is taken.

The stream wise velocity components are plotted along the channel length at various cross sections as shown in Figure 6.3 and Figure 6.4. The same has been compared with results obtained by (Anand et al. 2016). In Figure 6.3, the results obtained from the immersed boundary simulation are found to be in good agreement with that of (Anand et al. 2016). In Figure 6.4, good agreement in results is obtained for both the wider and narrow portion of the channel. The velocity contour plots are also obtained for the two membrane positions as shown in Figure 6.5 and Figure 6.6. As seen in these figures, the present IBM model can effectively capture the fluid flow dynamics surrounding the rigid membrane. All of these observations actively demonstrate the ability of the present model to simulate membrane in uniform flow.
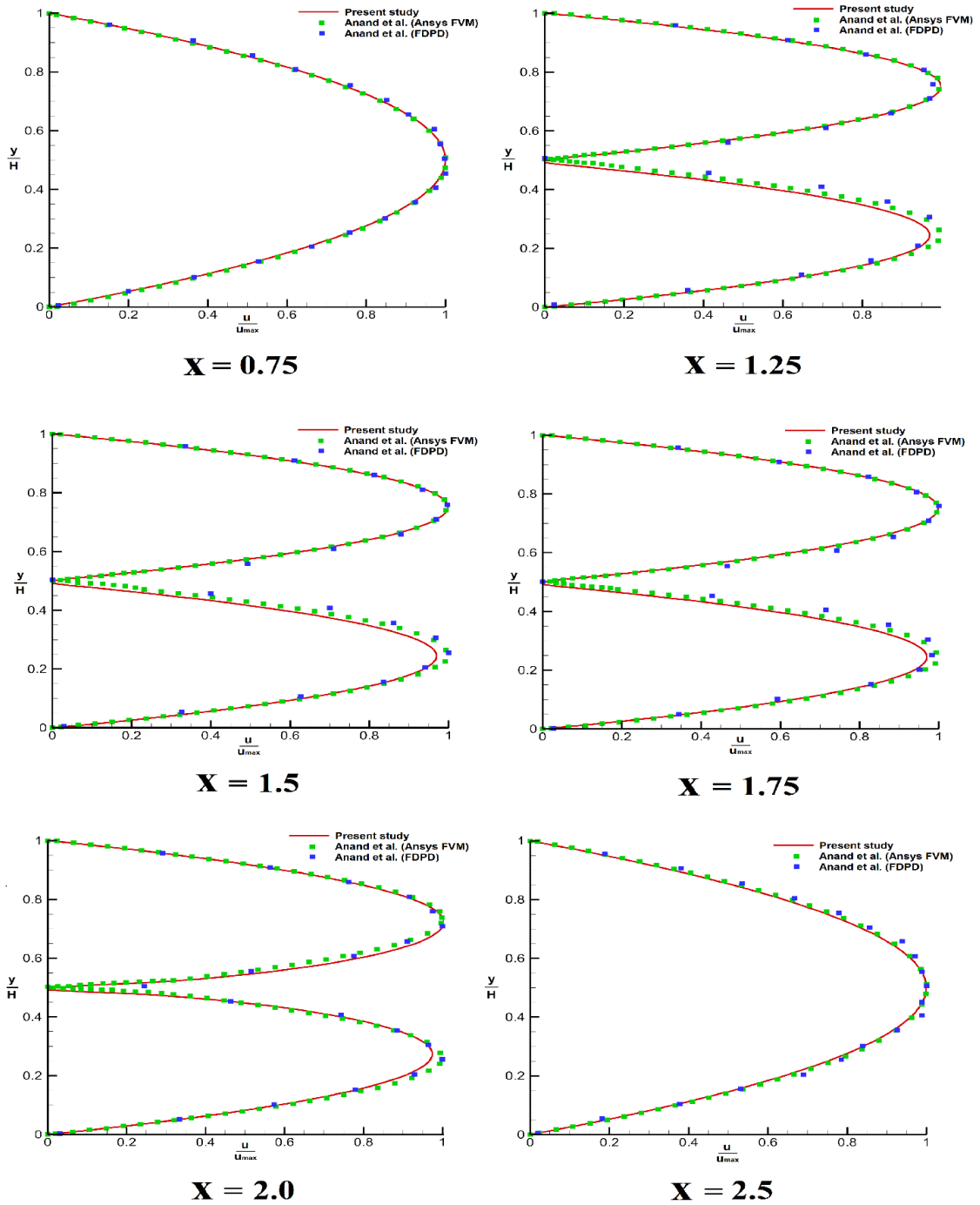
Figure 6.3 Comparison of streamline velocity profiles for $H_y = 0.5$, obtained from present study and (Anand et al. 2016) at different cross sections along the channel length for a rigid membrane.
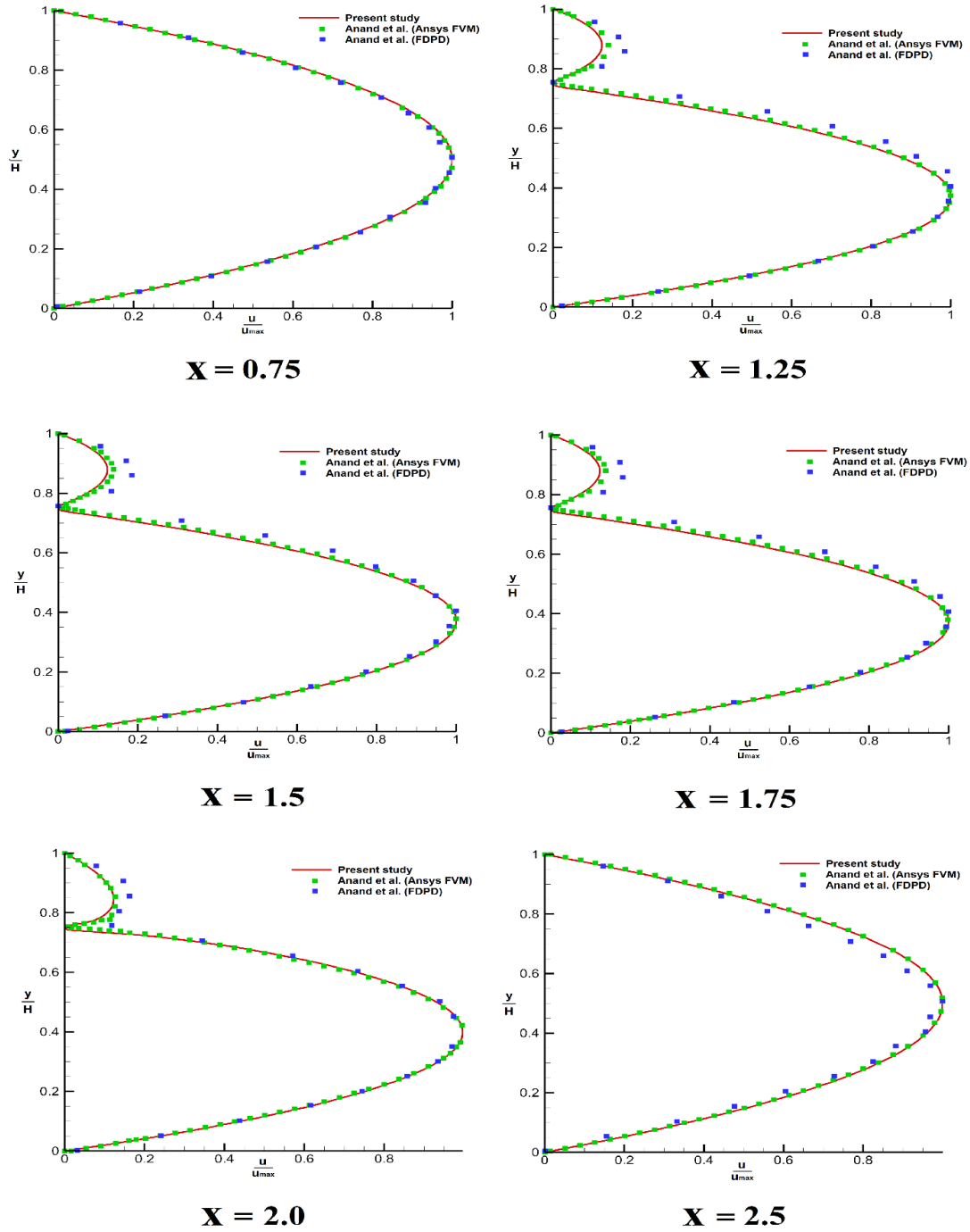
Figure 6.4 Comparison of streamline velocity profiles for $H_y = 0.75$, obtained from present study and (Anand et al. 2016) at different cross sections along the channel length for a rigid membrane.
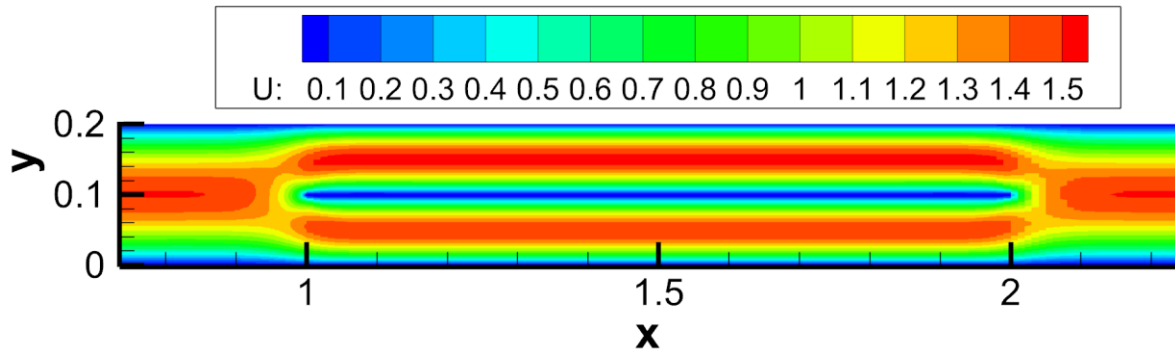
Figure 6.5 Velocity contour plot for rigid membrane placed at channel mid-plane.
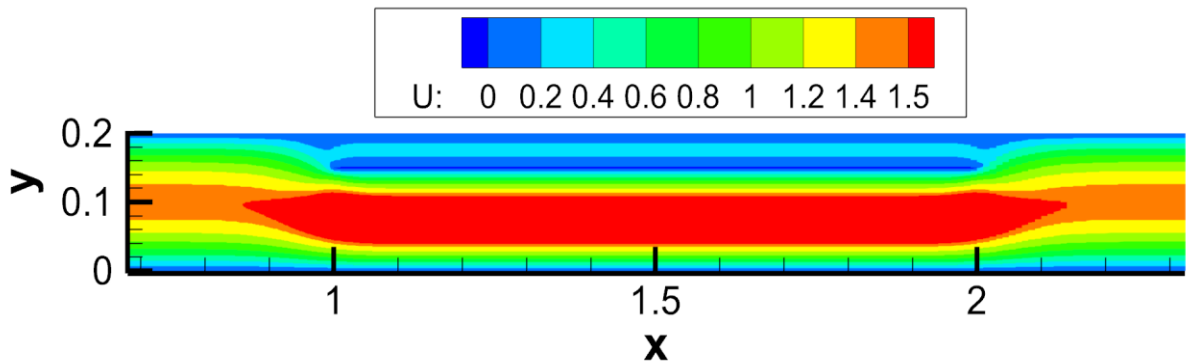
Figure 6.6 Velocity contour plot for rigid membrane placed at channel height H = 0.75.

6.3.2 Membrane deformation in flow

With the conclusion of validation study, two-dimensional numerical simulation using immersed boundary method is carried out to study the behavior of flexible membrane in channel flow. The geometry of the channel is modified such that $L_c = 4.0$ and $H = 1.0$. The initial position where the membrane resides is $L_x = 1.0$. The focus here is to study the impact of low Reynolds number and hence it is fixed as $Re = 1.0$. An inextensible condition is enforced for membrane movement by fixing the extensional stiffness as $K_s = 25000$. From literature it is known that extensional stiffness has negligible effect on membrane deformation but is highly influenced by bending rigidity (Anand et al. 2016). Thus, the extensional stiffness, T is assumed constant throughout the study. The effect of other

141

physical parameters on filament deformation is ascertained with the help of parametric analysis by considering different membrane lengths (L = 0.75, 1.0 and 1.25), bending rigidities (0.1 – 10.0) and membrane positions in channel (H_y = 0.25, 0.5 and 0.75). The total simulation time is fixed at t = 4.0. A brief discussion is given below.

The deformation of flexible membrane due to variation of bending rigidity for fixed location, H_y = 0.25 and three different lengths is captured in Figure 6.7(a) – 6.7(c). The membrane deforms in accordance with bending rigidity such that the one with the highest rigidity, K_b = 10.0 remains undeformed while bending rigidity, K_b = 0.1 buckles the most in the upward direction. As the length of membrane increases from 0.75 to 1.25, there is a progressive increment in buckling for membrane with rigidity, K_b = 1.0. A similar type of membrane deformation but in the downward direction is observed for membranes placed at location, H_y = 0.75 as seen from Figures 6.8(a) – 6.8(c). This deformation mechanism can be understood by taking an example of Figure 6.7(a). There exists mutual interplay between hydrodynamic forces of fluid and elastic forces of membrane. The membrane with rigidity, K_b = 10.0 resists the hydrodynamic stresses acting on its surface. Since the membrane is influenced by extensional and bending properties, the deformations are generated based on hydrodynamic force distribution. Thus, minor conformations for K_b = 1.0 and substantial buckling for K_b = 0.1 is observed.
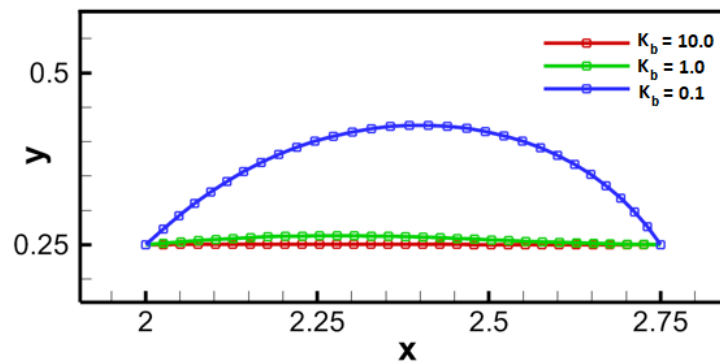
(a) L = 0.75
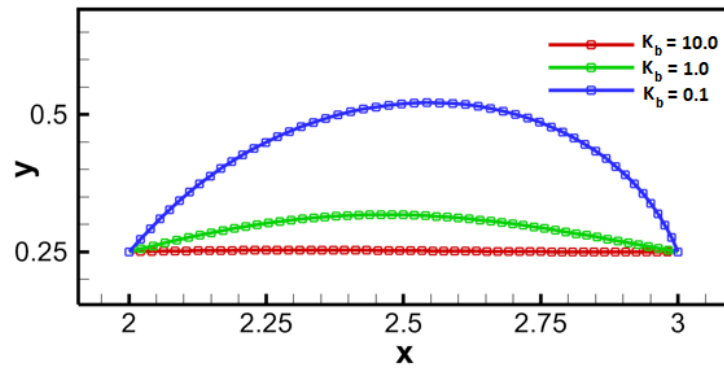
(b) L = 1.0
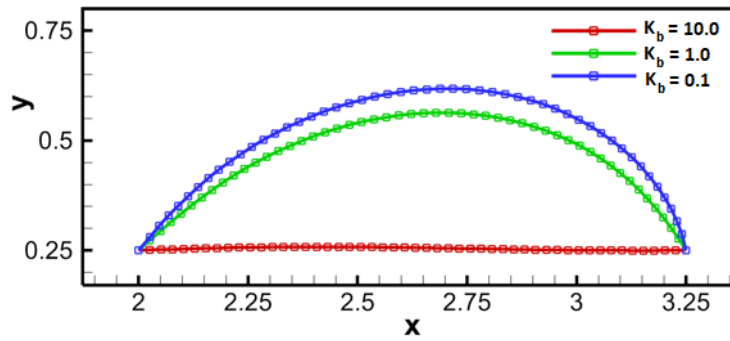
(c) L = 1.25

Figure 6.7 Deformation of flexible membrane at channel height $H_y = 0.25$ for different bending rigidities $K_b = 10.0, 1.0, 0.1$.

(a) L = 0.75

143
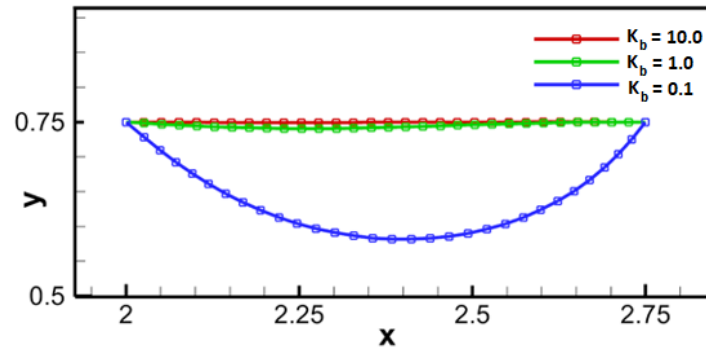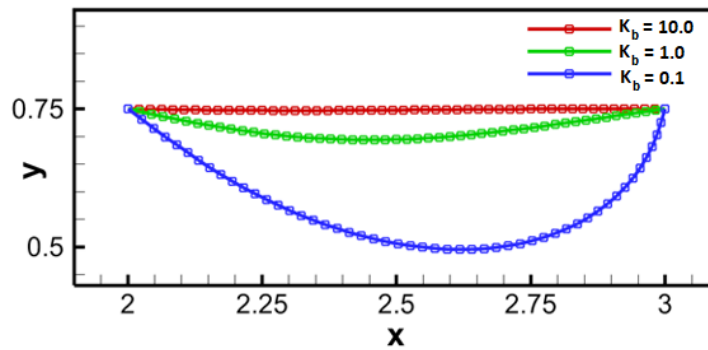
(b) L = 1.0
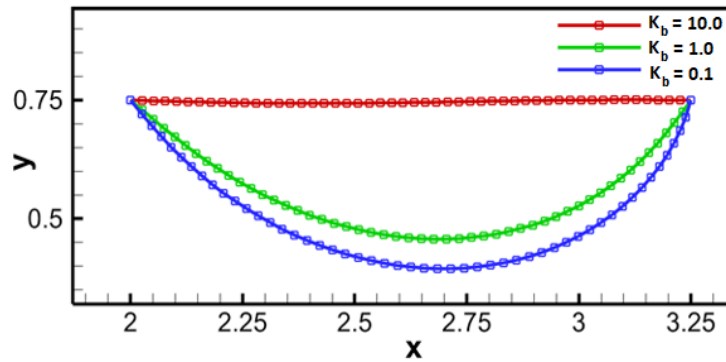
(c) L = 1.25

Figure 6.8 Deformation of flexible membrane at channel height $H_y = 0.75$ for different bending rigidities $K_b = 10.0, 1.0, 0.1$.

The variation in X-component of fluid velocity due to the presence of flexible membrane having length, L = 1.0 at location $H_y = 0.25$ is observed from Figures 6.9(a) – 6.9(c). All figures from 6.9(a) – 6.9(c) depicts the effect of different bending rigidities and its corresponding effect on flow features for the channel cross-sections at x = 2.25, x = 2.5 and x = 2.75 respectively. When comparing Figures 6.9(a) – 6.9(c), the velocity profile is somewhat similar for bending rigidities, $K_b = 10.0$ and $K_b = 1.0$ for all the initial, mid and final membrane portions. However, for rigidity $K_b = 0.1$ case, the velocity profile is different at all membrane portions. There is substantial spike in fluid velocity at the lower

channel section due to large membrane deformations. This also indicates variation in flow rate due to presence of deformable membrane.
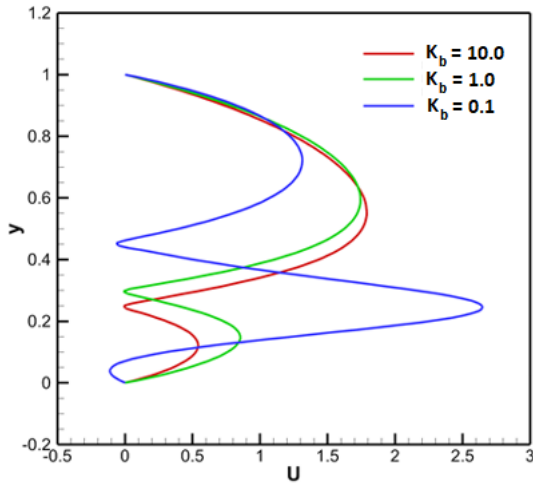
(a) channel x – location = 2.25
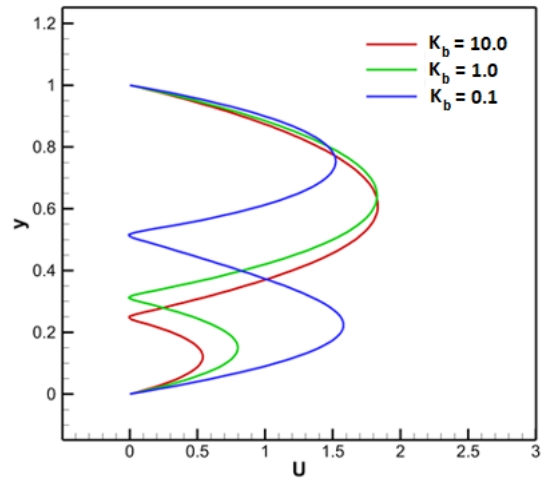
(b) channel x – location = 2.5
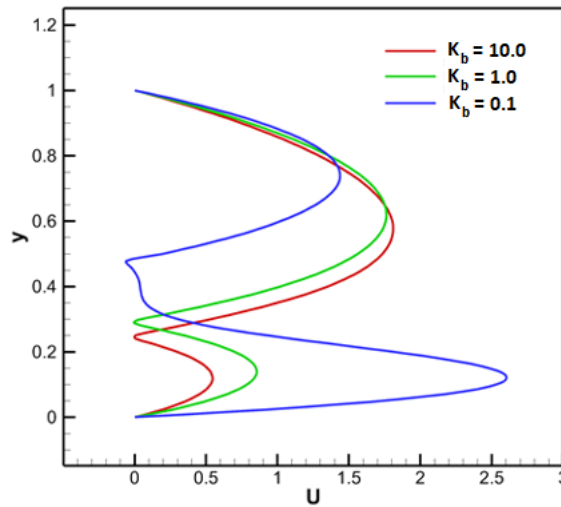
(c) channel x – location = 2.75

Figure 6.9 The effect of membrane deformation and bending rigidity ($H_y = 0.25$, length $L = 1.0$) on fluid flow is determined by plotting velocity profiles for time $t = 3.0$.
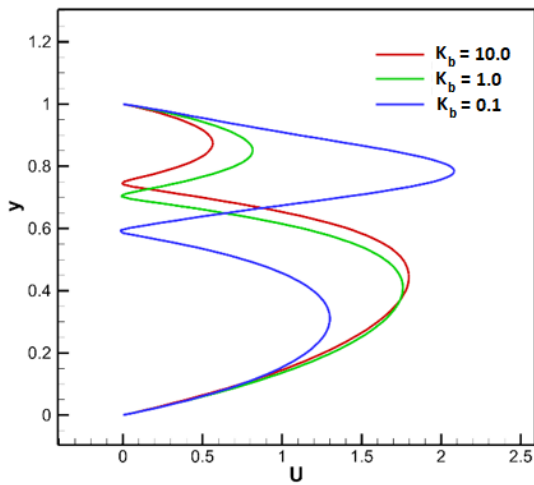
(a) channel x – location = 2.25
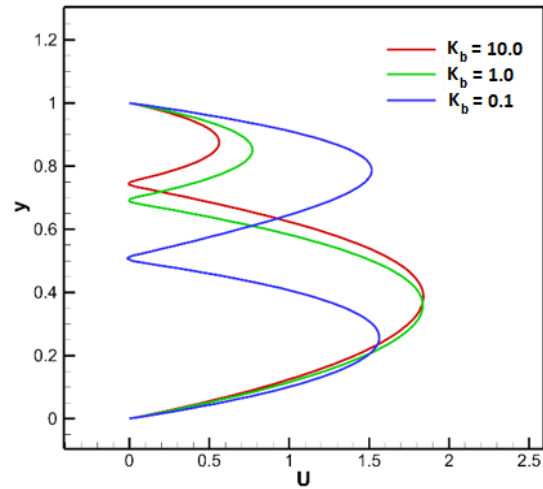
(b) channel x – location = 2.5
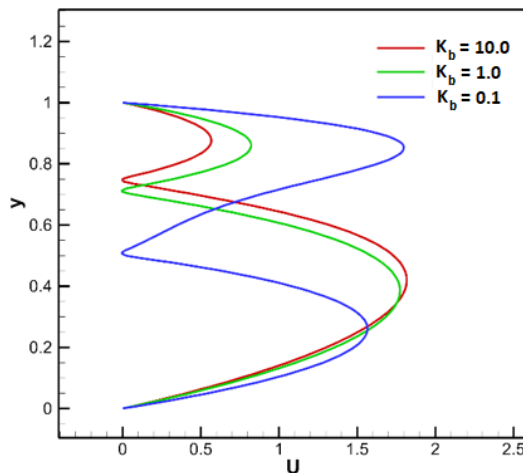
(c) channel x – location = 2.75

Figure 6.10 The effect of membrane deformation and bending rigidity ($H_y = 0.75$, length $L = 1.0$) on fluid flow is determined by plotting velocity profiles for time $t = 3.0$.

Next, the velocity profile is observed for membrane fixed at location $H_y = 0.75$ and compare it for different rigidities as seen in Figures 6.10(a) – 6.10(c). As earlier, velocity spike is seen for the lowest bending rigidity case, $K_b = 0.1$ but in the upper channel section. Thus, it is understood that by placing the membrane at lower channel section in the

direction of fluid motion causes it to deform upwards (Figure 6.7(b)) thereby increasing the flow area in the lower channel sections. Similarly, by placing the membrane at upper channel section causes the membrane to deform downwards (Figure 6.8(b)) and increases the flow rate in the upper channel side. This clearly indicates the possibility of using deformable membranes with varying bending rigidity to control flow rate in channel sections.

Table 6.1 The percentage change in length of membranes of different bending rigidity positioned at different channel heights.

Membrane Length (L)	Membrane position (H_y)	Bending rigidity (B)	Final membrane length	% change in length
0.75	0.25	10.0	0.75	-
		1.0	0.7507	0.0525
		0.1	0.8426	7.8025
	0.75	10.0	0.75	-
		1.0	0.7504	0.0300
		0.1	0.8381	7.3837
1.0	0.25	10.0	1.0	-
		1.0	1.0126	1.2443
		0.1	1.1560	13.4948
	0.75	10.0	1.0	-
		1.0	1.0089	0.8821
		0.1	1.1324	11.6920
1.25	0.25	10.0	1.2502	0.0160
		1.0	1.4266	12.3791
		0.1	1.4664	14.7572
	0.75	10.0	1.2502	0.0160
		1.0	1.4085	11.2531
		0.1	1.4564	14.1719

Next, the percentage change in length of membranes for different bending rigidities placed at varying membrane positions in channel, H_y is given in Table 6.1. All membranes having highest rigidity, $K_b = 10.0$ show negligible deformation. However, for long membrane, L = 1.25 a slight change in length is observed. This indicates that shorter

membranes up to length, $L = 1.0$ can resist deformation in a better way. When the individual membranes of fixed length are compared, it is seen that the membranes placed at lower position, $H_y = 0.25$ have higher percentage change in membrane length as compared to the ones placed at upper position, $H_y = 0.75$. The smallest deformation of 7.38% is seen for membrane length, $L = 0.75$ placed at upper position, $H_y = 0.75$ and highest deformation of 14.75% is observed for membrane length, $L = 1.25$ placed at lower position, $H_y = 0.25$. Both these observations are for lowest bending rigidity, $K_b = 0.1$. The calculation of percentage change in length of membrane for different bending rigidities and membrane length are done for upper and lower positions of membrane in channel (H_y). In these positions, the membrane deforms permanently and never regains their original shape. Thus, it is possible to calculate membrane arc length based on final deformed state.

A self-excited oscillation pattern is seen for membranes having length, $L = 1.0$ and $L = 1.25$ with bending rigidity, $K_b = 0.1$ and placed at position in channel, $H_y = 0.5$. The occurrence of self-excited oscillations or permanent deformed state behavior is observed by capturing flexible membrane deformations at instantaneous time intervals as shown in Figures 6.11(a) – 6.11(c). At different time intervals certain mode shapes are observed which are repetitive in nature thus indicating oscillation. In Figure 6.11(a) instantaneous deformation are recorded for total time $t = 2.0$. At $t = 0.25$, two-third length of the membrane undergoes buckling in the upward direction whereas the lower half deforms downwards. This continues for $t = 0.5$ at which point the entire membrane has buckled in the upward direction. A distinct mode shape is developed with progression in time at $t = 0.75$. This mode shape remains the same for the remainder of the time intervals as seen from $t = 1.0$ to $t = 2.0$ in Figure 6.11(a). It is a case of permanent membrane deformation without any signs of oscillation. The membrane is unable to resist hydrodynamic forces thus resulting in a fixed deformation state.
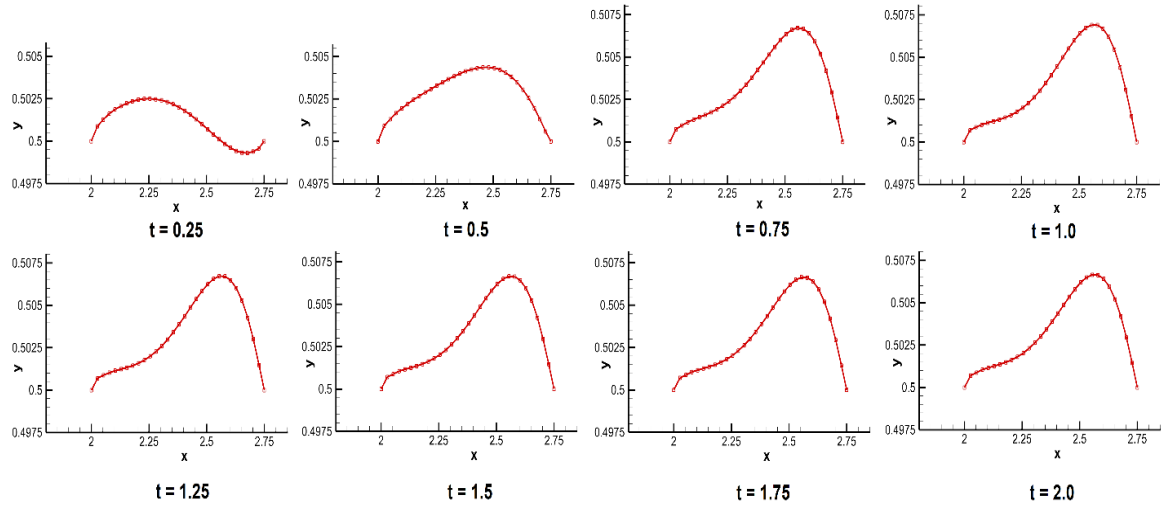
Figure 6.11(a) Deformation of flexible membrane (fixed at $H_y = 0.5$, length $L = 0.75$ and bending rigidity, $K_b = 0.1$) for different time intervals.

Next, deformations for membrane lengths, $L = 1.0$ and $L = 1.25$ as shown in Figure 6.11(b) and Figure 6.11(c) respectively is observed. The instantaneous deformations are captured at fixed time interval of $t = 0.25$. It is seen that the first four-time intervals from $t = 0.25$ to $t = 1.0$ for both Figure 6.11(b) and Figure 6.11(c), produce four different membrane mode conformations. The first shape at $t = 0.25$ involves a trough formation near the trailing edge of the membrane. The second mode shape at $t = 0.5$ consists of crest at the midpoint of the membrane with deep trough near the trailing edge. The third mode conformation at $t = 0.75$ is a flattened portion from leading edge to membrane midpoint and a high crest towards the trailing edge. Finally, the fourth mode shape at $t = 1.0$, contains deep trough at the membrane midpoint with a crest near the trailing edge. These mode shapes keep repeating in the subsequent time intervals from $t = 1.25$ to $t = 2.0$ and also for next time sequences from $t = 2.25$ to $t = 3.0$. This clearly indicates the development of self-excited oscillations in membrane. A dynamic equilibrium existing between the hydrodynamic forces and elastic forces of the membrane is responsible for this behaviour. On one side no such oscillations are seen for membrane length, $L = 0.75$ but on the other a systematic mode shape repetitions for $L = 1.0$ and above. Thus, along with lower bending rigidity and membrane position at channel mid-plane, the membrane length is a very crucial

149

factor for generation of self-excited oscillations in membranes. For this study the critical dimensionless membrane length is found to be L >= 1.0.
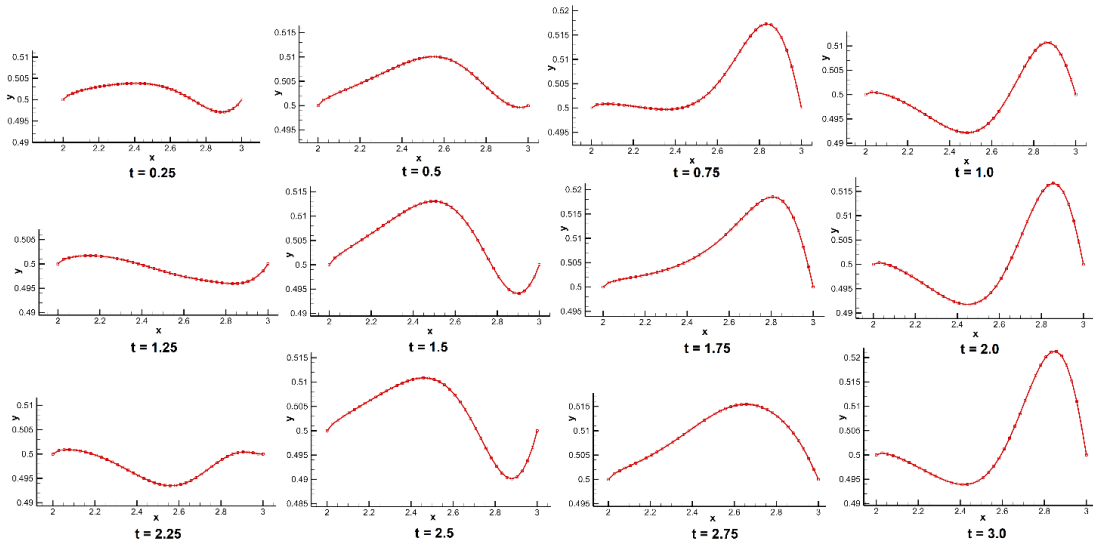
Figure 6.11(b) Deformation of flexible membrane (fixed at $H_y = 0.5$, length L = 1.0 and bending rigidity, $K_b = 0.1$) for different time intervals.
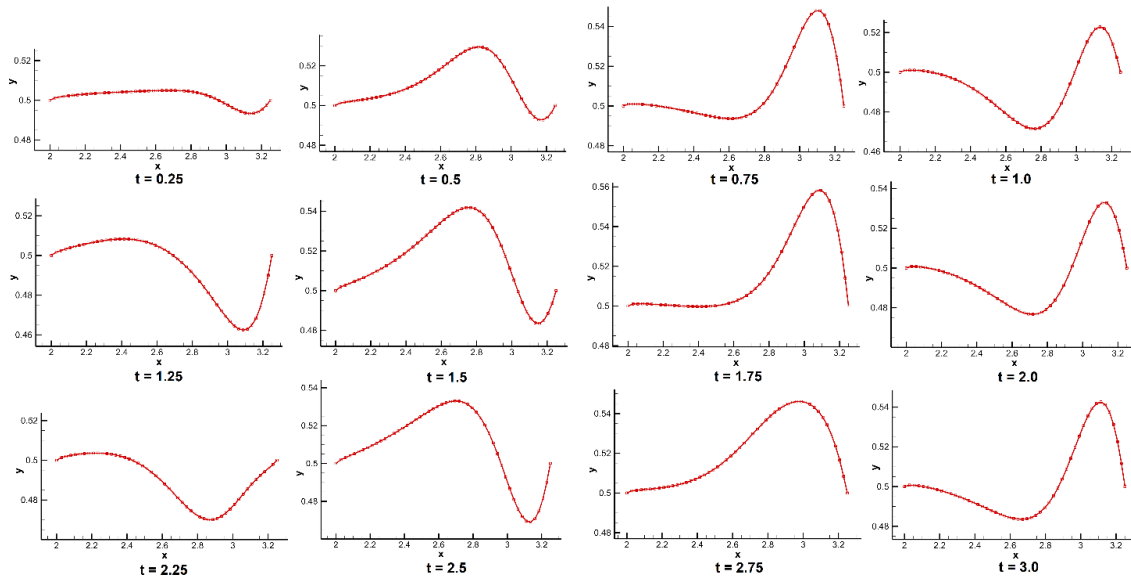
Figure 6.11(c) Deformation of flexible membrane (fixed at $H_y = 0.5$, length L = 1.25 and bending rigidity, $K_b = 0.1$) for different time intervals.

6.3.3 ANN prediction study

In section 6.3.2, the importance of FSI due to the presence of flexible membrane is understood in the two-dimensional channel and its resulting effects on membrane mode conformation and variation in X-component of fluid velocity. Also, in section 6.3.2 parametric analysis involving parameters like membrane length, bending rigidity and membrane position in channel is carried out. The resulting parametric study produced IBM simulation data with flow rate past a deformable membrane calculated for each case. The aim of this section is to develop an ANN model that can effectively predict flow rate for different membrane parameters.

As mentioned earlier, MATLAB is used for the implementation of ANN. The multi-layer network architecture in Figure 6.2 which is used for the prediction of flow rate is configured in MATLAB as shown in Figure 6.12. Before applying ANN, the input and output variables are normalized between 0 and 1 using equation (6.5) given below

$$\text{Normalized data} = \frac{\text{data value} - \text{minimum value}}{\text{maximum value} - \text{minimum value}} \qquad (6.5)$$
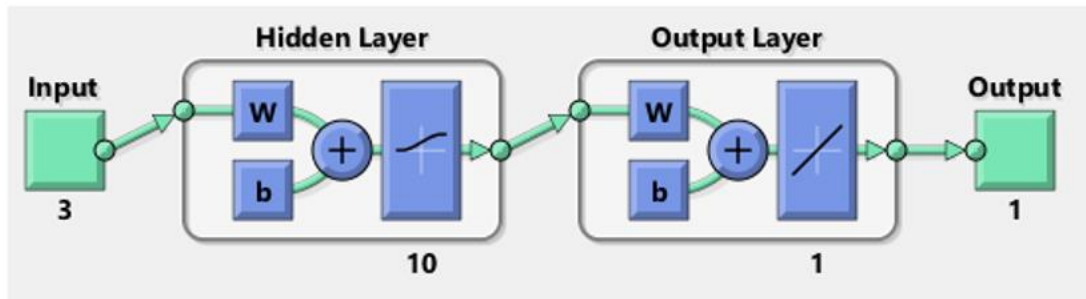
Figure 6.12 Neural network representation, 3-10-1 for the study.

The three input parameters are membrane length, bending rigidity and membrane position in channel. The transfer function used for the hidden layer is logistic sigmoid and linear transfer function is used for output variable. A single variable i.e., flow rate is taken as the output. The flow rate calculated in the present study is the ratio of flow rate between the bottom and top parts of the channel. In the present study, a total of 81 IBM simulation data is collected for developing the ANN model. The data is divided into two parts: training

data and testing data. The network is trained using two-third of the data set and remaining one-third is used for testing. An optimized number of neurons must be chosen for the hidden layer. Almost all non-linear functionality can be predicted by using an optimized number of neurons with one hidden layer (Cybenko 1989). A trial-and-error approach is used to decide the best possible number of neurons for the hidden layer. Since selection of large number of neurons resulted in over-fitting, an optimum neuron number for hidden layer is selected which produced the least mean squared error (MSE) between the sample data and network trained data. The neuron number is thus chosen to be 10. The performance plot is shown in Figure 6.13 and as seen from the figure, the training process stops when the MSE becomes constant.
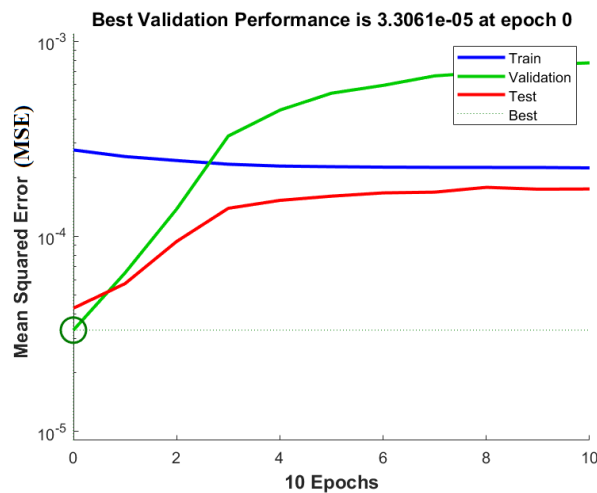
Figure 6.13 Neural network training performance plot.

The relationship between the observed flow rate results and the prediction obtained by ANN are found to vary linearly as shown in Figure 6.14. The value of R^2 (absolute fraction of variance) is 0.99905. Assuming a fit-line model given by $y = ax + b$, it is observed that the co-efficients for the ANN model a and b are approximately equal to 1 and 0. This indicates that the present ANN model has the best prediction capability. Finally, a comparison is provided between the observed flow rate data and predicted data in Figure 6.15. It can be seen that the predicted results from the present ANN model closely resembles that generated by IBM simulations. The ANN architecture as shown in Figure

6.12 can be further used to effectively predict new flow rate values for different input parameters. Thus, ANN can be used as an effective prediction tool for determining flow rate past deformable membranes in two-dimensional channels.
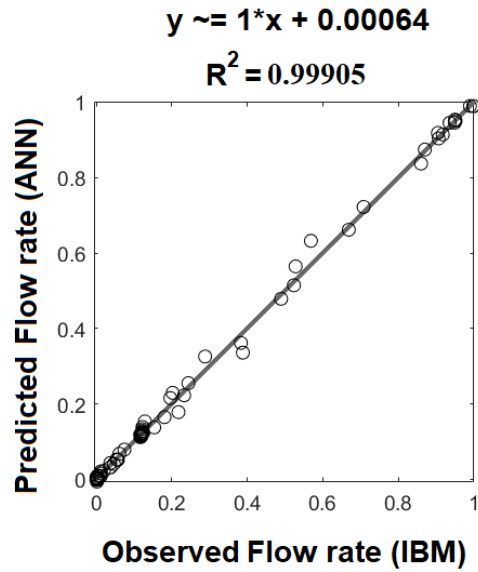
Figure 6.14 Regression plots obtained for the trained neural network.
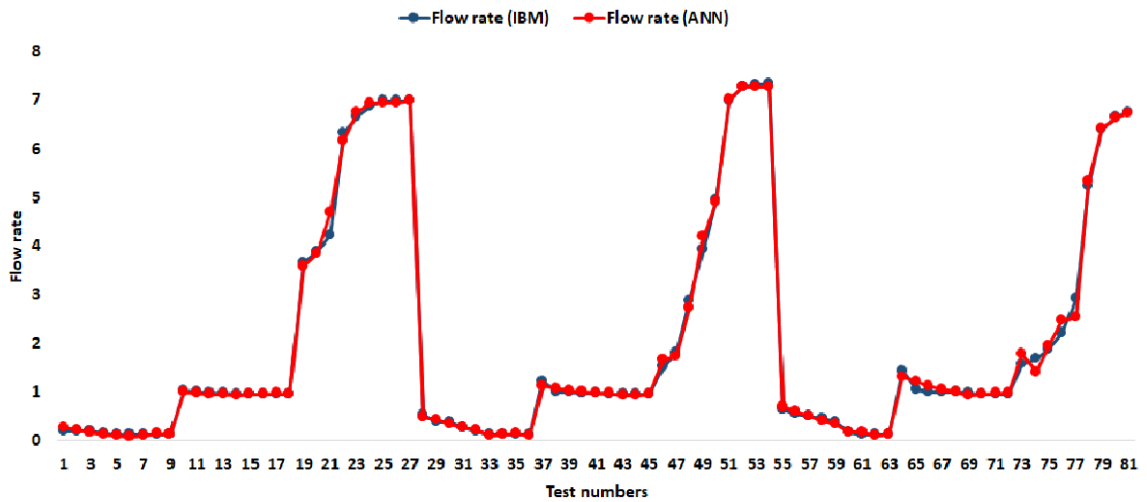
Figure 6.15 Comparison between simulation results and neural network predictions.

Thus the fluid-structure interaction of flexible membrane undergoing self-excited oscillations is studied in the present chapter. Also, an empirical model is developed from artificial neural networks to predict flow rate past the flexible membrane. In the next chapter analysis of the hydrodynamic and mutual interaction of multiple flexible filaments undergoing tumbling and buckling in viscous shear flow is carried out.

CHAPTER 7

7 SIMULATION OF MULTIPLE FLEXIBLE FILAMENTS IN SHEAR FLOW

7.1 Background

There is a growing interest in recent years to analyse the dynamics of flexible filaments in viscous shear flow at low Reynolds numbers. Experimental, numerical and theoretical studies have been carried out by researchers to capture the interaction of flexible filaments in fluid flow Numerical studies of (Slowicka et al. 2015) have shown that fibre dynamics largely depends on filament length, shear rate and bending rigidity. However, the role of filament length needs to be carefully analysed. In categorizing filaments into orbit classes, the main focus in literature was to use non-dimensional variables like bending number or Viscous Flow Forcing (VFF) values which depends on parametric variables. A better filament categorization can be achieved by using a new variable that segregates filament orbits according to the expansion or contraction aspect of filament deformation. Filaments deforming in shear flow tend to undergo periodic tumbling in clockwise or anti-clockwise direction depending on its initial position in the fluid domain. This tumbling motion affects filament migration and successive recuperation behaviour. A detailed analysis is essential in this direction. A very few research work has been carried out in understanding mutual interaction of two filaments placed side-by-side in shear flow. Studying the behaviour or motion of one filament with respect to another is certainly an interesting and novel approach to filament-filament interaction study. The present study focusses on this aspect as well. Further, development of suitable ANN model to predict tumbling counts for two filaments placed side-by-side in shear flow has never been carried out for such low Reynolds number fluid-structure interaction problems. These above mentioned factors serve as the background for the present simulation.

In the present chapter, a two-dimensional numerical model based on an immersed boundary method is employed to capture the hydrodynamic interaction of multiple flexible filaments in shear flow. A parametric analysis is carried out by varying filament length,

bending rigidity and shear rate. From the IBM simulation results an ANN prediction model is developed. The numerical method and ANN model developed for this study is provided in section 7.2. The simulation results and details regarding filament deformation along with ANN prediction study are provided in section 7.3.

7.2 Mathematical formulation and numerical procedure

The numerical procedure of the immersed boundary formulation along with detailed step-by-step description of its implementation has been explained in section 4.2 of chapter 4. The IBM formulation provided in section 4.2 is applied for the present work. The ANN architecture for the present study is provided in Figure 7.1. Also, the implementation of artificial neural networks is done in MATLAB and the governing equations for prediction model development used in the present study is identical to that explained in section 6.2.2.
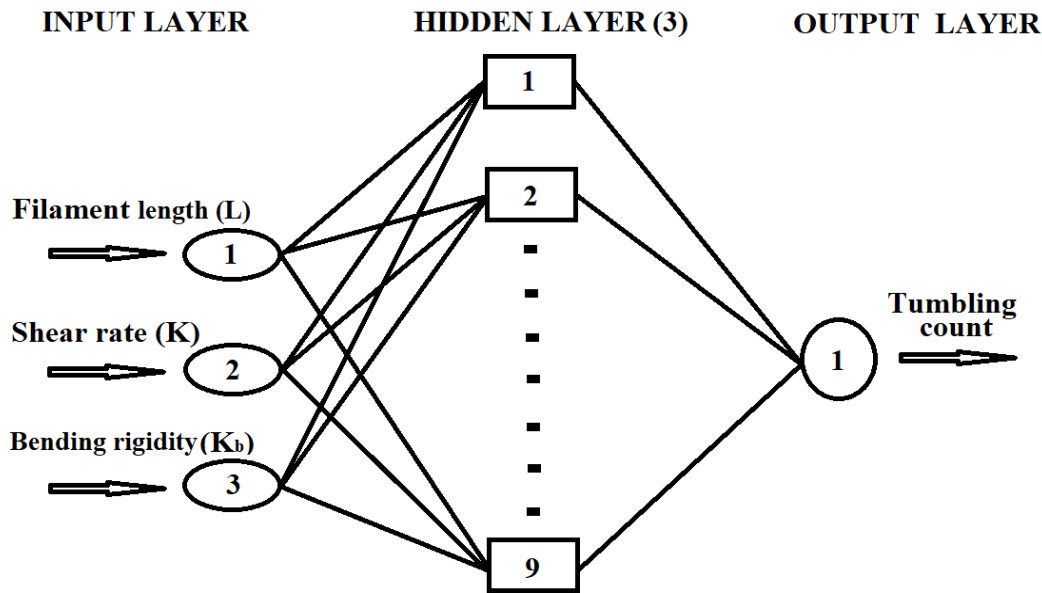
Figure 7.1 The ANN architecture used for the prediction of tumbling count.

7.3 Results and discussion

7.3.1 Two filaments placed side-by-side in shear flow

The focus of the present work is to study two filaments placed side-by-side in shear flow and also to analyse their deformation and mutual interaction. In this direction, two-dimensional numerical simulations are carried out. Two flexible filaments placed freely in channel and being subjected to viscous shear flow is depicted in Figure 7.2. The angle made by the filaments with respect to the vertical is taken as α. The dimensional physical parameters including channel dimensions, fluid properties and filament stiffness values which were considered in Chapter 4, section 4.3.2 and Table 4.3 is taken as reference for the present work and is provided in Table 7.1.
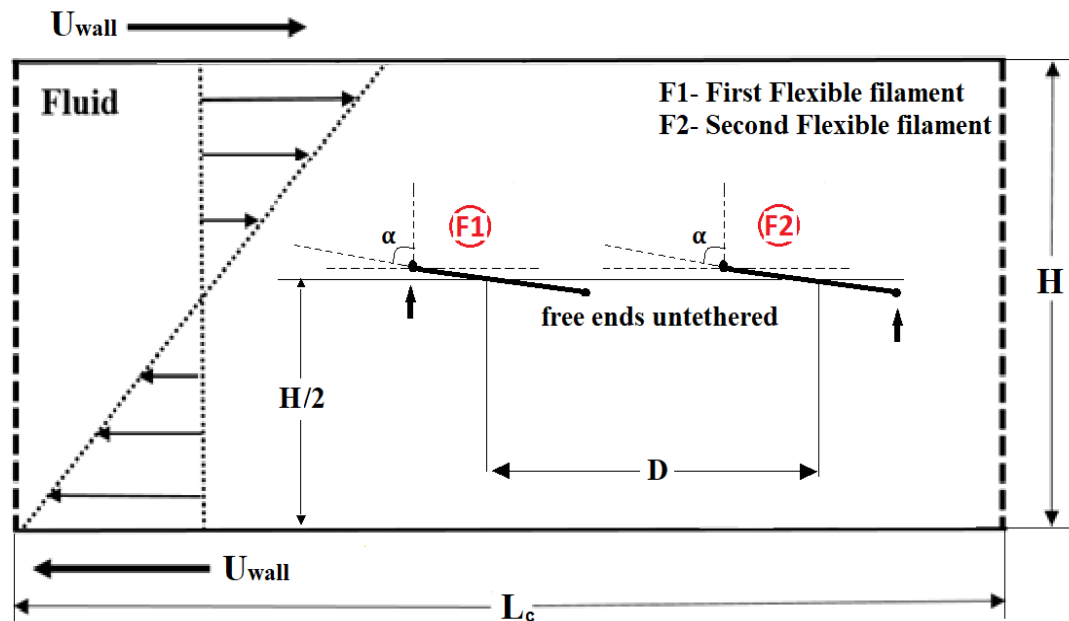
Figure 7.2 Schematic diagram of two flexible filaments placed untethered in viscous shear flow. Similar boundary conditions as specified in Figure 4.4.

Table 7.1 Physical parameters used for two filaments in shear flow simulation study

Physical parameters	Dimensional values
Channel height (H*)	0.5 cm
Channel width (L_c*)	2.0 cm
Fluid Density (ρ)	1.0 g/cm^3
Fluid Viscosity (μ)	8 – 10 g/cm.s
Shear rate (G*)	8 – 64 /s
Filament length (L*)	0.1 – 0.3 cm
Bending rigidity (K_b*)	1.0 – 5.0 × 10^{-4} g.cm^3/s^2
Distance between filament mid-points (D*)	0.3 cm

The filaments are initially placed at an inclination angle of 5° in order to bring about asymmetry in filament motion. Also, grid refinement study and filament inextensibility tests have been carried out in Chapter 4, section 4.3.1. Accordingly a grid size of 512 × 128 is chosen. The filament which consists of 100 IB points is made inextensible by assuming a large value of stretching co-efficient. The physical parameters are non-dimensionalized with respect to characteristic length and velocity. The dimensionless filament length, shear rate, and bending rigidity are given as L, K, and K_b respectively. The two filaments are placed side-by-side separated by a dimensionless distance D, which is defined as the horizontal distance between two filament mid-points. For the present study, D = 0.3 is chosen and the total simulation time, t = 3.0.

A detailed parametric study is carried out for three filament lengths (L = 0.1, 0.2, 0.3), three shear rates (K = 10, 16, 32) and 16 different values of bending rigidity. This results in a total of 144 parametric test cases. A dimensionless parameter called Viscous Flow Forcing value (VFF) is used to quantify viscous drag effects of the fluid with respect to filament elastic forces which is given in equation (7.1) as,

$$\text{VFF} = \frac{\mu G^*(L^*)^3}{K_b^*} \qquad\qquad (7.1)$$

where, $K_b^* = EI$ is the bending rigidity such that, E is Young's modulus of filament material, and I is the moment of area in the bending plane. The Viscous Flow Forcing value is related to the viscosity of the fluid, length of the filament, shear rate and bending rigidity of the filament.

For each of the parametric cases mentioned earlier, Viscous Flow Forcing (VFF) value is calculated and an additional term called exterior angle (β) is also determined. More details on the definition of exterior angle (β) and how to calculate it can be found in (Stockie and Green 1998) and in Chapter 4, section 4.3.2 and Figure 4.9. The exterior angle (β) is also used to categorize filament deformations into various regimes. The most common filament regimes in shear flow are: 1) Rigid, 2) Springy, 3) C-shape, 4) S-shape and 5) Complex. In Chapter 4, section 4.3.2 and Figure 4.10 filament orbit classes were categorized based on VFF values for dimensionless filament length, $L = 0.1$. This demarcation procedure was found to match perfectly well with previous experimental and numerical studies (Forgacs and Mason 1959; Stockie and Green 1998; Weins and Stockie 2015). The study is extend to observe filament orbit classes for two filaments placed side-by-side. Figure 7.3 depicts various filament orbit classes for filament length, $L = 0.3$, shear rate $K = 16$ and four different bending rigidities. The snapshots of filament motions are captured at time, $t = 0.5$ for all cases. Rigid motion is observed for high rigidity case ($K_b = 1.0$) as shown in Figure 7.3(a). The filament undergo rotation from initial inclined position and remains straight in an undeformed manner. Two large recirculation zones are formed, one at the leading edge of the first filament and another at the trailing edge of second filament. As the bending rigidity is reduced to $K_b = 0.5$ (Figure 7.3(b)), the filaments undergo bending in the centre to develop springy deformation. The large recirculation zones associated with their respective filaments are shifted to the centre of the filament. For both rigid and springy deformation regimes, the motion of both the filaments are identical with respect to changing time. Next, when the rigidity of the filament is lowered to $K_b = 0.05$ as shown in Figure 7.3(c), the deformation of both the first and second

filaments are different. The first filament produces C-shape motion while the second filament produces S-shape.

(a) Rigid ($K_b = 1.0$)

(b) Springy ($K_b = 0.5$)

(c) C-shape and S-shape ($K_b = 0.05$)

(d) Complex ($K_b = 0.01$)
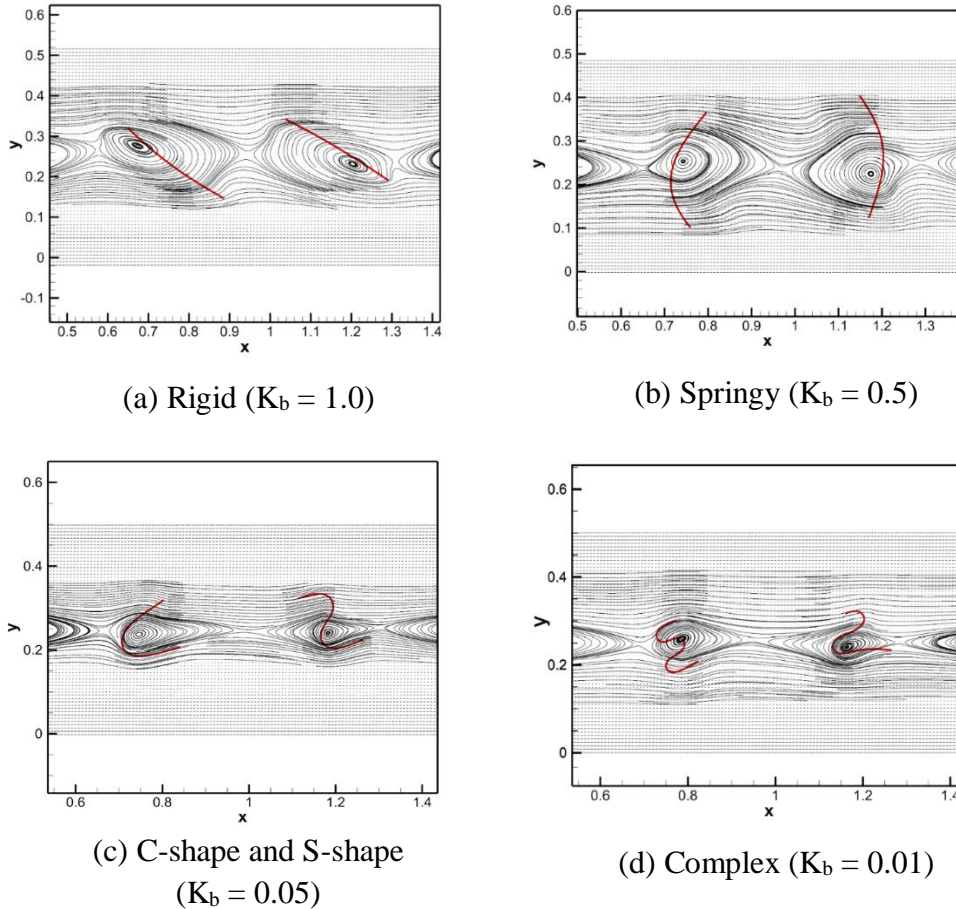
Figure 7.3 Various filament orbit classes and fluid flow streamlines for two filaments placed side-by-side in shear flow for parametric test case (L=0.3, K=16)

The centre of the recirculation zone for first filament undergoing C-Shape motion is at a small distance from the filament surface. This is in contrast to rigid and springy case where the centre of recirculation zone is close to filament surface. Also, the shape of recirculation zone for S-Shape deformation is found to be elliptical. Finally, the deformation of the filament for low rigidity $K_b = 0.01$ producing complex shapes is shown in Figure 7.4(d). The size of the recirculation is also smaller as compared to Figures 7.3(a) and 7.3(b). The formation of various shapes is clearly attributed to the reducing bending

rigidities of the filaments. Thus it can be seen that as bending rigidity reduces the filaments can no longer resist the hydrodynamics stresses and tend to align itself with the flow. It also demonstrates that the rotation of the filaments have a significant impact on the surrounding fluid flow.

The filament dynamics can be further analysed by calculating fractional contraction value as defined in equation (7.2). It will also help in understanding the mutual interaction effect between the two filaments.

$$\text{fractional contraction} = \left| 1 - \frac{\Delta L}{L} \right| \tag{7.2}$$

where, ΔL = change in length due to filament contraction, L = actual filament length. The term fractional contraction is indicative of the compressive state of the filament with respect to initial filament length. Figure 7.4 and Figure 7.5 plots the various filament regimes and fractional contraction values with respect to VFF for $L = 0.1$. The filament regimes for both the first and second filament are provided here. The regime overlap between the first and second filament indicates that the filaments deform identically for a particular bending rigidity and VFF values. In Figure 7.4 it is seen that the springy motion of second filament is spread towards the rigid side of first filament for bending rigidity values close to 1.0 and VFF values in the range close to 0.1. This points out the difference in shape formations between the first and second filament. In Figure 7.5 it is noted that the rigid filaments tend to have lowest contraction since they deform the least whereas contraction values steadily increase for springy, C-shape and complex regimes. For all the 48 test cases plotted in Figure 7.5, a large portion of filament deformation lies in rigid and springy zone for both filaments. Also, filaments having contraction value above 0.6 fall under C-shape and complex orbits.
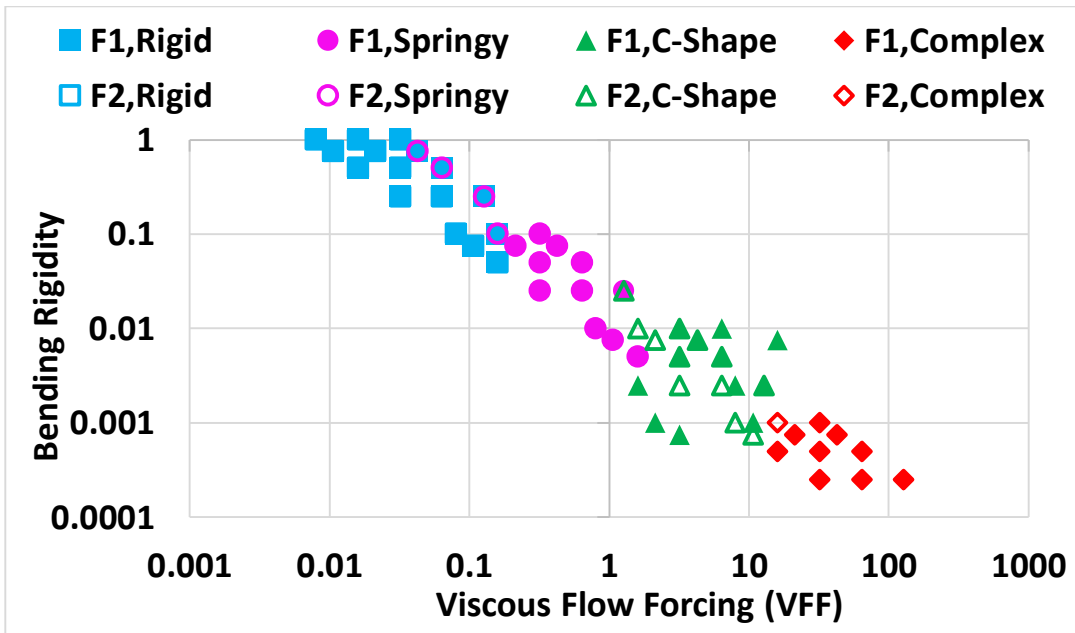
Figure 7.4 Classification of multiple flexible filament deformations for filament length, L = 0.1 into various orbit classes shapes.
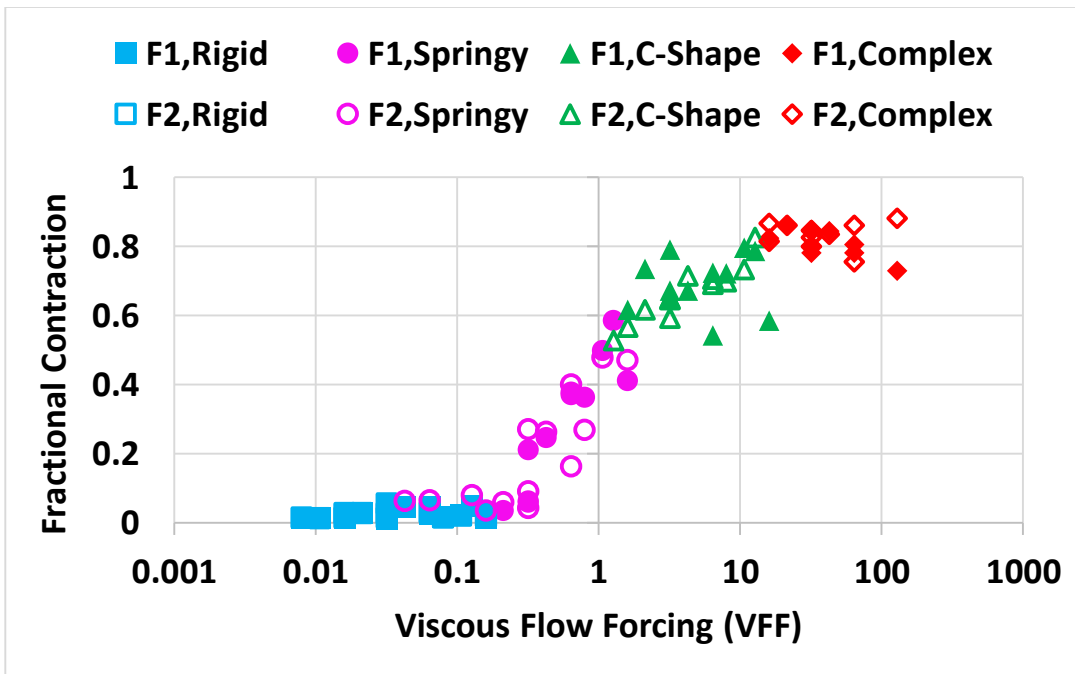
Figure 7.5 The distribution of various filament orbit classes with respect to fractional contraction and viscous flow forcing (VFF) for filament length, L = 0.1.

162

The classification of flexible filaments into different regimes and its distribution with respect to fractional contraction for filament length, L = 0.2 is shown in Figure 7.6 and Figure 7.7 respectively. In Figure 7.6, pronounced formation of C-shape and complex regimes as compared to rigid case are observed. A large band of deformations lie in C-shape zone. Two springy orbits each of second filament can be found in rigid and C-shape zones.
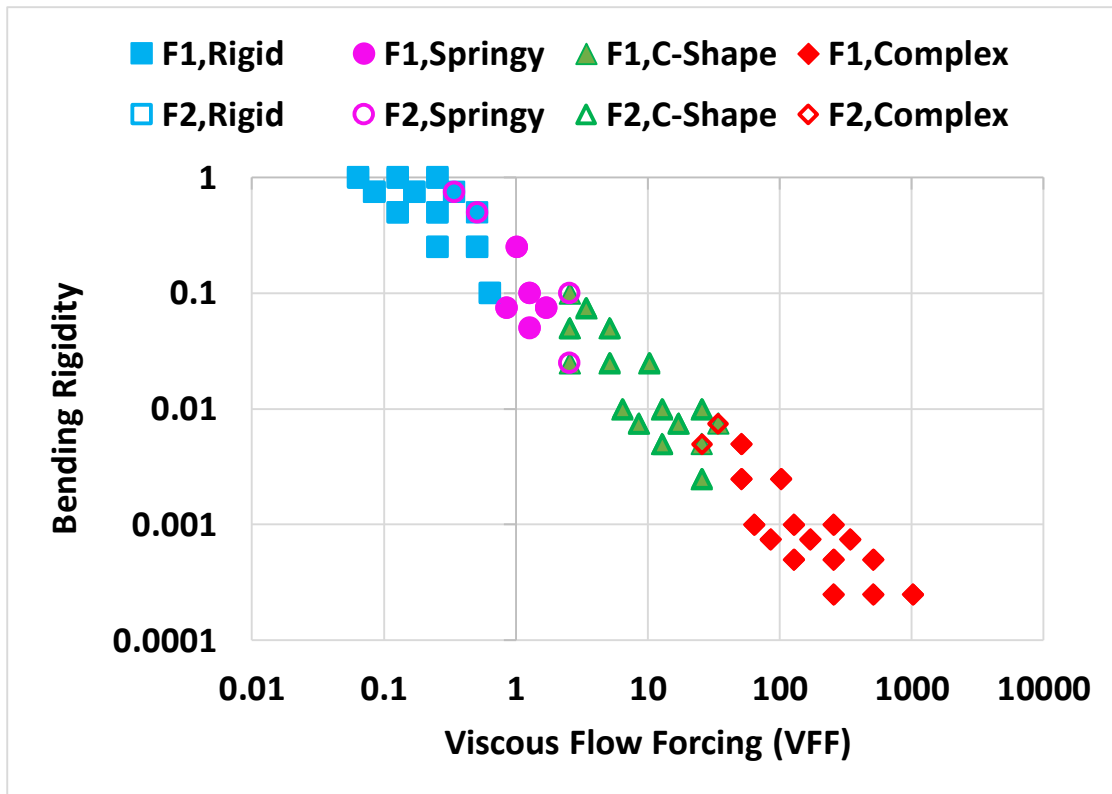
Figure 7.6 Classification of multiple flexible filament deformations for filament length, L = 0.2 into various orbit classes like Rigid, Springy, C – Shape and Complex shapes.

The fractional contraction values dividing springy and C-shape deformation is found to be 0.5 as seen in Figure 7.7. Filaments having fractional contraction values greater than 0.8 and VFF value higher than 60 can be easily grouped into complex regime. This clearly demonstrates that fractional contraction can be further used to assist classification of filament deformation orbits. Figure 7.8 shows the classification of filament orbits for length, L = 0.3. As observed a large portion of filament deformation lies in C-shape and

complex category. Only 5 test cases show rigid motion. All filament regimes show overlap between the first and second filament. Thus for filament length, L = 0.3 there is identical behaviour between the two filaments.
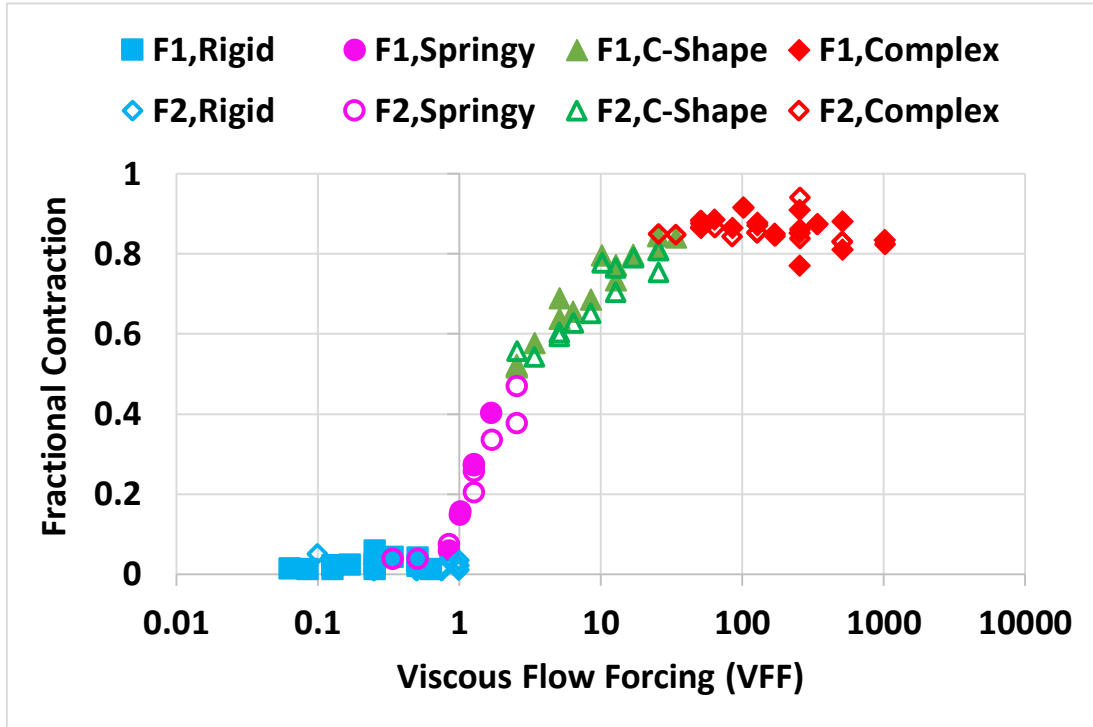
Figure 7.7 The distribution of various filament orbit classes with respect to fractional contraction and viscous flow forcing (VFF) for filament length, L = 0.2.

A large band of complex shape formations can be seen as well in Figure 7.9 which depict filament orbit distribution according to fractional contraction. The average contraction value for rigid motion is close to zero whereas for complex shape it is one. The average contraction value for springy deformation is approximately 0.3 and that for C-shape is 0.7. In Figure 7.9, it is also noted that for the same set of VFF values, the first filament shows an overall level of higher contraction as compared to second filament for all regimes.
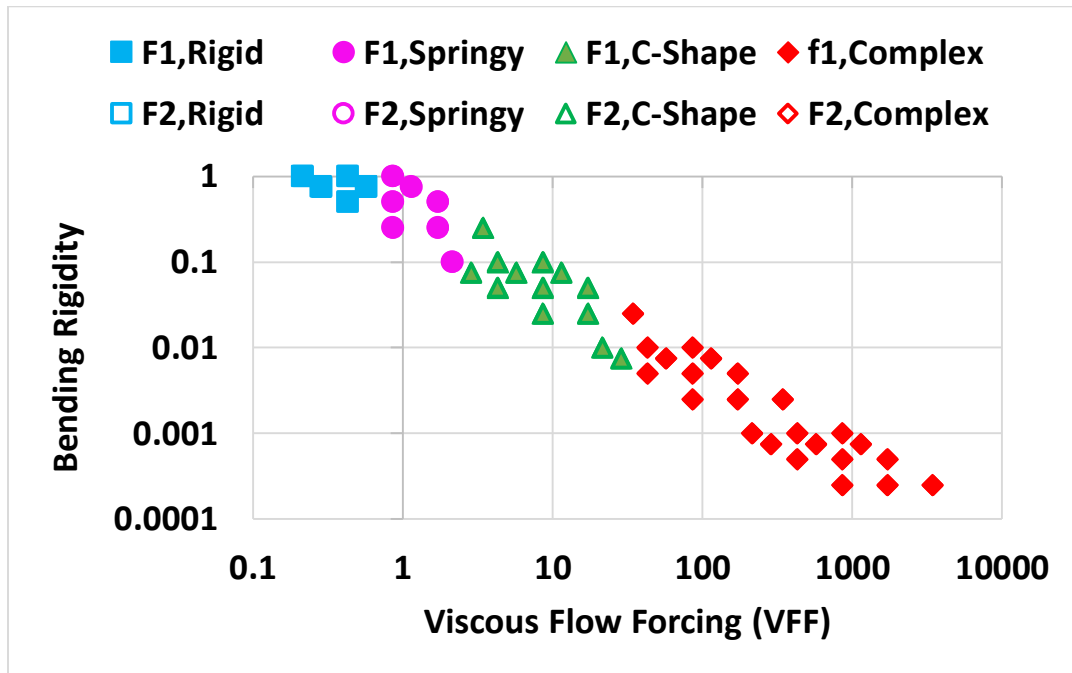
Figure 7.8 Classification of multiple flexible filament deformations for filament length, L = 0.3 into various orbit classes
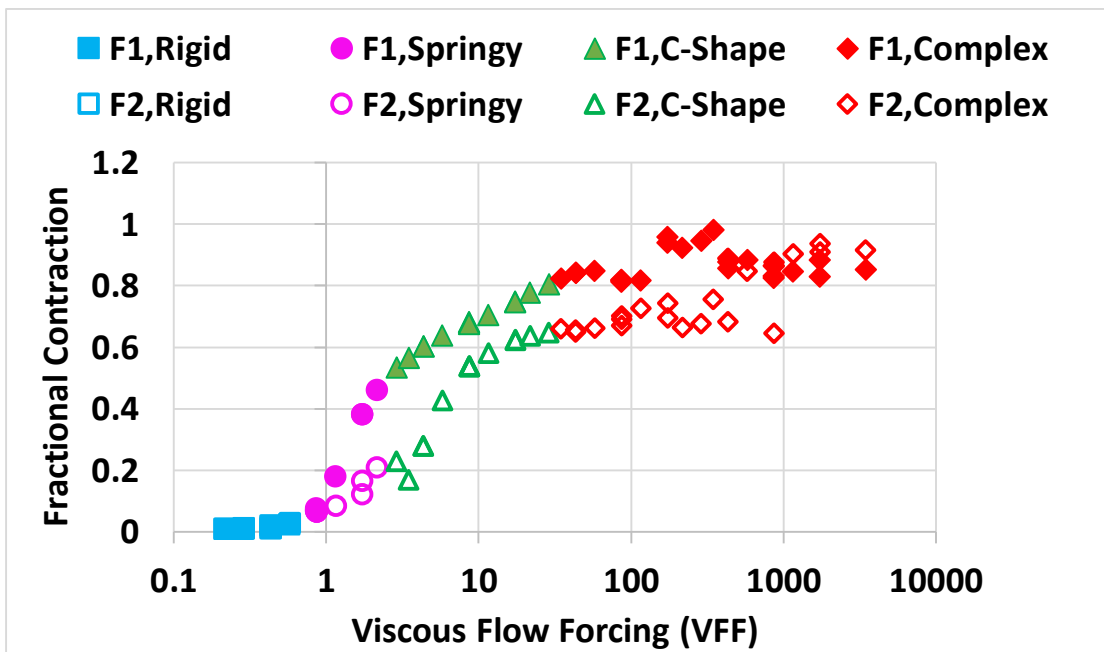
Figure 7.9 The distribution of various filament orbit classes with respect to fractional contraction and viscous flow forcing (VFF) for filament length, L = 0.3.

As the filaments deform in shear flow they also tend to tumble (rotate about their own axis). The amount of tumbling versus bending rigidity achieved by both the filaments for fixed filament length, L = 0.3 and three different shear rates (K = 10, 16 and 32) is plotted in Figures 7.10 – 7.12.
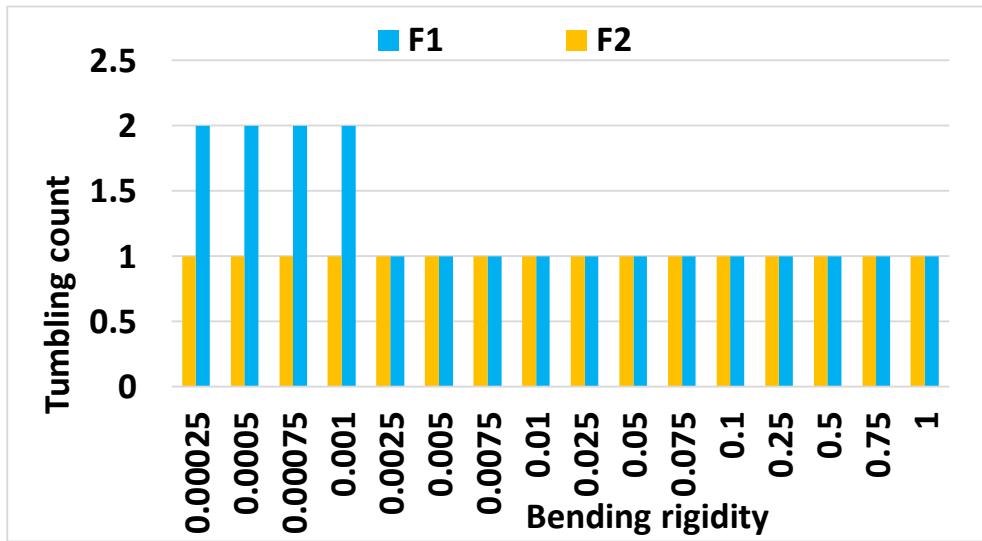
Figure 7.10 Tumbling count comparison between first and second filament with respect to bending rigidity for filament length, L = 0.3 and shear rate, K = 10.
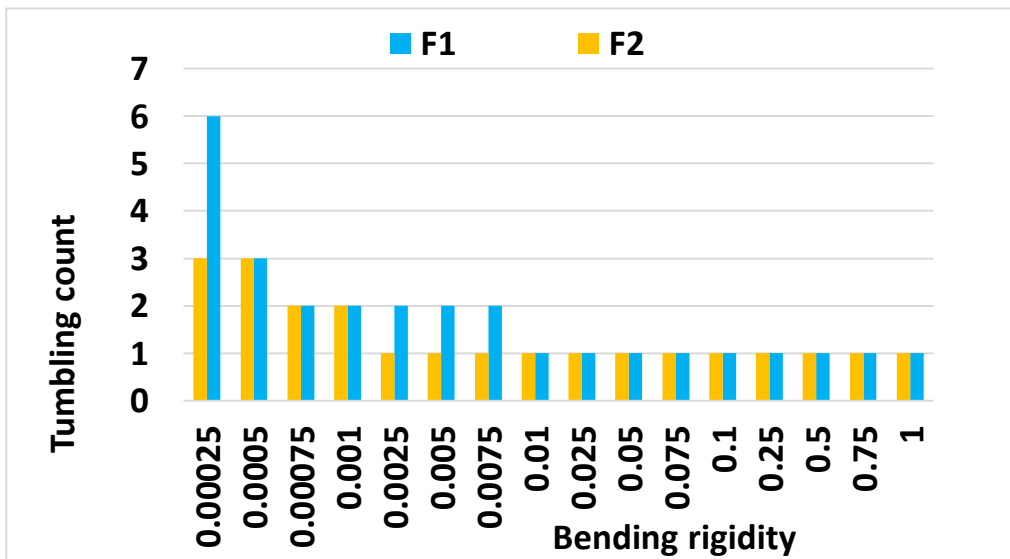
Figure 7.11 Tumbling count comparison between first and second filament with respect to bending rigidity for filament length, L = 0.3 and shear rate, K = 16.
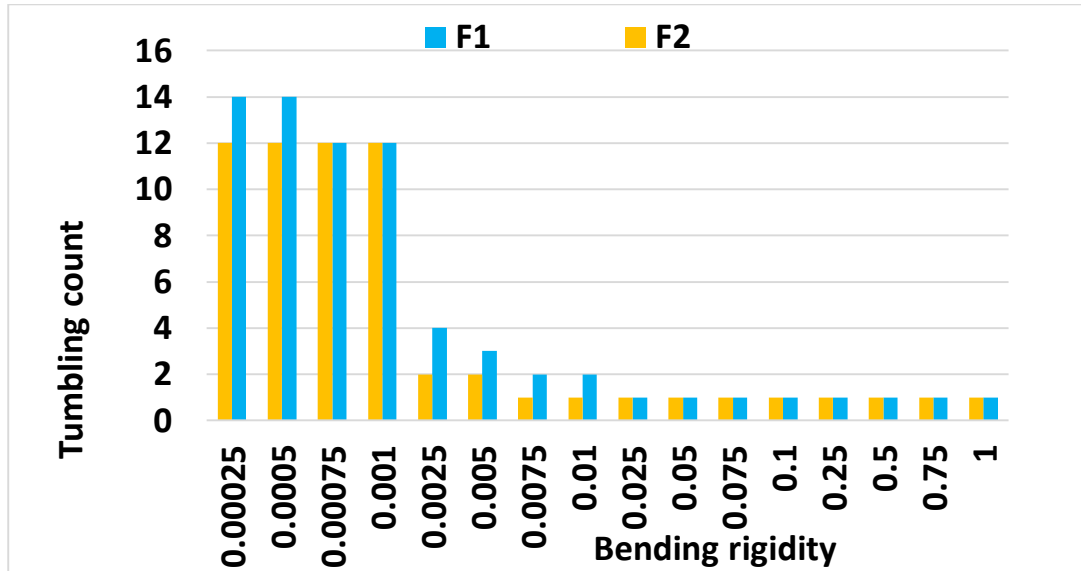
Figure 7.12 Tumbling count comparison between first and second filament with respect to bending rigidity for filament length, L = 0.3 and shear rate, K = 32.

For all the cases it is observed that the tumbling count is greater for first filament as compared to second. This also indicates that the motion of first filament hinders the movement of fluid around the second filament. However, these observation are seen only for filaments subjected to lower rigidity cases ($K_b \leq 0.025$). The filaments with higher rigidity ($K_b \geq 0.025$) tend to tumble with similar frequency. Keeping this aspect in mind the tumbling behaviour of first filament only is analysed for different lengths and different shear rates. This tumbling motion is recorded for the total simulation time and plotted with respect to bending rigidity in Figures 7.13 – 7.14. The highest tumbling count of 22 is observed for L = 0.1 in Figure 7.13. The magnitude of tumbling increase as shear rate increases and bending rigidity decreases. At lower rigidity, the filament offers least resistance to shear flow and thus undergoes tumbling frequently. The effect of shear rate on tumbling count and bending rigidity for filament length, L = 0.2 is shown in Figure 7.14. A similar pattern as observed in Figure 7.13 is also seen here. However, the tumbling count magnitude is reduced to 18. The tumbling count and its relationship with bending rigidity and shear rate for filament length, L = 0.3 is shown in Figure 7.15. The highest tumbling count magnitude observed for this case is 14.
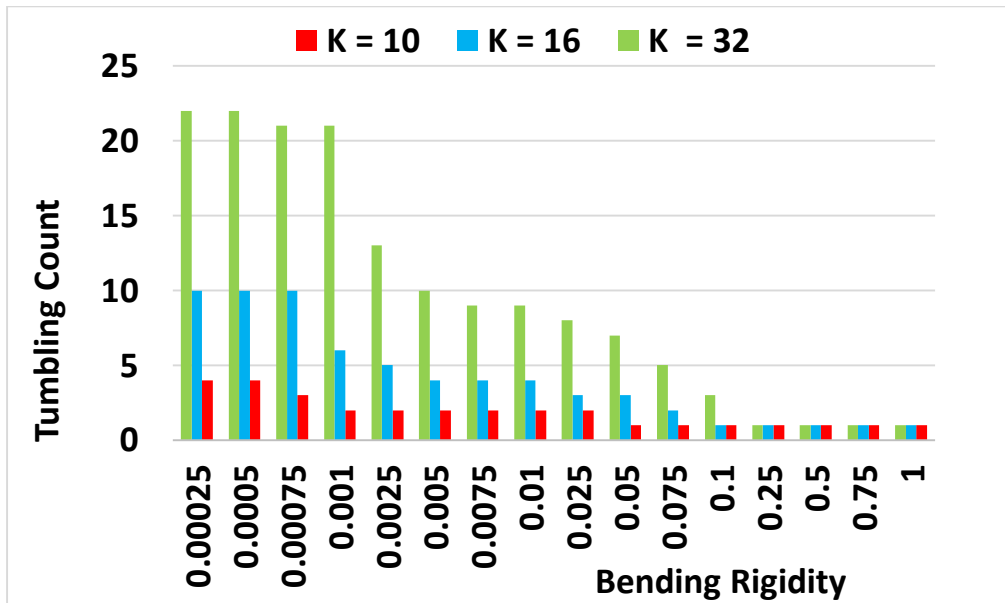
Figure 7.13 Effect of varying shear rate on tumbling count and bending rigidity for filament length, L = 0.1.
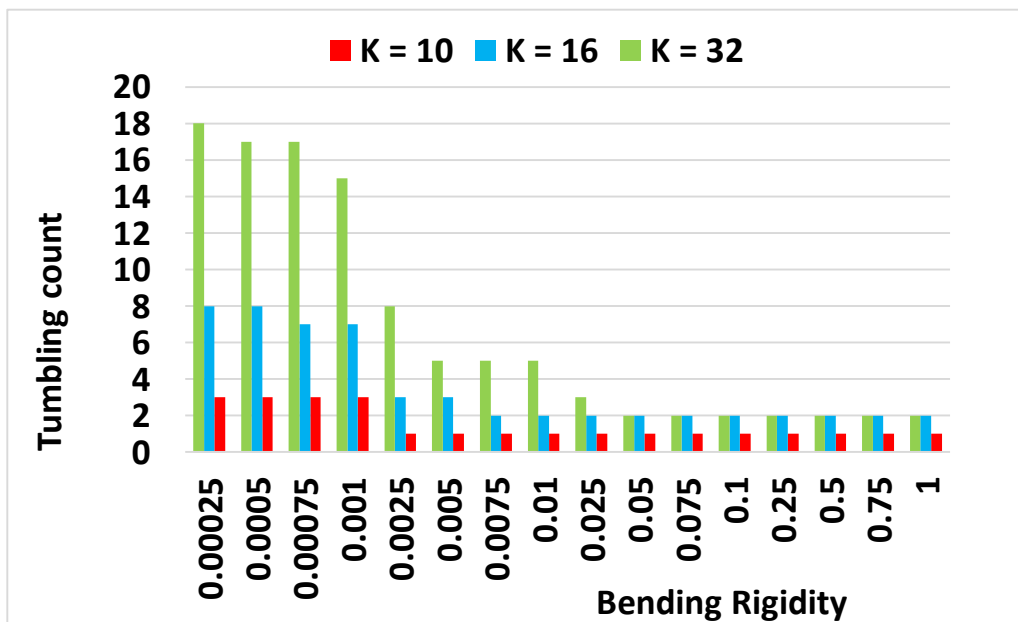
Figure 7.14 Effect of varying shear rate on tumbling count and bending rigidity for filament length, L = 0.2.

168
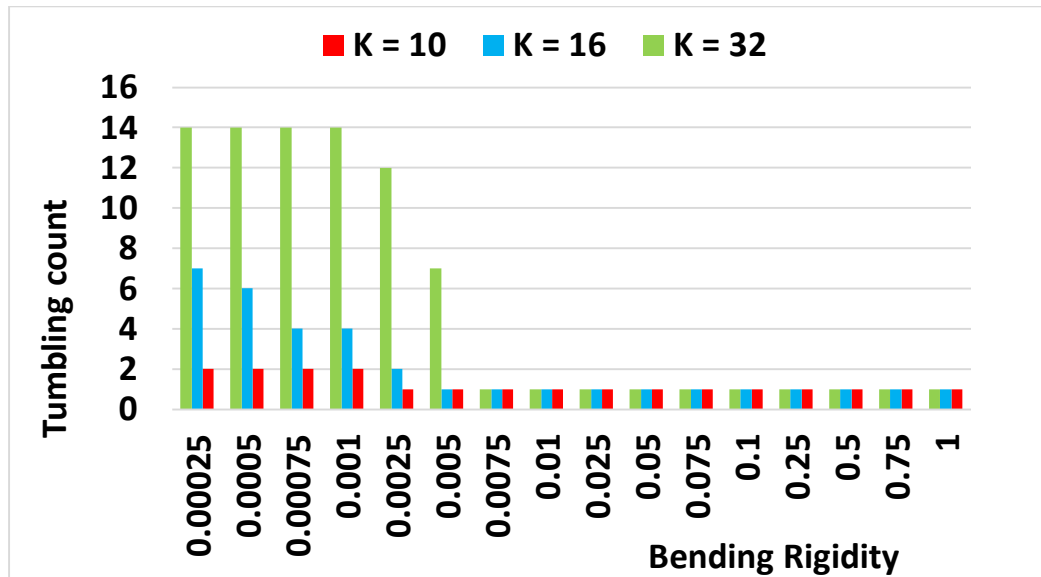
Figure 7.15 Effect of varying shear rate on tumbling count and bending rigidity for filament length, L = 0.3.

From the above discussion, it is seen that filaments with lower length, L = 0.1 tend to show high rigidity behaviour, filament with intermediate length, L = 0.2 show highest C-shape motion and filament with length i.e. L = 0.3 produce large sets of complex deformation. This clearly indicates that filament length is an important criterion along with shear rate and bending rigidity for demarcating filament deformation regimes. The bending rigidity varies linearly with VFF values for all filament length cases. Also, shear rate plays a major role in producing frequent filament tumbling. The bending rigidity versus VFF plots are also very useful in identifying whether both the first and second filament deform identically or differently. Further the magnitude of tumbling count reduces as filament length increases irrespective of shear rate and bending rigidity. It is also important to note the advantage of using fractional contraction as a measure to better classify filaments into different deformation regimes with respect to VFF values.

The displacement of the flexible filament and successive tumbling can cause the filament to undergo migration along lateral and longitudinal directions. The relationship between tumbling count and X-displacement of the filament is provided for different conditions from Figures 7.16 – 7.19 for the first filament only, the reason for which is explained earlier. In Figure 7.16, the filament having length, L = 0.1 subjected to lowest shear rate, K = 10 is allowed to deform in shear flow. The figure shows maximum X-displacement for the filament between intermediate bending rigidity values ranging from 0.005-0.025. In regions where tumbling is either lowest or highest, the X-displacement is also correspondingly at its lowest value. Figure 7.17 shows the effect of changing bending rigidity on tumbling count and X-displacement for filament length, L = 0.1 and high shear rate, K = 32. As it is seen from the figure and similar to Figure 7.16, highest displacement is seen for intermediate bending rigidity values ranging from 0.01-0.075. However, for maximum tumbling zones an increase in X-displacement is found. When comparing Figure 7.16 and Figure 7.17, the magnitude of displacement is highest for high shear rate case (Figure 7.17).
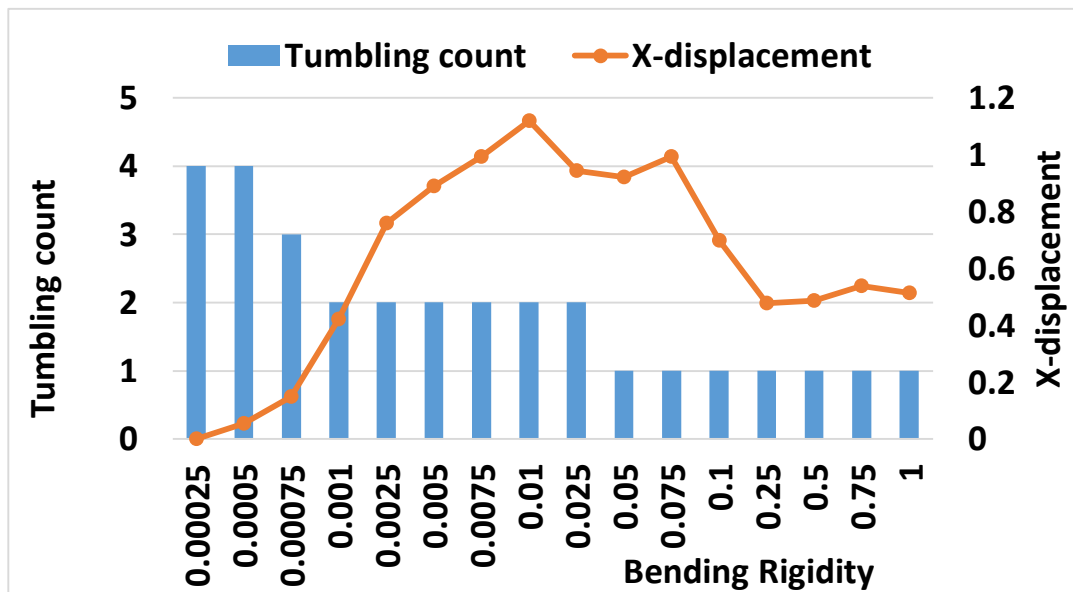
Figure 7.16 The relationship between tumbling count and X-displacement of filament with respect to bending rigidity for filament length, L = 0.1 and shear rate K = 10.

The plots in Figure 7.18 and Figure 7.19 shows the X-displacement and tumbling count variation for high filament length, L = 0.3 and shear rates, K = 10 and K = 32 respectively. The magnitude of both tumbling count and X-displacement is high for high shear rate cases irrespective of filament length. The peak in X-displacement is obtained for bending rigidity values from 0.05-0.1 which is slightly higher in value for those observed in Figure 7.16 and Figure 7.17. The displacement is almost constant for both high rigidity (K_b = 1.0) and low rigidity (K_b = 0.00025) values. Finally, in Figure 7.19 the X-displacement peak occurs for high rigidity values ranging from 0.075-1.0. The displacement also remains relatively lower for high tumbling regions. It is clear that the X-displacement of the filament is non-uniformly distributed along bending rigidity values. All the figures except Figure 7.17 show low X-displacement for high tumble regions. The peaks in X-displacements are observed for all figures and their range moves from low rigidity to high rigidity as filament length and shear rates are increased. The regions covered under X-displacement peaks report low filament tumbling for all cases. Thus it can be summarized that filaments that tumble the highest show low X-displacement while the ones being highly displaced tend to tumble the least.
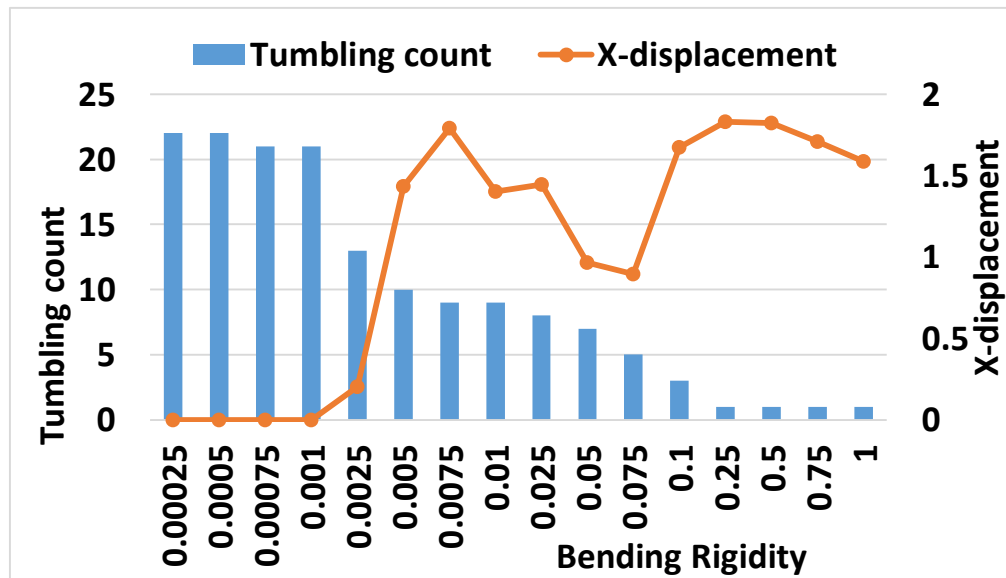
Figure 7.17 The relationship between tumbling count and X-displacement of filament with respect to bending rigidity for filament length, L = 0.1 and shear rate K = 32.
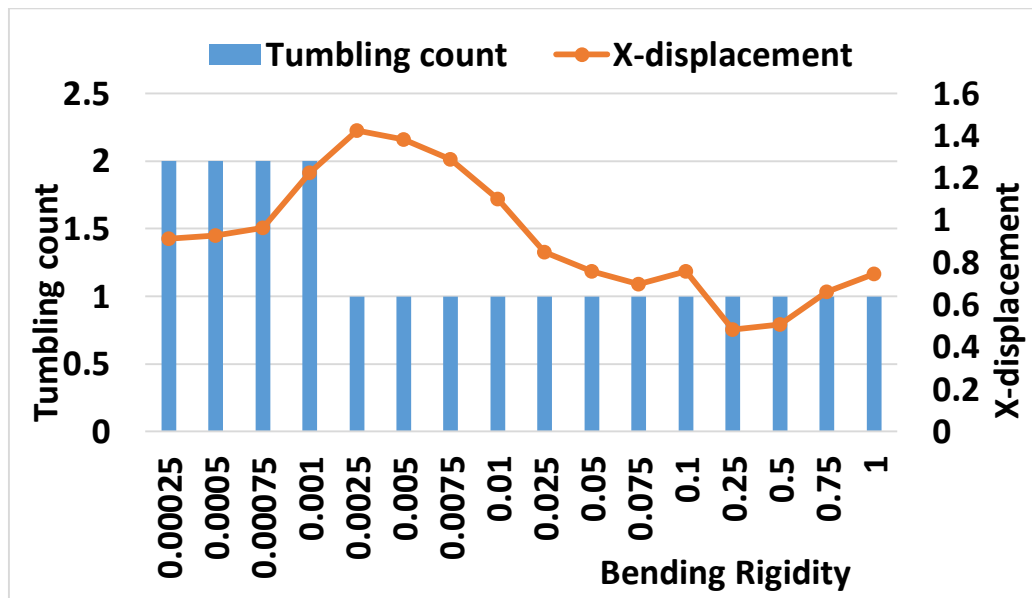
Figure 7.18 The relationship between tumbling count and X-displacement of filament with respect to bending rigidity for filament length, L = 0.3 and shear rate K = 10.
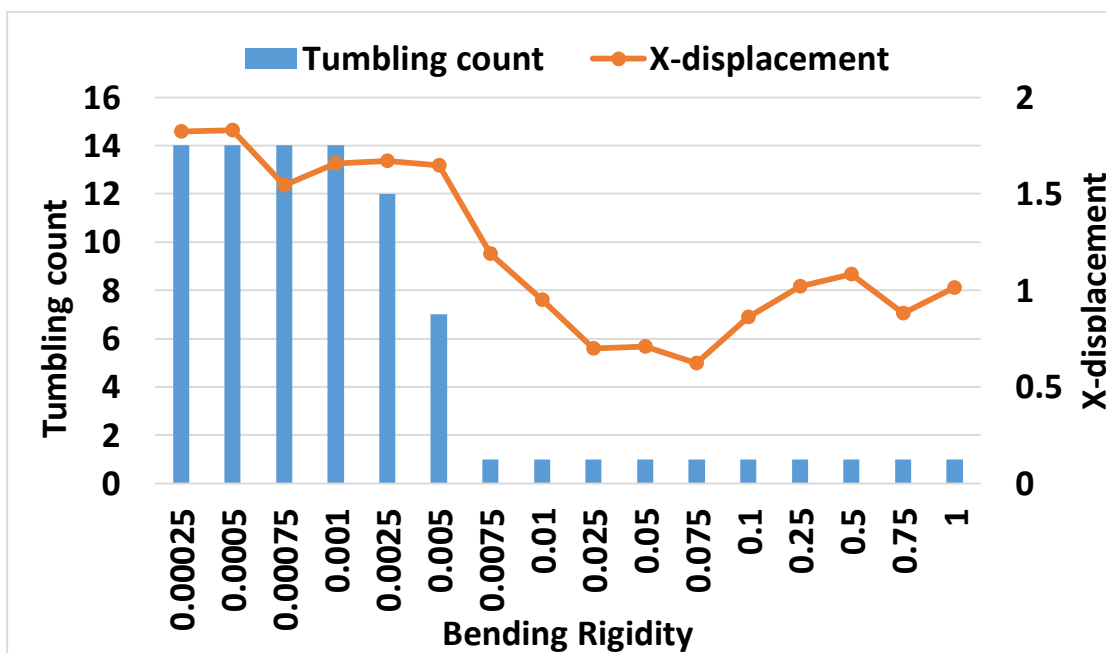
Figure 7.19 The relationship between tumbling count and X-displacement of filament with respect to bending rigidity for filament length, L = 0.3 and shear rate K = 32.

It is also very important to note the final distance between the two filaments at the end of simulation time. These distances are plotted with respect to bending rigidity and shear rates for different filament lengths as shown in Figure 7.20 – 7.22. In Figure 7.20, for shear rate cases $K = 10$ and $K = 16$, the final distance keeps on growing as bending rigidity increases. However for high shear rate, $K = 32$, the filaments show lower separation distance at intermediate bending rigidity values. This indicates that filaments that are subjected to higher shear rates end up closer to each other. A similar trend is observed in Figure 7.21 were the separation distance grows steadily for lower, $K = 10$ and $K = 16$ shear rates and highest fluctuations are seen for $K = 32$. However for filament length, $L = 0.3$ this pattern changes as shown in Figure 7.22. The final distance of filaments with shear rate, $K = 32$ fluctuates and decreases as usual but filaments subjected to $K = 10$ and $K = 16$ also show a decreasing pattern with respect to bending rigidity. This further indicates that filament length plays a crucial role in defining the mutual interaction behaviour of flexible filaments in shear flow.
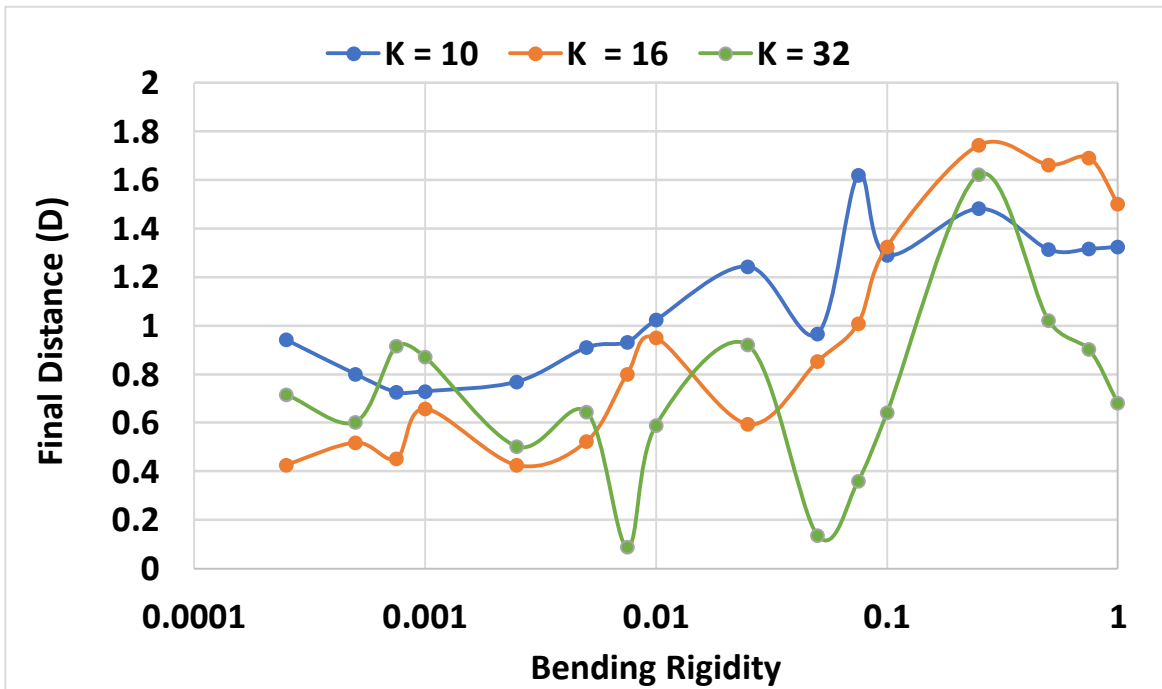
Figure 7.20 The final distance between two interacting filaments in shear flow with respect to bending rigidity for filament length, $L = 0.1$ at different shear rates.
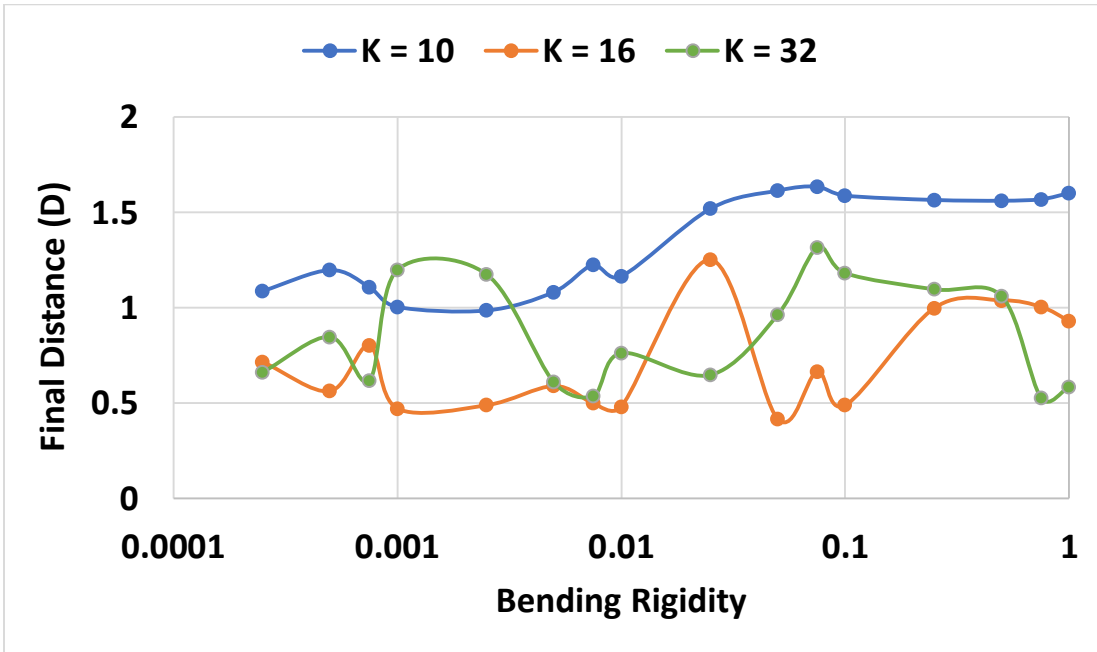
Figure 7.21 The final distance between two interacting filaments in shear flow with respect to bending rigidity for filament length, L = 0.2 at different shear rates.
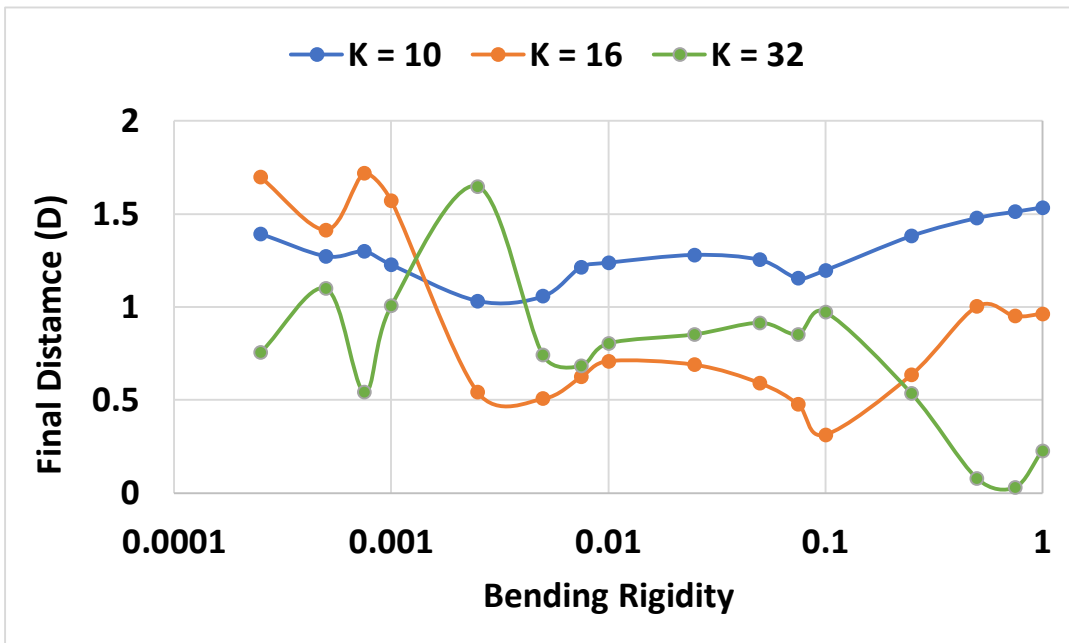
Figure 7.22 The final distance between two interacting filaments in shear flow with respect to bending rigidity for filament length, L = 0.3 at different shear rates.

7.3.2 ANN prediction study

In section 7.3.1, a detailed parametric study is carried out to study the effects of filament length, shear rate and bending rigidity on filament deformation, orbit regimes and tumbling count. Also, the presence of two side-by-side filaments and their mutual interaction effects are studied. It is found that filament tumbling has tremendous influence on filament dynamics and also filament migration in X-direction. It is thus important to develop a prediction model that can effectively determine tumbling count for two filament placed side-by-side in viscous shear flow. In order to achieve this, IBM simulations are used to produce parametric test cases and tumbling counts are obtained for the first and second filaments. Based on these results, an ANN prediction model is developed to forecast the tumbling counts for a wide range of parametric variable considering two filaments placed side-by-side.

As stated earlier, MATLAB software is used for the implementation of ANN. The multi-layer network architecture in Figure 7.1 is used for forecasting tumbling count. The architecture that is configured in MATLAB for this purpose is shown in Figure 7.23.
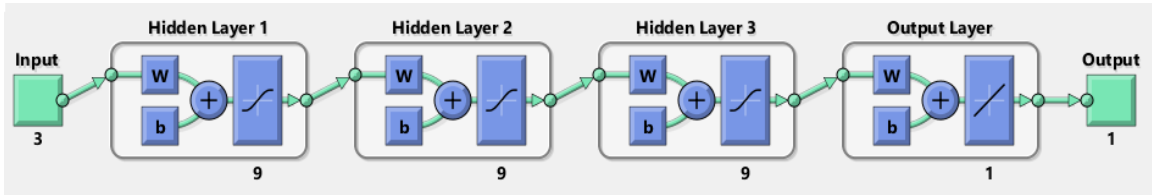
Figure 7.23 Neural network representation, 3-[9]-1 for the present study.

The three input parameters are filament length, shear rate and bending rigidity of filament. A tangent sigmoid transfer function is used for hidden layers and linear function is used for output layer. Two prediction models are developed, one for each filament by keeping tumbling count as output variable. In the present study, a total of 144 IBM simulation data is recorded for the purpose of constructing the ANN model. The entire data is divided into two parts: training data and testing data. Two-third portion of the simulation data is used for training and one-third is utilized for testing. An optimized number of nine neurons are chosen for the hidden layers and a total of three hidden layers are included.

The procedure for fixing the optimum number of neurons and hidden layers based on MSE calculation between the sample data and trained network data can be found in the previous chapter, section 6.3.3. The relationship between the observed tumbling count results and the prediction obtained by ANN are found to vary linearly as shown in Figure 7.24 and Figure 7.25 for first and second filament respectively. The value of R^2 (absolute fraction of variance) is 0.99906 for filament 1 (F1) and 0.99904 for filament 2 (F2). Assuming a fit-line model given by the expression output = (a × target) + b, the co-efficients for the ANN model "a" and "b" are approximately equal to 1 and 0 for both the filament cases. This indicates that the present ANN models have the best prediction capability. A comparison is done between the observed tumbling count results and network predicted results for both the first and second filaments as shown in Figure 7.26 and Figure 7.27. The results predicted by ANN closely resembles that generated during IBM simulation. Thus the ANN configuration as shown in Figure 7.23 can be effectively used to predict new tumbling count values for first and second filaments considering a wide range of input parameters.
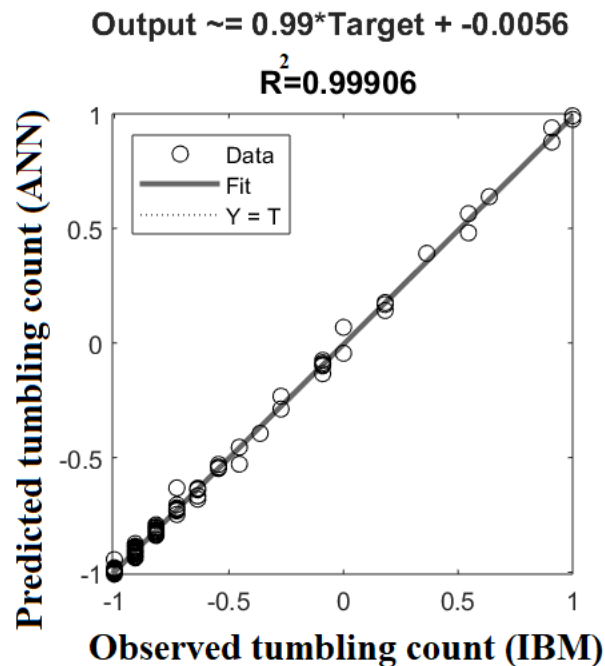
Figure 7.24 Regression plot obtained for the trained neural network (F1).

176
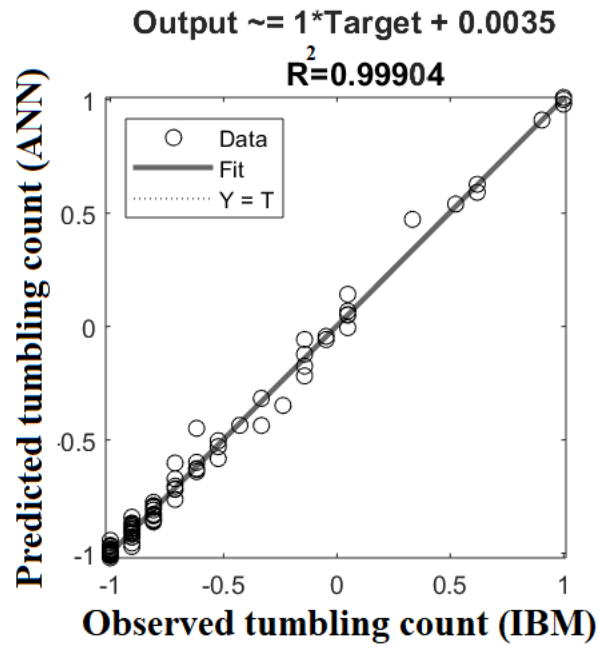
Figure 7.25 Regression plot obtained for the trained neural network (F2).
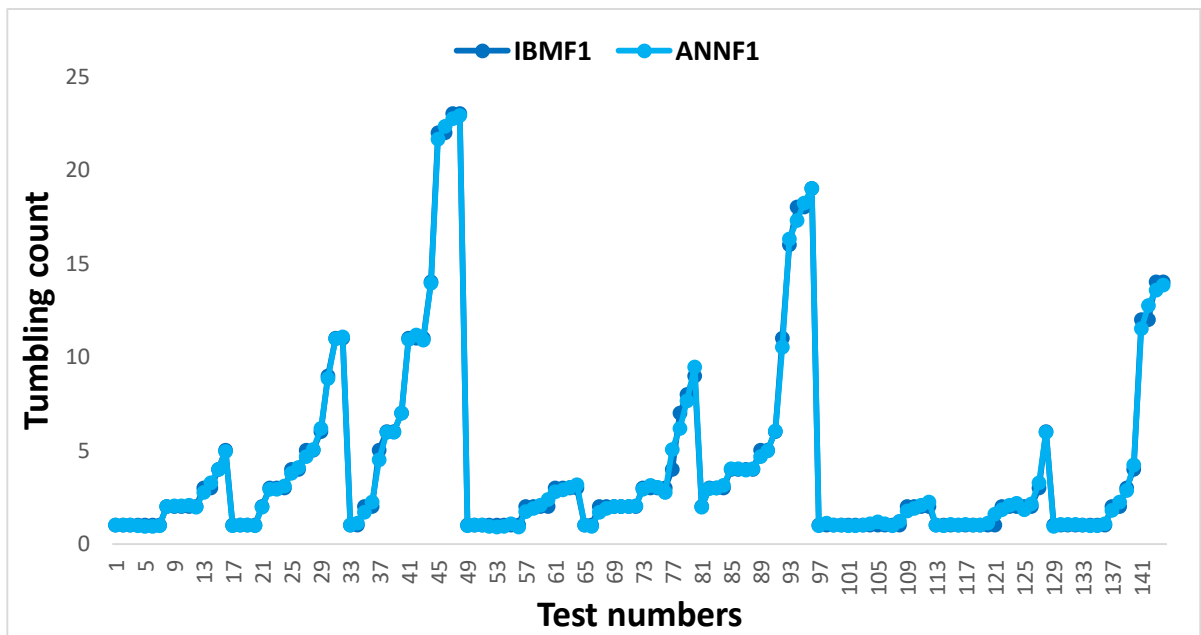
Figure 7.26 Comparison between simulation results and neural network predictions for first filament.
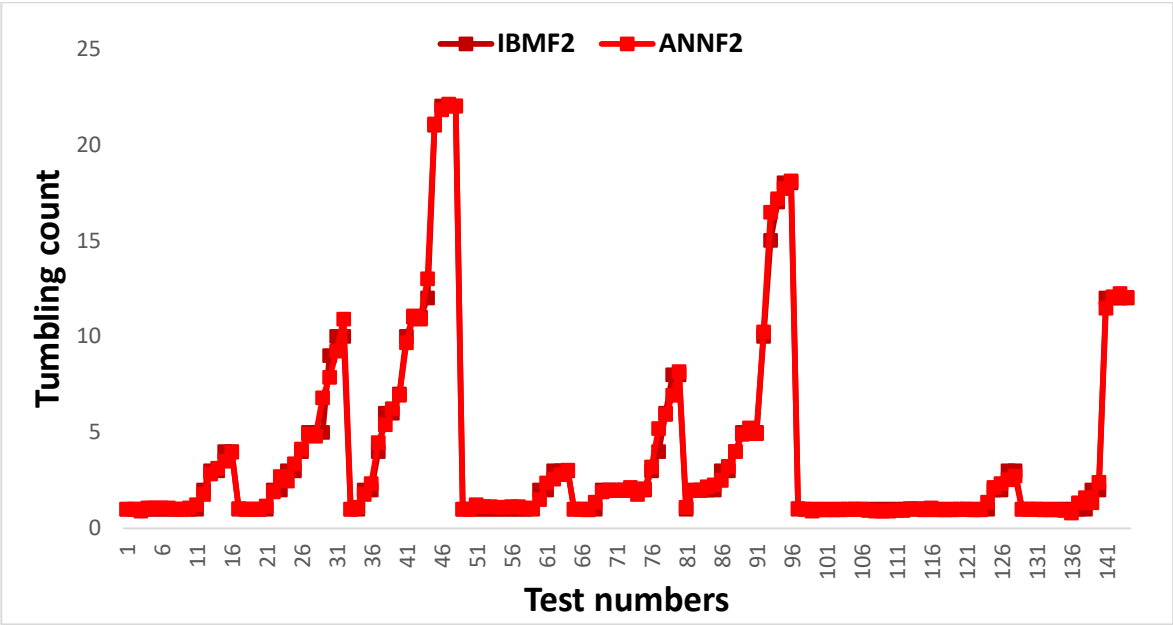
Figure 7.27 Comparison between simulation results and neural network predictions for second filament.

CHAPTER 8

8   CONCLUSION

The main objective of the present study is to develop two-dimensional computational models based on finite volume immersed boundary method in order to understand the dynamics and interaction of flexible filaments in different fluid flow conditions. The same has been carried out and the immersed boundary implementation along with detailed analysis is provided in Chapters 3 to 7. A summary of each chapters is provided below.

8.1   Simulation of fluid flow in straight and wavy rigid wall channels

The work presented in Chapter 3 involves developing a preliminary computational model based on an immersed boundary finite volume method to perform numerical simulation of straight and wavy rigid walled channels. This will help to study passive mixing effects and flow behavior. Wavy walls are probably the best possible alternatives to straight micro-channels with respect to mixing and thermal performance improvements. Numerical simulation of such complex wavy wall geometries are successfully carried out using immersed boundary method. It is found that the developed computational model can be easily extended for the case of flexible filament interacting with incoming fluid under different channel flow conditions. However, optimum results can be obtained only by proper selection of wavy wall geometry. Configurations of wavy walls having larger amplitude (A = 0.14) and intermediate wavelength (WL = 1.0) are preferred. From the analysis it can be concluded that crest-crest (CC) - model type wavy wall performs the best in terms of mixing enhancement in diffusion flow based micro-channels.

8.2   Simulation of flexible filament in viscous shear flow

The study in Chapter 4 focuses on understanding the fluid-structure interaction of non-motile diatom chains subjected to shear flow in a viscous fluid medium having constant nutrition flux. The simulation is carried out in a two-dimensional manner by considering a flexible filament as a diatom placed in a channel. The interplay of

hydrodynamics and filament properties like elasticity and bending are incorporated using an immersed boundary algorithm. The developed numerical model is validated by comparing with previous research works which involve deformation of a flexible filament tethered at leading end and free at trailing end subjected to plane channel flow and un-tethered flexible filament in a planar shear flow at low Reynolds number. Further, the model is modified to incorporate a flexible filament mimicking a diatom chain placed in shear flow conditions. Filament shape deformations such as snake turns (C-shape) buckling and S-turns, documented by previous researchers are also observed in the present study. In this study, filament which retains their original shape after initial deformation is considered to be springy recuperative and those who do not retain shape are termed as non-recuperative. This is very important to determine how the diatom chain reacts to nutrients in their surrounding fluid and understand the passive alignment of diatom chains based on an accurate representation of external turbulences or recirculation zones in its vicinity. As observed from this study diatom that has Viscous Flow Forcing (VFF) in the range $0 <$ VFF < 350 are considered to be recuperative and the ones having VFF beyond the value of 350 are non-recuperative. This helps us to identify the critical value of Viscous Flow Forcing (VFF) that govern the filaments ability to retain or attain permanent deformation from its original shape.

Based on the analysis of various factors such as symmetry breakage time, turning point time, deformation and recurrence time, optimum survival conditions for diatoms have been studied. Higher symmetry breakage time signifies that the filament remains in the undeformed state for a large portion of the time. This gives ample time for the filament to interact with the surrounding environment. In the case of diatom chains, it provides more time for it to absorb necessary nutrients. Low deformation time indicates a faster recovery for the filament to reach undeformed position. Thus, the diatom can regain the undeformed state in a shorter period of time. Finally, the filaments with high recurrence time tend to remain in the undeformed state longer. Therefore, the best possible condition is that filament must have high symmetry breakage time, low deformation time and high recurrence time (low recurrence frequency). The present study indicates that long

recuperative filaments subjected to low shear rate (Case 5: L = 0.3125, K = 1.0, $K_b = 1 \times 10^{-4}$) have high symmetry breakage time ($t_{sb} = 58.0$), short recuperative filaments (Case 2: L = 0.25, K = 2.0, $K_b = 1 \times 10^{-4}$) and long recuperative filaments (Case 6: L = 0.3125, K = 2.0, $K_b = 1 \times 10^{-4}$) placed in high shear rate show low deformation time ($t_d = 4.0$). Finally, short non-recuperative filaments (Case 3: L = 0.25, K = 1.0, $K_b = 1 \times 10^{-5}$) in low shear flow exhibit high recurrence time ($t_r = 25.0$). Non-recuperative filaments subjected to high shear (Case 4: L = 0.25, K = 2.0, $K_b = 1 \times 10^{-5}$ and Case 8: L = 0.3125, K = 2.0, $K_b = 1 \times 10^{-5}$), usually tend to deform regularly due to high recurrence frequency ($t_r = 11.0$ and $t_r = 7.4$) which makes it challenging for the diatoms to collect nutrients. The main focus of the present study is understanding the passive alignment of diatom chains based on an accurate representation of external turbulences or recirculation zones in its vicinity. Filament migration study shows that short and recuperative filaments tend to migrate faster and deform less in shear flow, which is another critical observation of the behavior of the diatom chain to external flow conditions. The developed two-dimensional computational model based on the immersed boundary finite-volume method has been successful in capturing fluid dynamics near the filament surface and thus can be easily extended to study other non-motile biological organism interacting with surrounding fluid flow under different conditions.

8.3   Simulation of flexible filament in viscous oscillating flow

The primary goal of Chapter 5 is to understand the fluid-structure interaction of a flexible filament subjected to oscillating fluid flow in a two-dimensional channel. Mechanical properties of the flexible filament like stretching and bending are incorporated into the governing fluid equations using a temporal second order immersed boundary method. The capability of the developed numerical model to capture the interaction of flexible filaments in oscillating fluid flow as compared to previous research works in the same field is clearly demonstrated. Parametric analysis is first carried out to study the interplay of hydrodynamic stresses acting on the filament surface for different filament length, bending rigidity, flow conditions and Reynolds number. The impact on fluid motion

due to increase in filament length is greater in the longitudinal direction as compared to transverse direction. Longer rigid filaments have a more pronounced influence in fluid motion for both longitudinal and transverse direction as compared to short flexible filaments. Flexible filaments of all lengths have similar sweeping span whereas the flapping span for rigid filaments keep increasing as length increases. It is also observed that the sweep span of rigid filament keeps decreasing as Reynolds number increases whereas in flexible filament case, the sweep span remains constant irrespective of changing Reynolds number. Filaments producing symmetrical sweep pattern were found to produce better mixing which is in agreement with previous similar studies. On analysing the curve obtained between mean angle made by the filament with respect to horizontal (Θ) and Reynolds number, it is seen that filament producing symmetrical sweep pattern has slope value of the above curve ranging between 0.09 and 0.35. The slope value existing outside this range produces either a retarded deformation or filament sweep with appreciable bend both of which are not ideal conditions for fluid mixing. The tip trajectories for filament length, Len = 0.6 and 0.8 results in formation of octave-shaped pattern similar to tip motion of beating cilia. The size of the pattern increases with filament length providing an indication of filament bending observed during deformation. A flattened behaviour in tip displacement is observed for all cases which indicates that filament remains aligned in the fluid flow direction. There is also greater retardation of filament displacement for rigid lower length filaments as Reynolds number increases. Retarded motion is observed for rigid filaments of length, Len = 0.4 and Len = 0.6 whereas sweep with appreciable bend is seen for flexible filament of length, Len = 0.8. This clearly shows that selection of right filament length and bending rigidity is crucial for fluid mixing scenarios. The phase shift in fluid motion is also found to critically effect filament displacement dynamics especially for rigid filaments. It is also found that aspect ratio i.e. ratio of filament length to channel height, suitable for mixing applications is directly dependent on channel geometry ratio i.e. ratio of channel height to channel length. It is clear that a minimum aspect ratio (L/H) of 0.4 is needed to produces the best results for mixing application with respect to channel geometry ratio (H/L_c) of 0.25.

On the basis of the parametric analysis done, filament displacement and corresponding flow streams are studied for two types of flow variations i.e. sinusoidally oscillatory flow with phase shift (SOFPS) and sinusoidally oscillatory flow without phase shift (SOF) for rigid filament cases $S_{ben} = 0.01$, 0.1 and 1.0 referred to as low, medium and high rigidity filaments. Presence of the filament and its interaction with these flow conditions produce complex filament deformations. The motion and fluid flow surrounding the filament are well captured for fixed time intervals throughout the simulation. Filaments having high and medium rigidity, show pronounced levels of elongation or stretching and have lower levels of bending. This results in sweeping filament conformation ideal for fluid mixing. Also, their filament deformations are symmetric in nature irrespective of flow conditions. Symmetric behaviors are also seen for medium and low rigidity filament subjected to SOFPS condition. However, filament deform asymmetrically for SOF condition. Filaments belonging to the same medium rigidity category but when placed in SOF condition produce a phenomenon similar to antiplectic metachronism. Another observation is that filament show high levels of buckling when the bending rigidity is low. The present study involves passive tethered filament moving with respect to oscillating fluid flow whose flow conditions (SOFPS and SOF) are assumed beforehand. However, actively propelling filaments surrounded by stationary fluid, deform in specific ways which are highly acceptable for engineering applications like fluid mixing or micro-pumping. It is possible in the present study to perfectly match these filament deformations with results obtained from assumed flow conditions, thereby indirectly defining the flow behavior for the above-mentioned practical engineering applications. Symmetric filament behavior is adequate for mixing scenarios while asymmetric behavior is favorable for pumping. Thus, the above observations can be concluded with two key findings. 1) Effective fluid mixing can be enabled in devices which consist of high and medium rigidity filaments that deform to produce SOFPS in an oscillating sequence and 2) Pumping in micro-devices can be attained by the use of medium rigidity filaments that deform to create SOF condition in the surrounding fluid.

8.4 Simulation of tethered flexible membrane and flow rate prediction using IBM and ANN techniques

In Chapter 6, the developed numerical model is used to understand the fluid-structure interaction effects of flexible membrane tethered at both ends in two-dimensional channel. The developed model has been successfully validated with previous research work involving flow past deformable membranes. The complex interaction of hydrodynamic forces on the flexible membrane is ascertained with the help of parametric studies involving parameters like membrane length, bending rigidity and membrane position in channel. Also, for all the parametric test cases, the flow rate past deformable membranes are also determined. Rigid membranes (K_b = 10.0) retained their original shape since the elastic forces resisted hydrodynamic stresses. However, the membranes made up of low rigidity (K_b = 1.0 and K_b = 0.1) underwent minor and substantial conformations with respect to hydrodynamic force distribution on its surface. Positioning the membrane at lower channel section (H_y = 0.25) in the direction of fluid motion causes it to deform upwards thereby increasing the flow area in the lower channel sections. Similarly, by placing the membrane at upper channel section (H_y = 0.75) causes the membrane to deform downwards and this increases the flow rate in the upper channel side. Thus, by changing the bending rigidity, membrane length and its position in channel, flow rate can be controlled in the two-dimensional channel. When a membrane whose length is beyond the critical condition $L >= 1.0$ is placed at channel mid-plane (H_y = 0.5), repetitive mode shapes are observed at subsequent time intervals. The membranes thus exhibit self-excited oscillations. A dynamic equilibrium existing between the hydrodynamic forces and elastic forces of the membrane is responsible for this behavior. Finally, a back-propagation feed-forward Artificial Neural Network (ANN) is developed to predict flow rate past deformable membranes. The results predicted by the ANN model closely resembles that generated by IBM simulations. Thus, by combining IBM and ANN techniques it is possible to accurately determine and predict flow rate past a deformable membrane.

8.5   Simulation of multiple flexible filaments in shear flow

A finite volume based immersed boundary model which was developed and successfully validated to study fluid-structure interaction of single flexible filament in Chapter 4 is extended to analyze mutual interaction of two filaments placed side-by-side in viscous shear flow. A detailed parametric study is carried out to ascertain the influence of hydrodynamics forces acting on the flexible filaments. The parameters used for this study are filament length, shear rate and bending rigidity of the filaments. A fractional contraction term is used in the study which indicates the compressive state of the filament with respect to initial filament length. The results show that, rigid filaments tend to have lowest contraction since they deform the least whereas contraction values steadily increase for springy, C-shape and complex regimes. The average contraction value for rigid motion is close to zero whereas for complex shape it is one. The contraction value for springy deformation is approximately 0.3 and that for C-shape is 0.7. It is also important to note the advantage of using fractional contraction as a measure to better classify filaments into different deformation regimes with respect to VFF values. It is also observed that, filament length plays an important role along with shear rate and bending rigidity in demarcating filament deformation regimes. Filaments with lower length, $L = 0.1$ tend to show high rigidity behavior, filament with intermediate length, $L = 0.2$ show highest C-shape motion and filament with length i.e. $L = 0.3$ produce large sets of complex deformation. The bending rigidity versus VFF plots are also very useful in identifying whether both the first and second filament deform identically or differently. Also, shear rate plays a major role in producing frequent filament tumbling. At lower rigidity, the filament offers least resistance to shear flow and thus undergoes tumbling frequently. It can be further observed that the magnitude of tumbling count reduces as filament length increases irrespective of shear rate and bending rigidity. The displacement of the flexible filament and successive tumbling can cause the filament to undergo migration along lateral and longitudinal directions. It is clear that the X-displacement of the filament is non-uniformly distributed along bending rigidity values. The peaks in X-displacement values are observed for all figures and their range moves from low rigidity to high rigidity as filament length and shear

rates are increased. The regions covered under X-displacement peaks report low filament tumbling for all cases. This shows that filaments that tumble the highest show low X-displacement while the ones being highly displaced tend to tumble the least. When analyzing two filaments placed side-by-side, it is seen that the tumbling count is greater for first filament as compared to second. The motion of the first filament hinders the movement of fluid around the second filament. However, these observation are seen only for filaments subjected to lower rigidity cases ($K_b \leq 0.025$). The filaments with higher rigidity ($K_b \geq 0.025$) tend to tumble with similar frequency. The importance of filament length in defining the mutual interaction behavior of flexible filaments in shear flow is further highlighted by analyzing the final separation distance achieved between the two filaments. Finally, a back-propagation feed-forward Artificial Neural Network (ANN) is developed to predict tumbling counts for first and second filaments. The results predicted by the ANN model closely resembles that generated by IBM simulations. Thus, by combining IBM and ANN techniques it is possible to accurately determine and predict tumbling counts for two filaments placed side-by-side in viscous shear flow.

REFERENCES

Adeeb, E., Haider, B.A. and Sohn, C.H., (2018). Influence of rounded corners on flow interference between two tandem cylinders using FVM and IB-LBM. *International Journal of Numerical Methods for Heat & Fluid Flow*, 28(7),1648-1663.

Ahmed, M. A., Yusoff, M. Z., Ng, K. C., and Shuaib, N. H. (2014). The effects of wavy-wall phase shift on thermal-hydraulic performance of Al 2 O 3–water nanofluid flow in sinusoidal-wavy channel. *Case Studies in Thermal Engineering*, 4,153-165.

Ahmed M.A., Yusoff M.Z., and Shuaib N.H. (2015) Numerical Investigation on the Nanofluid Flow and Heat Transfer in a Wavy Channel. *Engineering Applications of Computational Fluid Dynamics*, Shaari K., Awang M. (eds), Springer, Cham, 145-167.

Alben, S., Shelley, M. and Zhang, J., (2002). Drag reduction through self-similar bending of a flexible body. *Nature*, 420(6915), 479-481.

Alexeev, A., Yeomans, J.M. and Balazs, A.C., (2008). Designing synthetic, pumping cilia that switch the flow direction in microchannels. *Langmuir*, 24(21), 12102-12106.

Allen, J., Techet, A., Kelso, R. and Smits, A., (2001). Energy harvesting eel. *Journal of Fluids and Structures*, 15(3), 629-640.

Anand, D. V., Vedantam, S., and Patnaik, B. S. V., (2016). Dissipative particle dynamics simulation of shear flow in a microchannel with a deformable membrane. *Microfluidics and Nanofluidics*, 20(12), 161.

Ardekani, A.M., Dabiri, S. and Rangel, R.H., (2008). Collision of multi-particle and general shape objects in a viscous fluid. *Journal of Computational Physics*, 227(24), 10094-10107.

Arruda, J.M., e Silva, A.L.L., Neto, A.S. and Roma, A.M., (2002). Numerical simulation of channel flows using the immersed boundary method. *Mecánica Computacional*, 21, 148-162.

Aslan, E., Taymaz, I., and Islamoglu, Y. (2016). Finite volume simulation for convective heat transfer in wavy channels. *Heat and Mass Transfer*, 52(3), 483-497.

Baaijens, F.P., (2001). A fictitious domain/mortar element method for fluid–structure interaction. *International Journal for Numerical Methods in Fluids*, 35(7), 743-761.

Bahaidarah, H. M., Anand, N. K., and Chen, H. C. (2005). Numerical study of heat and momentum transfer in channels with wavy walls. *Numerical Heat Transfer, Part A*, 47(5), 417-439.

Bamiro, O.O. and Liou, W.W., (2013). A direct heating immersed boundary-lattice Boltzmann method for thermal flows. *International Journal of Numerical Methods for Heat & Fluid Flow*, 24(1), 169-200.

Barlow, D., Sleigh, M.A. and White, R.J., (1993). Water flows around the comb plates of the ctenophore Pleurobrachia plotted by computer: a model system for studying propulsion by antiplectic metachronism. *Journal of experimental biology*, 177(1), 113-128.

Batchelor, G.K., (1970). Slender-body theory for particles of arbitrary cross-section in Stokes flow. *Journal of Fluid Mechanics*, 44(3), 419-440.

Bertram, C.D., (2003). Experimental studies of collapsible tubes. *Flow past highly compliant boundaries and in collapsible tubes*, Carpenter P.W., Pedley T.J. (eds), Springer, Dordrecht, 51-65.

Bouzarth, E.L., Layton, A.T. and Young, Y.N., (2011). Modeling a semi-flexible filament in cellular Stokes flow using regularized Stokeslets. *International Journal for Numerical Methods in Biomedical Engineering*, 27(12), 2021-2034.

Chakraborty, D., Prakash, J.R., Friend, J. and Yeo, L., (2012). Fluid-structure interaction in deformable microchannels. *Physics of Fluids*, 24(10), 102002.

Chelakkot, R., Winkler, R.G. and Gompper, G., (2011). Semiflexible polymer conformation, distribution and migration in microcapillary flows. *Journal of Physics: Condensed Matter*, 23(18),184117.

Cho, C. C. (2008). A combined active/passive scheme for enhancing the mixing efficiency of microfluidic devices. *Chemical Engineering Science*, 63(12), 3081-3087.

Connell, B.S. and Yue, D.K., (2007). Flapping dynamics of a flag in a uniform stream. *Journal of Fluid Mechanics*, 581, 33-67.

Cortez, R., (2001). The method of regularized Stokeslets. *SIAM Journal on Scientific Computing*, 23(4),1204-1225.

Cybenko, G., (1992). Approximation by superpositions of a sigmoidal function. *Mathematics of Control, Signals and Systems*, 5(4), 455-455.

Dauptain, A., Favier, J. and Bottaro, A., (2008). Hydrodynamics of ciliary propulsion. *Journal of Fluids and Structures*, 24(8), 1156-1165.

De Marinis, D., de Tullio, M.D., Napolitano, M. and Pascazio, G., (2016). Improving a conjugate-heat-transfer immersed-boundary method. *International Journal of Numerical Methods for Heat & Fluid Flow*, 26(3/4), 1272-1288.

Diaz-Goano, C., Minev, P.D. and Nandakumar, K., (2003). A fictitious domain/finite element method for particulate flows. *Journal of Computational Physics*, 192(1), 105-123.

Eloy, C., Lagrange, R., Souilliez, C. and Schouveiler, L., (2008). Aeroelastic instability of cantilevered flexible plates in uniform flow. *Journal of Fluid Mechanics*, 611, 97-106.

Farnell, D.J.J., David, T. and Barton, D.C., (2004). Numerical simulations of a filament in a flowing soap film. *International Journal for Numerical Methods in Fluids*, 44(3), 313-330.

Flores, H., Lobaton, E., Méndez-Diez, S., Tlupova, S. and Cortez, R., (2005). A study of bacterial flagellar bundling. *Bulletin of Mathematical Biology*, 67(1), 137-168.

Forgacs, O.L. and Mason, S.G., (1959). Particle motions in sheared suspensions: X. Orbits of flexible threadlike particles. *Journal of Colloid Science*, 14(5), 473-491.

Francois, M., Uzgoren, E., Jackson, J. and Shyy, W., (2004). Multigrid computations with the immersed boundary technique for multiphase flows. *International Journal of Numerical Methods for Heat & Fluid Flow*, 14(1), 98-115.

Goetz, T., Klar, A., Unterreiter, A. and Wegener, R., (2008). Numerical evidence for the non-existence of stationary solutions of the equations describing rotational fiber spinning. *Mathematical Models and Methods in Applied Sciences*, 18(10), 1829-1844.

Gong, L., Kota, K., Tao, W., and Joshi, Y. (2011a). Parametric numerical study of flow and heat transfer in microchannels with wavy walls. *Journal of Heat Transfer*, 133(5), 051702.

Gong, L. J., Kota, K., Tao, W., & Joshi, Y. (2011b). Thermal performance of microchannels with wavy walls for electronics cooling. *IEEE Transactions on Components, Packaging and Manufacturing Technology*, 1(7), 1029-1035.

Gray, J. and Hancock, G.J., (1955). The propulsion of sea-urchin spermatozoa. *Journal of Experimental Biology*, 32(4), 802-814.

Guasto, J. S., Rusconi, R., and Stocker, R. (2012). Fluid mechanics of planktonic microorganisms. *Annual Review of Fluid Mechanics*, 44, 373-400.

Harrington, P.D.B., (1993). Sigmoid transfer functions in backpropagation neural networks. *Analytical Chemistry*, 65(15), 2167-2168.

Hayase, T., Humphrey, J. A. C., and Greif, R. (1992). A consistently formulated QUICK scheme for fast and stable convergence using finite-volume iterative calculation procedures. *Journal of Computational Physics*, 98(1), 108-118.

Haykin, S., (1994). *Neural networks: a comprehensive foundation*. Prentice Hall PTR, Upper Saddle River, NJ, United States.

Heil, M. and Jensen, O.E., (2003). Flows in deformable tubes and channels. *Flow past highly compliant boundaries and in collapsible tubes*, Carpenter P.W., Pedley T.J. (eds), Springer, Dordrecht, 15-49.

Holwill, M.E.J. and Burge, R.E., (1963). A hydrodynamic study of the motility of flagellated bacteria. *Archives of biochemistry and biophysics*, 101(2), 249-260.

Hu, H. H., Patankar, N. A., and Zhu, M. Y. (2001). Direct numerical simulations of fluid–solid systems using the Arbitrary Lagrangian–Eulerian technique. *Journal of Computational Physics*, 169(2), 427-462.

Hua, H., Shin, J. and Kim, J., (2014). Dynamics of a compound droplet in shear flow. *International Journal of Heat and Fluid Flow*, *50*, 63-71.

Huang, L., (2001). Viscous flutter of a finite elastic membrane in Poiseuille flow. *Journal of fluids and structures*, 15(7), 1061-1088.

Huang, W.X., Shin, S.J. and Sung, H.J., (2007). Simulation of flexible filaments in a uniform flow by the immersed boundary method. *Journal of Computational Physics*, 226(2), 2206-2228.

Huang, H.X. and Miao, Y.S., (2007). Finite element and neural network modeling of viscoelastic annular extrusion, *Journal of Fluids Engineering*, 129(2), 218-225.

Huang, W.X. and Sung, H.J., (2009). An immersed boundary method for fluid–flexible structure interaction. *Computer Methods in Applied Mechanics and Engineering*, *198*(33-36), 2650-2661.

Huang, W.X. and Sung, H.J., (2010). Three-dimensional simulation of a flapping flag in a uniform flow. *Journal of Fluid Mechanics*, 653, 301-336.

Huang, W.X., Chang, C.B. and Sung, H.J., (2012). Three-dimensional simulation of elastic capsules in shear flow by the penalty immersed boundary method. *Journal of Computational Physics*, 231(8), 3340-3364.

Jendrejack, R. M., Schwartz, D. C., De Pablo, J. J., and Graham, M. D. (2004). Shear-induced migration in flowing polymer solutions: Simulation of long-chain DNA in microchannels. *The Journal of Chemical Physics*, 120(5), 2513-2529.

Jeffery, G. B. (1922). The motion of ellipsoidal particles immersed in a viscous fluid. *Proceedings of the Royal Society of London. Series A, Containing papers of a mathematical and physical character*, 102(715), 161-179.

Jimenez-Martinez, M. and Alfaro-Ponce, M., (2019). Fatigue damage effect approach by artificial neural network. *International Journal of Fatigue*, 124, 42-47.

Jumars, P. A., Trowbridge, J. H., Boss, E., and Karp-Boss, L. (2009). Turbulence-plankton interactions: a new cartoon. *Marine Ecology*, 30(2), 133-150.

Karp-Boss, L., Boss, E., and Jumars, P. A. (1996). Nutrient fluxes to planktonic osmotrophs in the presence of fluid motion. *Oceanography and Marine Biology*, 34, 71-108.

Keller, J.B. and Rubinow, S.I., (1976). Slender-body theory for slow viscous flow. *Journal of Fluid Mechanics*, 75(4), 705-714.

Khatavkar, V.V., Anderson, P.D., den Toonder, J.M. and Meijer, H.E., (2007). Active micromixer based on artificial cilia. *Physics of Fluids*, 19(8), 083605.

Kim, Y. and Peskin, C.S., (2006). 2–D parachute simulation by the immersed boundary method. *SIAM Journal on Scientific Computing*, *28*(6), 2294-2312.

Kim, Y. and Peskin, C.S., (2007). Penalty immersed boundary method for an elastic boundary with mass. *Physics of Fluids*, 19(5), 053103.

Kim, Y. and Peskin, C.S., (2009). 3-D parachute simulation by the immersed boundary method. *Computers & Fluids*, 38(6), 1080-1090.

Kim, B., Chang, C.B., Park, S.G. and Sung, H.J., (2015). Inertial migration of a 3D elastic capsule in a plane Poiseuille flow. *International Journal of Heat and Fluid Flow*, *54*, 87-96.

Kim, B., Park, S.G., Huang, W. and Sung, H.J., (2016). Self-propelled heaving and pitching flexible fin in a quiescent flow. *International Journal of Heat and Fluid Flow*, 62, 273-281.

Kim, B., Park, S.G., Huang, W.X. and Sung, H.J., (2017). An autonomous flexible propulsor in a quiescent flow. *International Journal of Heat and Fluid Flow*, 68,151-157.

Kocabaş, F., Ünal, S. and Ünal, B., (2008). A neural network approach for prediction of critical submergence of an intake in still water and open channel flow for permeable and impermeable bottom. *Computers & Fluids*, 37(8),1040-1046.

Krafczyk, M., Tölke, J., Rank, E. and Schulz, M., (2001). Two-dimensional simulation of fluid–structure interaction using lattice-Boltzmann methods. *Computers & Structures*, 79(22-25), 2031-2037.

Krindel, P. and Silberberg, A., (1979). Flow through gel-walled tubes. *Journal of Colloid and Interface Science*, 71(1), 39-50.

Ladd, A.J., (1994). Numerical simulations of particulate suspensions via a discretized Boltzmann equation. Part 1. Theoretical foundation. *Journal of Fluid Mechanics*, 271, 285-309.

Lai, M.C. and Peskin, C.S., (2000). An immersed boundary method with formal second-order accuracy and reduced numerical viscosity. *Journal of Computational Physics*, 160(2), 705-719.

Lallemand, P. and Luo, L.S., (2003). Lattice Boltzmann method for moving boundaries. *Journal of Computational Physics*, 184(2), 406-421.

Lambert, R.A. and Rangel, R.H., (2010). The role of elastic flap deformation on fluid mixing in a microchannel. *Physics of Fluids*, 22(5), 052003.

Lazier, J. R. N., and Mann, K. H. (1989). Turbulence and the diffusive layers around small organisms. *Deep Sea Research Part A. Oceanographic Research Papers*, 36(11), 1721-1733.

Lighthill, J., (1976). Flagellar hydrodynamics. *SIAM review*, 18(2), 161-230.

Lindström, S.B. and Uesaka, T., (2007). Simulation of the motion of flexible fibers in viscous fluid flow. *Physics of Fluids*, 19(11), 113307.

Li, Y., Li, D., Bie, S., Wang, Z., Zhang, H., Tang, X. and Zhen, Z., (2018). Numerical simulation for fluid droplet impact on discrete particles with coupled SPH-DEM method. *International Journal of Numerical Methods for Heat & Fluid Flow*, 28(11), 2581-2605.

Liao, J.C., Beal, D.N., Lauder, G.V. and Triantafyllou, M.S., (2003). Fish exploiting vortices decrease muscle activity. *Science*, 302(5650), 1566-1569.

Liang, S.J., Neitzel, G.P. and Aidun, C.K., (1997). Finite element computations for unsteady fluid and elastic membrane interaction problems. *International Journal for Numerical Methods in Fluids*, 24(11), 1091-1110.

Liu, H.F., Luo, X.Y., Cai, Z.X. and Pedley, T.J., (2009). Sensitivity of unsteady collapsible channel flows to modelling assumptions. *Communications in Numerical Methods in Engineering*, 25(5), 483-504.

Liu, Y., Chakrabarti, B., Saintillan, D., Lindner, A., and du Roure, O. (2018). Morphological transitions of elastic filaments in shear flow. *Proceedings of the National Academy of Sciences*, 115(38), 9438-9443.

López, H.M., Hulin, J.P., Auradou, H. and D'Angelo, M.V., (2015). Deformation of a flexible fiber in a viscous flow past an obstacle. *Physics of Fluids*, 27(1), 013102.

Luo, X.Y. and Pedley, T.J., (1996). A numerical simulation of unsteady flow in a two-dimensional collapsible channel. *Journal of Fluid Mechanics*, 314, 191-225.

Luo, X.Y., Cai, Z.X., Li, W.G. and Pedley, T.J., (2008). The cascade structure of linear instability in collapsible channel flows. *Journal of Fluid Mechanics*, 600, 45-76.

Maniyeri, R. and Kang, S., (2012). Numerical study on the rotation of an elastic rod in a viscous fluid using an immersed boundary method. *Journal of Mechanical Science and Technology*, 26(5),1515-1522.

Maniyeri, R., Suh, Y.K., Kang, S. and Kim, M.J., (2012). Numerical study on the propulsion of a bacterial flagellum in a viscous fluid using an immersed boundary method. *Computers & Fluids*, 62, 13-24.

Maniyeri, R. and Kang, S., (2014a). Numerical study on bacterial flagellar bundling and tumbling in a viscous fluid using an immersed boundary method. *Applied Mathematical Modelling*, 38(14), 3567-3590.

Maniyeri, R. and Kang, S., (2014b). Hydrodynamic interaction between two swimming bacterial flagella in a viscous fluid–a numerical study using an immersed boundary method. *Progress in Computational Fluid Dynamics, an International Journal*, 14(6), 375-385.

Mittal, R. and Iaccarino, G., (2005). Immersed boundary methods. *Annual Review of Fluid Mechanics*, 37, 239-261.

Musielak, M. M., Karp-Boss, L., Jumars, P. A., & Fauci, L. J. (2009). Nutrient transport and acquisition by diatom chains in a moving fluid. *Journal of Fluid Mechanics*, 638, 401-421.

Nguyen, H., & Fauci, L. (2014). Hydrodynamics of diatom chains and semiflexible fibres. *Journal of The Royal Society Interface*, 11(96), 20140314.

Olson, S.D., Lim, S. and Cortez, R., (2013). Modeling the dynamics of an elastic rod with intrinsic curvature and twist using a regularized Stokes formulation. *Journal of Computational Physics*, 238,169-187.

Ouyang, K., Wu, S.J. and Huang, H.H., (2013). Optimum parameter design of microbubble drag reduction in a turbulent flow by the taguchi method combined with artificial neural networks. *Journal of Fluids Engineering*, 135(11),111301.

Pandya, D.A., Dennis, B.H. and Russell, R.D., (2017). A computational fluid dynamics based artificial neural network model to predict solid particle erosion. *Wear*, 378, 198-210.

Park, S.G., Chang, C.B., Huang, W.X. and Sung, H.J., (2014). Simulation of swimming oblate jellyfish with a paddling-based locomotion. *Journal of Fluid Mechanics*, 748, 731-755.

Park, S.G., Kim, B., Lee, J., Huang, W.X. and Sung, H.J., (2015). Dynamics of prolate jellyfish with a jet-based locomotion. *Journal of Fluids and Structures*, *57*, 331-343.

Pawłowska, S., (2016). Highly deformable nanofilaments in flow. *In Journal of Physics: Conference Series*, 760(1), IOP Publishing, Bristol, United Kingdom, 012022.

Pena, F.L., Casás, V.D., Gosset, A. and Duro, R.J., (2012). A surrogate method based on the enhancement of low fidelity computational fluid dynamics approximations by artificial neural networks. *Computers & Fluids*, 58, 112-119.

Peskin, C.S., (2002). The immersed boundary method. *Acta Numerica*, 11, 479-517.

Powers, T.R., (2010). Dynamics of filaments and membranes in a viscous fluid. *Reviews of Modern Physics*, 82(2), 1607.

Qi, D., (2007). A new method for direct simulations of flexible filament suspensions in non-zero Reynolds number flows. *International Journal for Numerical Methods in Fluids*, 54(1), 103-118.

Qin, F.H., Huang, W.X. and Sung, H.J., (2012). Simulation of small swimmer motions driven by tail/flagellum beating. *Computers & Fluids*, *55*, 109-117.

Ramgadia, A. G., and Saha, A. K. (2013). Numerical study of fully developed flow and heat transfer in a wavy passage. *International Journal of Thermal Sciences*, 67, 152-166.

Rejniak, K.A. and Dillon, R.H., (2007). A single cell-based model of the ductal tumour microarchitecture. *Computational and Mathematical Methods in Medicine*, 8(1), 51-69.

Rodenborn, B., Chen, C.H., Swinney, H.L., Liu, B. and Zhang, H.P., (2013). Propulsion of microorganisms by a helical flagellum. *Proceedings of the National Academy of Sciences*, 110(5), E338-E347.

Rosenblatt, F., (1958). The perceptron: a probabilistic model for information storage and organization in the brain. *Psychological review*, 65(6), 386.

Ross, R. F., & Klingenberg, D. J. (1997). Dynamic simulation of flexible fibers composed of linked rigid bodies. *The Journal of Chemical Physics*, 106(7), 2949-2960.

Rusconi, R. and Stocker, R., (2015). Microbes in flow. *Current Opinion in Microbiology*, 25,1-8.

Ryu, J., Park, S.G. and Sung, H.J., (2018). Flapping dynamics of inverted flags in a side-by-side arrangement. *International Journal of Heat and Fluid Flow*, 70, 131-140.

Sadlej, K., Wajnryb, E., Ekiel-Jeżewska, M.L., Lamparska, D. and Kowalewski, T.A., (2010), Dynamics of nanofibres conveyed by low Reynolds number flow in a microchannel. *International Journal of Heat and Fluid Flow*, 31(6), 996-1004.

Santarelli, C., Kempe, T. and Fröhlich, J., (2016). Immersed boundary methods for heat transfer. *International Journal of Numerical Methods for Heat & Fluid Flow*, 26(2), 504-514.

Sivanandam, S. N., and S. N. Deepa., (2006). *Introduction to neural networks using Matlab 6.0*, Tata McGraw-Hill Education, New York, United States.

Shaqfeh, E.S., (2005). The dynamics of single-molecule DNA in flow. *Journal of Non-Newtonian Fluid Mechanics*, 130(1), 1-28.

Shelley, M.J. and Ueda, T., (2000). The Stokesian hydrodynamics of flexing, stretching filaments. *Physica D: Nonlinear Phenomena*, 146(1), 221-245.

Shelley, M., Vandenberghe, N. and Zhang, J., (2005). Heavy flags undergo spontaneous oscillations in flowing water. *Physical Review Letters*, 94(9), 094302.

Shelley, M.J. and Zhang, J., (2011). Flapping and bending bodies interacting with fluid flows. *Annual Review of Fluid Mechanics*, 43, 449-465.

Shen, L., Zhang, X., Yue, D.K. and Triantafyllou, M.S., (2003). Turbulent flow over a flexible wall undergoing a streamwise travelling wave motion. *Journal of Fluid Mechanics*, 484, 197-221.

Shin, S.J. and Sung, H.J., (2010). Three-dimensional simulation of a valveless pump. *International Journal of Heat and Fluid Flow*, 31(5), 942-951.

Shin, S.J. and Sung, H.J., (2012). Dynamics of an elastic capsule in moderate Reynolds number Poiseuille flow. *International journal of Heat and Fluid Flow*, 36, 167-177.

Shin, S.J., Chang, C.B. and Sung, H.J., (2012). Simulation of a valveless pump with an elastic tube. *International Journal of Heat and Fluid Flow*, 38, 13-23.

Shu, C., Ren, W.W. and Yang, W.M., (2013). Novel immersed boundary methods for thermal flow problems. *International Journal of Numerical Methods for Heat & Fluid Flow*, 23(1), 124-142.

Silva, J., Cioncolini, A., and Filippone, A., (2017), Experiments on vertical flexible filaments in crossflow. *Proceeding of MACE PGR Conference*, University of Manchester, UK.

Słowicka, A.M., Ekiel-Jeżewska, M.L., Sadlej, K. and Wajnryb, E., (2012). Dynamics of fibers in a wide microchannel. *The Journal of Chemical Physics*, 136(4), 044904.

Słowicka, A.M., Wajnryb, E. and Ekiel-Jeżewska, M.L., (2013). Lateral migration of flexible fibers in Poiseuille flow between two parallel planar solid walls. *The European Physical Journal E*, 36(3), 31.

Słowicka, A.M., Wajnryb, E. and Ekiel-Jeżewska, M.L., (2015). Dynamics of flexible fibers in shear flow. *The Journal of Chemical Physics*, 143(12), 124904.

Stockie, J.M. and Green, S.I., (1998). Simulating the motion of flexible pulp fibres using the immersed boundary method. *Journal of Computational Physics*, 147(1), 147-165.

Stockie, J.M. (2002) Simulating the dynamics of flexible wood pulp fibres in suspension, in: Proceedings of the 16th Annual International Symposium on High Performance Computing Systems and Applications, IEEE Computer Society, p. 154.

Sui, Y., Teo, C. J., and Lee, P. S. (2012). Direct numerical simulation of fluid flow and heat transfer in periodic wavy channels with rectangular cross-sections. *International Journal of Heat and Mass Transfer*, 55(1), 73-88.

Sygulski, R., (2007). Stability of membrane in low subsonic flow. *International Journal of Non-Linear Mechanics*, 42(1), 196-202.

Taheri, M.H., Abbasi, M. and Jamei, M.K., (2019). Using artificial neural network for computing the development length of MHD channel flows. *Mechanics Research Communications*, 99, 8-14.

Taneda, S., (1968). Waving motions of flags. *Journal of the Physical Society of Japan*, 24(2), 392-401.

Tatsuo, N., Shinichiro, M., Shingho, A., and Yuji, K. (1990). Flow observations and mass transfer characteristics in symmetrical wavy-walled channels at moderate Reynolds numbers for steady flow. *International Journal of Heat and Mass Transfer*, 33(5), 835-845.

Thaokar, R.M. and Kumaran, V., (2002). Stability of fluid flow past a membrane. *Journal of Fluid Mechanics*, 472, 29-50.

Tornberg, A.K. and Shelley, M.J., (2004). Simulating the dynamics and interactions of flexible fibers in Stokes flows. *Journal of Computational Physics*, 196(1), 8-40.

Ulrike, K.M., (2003). Fish'n flag. *Science*, 302(5650), 1511-1512.

Usta, O.B., Butler, J.E. and Ladd, A.J., (2007). Transverse migration of a confined polymer driven by an external force. *Physical Review Letters*, 98(9), 098301.

Vahidkhah, K., and Abdollahi, V. (2012). Numerical simulation of a flexible fiber deformation in a viscous flow by the immersed boundary-lattice Boltzmann method. *Communications in Nonlinear Science and Numerical Simulation*, 17(3), 1475-1484.

Vanella, M., Posa, A., & Balaras, E. (2014). Adaptive mesh refinement for immersed boundary methods. *Journal of Fluids Engineering*, 136(4), 040909.

Vogel, R. and Stark, H., (2012). Motor-driven bacterial flagella and buckling instabilities. *The European Physical Journal E*, 35(2),15.

Vogel, S., (1994). *Life in moving fluids: the physical biology of flow*. Princeton University Press, Princeton, New Jersey, United States.

Vogl, T.P., Mangis, J.K., Rigler, A.K., Zink, W.T. and Alkon, D.L., (1988). Accelerating the convergence of the back-propagation method. *Biological Cybernetics*, 59(4-5), 257-263.

Wang, G. V., and Vanka, S. P. (1995). Convective heat transfer in periodic wavy passages. *International Journal of Heat and Mass Transfer*, 38(17), 3219-3230.

Watanabe, Y., Suzuki, S., Sugihara, M. and Sueoka, Y., (2002). An experimental study of paper flutter. *Journal of Fluids and Structures*, 16(4), 529-542.

Werbos, P., (1974), Beyond Regression: New Tools for Prediction and Analysis in the Behavioral Sciences. Ph. D. dissertation, Harvard University, Cambridge, MA, United States.

Wiens, J.K. and Stockie, J.M., (2015). Simulating flexible fiber suspensions using a scalable immersed boundary algorithm. *Computer Methods in Applied Mechanics and Engineering*, 290, 1-18.

Xia, G. and Lin, C.L., (2008). An unstructured finite volume approach for structural dynamics in response to fluid motions. *Computers & Structures*, 86(7-8), 684-701.

Yamamoto, S. and Matsuoka, T., (1993). A method for dynamic simulation of rigid and flexible fibers in a flow field. *The Journal of Chemical Physics*, 98(1), 644-650.

Young, A. M., Karp-Boss, L., Jumars, P. A., and Landis, E. N. (2012). Quantifying diatom aspirations: Mechanical properties of chain-forming species. *Limnology and Oceanography*, 57(6), 1789-1801.

Yu, Z., (2005). A DLM/FD method for fluid/flexible-body interactions. *Journal of Computational Physics*, 207(1), 1-27.

Zhang, J., Childress, S., Libchaber, A. and Shelley, M., (2000). Flexible filaments in a flowing soap film as a model for one-dimensional flags in a two-dimensional wind. *Nature*, 408(6814), 835-839.

Zhang, L.T. and Gay, M., (2007). Immersed finite element method for fluid-structure interactions. *Journal of Fluids and Structures*, 23(6), 839-857.

Zhu, L. and Peskin, C.S., (2002). Simulation of a flapping flexible filament in a flowing soap film by the immersed boundary method. *Journal of Computational Physics*, 179(2), 452-468.

Zhu, L. and Peskin, C.S., (2007). Drag of a flexible fiber in a 2D moving viscous fluid. *Computers & Fluids*, 36(2), pp.398-406.

Zontul, H., Kurtulmuş, N., and Şahin, B. (2017). Pulsating Flow and Heat Transfer in Wavy Channel with Zero Degree Phase Shift. *European Mechanical Science*, 1(1), 31-38.

List of Publications based on Ph.D. Research Work

The thesis outlined "Investigation on the Dynamics of Flexible Filaments in Viscous Fluid" is a result of the research work carried out at the Department of Mechanical Engineering, National Institute of Technology Karnataka between July 2016 and March 2020. The research during this period has resulted in the following publications and conference proceedings.

Sl. No.	Title of the paper	Authors (in the same order as in the paper. Underline the Research Scholar's name)	Name of the Journal/ Conference, Vol., No., Pages	Month, Year of Publication	Category *
1	Numerical Analysis of the Buckling and Recuperation Dynamics of Flexible Filament using an Immersed Boundary Framework	<u>Mithun Kanchan</u> and Ranjith Maniyeri	International Journal of Heat and Fluid Flow, 77(1), pp. 256 – 277. (SCI Indexed)	April 2019	1
2	Numerical Simulation of Buckling and Asymmetric Behavior of Flexible Filament using Temporal Second-order Immersed Boundary Method	<u>Mithun Kanchan</u> and Ranjith Maniyeri	International Journal of Numerical Methods for Heat and Fluid Flow, 30 (3), pp. 1047 – 1095. (SCIE Indexed)	August 2019	1
3	Fluid-Structure Interaction Study and Flow Rate Prediction Past a Flexible Membrane using IBM and ANN Techniques	<u>Mithun Kanchan</u> and Ranjith Maniyeri	Journal of Fluids Engineering- Transactions of the ASME, 142(5): 051501. (SCI Indexed)	February 2020	1
4	Numerical Simulation and Prediction Model Development of Multiple Flexible Filaments in Viscous Shear Flow using IBM and ANN	<u>Mithun Kanchan</u> and Ranjith Maniyeri	Fluid Dynamics Research, 52(4): 045507 (SCI Indexed)	August 2020	1
5	Numerical Simulation of Flow in a Wavy Wall Microchannel Using Immersed Boundary Method	<u>Mithun Kanchan</u> and Ranjith Maniyeri	Recent Patents on Mechanical Engineering, 13(2), pp. 118 – 125. (SCOPUS Indexed)) (Research article presented in 44th National Conference on Fluid Mechanics and Fluid Power, FMFP 2017, Amrita University, Amritapuri Campus, Kollam, Kerala, India.)	May 2020	1

6	Computational Study of Fluid Flow in Wavy Channels using Immersed Boundary Method	Mithun Kanchan and Ranjith Maniyeri	Book Chapter in Soft Computing for Problem Solving, pp. 283-293, 2018, Springer Nature. (Presented in 7th International Conference on Soft Computing for Problem Solving, SocProS 2017, Indian Institute of Technology, Bhuvaneshwar, India.)	December 23 - 24, 2017	3
7	Flow Analysis for Efficient Design of Wavy Structured Microchannel Mixing Devices	Mithun Kanchan and Ranjith Maniyeri	International Conference on Design, Materials and Manufacture, IcDeM 2018, National Institute of Technology Karnataka, Surathkal. (Published in AIP Conference Proceedings, 1943, pp. 020042, 2018)	January 29 - 31, 2018	3
8	Dynamics of Flexible Filament in Viscous Oscillating Flow	Mithun Kanchan and Ranjith Maniyeri	Book Chapter in Recent Asian Research on Thermal and Fluid Sciences, pp. 147-160, 2020, Springer Nature. (Presented in 7th Asian Joint Workshop on Thermophysics and Fluid Science, AJWTF 2018, Trivandrum, India.)	November 21 - 24, 2018,	3
9	Dynamics of Flexible Filament in Viscous Oscillating Flow – A Numerical Study	Mithun Kanchan and Ranjith Maniyeri	7th International and 45th National Conference on Fluid Mechanics and Fluid Power, FMFP 2018, IIT Bombay, Mumbai, India	December 10 - 12, 2018	3
10	Numerical Analysis of Deformable Membrane in Viscous Uniform Flow	Mithun Kanchan and Ranjith Maniyeri	International Conference on Numerical Heat Transfer and Fluid Flow, NHTFF 2020, NIT Warangal, India	January 17- 19, 2020	3

*Category: 1: Journal paper, full paper reviewed   2: Journal paper, Abstract reviews   3: Conference/Symposium paper, full paper reviewed
4: Conference/Symposium paper, abstract reviewed   5: Others (including papers in Workshops, NITK Research Bulletins, Short notes etc.)

Mithun Vijay Kanchan
Research Scholar
Name & Signature, with Date

Dr. Ranjith M
Research Guide
Name & Signature, with Date

BIODATA

NAME: MITHUN VIJAY KANCHAN

DATE OF BIRTH: 12-08-1991

Mobile No.: +91 8050285780

Email: mvk1291@gmail.com

ADDRESS:

H. No. 5/74, Site No 87/3, Chitrapura – Kulai, Mangalore - 575019

QUALIFICATION:

Examination	Board/Institute	Year	Percentage/ CGPA
Ph. D (course work)	NITK, Surathkal	2016	8.25
M. Tech (Product Design)	RVCE Bangalore	2013-15	81%
B. E. (Mechanical Engg)	SJEC, Mangalore	2009-13	76%
PUC	Karnataka State Board	2007-09	90%
SSLC	Karnataka State Board	2007	92%

PROJECT EXPERIENCE:

Sr. No	Name of the company	Designation	Description	From	To
1	Ingersoll Rand India Pvt. Ltd. (in collaboration with IISc Bangalore)	Research Intern	Design of adsorption based refrigeration system	August 2014	July 2015

ACHIEVEMENTS:

1. Received MHRD scholarship while pursuing B.E degree.
2. Secured 5th Rank in Karnataka PGCET Exam under Mechanical Engineering category
3. Received TEQIP fellowship while studying M. Tech.
4. Received Best paper award at IIT Bhubaneshwar.